Doctoral Dissertation

Doctoral Program in Mechanical Engineering (30^{th}cycle)

Hydrodynamic analysis and mooring design of a floating pitching Wave Energy Converter

By

Biagio Passione

******

Supervisor(s):

Prof. Giuliana Mattiazzo

Doctoral Examination Committee:

Prof. Domenico Coiro, Referee, Università degli Studi di Napoli Federico II (Italy)

Prof. John Ringwood, Referee, Maynooth University (Ireland)

Prof. Ermina Begovic, Università degli Studi di Napoli Federico II (Italy)

Prof. Alessandro Fasana, Politecnico di Torino (Italy)

Prof. Stefano Mauro, Politecnico di Torino (Italy)

Politecnico di Torino

2018

Declaration

I hereby declare that, the contents and organization of this dissertation constitute my own original work and does not compromise in any way the rights of third parties, including those relating to the security of personal data.

Biagio Passione
2018

* This dissertation is presented in partial fulfillment of the requirements for **Ph.D. degree** in the Graduate School of Politecnico di Torino (ScuDo).

Alla mia famiglia
Agli amici di una vita
A chi mi ha accompagnato
A me

Acknowledgements

I would like to acknowledge professor Giuliana Mattiazzo for the great opportunity to join her research team at Politecnico di Torino, for the continuous support received, the motivation and all the unique experiences offered and shared during these years. A very special gratitude goes out to all the team who shared with me interests, challenges, failures and goals of the research projects. Vincenzo Orlando for sharing his large experience, for his supervision and the unlimited suggestions. Giovanni Bracco for his rigorous approach and coordination. My colleagues, for all the fun we had: Giacomo Vissio, Nicola Pozzi and Antonello Sirigu with whom I shared the entire path. Mauro Bonfanti and Panagiotis Dafnakis for the stimulating discussions and for filling the work environment with unexpected energy. My sincere thanks also goes to the Wave for Energy staff, especially Maurizio Ponzetta e Calogero Di Carlo, for their support and hard work attitude that always make a difference. I am also grateful to Professor Stefano Brizzolara and the Massachusetts Institute of Technology Sea Grant for the enrichment provided during the amazing experience in Boston. A big thanks to all the people I met and who shared with me also a short part of this exciting and irreplaceable journey. A special mention to the Marine Hydrodynamics group of Università di Napoli Federico II that has been a fundamental support for the experimental campaigns of the ISWEC device. Last but by no means least, a special thanks goes to the Polito Sailing Team for giving me always more than what I could ever give them back.

Abstract

The work presented in this thesis is part of an integrated research carried out for the development of the ISWEC technology. The key aspects of this WEC that can experience relevant improvement for the technology design and optimization are found to be hydrodynamics modelling and mooring design. These two topics are investigated in order to achieve a high reliability numerical tool for the performance analysis and testing of the ISWEC device.

The existing numerical model has been upgraded and validated against experimental results, introducing non-linear phenomena. A mooring system has been designed to be general, considering all the requirements needed for the device deployment. A design procedure has been used according to offshore conservative standards, to guarantee the feasibility of the project. The survivability of the moored device has been tested in a wave tank, reproducing the full storm duration for a severe installation site. Different mooring configurations have been tested and the best one has been identified.

The two experimental campaigns have been carried out in Napoli, at the towing tank of the Department of Industrial Engineering of Università degli studi di Napoli Federico II.

Methodologies and results presented in this thesis will be used for the design and deployment of a new ISWEC prototype to be installed in the next future.

The tools and methodologies here presented can be considered as general and used for the development of different floating WECs. More in detail, the mooring study is useful for all the floating and submerged WECs that require slack mooring systems. On the other hand, the hydrodynamic aspect analyzed in this work are common to the majority of point absorber WECs, with a particular relevance for WECs that exploit pitch or roll motions.

Contents

List of Figures

List of Tables

Chapter 1

Introduction

1.1 Motivation and scope

The global scene of the energy sector is governed by a continuous growth of the economy, driven by industrialization and urbanization that are pursued by each country all over the world, if also at different velocities. According to the International Energy Agency, the World Energy Outlook projections [89] report an average rate of economy growth of 3.4% per year and a population growth of more than 18% from today to 2040. The continuous growth is translated in the increase of energy demand [23, 88] with a forecast of a 30% expansion between today and 2040 [54, 88]. Furthermore, the present and future challenges of the global energy sector are summarized in the so-called energy trilemma defined by the World Energy Council, that pursue the balance between environmental sustainability, energy security and energy equity [184].

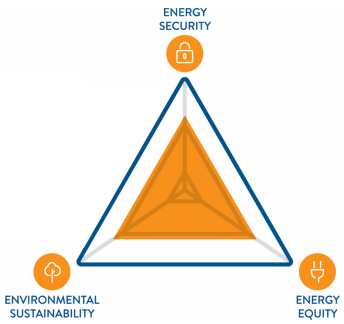

Fig. 1.1 Energy Trilemma definition. World Energy Council [184]

To meet the balance, three main trends are identified for the next future: decarbonization, digitization and decentralization of energy [183]. Renewable energies play a key role in the energy transition [151] and are in continuous rising, constituting the 61% of the new installed power capacity in 2015 [92], with a 8.3% growth during 2017 only [93]. At date, renewables represent a fundamental share of the energy production mix, contributing in 2016 for the 24% of the global electricity production [150].

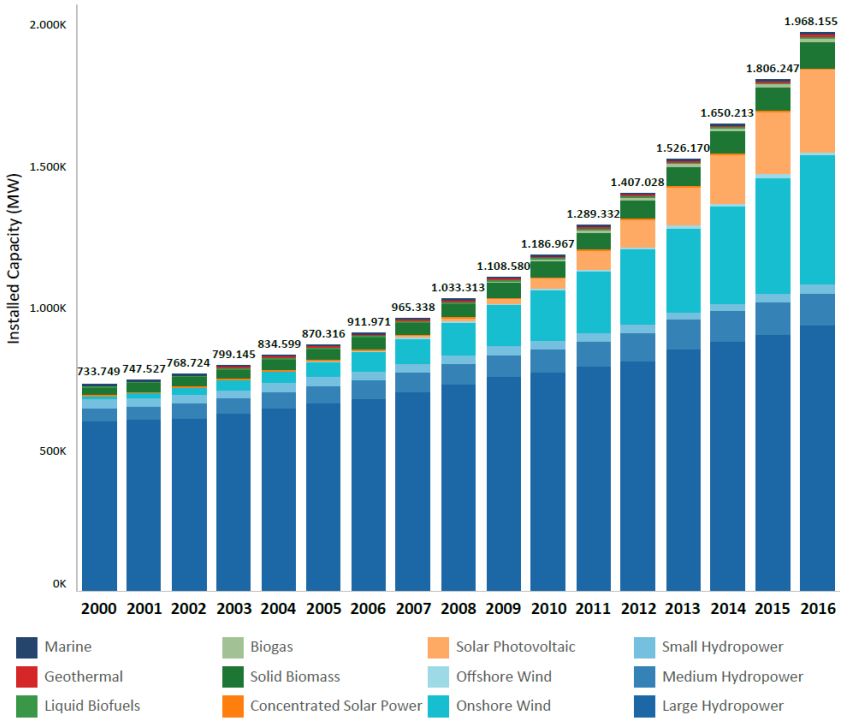

Fig. 1.2 Renewable power capacity, 2000-2016 [91]

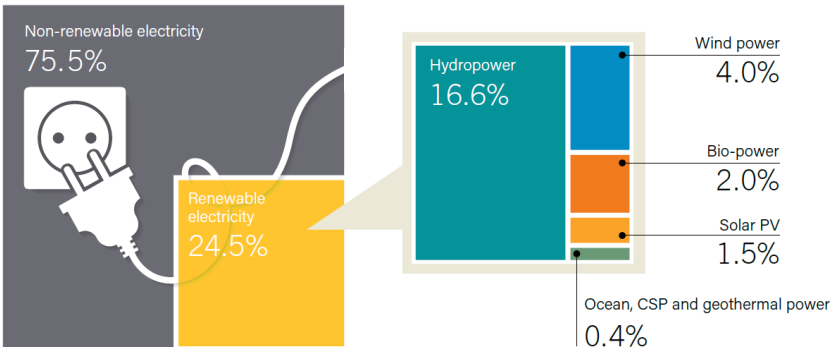

Fig. 1.3 Renewable Energy Share of Global Electricity Production, 2016 [150]

Renewable energy systems can exploit mainly three different types of sources: solar, wind and ocean energy. Among them, ocean energy has the potential to play a significant role in the future of energy, being geographically distributed and characterized by a huge capacity. Moreover, compared to wind and solar energy sources, waves are characterized by a more predictable energy output because of the high storage capacity of the sea. Waves can be forecasted 1-2 days in advance and have a longer intermittency time compared to wind and solar [51, 113]. In particular, oceans constitute over 70% of the earth's mass [103] and the population distribution is for the 44% located nearby coasts [172]. The total ocean energy is divided among tidal currents, water wave and thermal gradients. More in detail, the most promising is the wave power[103], with a potential of 2985 GW [75, 113], corresponding to a wave energy potential of 32 PWh [182], and representing a large part of the overall world energy consumption that accounts for around 159 PWh (last official data are available for 2014)[150].

Nowadays, while wind and solar energy systems are widely used all over the world, marine energy, and in particular wave energy sector delays its take-off. This delay is due to a combination of intrinsic technical challenges connected to the harsh marine environment together with a combination of high up-front and capital costs [128]. Nevertheless, thanks to its promising features [43, 173], the support of ocean energy development is rising from a policy standpoint, leading to strategic roadmaps and governmental initiatives around the world. The European Union is currently at the forefront of ocean energy technology development [114], that has been identified as a key technological area within the Strategic Energy Technology Plan [101].

During the last few decades, several technologies have been proposed for wave energy harvesting, that currently present different levels of development. Details on the possible solutions and different classifications can be found in [51, 47, 113]. To lead the wave energy sector at a commercial stage, cost-reduction targets have been identified to let the levelized cost of energy (LCOE) for wave energy converters (WECs) to be competitive with other renewables [44, 45].

The last generation of WECs is represented by different concepts that can be grouped in a unique category: *offshore floating devices*. The development of these devices is founded of two fundamental aspects: the technology innovation that provides the tools for exploring new environments and the availability of a higher power density far from coasts. On the other hand, the extreme environment is a

source of higher loads for the device, resulting in the need of a more accurate design procedure. To meet the policy and market requirements, research is still needed on the key aspects of the design and development of these WECs.

For the design, development and optimization process of a floating WEC, it is necessary to develop reliable numerical models that consider the complete power conversion chain, from the waves to the electrical grid connection. Furthermore, despite the crucial role of the numerical tools, experimental campaigns are fundamental during all the development stages, to confirm the expectation, tune and validate the design tools[181]. The economic viability of wave energy can be substantially improved optimizing the analysis and design methodologies, and acting on several parameters [36] of the considered technology. According to different studies present in literature, two key topics have been identified as most relevant for an improvement in the design and development tools and methodologies for floating wave energy converters: the hydrodynamics of the floating device [139, 163] and the mooring system [42, 168, 169].

In this thesis, a deep hydrodynamic analysis is proposed for a floating pitching wave energy converter. The hydrodynamic model is presented and the theory at the basis of its formulation is examined in depth. The possible improvements are highlighted and introduced. Different numerical techniques have been explored, presenting advantages and limitations. Eventually, a combination of these techniques is identified as the most suitable for WEC preliminary design, productivity analysis and control logic development.

In the second part of this thesis, the mooring system of a floating pitching wave energy converter is studied. The state of the art has been analyzed and a solution has been identified as the most reliable and best one to meet all the system requirements. Mooring system is a key component of a floating wave energy converter, from both survivability and economic points of view, representing from the 18% [61] to the 30% [62] of the total investment. Based on the specific ongoing research studies [62, 133, 187], a design methodology has been identified and pursued for the design of the mooring system for a pitching floating WEC.

All the work is validated against experimental tests performed during two different experimental campaigns on a 1:20 scaled model of a specific WEC. A good agreement was obtained for the majority of tests and key aspects of the WEC design. Thus, methodologies and models have been successfully validated.

The main goal of this work, is to present the major developments in the design tools and methodologies used for a specific WEC. Nevertheless, the major findings can be generalized and the developed tools can be used for the design and development of different floating WECs.

1.2 Case study

This work is part of the development framework of the Inertial Wave Energy Converter (ISWEC) technology.

The ISWEC is single body offshore floating wave energy converter. Its main characteristics consist in the monolithic hull that is the only interface with the incident waves, and the gyroscopic system that enables the conversion of the kinetic energy into electrical energy. All the mechanical parts are sealed in the inner volume of the floating hull. Two gyroscopic units are installed with their respective electric PTO for power conversion. A power conditioning system is installed on-board to provide a smooth power output, suitable for the grid connection. The *plug and play* connection is obtained by the electric cable, that is the only component that goes through the hull structure by means a proper sealed connection.

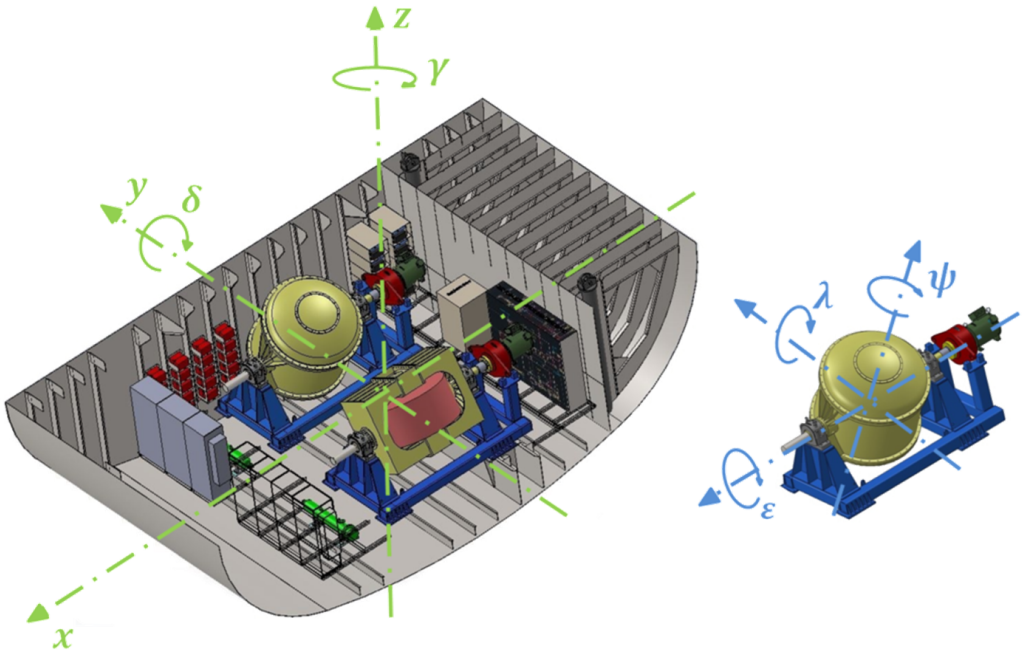

Fig. 1.4 ISWEC prototype drawings

In operational conditions, the device is aligned towards the incident wave direction. The waves induce a pitch motion of the hull around the δ axis (see Figure 1.4). Inside the floater, the flywheels that represent the core component of the gyroscopic unit rotate around their spinning axis ψ, in opposite direction between each others. The combination of pitch and flywheel motion originate a inertial gyroscopic torque acting on the ε precession axis. An electric generator (PTO) is mounted on the precession axis and controlled in torque. Braking the gyroscope motion, mechanical power is converted into electricity.

The complete power conversion chain is obtained coupling the pitch motion induced by the wave power input to the precession motion of the inner gyroscope. A singular feature of this technology, that represent a competitive advantage with respect to other WECs, is the possibility to tune the angular momentum of the flywheel, regulating its spinning velocity. This feature allows a long term active control by varying the natural frequency of the mechanical inner system that can be set to match the foreseen incoming wave climates. Furthermore, the gyroscopic system acts like an amplifier from the pitch oscillations (about 10 deg in average)

to the gyroscope oscillations (about 60 deg). This characteristic allows a more intelligent sizing of the mechanical gearbox and the electric torque motor.

Eventually, device mooring system needs to be designed in a slack configuration to minimize its influence on the floater dynamics.

Fig. 1.5 ISWEC prototype in operation. Pantelleria, Italy, 2015

The ISWEC technology was born to exploit the features of closed seas like Mediterranean, that are characterized by reduced fetches and consequently high steepness and high frequency waves. The first concept was conceived in 2005 by the Renewable Energy Research Group of the Mechanical and Aerospace Department of Politecnico di Torino [147, 175]. Through the years, the project pursued continuous success and development at different model scales [31–33, 35], passing from the first proof of concept in 2007 [24, 1] and reaching the first full scale prototype development at Pantelleria, Italy in 2015.

In Figure 1.6 a summary of the development stages of the ISWEC technology is reported. Further details of the project history are discussed in [24, 147, 175]. The author contributed to the final part of the ISWEC full scale design, construction and deployment and further improvements in the design of future ISWEC devices, derived from the gained experience.

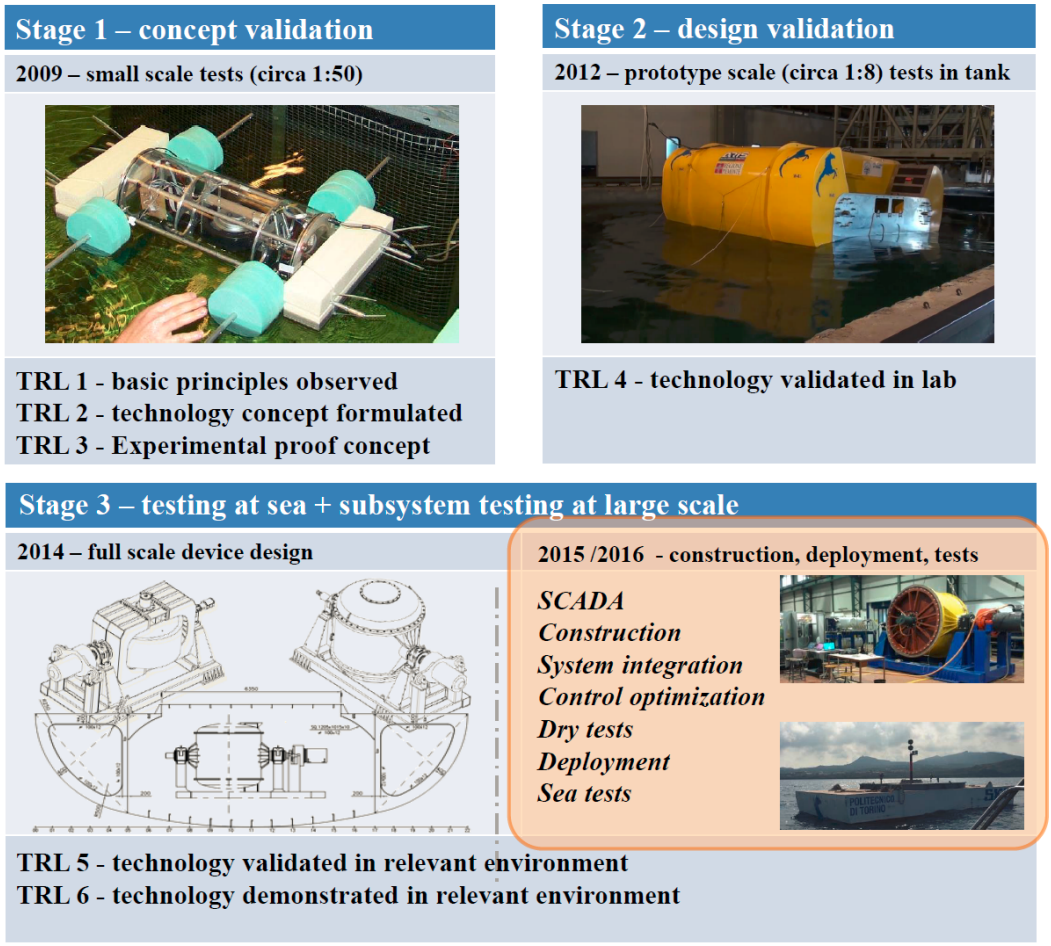

Fig. 1.6 ISWEC prototype in operation. Pantelleria, Italy, 2015

1.3 Objectives

The main objectives of this thesis are:

- Hydrodynamic analysis of a floating pitching WEC.
- Non-linear hydrodynamic forces identification and modeling for the analyzed WEC.
- Development of a high fidelity simulation setup for the detailed analysis of hydrodynamics effects on the WEC and to perform experiments in numerical wave tanks environment, with a consequent cost reduction.

- Derivation of a lumped parameters formulation of the non-linear viscous forces, to be used in a wave-to-wire model that allows low computational costs analyses.
- Deployment of a 1:20th scale ISWEC device for wave-tank testing.
- Validation of the numerical hydrodynamic model.
- Identification of the design methodology for the ISWEC mooring system
- Design and verification of the ISWEC mooring system.
- Design of a system setup for wave-tank testing of a 1:20th mooring system for the ISWEC device.
- Tank tests for the hydrodynamics of the ISWEC device and the mooring system analysis in both operational and survival conditions.

1.4 Structure and contents of the thesis

The thesis is composed of six additional Chapters, following the Introduction. Two main parts can be distinguished. In the first part, the hydrodynamic problem is addressed and in the second part the station keeping and survivability problems are discussed.

In Chapter 2 the hydrodynamics theoretical background required for the numerical modelling is presented and discussed. Particular attention is focused on the wave excitation forces and non-linear contributions.

In Chapter 3 the numerical wave to wire model of the ISWEC device is presented. The proposed model is a time-domain lumped parameters model that represents a powerful tool for productivity analysis in operational sea states. The attention of this thesis is focused on the hydrodynamic part of the model. First, the potential flow tools are used to identify the hydrodynamic properties of the ISWEC device. According to the ISWEC working principle, a detailed discussion of the main properties is proposed. Then, the non-linear hydrodynamics is studied and the best tool for the viscous forces modeling is identified. A numerical wave tank has been modeled and CFD URANS simulation are performed to identify non-linear viscous forces

contributions. Viscous forces are then identified and modeled in a simplified form, suitable to be coupled to the wave-to-wire lumped parameters model.

In Chapter 4 an experimental campaign on a 1:20th scale model is presented. The experimental campaign is performed on the free floating device to identify its hydrodynamic properties. Sea keeping regular waves tests and free decay tests are performed. Results are compared against numerical model showing a general good agreement.

In Chapter 5 the mooring system has been analyzed. A state of the art review is proposed about the existing mooring layouts for floating WECs. Requirements of the ISWEC device mooring system are presented and a suitable layout solution is found. A design methodology is proposed and pursued for the correct sizing and verification of the mooring system. A first preliminary design is performed using a quasi-static approach. The quasi-static approach, due to its light computational cost and thanks to its formulation, is particularly suitable for the integration within the time domain wave-to-wire lumped parameters model. Therefore, a deepen dynamic analysis is performed using suitable numerical tools. Key aspects of the mooring dynamic behavior are identified, highlighting advantages and drawbacks of the studied solution.

In Chapter 6 a second experimental campaign on the 1:20th scale ISWEC device is presented. This campaign is aimed to analyze the mooring performances and the survivability of the system in extreme conditions. According to a test installation site, extreme waves have been tested, simulating the whole storm duration. Survivability has been demonstrated and key findings on the dynamic behavior of the moored device have been confirmed. The results of the experimental campaign have been used as indications for further improvements of the mooring layout, in order to reduce mooring loads and optimize the overall performances.

Eventually, in Chapter 7 conclusions are outlined and possible future directions of this research work are summarized.

1.5 Candidate publications and research interests

The candidate publications produced during the PhD program demonstrate his involvement in the different areas of the ISWEC project. It is worth noticing that

several publications do not regard the specific topics of the thesis, since the research work during these years was wide and focused on all the possible aspects of the wave energy sector, in order to develop a broad view of the research field, maturing experience and increasing interests.

The list of publications in which the candidate has been involved is hereafter presented, with the detail of his specific contributions:

- Control
  - *Application of Linear Model Predictive Control to the ISWEC* [34]: the candidate contributed to the development of the reduced state space model of the ISWEC.
  - *Application of sub-optimal control techniques to a gyroscopic Wave Energy Converter* [28]: formulation of the sub-optimal control for the ISWEC and development of the numerical model.
  - *Stochastic Control of Inertial Sea Wave Energy Converter* [29, 149]: formulation of the stochastic control for the ISWEC and development of the numerical model of the control logic in Matlab.
  - *Application of a Passive Control Technique to the ISWEC* [22]: contribution to the setup and debug of the numerical model.

- Modelling
  - *Expanding ISWEC Modelling with a Lumped-Mass Mooring Line Model* [79]: contribution to the modeling of the ISWEC mooring system in MoorDyn. Characterization of the hydrodynamics inputs to the model.
  - *Modeling and optimization of a Wave Energy Converter using ANSYS AQWA* [26]: development of the ISWEC model in Ansys Aqwa environment.
  - *Integration of renewable energy to power public transport at the Island of Pantelleria* [25]: contribution to the development of the ISWEC model used for the specific application.

- Design procedures and performance analysis

  - *ISWEC Design Tool* [158, 177]: contribution to the linear model development and debug of the tool.
  - *Performance assessment of the full scale ISWEC system* [30]: contribution to the development of the ISWEC wave-to-wire model.
  - *A performance assessment methodology for floating pitching WEC arrays* [159]: contribution to the hydrodynamic modelling of the ISWEC in Ansys Aqwa.

- Experiments
  - *Identification of the hydrodynamic parameters of a wave energy converter* [148]: contribution to the design of the experiments and post-processing of the data output from the experimental campaign.
  - *Wave Tank Testing of a Pendulum Wave Energy Converter 1:12 Scale Model* [145]: contribution to the hydrodynamic model used in the design stage.
  - *Experimental evaluation of different hydrodynamic modelling techniques applied to the ISWEC* [146]: contribution to the hydrodynamic modelling in Ansys Aqwa.
  - *Numerical and Experimental Analysis of Oscillating Fluid Tanks* [135]: contribution to the simplified numerical model development. Development of the high fidelity CFD model. Design of the experiments. Post-processing of the experimental data.

Chapter 2

Hydrodynamics of a floating WEC

In this Chapter, a theoretical background is given on the hydrodynamics of floating bodies in ocean waves. A proper evaluation of the hydrodynamic loads acting on the body and their derived motions is crucial for both design stage and operational analyses of a WEC. The aim of this Chapter is to recall the theories applied in the numerical modelling of WECs, presenting a description of the different phenomena involved and clarifying how the forces acting on the body are determined. The focus is on the methods used in this work with the purpose to identify the best trade-off to obtain a suitable model according to the analysis stage.

2.1 Hydrodynamic loads and motions

The hydrodynamic interaction between ocean waves and floating bodies is a complex process that involves both linear and non-linear phenomena, therefore it is important to investigate which are the most relevant to the specific case under analysis. An accurate wave-to-wire model of a WEC needs to correctly simulate its motions in waves, that result from the hydrodynamic forces and moments acting on its structure [57]. The model is in fact based on Newton's second law that describes the balance between the inertia force of the WEC and the total forces acting on it. The loads experienced by a floating device in motion are the following [57, 100]:

- ***Hydrostatic force***: the net contribution of buoyancy and gravity forces. It is usually seen as a restoring force, due to the action of the hydrostatic pressure on the WEC's wet surface.
- ***Excitation loads***: pressure forces due to the incident waves on motionless body.
- ***Radiation loads***: pressure forces due to the disturbance waves generated by the body when it is forced to move in calm water.
- ***Drift forces***: second order pressure forces mainly due to non-symmetric wave loads and interaction between waves of different period. The result is a low frequency excitation which becomes important in large waves.
- ***Drag forces***: *form* drag and *skin friction* drag are mainly due to vortex shedding. In general, drag is proportional to the square of the relative velocity between body and fluid. These contributions may become important in storm conditions.

In general it is not possible to build a mathematical model that includes all forces contributions simultaneously [100]. Therefore it is useful first to estimate separately the orders of magnitude of the different mechanisms (inertia, gravity, viscous forces).

The motions modes are strictly connected to the excitation characteristics and can be divided in:

- ***Wave-frequency motions***: linearly excited motion associated with the significant wave energy.
- ***Slow-drift motions***: non-linear excited motion at low frequency.
- ***Mean-drift motions***: mean motions mainly induced by currents or wind.

The characterization here presented is useful for a first distinction: to assess the WEC performances it will be necessary to have a correct evaluation of the wave-frequency loads, that are responsible for the main power transfer from the waves through the device. On the other hand, for a correct design of the mooring system, it is necessary to consider drift forces that could excite the mooring resonance period [57].

The very first step in the hydrodynamic modelling of a WEC is the determination of wave induced loads, that depend on the motion field of the fluid. The fluid motion around a free moving body can be described by the equation of continuity together with the Navier-Stokes equations. The latter equations are the basis of the Computational Fluid Dynamics (CFD) and they represent the most accurate description of the physics of the problem. The solution of these equations is however difficult and time consuming, thus simplified theories have been developed under some assumptions, valid in most of the device's operational regime [55].

The estimation of radiation and excitation loads can be carried out under simplifying hypotheses using boundary element methods (BEM) codes. The BEM for hydrodynamic interaction was firstly developed by Newman [124] and allows the calculation of hydrodynamic coefficients, necessary as input in the differential equation that describes the motion of the WEC. Several books are available in literature on hydrodynamics theory. In the next section, the potential flow theory is briefly reviewed, which is the fundamental basis of the boundary elements methods (BEMs). Further details can be found in [57, 100, 38, 64].

2.2 Potential flow theory

Basic assumptions and linear theory derivation

The fluid motion is generally described by the continuity equation together with the Navier-Stokes equations. In case of water, the assumption of *incompressible Newtonian fluid*, i.e. constant density ρ, is valid:

$$\nabla \vec{\boldsymbol{u}} = \frac{\partial u}{\partial x} + \frac{\partial u}{\partial y} + \frac{\partial u}{\partial x} = 0 \tag{2.1}$$

$$\frac{\partial \vec{\boldsymbol{u}}}{\partial t} + \vec{\boldsymbol{u}} \nabla \vec{\boldsymbol{u}} = -\nabla \left(\frac{p}{\rho} + gz \right) + \nu \nabla^2 \vec{\boldsymbol{u}} \tag{2.2}$$

where (x, y, z) is a Cartesian coordinate system with the z-axis assumed vertical and directing upward, $\vec{\boldsymbol{u}} = (u, v, w)$ is the fluid velocity vector, p is the fluid pressure and ν is the kinematic viscosity of the fluid. In this formulation only gravity forces are taken into account as body forces acting on the fluid. Furthermore, linear potential theory is based on the assumption of ideal flow, i.e. *inviscid* and *irrotational*. Under

the latter hypotheses, the velocity may be expressed in terms of a so-called *velocity potential*, ϕ such that

$$u = \frac{\partial \phi}{\partial x} \qquad u = \frac{\partial \phi}{\partial y} \qquad u = \frac{\partial \phi}{\partial z} \tag{2.3}$$

Introducing the potential in the continuity equation (2.1), the *Laplace equation* is obtained:

$$\nabla^2 \phi = \frac{\partial^2 \phi}{\partial x^2} + \frac{\partial^2 \phi}{\partial y^2} + \frac{\partial^2 \phi}{\partial z^2} = 0 \tag{2.4}$$

The Navier-Stokes equations (2.2) can be written also in terms of velocity potential. Moreover, they can be simplified for inviscid fluids, neglecting the diffusive term on the right hand side and leading to the *Euler equation* in scalar form:

$$\nabla \left(\frac{\partial \phi}{\partial t} + \frac{1}{2} |\nabla \phi|^2 \right) = -\nabla \left(\frac{p}{\rho} + gz \right) \tag{2.5}$$

Integrating Eq. (2.5) yields to the *Bernoulli equation* in its unsteady form:

$$p = -\rho \frac{\partial \phi}{\partial t} - \frac{1}{2} \rho |\nabla \phi|^2 - \rho g z + p_{atm} \tag{2.6}$$

A *hydrostatic* part and a *hydrodynamic* part constitute the total pressure:

$$p_{static} = -\rho g z + p_{atm} \qquad p_{dyn} = -\rho \frac{\partial \phi}{\partial t} - \frac{1}{2} \rho |\nabla \phi|^2 \tag{2.7}$$

The hydrodynamic pressure is non-linear, as presents a quadratic term. To linearize the theory and apply it to the waves problem it is necessary to assume that the wavelength is much larger than the wave amplitude, i.e. *small steepness* waves. The second-order term can thus be neglected. This assumption is valid in most wave-induced motion but may be not adequate for severe sea states.

Boundary conditions

To determine the hydrodynamic pressure distribution around the floating body it is necessary that the potential satisfies the Laplace equation (2.4) along with several constraints. The boundary conditions are defined at the seabed, the water free-surface and on the body surface and are divided in kinematic and dynamic.

On the *body surface* and the *seabed*, the *kinematic boundary condition* must be satisfied. This means that both the seabed and the body are impermeable and the component of the fluid velocity normal to the surface u_n is equal to the surface velocity. For the floating body, under the *linear hypothesis*, the condition is defined for its equilibrium position that is on the body mean wet surface:

$$\frac{\partial \phi}{\partial n} = \vec{\boldsymbol{u}} \cdot \vec{\boldsymbol{n}} = u_n \tag{2.8}$$

At the seabed, assuming that it is flat, the vertical velocity of water particles is zero:

$$\frac{\partial \phi}{\partial z} = 0 \quad \text{on} \quad z = -h \tag{2.9}$$

where h is the water depth.

On the *water free-surface* both *dynamic* and *kinematic* conditions must be satisfied. As for the floating body, the linear theory assumes that the boundary conditions on the free-surface are applied at its equilibrium position instead of the instantaneous position. The dynamic condition relies on the assumption that the water pressure is equal to the constant atmospheric pressure p_{atm}. Introducing this condition in Eq. (2.6) and applying the *linear hypothesis*, it results:

$$\frac{\partial \phi}{\partial t} + g\eta = 0 \quad \text{on} \quad z = 0 \tag{2.10}$$

where the free-surface is defined as $z = \eta(x,y,t)$ and η is the wave elevation, i.e. the free-surface elevation, positive for $z > 0$. The kinematic condition, so-called *no-leak condition* states that the fluid velocity component normal to the free-surface must be equal to the surface velocity:

$$\frac{\partial \eta}{\partial t} = \frac{\partial \phi}{\partial z} \quad \text{on} \quad z = 0 \tag{2.11}$$

Combining Eqs (2.10) and (2.11) a general form of the free-surface boundary condition is obtained, so-called *Cauchy-Poisson condition*:

$$\frac{\partial^2 \phi}{\partial t^2} + g\frac{\partial \phi}{\partial z} = 0 \quad \text{on} \quad z = 0 \tag{2.12}$$

In general, the free-surface boundary condition depends on the body forward speed. The potential theory is valid with the assumption of *zero forward speed*.

The last boundary condition to be satisfied is the *radiation condition*: the potential must decay as the distance from the body increases. This physically means that the wave field will coincide to the undisturbed wave field far from the body:

$$\phi \propto \frac{e^{-jkR_b}}{\sqrt{kR_b}} \quad \text{for} \quad R_b \to \infty \tag{2.13}$$

where k is the *wave number* and R_b is the radial distance from the body.

2.3 Waves interaction with a floating body

Motion modes of a floating body

A free floating rigid body in ocean waves has six degrees of freedom (DoFs): three translational and three rotational. The oscillatory motions of the body are defined with respect to a set of three orthogonal axes centered in the center of gravity (COG) of the body. Using the seakeeping notation the motions are defined as:

- ***Surge***: translational (longitudinal) motion about the x-axis.
- ***Sway***: translational (transverse) motion about the y-axis.
- ***Heave***: translational (vertical) motion about the z-axis.
- ***Roll***: rotational motion about the x-axis.
- ***Pitch***: rotational motion about the y-axis.
- ***Yaw***: rotational motion about the z-axis.

Monochromatic wave potential

To use the linear potential flow theory for the waves-body interaction problem, it is necessary to follow the linear wave theory developed by Airy [2] and based on the *small steepness* assumption. According to it, the simplest wave motion may be represented by a sinusoidal (monochromatic), long-crested, progressive wave.

Therefore, the velocity potential is sinusoidal and can be expressed in a complex form:

$$\phi_w(x,y,z,t) = \mathrm{Re}\{\hat{\phi}_w(x,y,z,t)e^{j\omega t}\} \tag{2.14}$$

The *Linear Superposition Theorem* can be applied to describe the wave field surrounding a floating body as the sum of three different contributions: *Incident*, *Diffracted* and *Radiated* wave field. Then wave potential can be written as:

$$\phi_w = \phi_I + \phi_D + \phi_R \tag{2.15}$$

The different parts of the wave potential are defined as follows:

- ***Incident wave potential***, ϕ_I: related to the undisturbed incident wave field defined as the wave propagating in the absence of the body. It must satisfy the *free-surface* condition and the boundary condition at the *seabed*. The complex amplitude of the potential of the undisturbed wave field is given by:

$$\hat{\phi}_I = \frac{jga_w}{\omega}\frac{\cosh[k(z+h)]}{\cosh kh}e^{\{-jk(x\cos\beta+y\cos\beta)\}} \tag{2.16}$$

  where:

  - a_w: sinusoidal wave amplitude
  - ω: angular frequency of the incident wave
  - k: wave number
  - h: water depth
  - β: wave direction (angle between the wave propagation direction and the positive x-axis

- ***Diffracted wave potential***, ϕ_S: related to the diffracted or scattered wave which is generated by the interaction of the incident wave and the motionless body. *Free-surface* and *seabed* conditions must be fulfilled together with the far field *radiation* condition. Furthermore, the sum of the incident and diffracted potential must satisfy the *body* boundary condition on the floater wet surface S_b:

$$-\frac{\partial\hat{\phi}_D}{\partial n} = \frac{\partial\hat{\phi}_I}{\partial n} \quad \text{on} \quad S_b \tag{2.17}$$

- ***Radiated wave potential***, ϕ_R: related to the radiation wave which is generated by the body oscillatory motions in the absence of the incident wave field, i.e. in calm water. This potential must satisfy the *free-surface*, *seabed* and *body* boundary conditions. The complex amplitude of the potential is expressed as:

$$\hat{\phi}_R = j\omega \sum_{i=1}^{N} \hat{\xi}_i \hat{\phi}_i \tag{2.18}$$

  where $\hat{\xi}_i$ is the complex amplitude of the body harmonic motion mode i and ϕ_i is the radiation potential related to the motion mode i with unit amplitude.

2.4 First Order pressure forces

The pressure forces are the external forces acting on a floating WEC interacting with ocean waves, and can be divided in *hydrostatic* and *hydrodynamic*. The potential flow hydrodynamic F_{pd} and the hydrostatic F_{ps} forces are determined by integrating the pressure field on the mean submerged body surface S_b:

$$F_{p,tot} = F_{ps} + F_{pd} = -\int_{S_b} p_{static}\vec{\boldsymbol{n}}\, dS_b - \int_{S_b} p_{dyn}\vec{\boldsymbol{n}}\, dS_b \tag{2.19}$$

Introducing the Bernoulli equation (2.6) under the linear hypothesis, it results:

$$F_{ps} = \rho g \int_{S_b} z\vec{\boldsymbol{n}}\, dS_b \quad \text{and} \quad F_{pd} = \rho \int_{S_b} \frac{\partial \phi}{\partial t}\vec{\boldsymbol{n}}\, dS_b \tag{2.20}$$

In accordance with the linear theory, assuming that all phenomena involved in the wave-body interaction are harmonic in time, both the motions and the forces can be expressed by a complex quantity that oscillates with the same angular frequency ω of the wave:

$$\xi(t) = \mathrm{Re}\{\hat{\xi}(\omega)e^{j\omega t}\} \tag{2.21}$$

$$F(t) = \mathrm{Re}\{\hat{F}(\omega)e^{j\omega t}\} \tag{2.22}$$

Hydrostatic Force

The linearized hydrostatic force resulting from the integration over the mean wet surface provides an accurate approximation for small amplitude motions of the body. In this case the force is proportional to the displacement and it results:

$$\hat{F}_{ps} = -K\hat{\xi} \tag{2.23}$$

where K is the *hydrostatic stiffness*.

Hydrodynamic Force

To calculate the hydrodynamic pressure distribution around a floating body, the boundary value problem presented in section 2.2, along with the Airy linear theory which defines the wave potential (section 2.3), are used.

The hydrodynamic force due to the interaction of the unit amplitude incident wave with the diffraction wave and the radiation wave generated by the unit amplitude motions can be written as:

$$\hat{F}_{pd} = \hat{F}_{exc} + \hat{F}_{rad} = j\omega\rho \int_{S_b} \left(\hat{\phi}_I + \hat{\phi}_D\right) \vec{\boldsymbol{n}}\, dS_b - \omega^2\rho \int_{S_b} \sum_{i=1}^{6} \hat{\xi}_i \hat{\phi}_i \vec{\boldsymbol{n}}\, dS_b \tag{2.24}$$

Eq. (2.24) allows to divide the force in two effects: the *wave excitation force* F_{exc} and the *radiation force* F_{rad}. The excitation force considers the effect of the pressure forces acting on the fixed body in regular wave and represents the active component of the total F_{pd}. The radiation force represents the reactive component and it is due to the displacement of water induced by the forced motion of the body in absence of an incident wave field.

Moreover, the *wave excitation force* can be divided in two components:

$$\hat{F}_{exc} = \hat{F}_{FK} + \hat{F}_D = j\omega\rho \int_{S_b} \hat{\phi}_I \vec{\boldsymbol{n}}\, dS_b + j\omega\rho \int_{S_b} \hat{\phi}_D \vec{\boldsymbol{n}}\, dS_b \tag{2.25}$$

where:

- ***Froude-Krylov force***, F_{FK}: takes into account the undisturbed incident wave velocity potential on the mean wet surface of the motionless body. This

contribution is so-called *linear Froude-Krylov force* and it will be the one considered within this work.

- ***Diffraction force***, F_D: results from the integration of the scattered wave potential over the mean wet surface of the motionless body. It represents a correction to the Froude-Krylov term that considers the effective disturbance of the wave field due to the presence of the body.

The *radiation force* in its complex form can be expanded in real and imaginary parts, corresponding respectively to the real and imaginary parts of the radiation potential. For a single DoF:

$$\hat{\phi}_i = \mathrm{Re}\{\phi_i\} + j\,\mathrm{Im}\{\phi_i\} \tag{2.26}$$

that was introduced in (2.24), gives:

$$\hat{F}_{rad} = -j\omega B_i \hat{\dot{\xi}}_i + \omega^2 A_i \hat{\xi}_i \tag{2.27}$$

where:

- $B_i = -j\omega\rho \int_{S_b} \mathrm{Re}\{\phi_i\}\,\vec{\boldsymbol{n}}\,dS_b$: ***hydrodynamic wave damping*** coefficient for the i_{th} motion.
- $A_i = -j\omega\rho \int_{S_b} \mathrm{Im}\{\phi_i\}\,\vec{\boldsymbol{n}}\,dS_b$: ***hydrodynamic added mass*** coefficient for the i_{th} motion.

The damping part of the radiation force is in phase opposition with the body velocity while the added mass part is in phase with the body acceleration. Using the electric analogy, the radiation forces can be seen as an hydrodynamic impedance. The *resistive* contribution to the impedance is the *damping*, which constitutes the dissipation effect related to the energy transfer from the body to the water. The *reactive* contribution related to the energy storage is the *added mass*. This term physically represents an inertia force related to the mass of water entrained with the body motion. With the assumption of harmonic response, when averaged over time, the net power flow between the body and the fluid due to the added mass interaction is equal to zero.

2.5 Second Order pressure forces

Second order wave forces are calculated using the potential theory up to the second order of the velocity potential. They follow from the combination of the quadratic terms in the pressure, the quadratic terms in the wave height and the first-order body motions. The results are forces proportional to the square of the incident wave amplitude that are present if waves are characterized by more than a single frequency (wave spectrum) [57, 100, 109]. These forces are in general a function of two frequencies and can be divided in: mean loads, high frequency oscillating loads and low frequency oscillating loads.

The high frequency components are so called *sum-frequency* effects and are characterized by a frequency which is double the waves frequencies. These effects are present only when the body interacts with waves that propagate in opposite directions and are due to the quadratic velocity term in the Bernoulli's equation [57]. High frequency contributions may excite heave, pitch and roll motions of fixed structures or very stiff mooring systems. This is not the case of floating WECs. Moreover, sum-frequency effects are inversely proportional to the depth [57] and they are worth to analyze for structures with deep submerged parts.

Mean and *slowly-varying* (*difference-frequency*) second-order forces also are present in waves with more than a single frequency component. These loads are particularly important for moored structures:

- ***Mean wave drift forces*** result in a constant load that together with the mooring system determine the new equilibrium position on the horizontal plane.
- ***Low-frequency wave drift forces*** can excite the natural frequency of the moored structure in surge resulting in large amplitude oscillations that can stress the mooring line.

The constant second-order drift forces and moments in the zero-forward-speed can be determined from the first-order velocity potential flow problem, as demonstrated by Maruo [117] and Newman [122]. The mathematical demonstration can be found in several books and papers [57, 100, 109, 86]. In this work, only the summary considerations are reported, which are useful for the WEC analysis. Basically, two alternative approaches can be used to calculate mean wave drift forces: *Far Field solution* and *Near Field solution*.

Far Field Solution

The solution is based on the conservation of the momentum in the fluid surrounding the body. With this method is possible to evaluate the mean drift forces on the horizontal plane. Maruo derived the equation for horizontal drift forces on a two-dimensional body in regular waves:

$$\overline{F}_{2D} = \frac{\rho g}{2} {a_R}^2 \tag{2.28}$$

where a_R is the amplitude of wave reflected by the body. The direction of $\overline{F}_{2D}$ always coincides with the wave propagation direction. This formula is useful to understand that the drift forces are strictly connected with the capability of the body to generate waves. This capability significantly reduces for long wavelengths compared to the body size while it is maximized near the body's resonance where a peak of mean drift forces is experienced. Moreover, the amplitude of the reflected wave can never be higher than the amplitude of the incident wave a_w. If the wave is fully reflected, $a_r = a_w$. This results in an upper limit for the mean wave drift force. In case of WECs, the upper limit would be even lower because of the power absorption from the incident wave.

Near Field Solution

The method is based on the direct integration of the pressure on the wet surface of the body and was developed by Pinkster [144]. Near Field solution is usually recommended because it allows to evaluate wave drift forces on both horizontal and vertical planes and it is valid also for the analysis of multiple interacting bodies. Furthermore, this method allows to include in the solution both the mean drift and slow-varying drift effects present in irregular waves. The result of the application of the direct integration are time domain equations, non linear functions of the first and second order velocity potential. These equations are then used to compute the so called ***Quadratic Transfer Fucntions*** (QTFs) that summarize the mean and the low frequency forces effects in frequency domain.

2.6 Equation of Motion of a floating WEC

The dynamic of a rigid body is described by the Newton's second law. For a floating body in waves, the general equation of motion in time domain is given by

$$M\ddot{X}(t) = F_{ext}(t) \tag{2.29}$$

In general, this is a matrix equation in which all the DoFs of the body are considered. The different terms of the equation are:

- $M(6x6)$ is the diagonal inertia matrix of the six DoFs body

$$M = diag(m, m, m, I_{xx}, I_{yy}, I_{zz}) \tag{2.30}$$

  where m is the total mass of the body and I_{xx},I_{yy} and I_{zz} are the inertia moments calculated with respect to the reference frame centered in the COG with the principal axes of inertia.

- $X(6x1)$ is the vector composed by the six DoFs of the floating body

$$X = \begin{Bmatrix} surge \\ sway \\ heave \\ roll \\ pitch \\ yaw \end{Bmatrix} = \begin{Bmatrix} x \\ y \\ z \\ rx \\ ry \\ rz \end{Bmatrix} \tag{2.31}$$

- F_{ext} is the vector of the external forces applied to the floating body. As presented in the previous sections, the external forces are the pressure forces due to the interaction with the incident wave.

The pressure forces need to be calculated by solving the potential flow boundary value problem presented in the previous sections. This problem has no analytic solution unless the geometry of the body is very simple. As stated in section 2.1, panel methods are used to solve the boundary integral equation using the Green function [57, 100, 64]. Different commercial codes are available for the solution of the problem as WAMIT [179], developed by Newman, MOSES [17] and ANSYS

Aqwa [6]. In this work ANSYS Aqwa will be used to determine the hydrodynamic forces. Aqwa allows the calculation of both first order and second order drift forces. The main library is a three-dimensional, frequency domain, free surface, radiation/diffraction code that allows the calculation of the different contributions for monochromatic waves at different frequencies and incidence direction, set by the user according to the problem.

Frequency domain model

The first step in building a dynamic model of a floating WEC, is to use a frequency domain approach, based on the linear theory presented in the previous sections. Under the assumption of harmonic motions and incident monochromatic wave, it is possible to write the seakeeping matrix equation of motion in frequency domain [124, 65]:

$$\{-\omega^2 [M + A(\omega)] + j\omega B(\omega) + K\} X(j\omega) = F_w(j\omega) \tag{2.32}$$

where

- ω is the angular frequency of the incident wave.
- $A(6x6)$ and $B(6x6)$ are respectively the frequency dependent hydrodynamic linear added mass matrix and linear hydrodynamic damping matrix, which elements are derived from Eq. (2.27). The radiation forces matrices are both symmetric and, according to the radiation boundary condition, the damping matrix is positive definite. It is worth noting that off diagonal terms are present, representing the couplings between the different DoFs. For a moored pitching floating WEC the coupling between surge and pitch is the most important.
- $K(6x6)$ is the linear hydrostatic stiffness matrix, which elements are derived from Eq. (2.23).
- $F_w(6x1)$ is the frequency dependent wave excitation forces vector, calculated as:

  $$F_w(j\omega) = a_w f_w(j\omega) \tag{2.33}$$

  According to the linear potential flow theory, the first order excitation forces are proportional to the incident wave amplitude a_w and derived from Eq. (2.25). The force coefficients per unit amplitude f_w are the so called *Froude-Krylov*

and diffraction coefficients and are dependent on the wave direction also, since the incident wave field is influenced by the body geometry.

All the coefficients of Eq. (2.32) are the outputs of the radiation and diffraction analysis in Ansys Aqwa [6] and constitutes the hydrodynamic database used to build the wave-to-wire model of a floating WEC.

The performances of the WEC floater can be evaluated starting from the motion response in regular waves. The transfer function that determines the dynamic response of a floating body as a function of the frequency of the incident wave is called *Response Amplitude Operator* (RAO). It is defined for each DoF and wave direction as the ratio between the amplitude of the floater motion in the i_{th} DoF and the wave amplitude:

$$RAO_i(\omega) = \frac{X_i}{a_w} = \frac{f_{w,i}(\omega)}{-\omega^2 [M_{ii} + A_{ii}(\omega)] + j\omega B_{ii}(\omega) + K_{ii}} \tag{2.34}$$

Time domain model

The time domain model of a floating WEC is based on the Cummins' integro-differential equation (1962), that uses the same approach of the frequency domain model [40].

$$(M + A_\infty)\ddot{X}(t) + \int_0^t h_r(t-\tau)\dot{X}(t)d\tau + KX(t) = F_w(t) \tag{2.35}$$

Two different terms are present with respect to Eq. (2.32):

- A_∞ is the matrix of the added mass at infinite frequency
- $h_r(t)$ is the *radiation impulse response function*. The convolution term models the radiation hydrodynamic problem in an ideal fluid with a linear pressure force distribution and it is often referred as *fluid memory effect*, because takes into account the energy of the radiated waves due to the past motion of the body.

It is worth noting that in Eq. (2.35) there are no linearity limitations on the external forces, hence the model is potentially capable to deal with non-linear contributions. It is possible to introduce non-linear hydrodynamic forces as well non linear control laws, useful to test the WEC performances in more realistic conditions.

Radiation forces in time domain

The calculation of the convolution term in Eq. (2.35) requires a high computational time and it is not well suited for the design and analysis of a Wave Energy Converter. A solution to overcome this problem was found by Perez and Fossen [142, 141], and it is the one used in this work.

First, the radiation impulse response function is calculated from the frequency dependent hydrodynamic damping coefficient. The relation between time and frequency domain was found by Ogilvie [129], who converted Cummins' equation in the frequency domain under only wave excitation forces, obtaining Eq. (2.32). He found the following relationships:

$$A(\omega) = A_\infty - \frac{1}{\omega}\int_0^\infty h_r(t)\sin(\omega t)dt \tag{2.36}$$

$$B(\omega) = \int_0^\infty h_r(t)\cos(\omega t)dt \tag{2.37}$$

Therefore, in time domain the impulse response function results:

$$h_r(t) = \frac{2}{\pi}\int_0^\infty [B(\omega) - B(\infty)]\cos(\omega t)dt \tag{2.38}$$

and in the corresponding frequency domain:

$$H_r(j\omega) = B(\omega) + j\omega\,[A(\omega) - A_\infty] \tag{2.39}$$

Fossen and Perez converted the radiation force F_r in a linear ordinary differential equation, applying the properties of the convolution term that is a linear dynamic operator. For each element of the matrix h_r, they expressed the differential equation using a state space representation:

$$F_r = \int_0^t h_r(t-\tau)\dot{X}_i d\tau \simeq \begin{cases} \dot{\zeta}_r = A_r\zeta_r + B_r\dot{X}_i \\ F_r = C_r\zeta_r + D_r\dot{X}_i \end{cases} \quad \text{with} \quad \zeta_{r,0} = \zeta_r(t_0) = 0 \tag{2.40}$$

from which the radiation transfer function is calculated:

$$H_r(j\omega) = C_r(j\omega I - A_r)B_r \tag{2.41}$$

This representation is suitable for the numerical model implementation in time domain simulation tools.

The radiation frequency response function $H_r(j\omega)$, based on (2.39) can be approximated by a parametric frequency domain identification. The target is to find an appropriate order transfer function which satisfies the criteria of minimum approximation error, stability and passivity (i.e. resulting a positive damping for each frequency value).

The method here present will be applied in the time domain model of the ISWEC device.

2.7 Excitation Force modeling

In the previous sections, the hydrodynamic theory at the basis of the numerical modeling of a floating body motion in waves has been explained. In a wave-to-wire WEC model, the forcing input of the dynamic system are the wave excitation forces, which different contributions were presented in sections 2.4 and 2.5. To determine the input forces to the model a sea state representation needs to be defined. The sea state can be considered either *regular* or *irregular*, depending on the objective and the analysis stage of the system. A brief description of the sea state modeling used for this work will be given here.

Regular sea state

The most simple sea state representation is based on the *Airy linear wave theory* [2] that describes the wave as a sinusoidal, long-crested, progressive. The wave that satisfies linear theory is also called *regular* and it presents the following proprierties [189]:

- *Amplitude*, $a_w\,[m]$: is the magnitude of the maximum displacement from the mean sea-level.
- *Height*, $H_w\,[m]$: is the difference in surface elevation between the wave crest and the previous trough. For a simple sinusoidal wave is $H_w = 2a_w$.
- *Wavelength*, $\lambda\,[m]$: is the horizontal distance between two successive crests.

- *Period*, $T_w\,[s]$: is the time interval between two successive crests passed from a fixed point.
- *Phase velocity*, $c\left[\frac{m}{s}\right]$: is the speed at which the wave profile travels. For a simple sinusoidal wave is $c = \lambda/T_w$.
- *Steepness*, H_w/λ: height to wavelength ratio.
- *Wave Number*, $k = \frac{2\pi}{\lambda}\left[\frac{rad}{m}\right]$: defines the wave periodicity in space.
- *Angular frequency*, $\omega = \frac{2\pi}{T}\left[\frac{rad}{s}\right]$: defines the wave periodicity in time.

The regular wave evolution in space and time is described by its *wave profile*, i.e. free-surface elevation:

$$\eta(x,t) = a_w \sin(\omega t - kx) \tag{2.42}$$

For the wave power conversion it is important to evaluate the energy carried along with the waves. Wave energy depends on the propagation conditions that is described by the *dispersion phenomenon*, according with the energy propagates with a *group velocity* c_g that depends on the water depth. The water depth influence reflects on the waves particles motion. In *deep water* conditions, the particles describe circular orbits which radius decreases exponentially with depth. In *shallow water* the sea floor influences the waves, reducing its velocity, and the particle motion becomes elliptical, until it will be disrupted. The seabed influence on the group velocity and consequently on the wave energy can be considered negligible for water depth greater than $\frac{\lambda}{4}$. When this condition is verified, the *deep water* approximation is valid and the *Wave Power Density* is defined as:

$$WPD = \frac{\rho_w g^2 H_w^2 T_w}{32\pi} \simeq H_w^2 T_w \qquad \left[\frac{kW}{m}\right] \tag{2.43}$$

Wave Power Density is the physical quantity that expresses the wave power per unit of wave front. In this work the deep water condition will be assumed for the pitching floating WEC analysis.

The first order wave excitation forces correspondent to a monochromatic wave can be evaluated, according to the theory presented in section 2.4 and the numerical solution described in section 2.6. Given the wave amplitude a_w, the wave period T_w and the correspondent Froude-Krylov and diffraction forces coefficient at the wave

frequency, the excitation force on the i_{th} DoF is calculated as:

$$F_{w,i}(t) = a_w |f_{w,i}(j\omega)| \cos\left[\omega t + \angle\big(f_{w,i}(j\omega)\big)\right] \tag{2.44}$$

For the horizontal surge motion, it is also important to consider the drift contribution that in regular wave is equal to the mean drift load. As explained in section 2.5, the mean drift force coefficient $f_{d,i}(\omega)$ are calculated by the BEM code and the resulting force on the i_{th} degree of freedom is:

$$F_{d,i}(t) = {a_w}^2 f_{d,i}(\omega) \tag{2.45}$$

Irregular sea state

In general, regular waves are not a realistic description of the sea and only swell waves are close to a monochromatic wave description. A real sea state is characterized by a continuously changing water surface obtained by different waves coming from different directions and crossing each others. To numerically describe a real sea state, several methods can be used based on the idea of the superposition of infinite monochromatic waves with different height, frequency, wavelength and phase, moving in different directions. The sea surface resulting from wind and swell waves is described using the *random linear wave theory*. This theory is based on the assumption that the sea state is stationary, i.e. the sea state is a stochastic process whose joint probability distribution does not change when shifted in time. In this case a limited time record will contain the statistical properties necessary to accurately describe a sea state. Moreover, the wavelengths range in a sea state is commonly not broad, thus it can be assumed as a Gaussian, centered, stationary, homogeneous and ergodic random process [100].

To build a numerical wave record the Fourier series is used. This series provides an approximation of the irregular sea surface given by a finite sum of planar waves which can be written as:

$$\eta(x,t) = \eta_0 + \sum_{n=1}^{N} a_{w,n} \sin(\omega_n t - k_n x + \theta_n) \tag{2.46}$$

where:

- $\eta(x,t)$: recorded wave elevation of the water surface at time t.
- η_0: mean elevation related to the water depth.
- $a_{w,n}$: wave amplitude of the n_{th} component.
- k_n: wave number of the n_{th} component.
- θ_n: phase angle of the n_{th} component. This angle takes into account the fact that the maxima of the different components occur at different times.
- N: total number of harmonic components for the Fourier analysis.

According to these assumptions, the statistical properties of an irregular wave are completely described by a *wave energy spectrum* $S_\eta(f)$ that defines the level of energy transported by the different frequency components f_n in which the real sea state has been decomposed.

The wave energy spectrum is site dependent but standard spectra can be defined on the basis of long term experimental campaign. In Ocean Engineering application two wave spectra are commonly used: the *JONSWAP* spectrum is used to describe close seas and the *Bretschneider* spectrum for oceanic sites [57, 100, 189, 160].

The statistical wave parameters can be defined by means of the spectral moments of the wave energy spectrum. In general, the n_{th} order spectral moment is defined as:

$$m_n = \int_0^\infty f^n S_\eta(f) df \tag{2.47}$$

The most important wave parameters, used for the statistical analyses presented in this work, are [189]:

- ***Maximum wave height***, H_{max}: is the maximum wave height occurring in a wave record.
- ***Signifant wave height***, H_s: defined as the average of the highest one-third of the individual trough-to-crest heights in a wave record:

  $$H_s = 4\sqrt{m_0} \tag{2.48}$$

  Because of its definition, the significant height of a generic signal is often reported as H_{m0}.

- ***Peak period***, T_p: the period corresponding to the frequency f_p at which the wave spectrum has its maximum value.
- ***Average zero-crossing wave period***, T_z: time interval between two consecutive instants where the wave elevation crosses the zero level in the upward or downward direction.
- ***Energy period***, T_e: it is strictly related to the lower frequency band of the spectrum, where most of the power is contained. This parameter is fundamental for the evaluation of the energy transported by the wave

$$T_e = \frac{m_{-1}}{m_0} \tag{2.49}$$

The combination of the *significant wave height* and the *energy period* of a sea state, defines the *Wave Power Density* of an irregular wave:

$$WPD = \frac{\rho_w g^2}{64\pi} {H_s}^2 T_e \simeq 0.49 {H_s}^2 T_e \qquad \left[\frac{kW}{m}\right] \tag{2.50}$$

If the wave profile and the corresponding wave energy spectrum are known, it is possible to define the irregular wave excitation forces. For the calculation, the excitation force coefficients f_w resulting from the hydrodynamic analysis of the floating device are needed. The *time history* of the first order irregular wave forces acting on the i_{th} DoF results from a sum of N finite harmonic excitation forces:

$$F_{w,i}(t) = \sum_{n=1}^{N} F_{w0,i,n} \cos(\omega_n t + \phi_{i,n} + \theta_n) \tag{2.51}$$

where $F_{w0,i,n}$ is the amplitude of the n_{th} force component, function of the Froude-Krylov and diffraction coefficients and the wave amplitude evaluated at the n_{th} spectrum frequency component:

$$F_{w0,i,n} = |f_{w,i}(\omega_n)| \sqrt{2 S_\eta(\omega_n) \Delta\omega} \tag{2.52}$$

The angle $\phi_{i,n}$ corresponds to the phase of the Froude-Krylov coefficients, while θ_n is the phase angle between the harmonic components of the spectrum. The latter is chosen randomly if the wave record is not available. In case of acquired real wave

records, the phase angle is given by the Fast Fourier Transform (FFT) of the wave time-history.

As described in section 2.5, to analyze the dynamics of a moored floating structure, also the second-order wave forces are important. Drift forces are in general a function of the square of the wave amplitude. The information about the *slowly-varying* second-order forces are provided by the amplitudes envelope of the irregular wave. More precisely, the spectral density (PSD) of the wave amplitudes provides information about the mean period and the magnitude of the low frequency wave forces. Usually a long wave record is required to obtain an accurate envelope spectrum [100], thus low frequency wave drift forces are derived using the Quadratic Transfer Function (QTFs) output of the potential flow hydrodynamic analysis. The expression for the second-order wave drift forces in irregular waves is:

$$\begin{aligned} F_d, i(t) = \sum_{m=1}^{N}\sum_{n=1}^{N} a_{w,m}a_{w,n}\Big[P^{+}_{i,m,n}\cos\big((\omega_m+\omega_n)t-(\varepsilon_m+\varepsilon_n)\big)+ \\ Q^{+}_{i,m,n}\sin\big((\omega_m+\omega_n)t-(\varepsilon_m+\varepsilon_n)\big)\Big]+ \\ \sum_{m=1}^{N}\sum_{n=1}^{N} a_{w,m}a_{w,n}\Big[P^{-}_{i,m,n}\cos\big((\omega_m-\omega_n)t-(\varepsilon_m-\varepsilon_n)\big)+ \\ Q^{-}_{i,m,n}\sin\big((\omega_m-\omega_n)t-(\varepsilon_m-\varepsilon_n)\big)\Big] \end{aligned} \tag{2.53}$$

where:

- $a_{w,m}$: wave amplitude of the m_{th} frequency component.
- $a_{w,n}$: wave amplitude of the n_{th} frequency component.
- $P^{+}_{i,m,n}$: real part of the QTF for the sum frequency of two wave components, evaluated for the i_{th} DoF.
- $Q^{+}_{i,m,n}$: imaginary part of the QTF for the sum frequency of two wave components, evaluated for the i_{th} DoF.
- $P^{-}_{i,m,n}$: real part of the QTF for the difference frequency of two wave components, evaluated for the i_{th} DoF.
- $Q^{-}_{i,m,n}$: imaginary part of the QTF for the difference frequency of two wave components, evaluated for the i_{th} DoF.

In Eq. (2.53) also high frequency components are present. As explained in previous sections these components can be neglected because do not contribute to the excitation of the mooring system. This is due to the low natural frequency of the mooring-floater coupled system.

Despite of this approximation, the direct summation is still time consuming. To overcome the problem, Newman [123] proposed a further approximation. The off diagonal terms $P^-_{i,m,n}$ and $Q^-_{i,m,n}$ can be obtained from the diagonal coefficients $P^-_{i,n,n}$ and $Q^-_{i,n,n}$. This means that the second-order velocity potential is not required for the solution, since the QTF diagonal terms coincide with the mean-drift force coefficients obtained from the solution of the first-order problem:

$$P^-_{i,m,n} = P^-_{i,n,m} = \frac{1}{2}\left(P^-_{i,m,m} + P^-_{i,n,n}\right) \tag{2.54}$$

$$Q^-_{i,m,n} = Q^-_{i,n,m} = 0 \tag{2.55}$$

Moreover, the double summation can be elaborated and expressed as the square of a single series. This implies that only N components need to be added together at each time step, compared to N^2 terms of (2.53). The resulting expression is:

$$\begin{aligned} F_{d,i}(t) &= 2\left(\sum_{n=1}^{N} a_{w,n}\sqrt{P_{i,n,n}}\cos(\omega_n t + \phi_n)\right)^2 = \\ &= 2\left(\sum_{n=1}^{N} a_{w,n}\sqrt{f_{d,i}(\omega_n)}\cos(\omega_n t + \phi_n)\right)^2 \end{aligned} \tag{2.56}$$

Newman's approximation is normally accepted for the hydrodynamic analysis of moored offshore structures in moderate and deep water depth in long crested waves [57, 6].

Chapter 3

ISWEC Hydrodynamic model

The general hydrodynamics theory used for the development of a Wave Energy Converter was introduced and explained in Chapter 2. In this Chapter, the theory will be applied to the ISWEC case study. First, the ISWEC working principle will be briefly presented analytically, with the purpose to explain the coupling between the hydrodynamic properties of the floater and the power conversion mechanism. Then, the ISWEC hydrodynamic model will be presented and analyzed in detail, focusing on the improvements needed to have a more reliable model.

3.1 ISWEC working principle

ISWEC is a system using the gyroscopic reaction provided form a spinning flywheel to extract power from sea waves. The gyroscopic structure is accommodated in a sealed floating body excited to oscillate at pitch motion by the incident waves. Thus, the inside flywheel reacts with a precession motion that is braked by an electrical PTO, converting power into electricity. The derivation of the dynamic model equations for the complete system is not the scope of this work and details can be found in [147, 175]. In this section, the linearized model equations will be recalled, with the only purpose to highlight the importance of the floater and its motion response in the power conversion chain.

The power conversion core of the ISWEC system is the gyroscopic unit, which is excited by the pitch motion of the hull only. Thus, the single DoF model describes, with a good approximation, the system dynamics. In time domain, the numerical

model is reduced to a system of one integro-differential equation that expresses the pitch motion of the floater (see Eq. (2.35)) and one differential equation that describes the dynamics of the precession axis of the gyroscope which coincides with the electrical PTO axis:

$$\begin{cases} T_\varepsilon = I_g\ddot{\varepsilon} + J\dot{\varphi}\dot{\delta}\cos\varepsilon \\ F_{w,55} = (I_{55} + A_{\infty,55})\ddot{\delta} + \int_0^t h_{r,55}(t-\tau)\dot{\delta}(t)d\tau + K_{55}\delta - J\dot{\varphi}\dot{\varepsilon}\cos\varepsilon \end{cases} \tag{3.1}$$

where:

- T_ε, is the PTO torque.
- ε, is the rotation angle of the gyroscope structure around the PTO axis.
- I_g, is the momentum of inertia of the gyroscope structure around the PTO axis.
- $\dot{\varphi}$, is the flywheel angular velocity.
- J, is the flywheel momentum of inertia about its rotation axis.

In the system of equations (3.1), all the terms with the subscript $_{55}$ are referred to the pitch DoF. It is possible to notice that the coupling between the mechanics and the hydrodynamics lies in the gyroscopic effect governed by the angular momentum of the flywheel $J\dot{\varphi}$. The torque T_ε applied by the electrical PTO to the gyroscope unit, is controlled in order to brake the motion of the gyroscope and extract power. To complete the power conversion chain, the control law will be here assumed linear and composed of a damping term that contributes to the power generation and a restoring term that helps the gyroscope to keep oscillating around an equilibrium position:

$$T_{\varepsilon,PTO} = -c_\varepsilon\dot{\varepsilon} - k_\varepsilon\varepsilon \tag{3.2}$$

where the two torque contributions on the right hand side are respectively proportional to the angular velocity $\dot{\varepsilon}$ and to the angular position ε of the gyroscope about the PTO axis.

This control law is a linear reactive control, because the power transfer due to the restoring term is a reactive component that does not contribute to the power extraction from the wave source. In particular, assuming harmonic oscillations

excited by harmonic waves, the average power available for electricity production on the oscillation period T, results [147, 175]:

$$P_{PTO,avg} = \frac{1}{T}\int_0^T P_{act,PTO}dt = \frac{1}{2}\omega^2 c_\varepsilon {\varepsilon_0}^2 \tag{3.3}$$

where ω and ε_0 are respectively the angular frequency and the amplitude of the oscillations.

The system in (3.1) can be linearized around $\varepsilon = 0$, the equilibrium position for the gyroscope (vertical axis of the flywheel) for which the gyroscopic effect is null. Moreover, introducing the control law of Eq. (3.2), it results:

$$\begin{cases} I_g\ddot{\varepsilon} + k_\varepsilon\varepsilon + c_\varepsilon\dot{\varepsilon} = -J\dot{\varphi}\dot{\delta} \\ F_{w,55} = (I_{55} + A_{\infty,55})\ddot{\delta} + \int_0^t h_{r,55}(t-\tau)\dot{\delta}(t)d\tau + K_{55}\delta - J\dot{\varphi}\dot{\varepsilon} \end{cases} \tag{3.4}$$

The complete model is constituted by two second order systems coupled by the gyroscopic effect. In the first equation, the gyroscopic effect is the forcing function for the PTO system. In the second equation, the gyroscopic effect is the reaction force of the mechanical system towards the hull.

To highlight the importance of the floater motion response for the power generation, it is possible to analyze the linear system in the frequency domain:

$$\begin{cases} \left[-\omega^2 I_g + j\omega c_\varepsilon + k_\varepsilon\right]\varepsilon_0 e^{j(\omega t+\theta)} = -j\omega J\dot{\varphi}\delta_0 e^{j\omega t} \\ \{-\omega^2\left[I_{55} + A_{55}(\omega)\right] + j\omega B_{55}(\omega) + K_{55}\}\delta(j\omega) = \\ \qquad\qquad = a_w f_{w,55}(j\omega) - j\omega J\dot{\varphi}\varepsilon(j\omega) \end{cases} \tag{3.5}$$

where θ is the phase angle between the pitch motion and the PTO oscillatory motion.

In frequency domain, the transfer functions of the two second order systems can be evaluated. For the mechanical system, the transfer function between the pitch angle δ and the PTO angle ε is:

$$H_{\varepsilon\delta} = \frac{\varepsilon_0}{\delta_0} = \frac{-j\omega J\dot{\varphi}e^{-j\theta}}{-\omega^2 I_g + j\omega c_\varepsilon + k_\varepsilon} \tag{3.6}$$

The hydrodynamic transfer function of a free floating system was defined in 2.6 as the Response Amplitude Operator (RAO). At this step, the ISWEC hull can not be studied as a free floating body because of the gyroscopic reaction torque. Thus, a

new response amplitude operator RAO^* will be defined for the pitch DoF, starting from (3.5):

$$\begin{aligned} RAO^*(\omega) &= \frac{\delta_0}{a_w} = \\ &= \frac{f_{w,55}(j\omega)}{\{-\omega^2\left[I_{55}+A_{55}(\omega)\right]+j\omega B_{55}(\omega)+K_{55}\}+j\omega J\dot{\varphi}H_{\varepsilon\delta}(\omega)e^{j\theta}} \end{aligned} \tag{3.7}$$

At this point, the average power production can be calculated by means of the overall transfer function of the hydro-mechanical system, written for the pitch DoF:

$$P_{PTO,avg} = \frac{1}{2}\omega^2 c_\varepsilon {\varepsilon_0}^2 = \frac{1}{2}\omega^2 c_\varepsilon |H_{\varepsilon\delta}(\omega)|^2 |RAO^*(\omega)|^2 {a_w}^2 \tag{3.8}$$

Eq. (3.8), if also in a simplified manner, explains the importance of the pitch motion response of the floater in the power conversion chain. The system will reach its maximum performance if the resonance with the incident wave is achieved [147, 175, 149]. In order to optimize the ISWEC performances, it is necessary to maximize the hydrodynamic response in waves about the pitch degree of freedom. On the other hand, to have a reliable representation of the performances it is necessary to have a correct definition of the hydrodynamics of the ISWEC hull.

3.2 The ISWEC hull

The design of the ISWEC hull is a site specific procedure. In section 3.1 it was explained the importance of the hydrodynamic response for the power extraction. It is thus fundamental an appropriate definition of the hydrodynamic properties of the floater to guarantee the best performances. More in detail, the peak of the dynamic response of the floater has to fall in the range of frequencies identified by the sea states characteristics of the installation site.

The first step in the definition of the floater dimensions, is the selection of the *Design Wave* of the WEC. Several criteria can be adopted in the choice of the design wave, involving different aspects, that relate both the economics and technical design of the WEC. For example, depending on the installation site, the design point can be chosen as:

- ***Most occurrent wave***: the sea state with the highest occurrence probability, based on the meteocean data.
- ***Most energetic wave***: the sea state characterized by the highest Wave Power Density (see Eq. (2.43).
- ***Power threshold***: a sea state power threshold can be defined according to the assumption that a WEC would be commercially viable if it works at full capacity for at least one third of the year [56]. In this case, the design wave would be the one which power is exceeded for only one third of the year.

It is not the aim of this work to discuss the suitable criteria for the selection of the design point for the ISWEC device. A more detailed discussion can be found in [175].

Once the design wave has been selected, the main properties of the floater need to be defined:

- ***Hull Length***, L: for the floating pitching device, the device length is the most important dimension to be determined. Indeed, it needs to be defined to guarantee and facilitate the pitch motion. According to [175], a suitable length of the device should be in the range:

$$\frac{\lambda}{3} \leq L \leq \frac{\lambda}{2} \tag{3.9}$$

  where λ is the design wavelength, chosen according to the meteocean data of the installation site. For higher values of the length, the device behaves like a filter on high frequency waves, whilst for lower values the heave motion is enhanced with respect to the pitch motion.

- ***Hull Width***, W: the floater width is directly connected to the definition of the power performances of the WEC. It is a function of the expected power output P_e, the power density of the design wave WPD, the *Relative Capture Width* RCW of the device and the PTO overall efficiency η_{PTO}:

$$W = \frac{P_e}{(WPD)(RCW)(\eta_{PTO})} \tag{3.10}$$

  where the RCW is a parameter that defines the overall efficiency of the WEC, and in particular depends on the device capability to absorb the incident wave

power. For the ISWEC device, values of $RCW = 0.5$ and $\eta_{PTO} = 0.7$ can be assumed [175].

- ***Hull Inertia Matrix***, M: the inertia properties of the hull, together with the hydrostatic stiffness, define the pitch natural frequency of the device:

$$\omega_n = \sqrt{\frac{K_{55}}{I_{55} + A_{55}}} \tag{3.11}$$

where K_{55} is a function of the geometry and displaced volume of the device.

The definition of the mass properties of the device is not a straightforward task. An optimization process is needed, starting from an initial guess and adopting iterative procedures. In this work, the hull shape and properties are given. The Pantelleria's ISWEC prototype is considered as case study. The details of the study that lead to the hull design are reported in [147, 26].

The ISWEC hull is the result of a study aimed to find the best solution between costs and performances. To reduce costs, the shape of the floater needs to be as simple as possible for the manufacture in the yard. Eventually, the best solution resulted in a hull with two symmetry planes: the longitudinal plane (x,z) and the transverse plane (y,z). On the other hand the keel is curve up to the deck, improving the pitching capacity. Table 3.1 reports the main hull properties.

3.3 Frequency domain analysis

Once geometry and mass properties have been defined, the hydrodynamic analysis of the free floater is run in frequency domain on ANSYS Aqwa [6]. In this section the results are reported and commented in detail. The output of the frequency domain analysis are then used to build the time-domain model in Matlab Simulink environment.

Hydrostatic stability

The first property to be checked for a floating structure is the hydrostatic stability. The stability refers to the up-righting properties of the floater when it is forced out of its equilibrium. Wave Energy Converters, for their working principle, do not have

Table 3.1 ISWEC hull properties

Property	Symbol	Units	Value
Total mass	M	kg	288000
Hull mass	M_h	kg	56000
Gyroscopic unit mass	M_g	kg	30000
Length	L	m	15.33
Width	W	m	8.0
Height	H	m	4.5
Freeboard	FB	m	1.52
COG vertical coordinate wrt water plane	z_{COG}	m	-0.57
Inertia moment about the x-axis	I_{xx}	$kg\ m^2$	$1.824\ 10^6$
Inertia moment about the y-axis	I_{yy}	$kg\ m^2$	$7.712\ 10^6$
Inertia moment about the z-axis	I_{zz}	$kg\ m^2$	$7.136\ 10^6$

the same stability requirements of the traditional offshore structures. Anyway, roll and pitch stability of the ISWEC needs to be checked for safety reasons and naval standards requirements [6, 57, 100]. To verify the stability of the ISWEC hull, the small angle stability theory has been used. According to this theory, the stability is determined by the position of the metacenter, which is the intersection point between the vertical lines passing through the center of buoyancy at equilibrium position and at a non zero angle of rotation with respect to the equilibrium position. To guarantee the stability for both roll and pitch motions, the transverse and longitudinal metacentric heights need to be greater than zero:

$$\begin{cases} \overline{GM}_X = \frac{K_{44}}{\rho_w g \nabla} > 0 \\ \overline{GM}_Y = \frac{K_{55}}{\rho_w g \nabla} > 0 \end{cases} \tag{3.12}$$

where ρ_w is the water density, ∇ is the submerged volume of the hull, K_{44} and K_{55} are the roll and pitch restoring moments coefficients, that are the hydrostatic stiffness coefficients.

The hydrostatic analysis results are given in Table 3.2. It can be observed that the stability is guaranteed on both pitch and roll DoFs. The transverse metacentric height is low, but given the shape of the floater and its working principle, the hull

Table 3.2 ISWEC Hydrostatic properties

Property	Symbol	Units	Value
Heave Hydrostatic Stiffness	K_{33}	N/m	$1.186\ 10^6$
Roll Hydrostatic Stiffness	K_{44}	$(Nm)/deg$	$7.569\ 10^4$
Pitch Hydrostatic Stiffness	K_{55}	$(Nm)/deg$	$1.906\ 10^7$
Volumetric Displacement	∇	m^3	281
Water Plane Area	WPA	m^2	118
Transverse Metacentric Height	$\overline{GM}_X$	m	1.56
Longitudinal Metacentric Height	$\overline{GM}_Y$	m	7.02

will be orientated towards the incident wave and roll motion will be rarely excited. On the other hand, the pitch hydrostatic stiffness is very large: consequently, a large inertia moment about the pitch axis is necessary to reduce the pitch natural frequency of the floater. This is a specific requirement for high frequency sea states, distinctive of closed seas.

From the hydrostatic analysis some suggestions for further improvements can be highlighted. The pitch hydrostatic stiffness is a function of the water plane shape of the floater. In particular, reducing the moment of inertia of the waterplane shape, it is possible to reduce the hydrostatic stiffness. Thus would not be necessary anymore to have huge ballasts to meet the required natural frequency of the hull.

Radiation and Diffraction analysis

The output of the radiation and diffraction analysis are the incident wave forces coefficients and the radiation forces coefficients. Figure 3.1 shows the added mass and linear hydrodynamic damping coefficients for the six DoFs. The radiation forces coefficients show a strong dependence on the frequency. In general, radiation force coefficients curves may present strong irregular behaviors. This is not the ISWEC case, thanks to the absence of singularities in the hull geometry. It is possible to observe that the radiation forces decreases with the wave period for most of the cases. The only exception is the added mass for heave that goes to infinity with the period. For high frequency waves, again, there is no fluid moved by the body. Recalling Falnes [55], a good Wave Energy Converter should be also a good wave generator.

The radiation forces give an indication of the capability of the floater to generate waves. This capability is enhanced in resonance conditions and far from that, the damping coefficient go fast to zero, canceling the radiated wave.

The Froude-Krylov and diffraction coefficients represent the fundamental force input to the WEC system. These coefficients are calculated for different incident wave directions with respect to the device. The ISWEC device is designed to always weathervane and thus working in head seas. This characteristic will be investigated in detail and demonstrated in the second part of the thesis, where the ISWEC mooring design is discussed. Assuming valid the weathervane hypothesis, the wave direction of interest for the device will be parallel to the longitudinal axis of the device. Moreover, the motion modes excited in this direction will be *surge*, *heave* and *pitch*. In Figure 3.2 the forces coefficients are reported for different wave directions, where β is the direction angle of the wave with respect to the x-axis of the device. Increasing β, the input forces decrease for pitch, while they increase for roll. Nevertheless, the ISWEC in beam seas is less excited due to its shape which is designed to work at pitch motion. All the force coefficients present a decreasing behavior with the wave period and a peak at the resonance of the device. Exception is always the heave motion which is independent from the other DoFs: in fact, the heave force coefficients follow the incident wave power, increasing with the wave period.

The motion performances of the ISWEC hull are summarized by the Response Amplitude Operators (see Eq. (2.34)). From now on, assuming the device weathervaning with the incident waves, surge, heave and pitch DoFs only will be considered (Figure 3.3). Hence, the ISWEC time domain model, that will be presented in the next Chapter, is developed for three DoFs.

The *surge* motion response presents a peak in correspondence of the hull resonance and then increases with the wave period. The device will be prevented to move away by the mooring system that introduces a restoring force in surge direction. In *heave* motion the device works as a low-pass filter. For long waves it follows exactly the wave profile. The *pitch* RAO is the most important parameter for wave power conversion purposes. The motion response presents a narrow frequency band around the natural frequency of the device. This band has to match the wave frequency band characteristic of the installation site, to let the device work properly. New solutions to broaden the band are currently under study for the ISWEC device, in order to

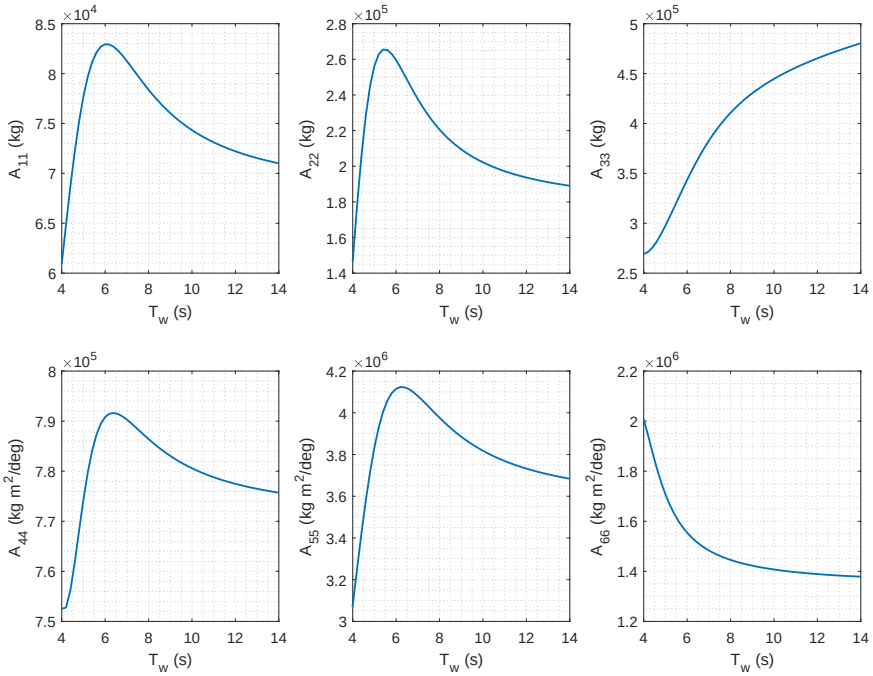

(a) Added Mass Coefficients

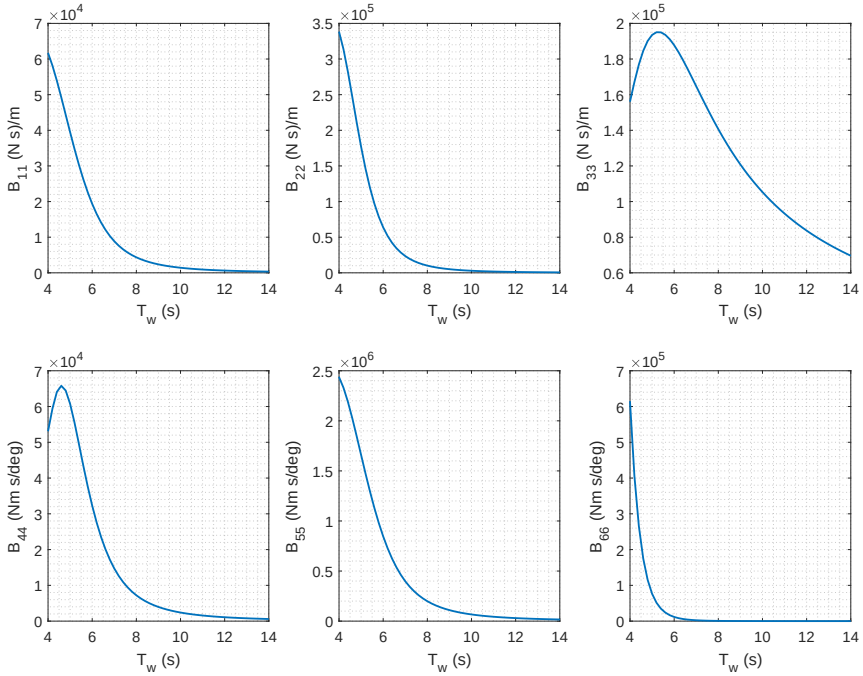

(b) Linear Hydrodynamic Damping Coefficients

Fig. 3.1 ISWEC Radiation Forces Coefficients

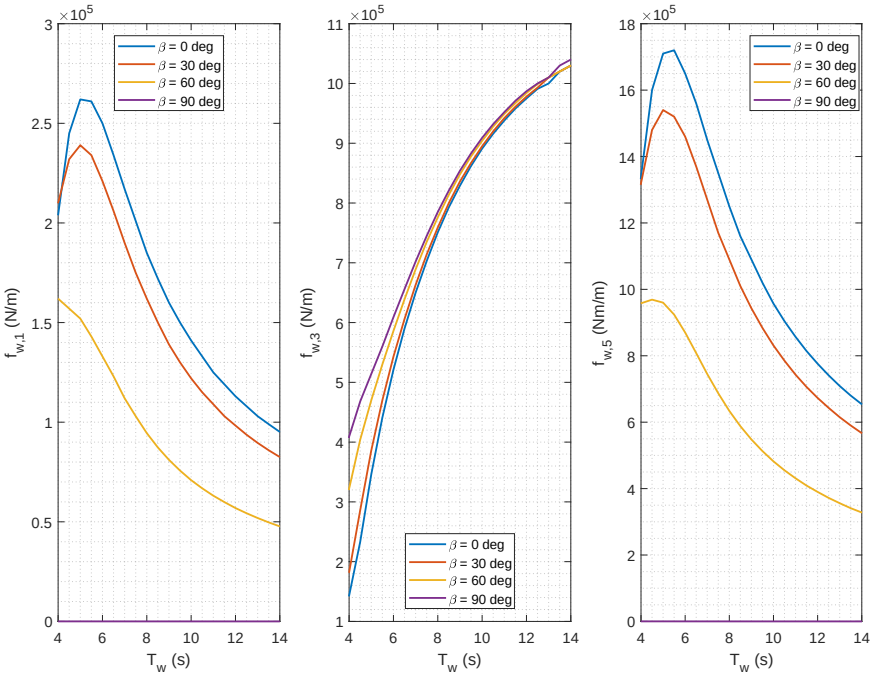

(a) *Surge*, *Heave* and *Pitch*

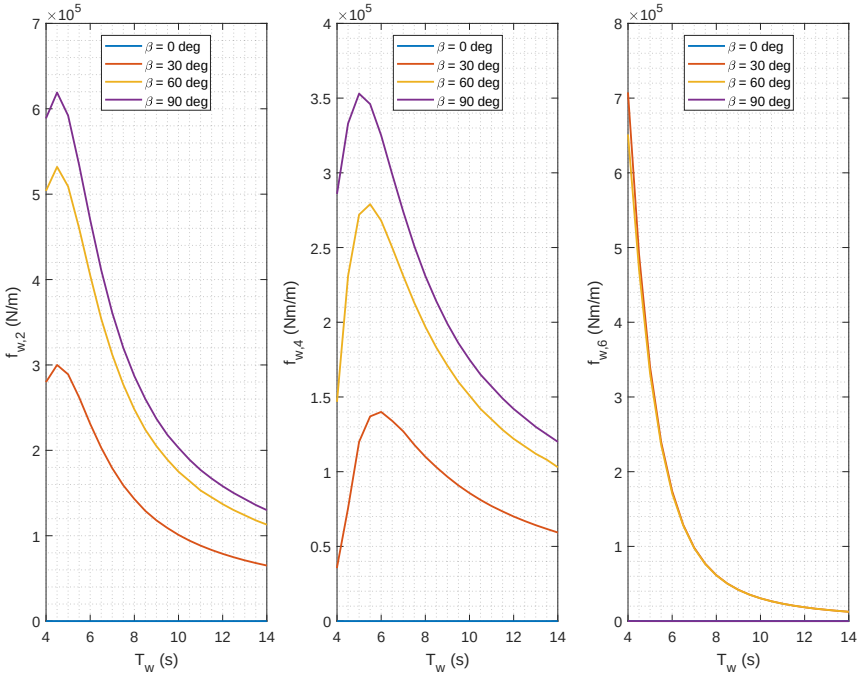

(b) *Sway*, *Roll* and *Yaw*

Fig. 3.2 Froude-Krylov and Diffraction Force Coefficients for different Wave directions

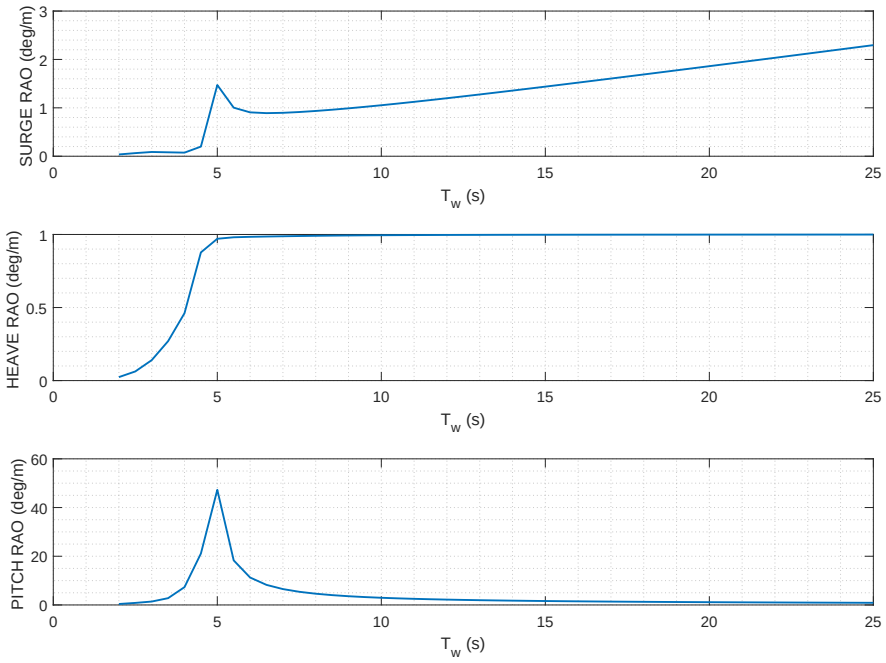

Fig. 3.3 ISWEC RAOs for *Surge*, *Heave* and *Pitch* at $\beta = 0$ *deg*

harvest the energy from longer periods waves. On the other hand, considering the full equipped device, with the gyroscope unit installed (i.e. *active device*), a ISWEC's competitive advantage with respect to other WECs, is the possibility to tune the angular momentum of the flywheel by varying its speed. This capability allows the device to modify the motion response (see Eq.(3.7)), broadening its working range. A deep explanation and the demonstration of this property is reported in [175].

From the pitch RAO, it can be evaluated and verified, according to the design requirements, the wave period for which the hull is designed to maximize its oscillations, i.e. the pitch response peak. For the ISWEC device it results:

$$T_{n,5} = T\left(\max(RAO_5)\right) = 5\ s \tag{3.13}$$

It is due to notice that real sea states are never uni-directional. They are a superposition instead of waves coming from different directions, with a prevalent direction characterized by most of the energy content. Thus, it can be interesting to evaluate the performances of the floater as a function of the incident wave direction. Figure

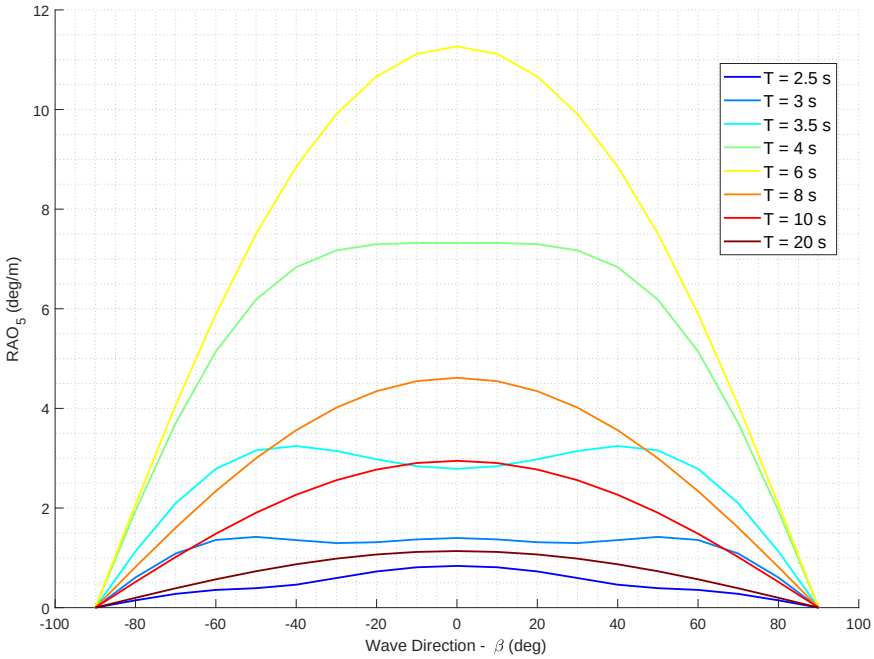

Fig. 3.4 Pitch RAO vs wave direction, at different wave periods

3.4 shows the pitch RAO for a range of periods at different wave directions. The curves demonstrate how the hull geometry helps to maximize the motion response in head seas. Consequently, for irregular sea states, the ISWEC hull should be capable to harvest the higher energy contribution, present in the prevalent direction.

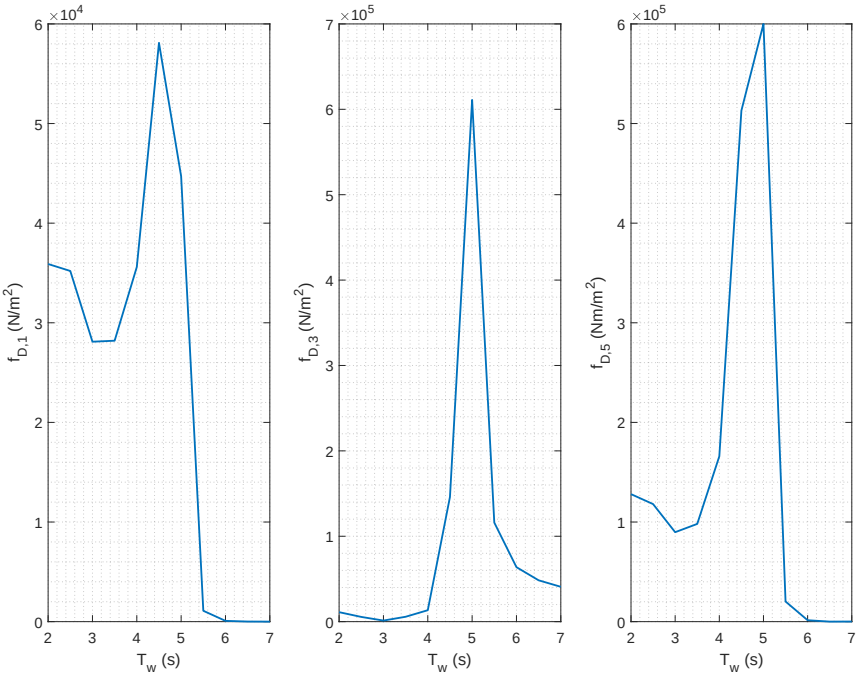

Fig. 3.5 Mean Drift forces coefficients for *Surge*, *Heave* and *Pitch*. $\beta = 0\ deg$

Last outputs of the frequency analysis are the 2^{nd} order forces coefficients. As explained in section 2.7, to calculate the drift forces contribution in both regular and irregular sea states, only the *mean drift* forces coefficients are needed. Figure 3.5 reports the drift forces coefficients for *surge*, *heave* and *pitch* motions. It is possible to see that the contribution of the drift forces is important in the resonance neighborhood. For long period waves, this contribution goes fast to zero. The drift forces coefficients absolute values are lower than the Froude-Krylov and diffraction coefficients. Nevertheless, being second order terms, drift forces are proportional to the square of the wave amplitude. This means that they become relevant for high amplitude waves, such as extreme sea states.

3.4 ISWEC 3DoFs time domain model

In the previous sections all the elements needed to build a time domain model for the ISWEC device hydrodynamics have been explained. The time domain model is useful to obtain more realistic analysis of the dynamic behavior of the device. It

is possible to introduce the effect of non-linearities and test the device in specific conditions. The ISWEC hydrodynamics time domain model is an essential part of the wave-to-wire model developed to evaluate the device performances in different installation sites. The Matlab Simulink environment was chosen to develop the time domain model because of its flexibility and its low computational time needed to simulate systems which can be described as a system of differential equations. The result is a lumped parameters model based on the outputs of the hydrodynamic analysis in frequency domain.

Simulink Block Diagram

The Simulink time domain model is build to solve the matrix equation of motion presented in section 2.6 for the three degrees of freedom of interest: Surge, Heave and Pitch. As previously explained, it is a subsystem of the complete wave-to-wire model where also the internal mechanical system and the controller are present [175]. In this work, only the hydrodynamics will be considered.

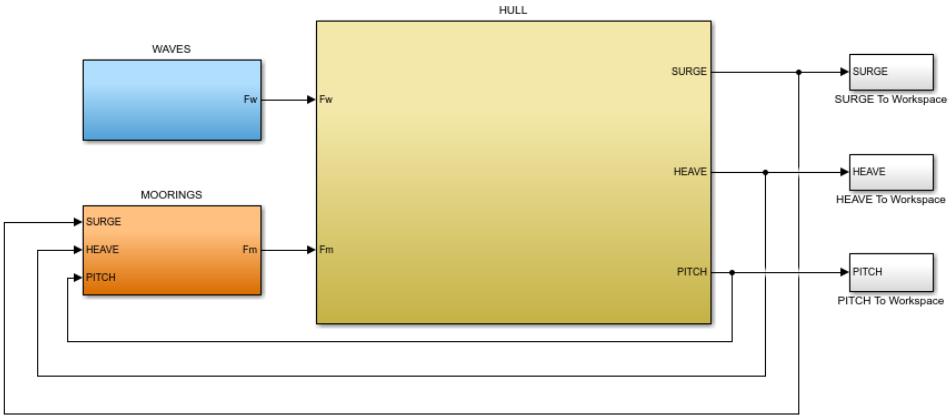

Fig. 3.6 ISWEC 3DoFs Hydrodynamics Simulink block diagram

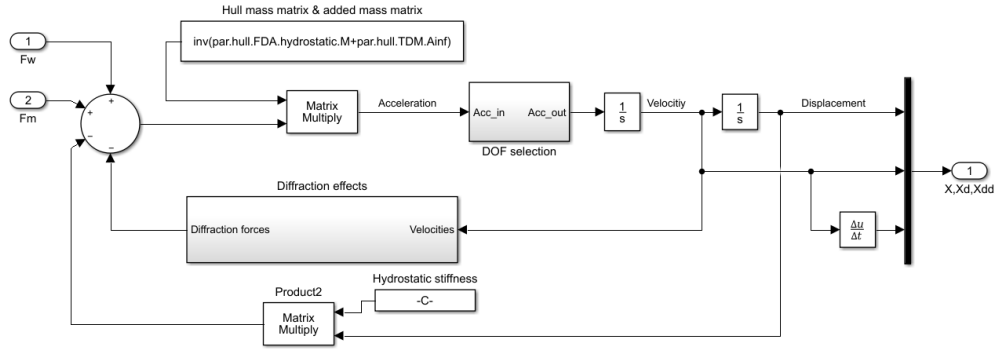

Fig. 3.7 Hull 3DoFs subsystem

Figure 3.6 shows the block diagram of the hydrodynamics sub-system:

- ***Waves block***: in this block, the time histories of the modeled wave forces are present. They can be either regular or irregular and both first order and second order forces are present.
- ***Moorings block***: the mooring system is modeled in the wave-to-wire with a quasi-static approach that will be presented in the second part of the thesis. The result is a mooring forces map function of the displacements from the equilibrium position in surge, heave and pitch.
- ***Hull block***: the motion differential equation of the floater is integrated in this block (Figure 3.7). The system has the forces in input and the motions time histories in output.

With reference to the matrix equation Eq. 2.35, it is due to notice that all the components of the equation that can be recognized in the block diagram (e.g F_w and F_m) are vectors of three components, one for each of the DoFs considered.

Radiation Forces implementation

In modeling the full dynamic problem in the (x,z) plane, it is important to remember that the surge and pitch motions are coupled. This couplings are fundamental in the simulation of the moored device. The coupling terms are present in the radiation forces and reported for the ISWEC in Figure 3.8.

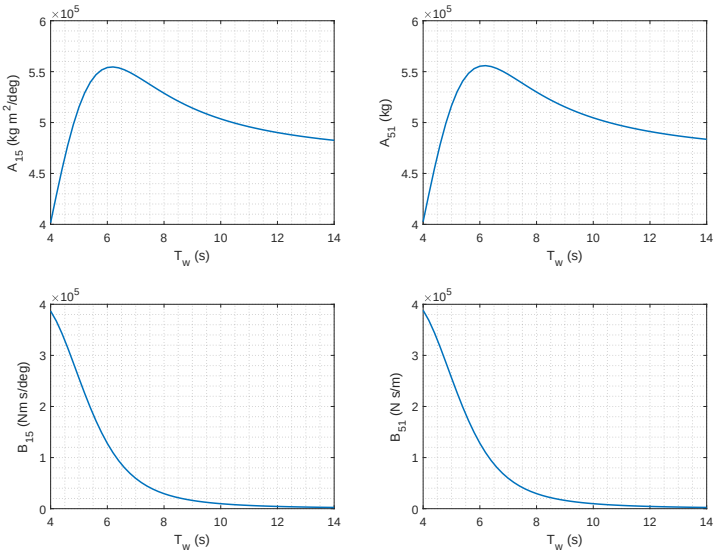

Fig. 3.8 Couplings terms between *Surge* and *Pitch*. $\beta = 0\ deg$

To solve the equation of motion, the approximation of the convolution integral proposed by Perez and Fossen [143] has been used. Thus, a transfer function is identified for the estimation of the added mass and damping coefficients in frequency domain for each degree of freedom. Figure 3.9 reports the identification of the radiation forces for the diagonal terms of the three degrees of freedom modeled. In red, the discrete points obtained with the BEM codes are plotted. The blue dashed lines are the best fit obtained with the state space models. In particular, a $8th$ order transfer function has been identified for surge motion and a $5th$ order for heave and pitch motions.

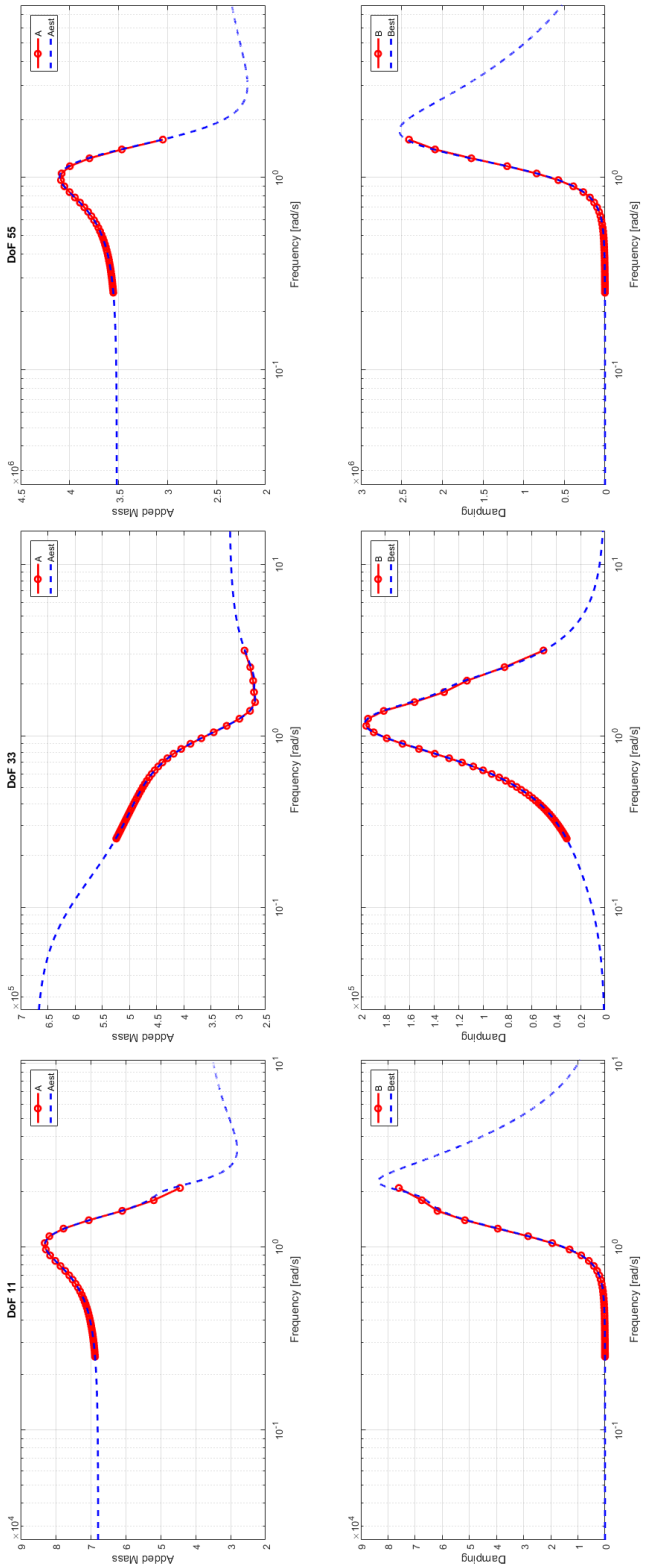

Fig. 3.9 Radiation Forces identification for *Surge*, *Heave* and *Pitch* degrees of freedom

3.5 Non-linear hydrodynamic force modeling

The Simulink lumped parameters (LP) time domain model is a powerful tool for the power absorption assessment of the ISWEC device. This model is used to reproduce the behavior of the device in operational conditions. Differently from traditional offshore structures, WECs are designed to maximize their motion, therefore non-linear dynamics can be important also in operational conditions. Several non-linear effects can affect the dynamics of a WEC and they are distributed along the entire power conversion chain: different ways of modeling the incoming waves can be used [58, 70, 85]; the hydrodynamic wave-floater interaction, that can be influenced by viscous effects [72, 69, 76], mooring forces [132, 174] and the instantaneous variation of the device's wetted surface [71, 107, 140]; Power Take Off systems and its control logics are usually non linear [8, 27, 46, 111, 145, 153, 176]. The focus of this work is on the hydrodynamics of a floating pitching WEC. Different works are present in literature, describing numerical methods used to model the non-linear hydrodynamics [60, 110, 139]. Penalba [139] proposed the most updated and complete review of these methods, specifying the relevance of the non-linear effects relating it to the different devices working principles. According to Penalba, the appropriate modeling approach depends on the specific WEC characteristics. Moreover, a first comparison between different effects for various types of WECs is proposed and a review of the suitable approaches for the effects identification is outlined.

ISWEC Viscous Forces

In general, for oscillating pitching converters, both non-linear Froude Krylov forces and viscous forces can be relevant. Referring to the ISWEC device, it has been observed during previous experimental campaigns [146, 148, 175] that, for operational sea states, the non-linear hydrodynamic effects become relevant only around pitch resonance conditions. It is well known [55, 57] that near resonance conditions viscous forces contribution become a relevant part of the hydrodynamic forces. On the other hand, non-linear Froude Krylov forces depend on the variation of the hydrodynamic pressure field on the body, due to the variation of the instantaneous wetted surface. This contribution can be of high importance for WECs characterized by asymmetrical or particular hull shapes such as, for example, the *Wello Penguin*

[186]. Indeed, for those types of WECs the wetted surface is subject to important variations during the motion, with a consequent non negligible dependence of the Froude Krylov forces from the instantaneous wetted surface. To take into account this contribution, it would be necessary to calculate for each integration time step the instantaneous pressure field on the immersed body, increasing considerably the computational cost of the numerical model.

The main advantages of the time-domain model here proposed are the low computational time and the possibility to easily develop and test different control techniques. To improve the numerical model, continuing to exploits its advantages, a trade-off solution needs to be identified to model non-linear hydrodynamic effects. Within this work, the time domain numerical model has been already expanded with the addition of the drift forces. As a matter of fact, the geometry of the ISWEC device is such that there is no relevant variation of the wetted surface during the pitch motion. Consequently, the non-linear Froude Krylov forces can be considered not of high importance for the current work. To improve the numerical hydrodynamic model, the further step, here discussed, is the implementation of the non linear viscous forces, consisting in the main source of non linear effects for the ISWEC device.

For this contribution, the only pitch degree of freedom is of interest and the dynamic can be described by a single degree of freedom system. Pitch, indeed, is the motion exploited for the energy harvesting from waves. Moreover, in case of free body, pitch DoF does not couples with other degrees of freedom. Nevertheless, if the device is moored, possible couplings can be present with surge or roll. As it will be presented in the second part of this work, the surge drift of the device has not a high relevance with respect to the pitch motion. Hence, within this work, viscous forces on surge motion will not be analyzed.

The viscous effects are modeled with the addition of a quadratic damping coefficient B_{55-2} in the Cummins' equation:

$$(I_{55}+A_{\infty})\ddot{\delta}(t)+\int_0^t h_{r,\delta}(t-\tau)\dot{\delta}(t)d\tau+B_{55-2}\dot{\delta}(t)|\dot{\delta}(t)|+K_{55}\delta(t)=F_{w,55}(t) \tag{3.14}$$

where δ is the pitch angle.

The viscous contribution is significant with respect to the wavemaking contribution (radiation) because, in general, the capability of rounded bodies to generate waves is limited [78]. Moreover, the viscous effects are in general negligible for large floating bodies engineered to minimize their motions. On the other hand, WECs are commonly small devices that must undergo large motions to absorb wave power. In this case, the resistance is due to the frictional drag on the device surface, flow separation (pressure drag) and eddy formation. In offshore engineering, the most common and validated practice to identify the viscous damping is the free decay test [39, 100, 109]. This test, is usually performed to identify the roll damping for ships and consists in inducing a certain inclination angle to the device in still water. The hull is then released and its subsequent motion is measured. The same approach can be used for wave energy devices, as explained in [138] and [83].

WECs' motion is in general influenced by the PTO action that damps the wave induced motion to harvest energy from waves. Hence, in operating condition, when the PTO system is on, the activated body motion is less amplified. In this work, the influence of the PTO system will not be considered for the identification of the damping coefficient. This decision is motivated by the choice to have a conservative approach that is fundamental during the preliminary design stage based on numerical modeling. On the other hand, the decision is coherent with the possibility to compare the numerical model against the experimental results obtained with the campaign that will be presented and discussed in Chapter 4. Nonetheless, the scope of this work is focused on the hydrodynamics of the ISWEC device, which comprehension is a necessary step that introduces further investigations.

For the free decay test, the system oscillates at its single natural frequency, thus it is possible to determine both the natural period and the hydrodynamic damping. The system single degree of freedom equation for unforced pitch motion results:

$$(I_{55} + A_{55})\ddot{\delta} + B_{55-total}(\dot{\delta}) + K_{55}\delta = 0 \tag{3.15}$$

where the added mass is calculated at the natural frequency of the system. The non-linear damping term can be divided and approximated to the sum of two contribution, the first linear and the second quadratic:

$$B_{55-total} = B_{55-1}\dot{\delta} + B_{55-2}\dot{\delta}|\dot{\delta}| \tag{3.16}$$

Once performed the free-decay test, it is possible to identify the damping coefficient in different ways, that will be further described.

Fully viscous CFD approach

For the numerical estimation of the damping factor, different procedures are present in literature, derived from experience in offshore industry. Most of the procedures are either based on empirical coefficients, calculated according to the device geometry, or require experimental testing. These procedures are collected by the International Towing Tank Conference (ITTC) in their recommended practices [95]. Nevertheless, empirical coefficients are available for standard structures while experimental tests, if also necessary in the development of a WEC, are always expensive. In this work an alternative methodology is proposed, exploiting the state of the art numerical tools that can be easily integrated in a design procedure, improving the fidelity of the numerical model.

To simulate the free decay test, a fully non-linear method needs to be adopted. In particular, viscous computational fluid dynamic (CFD) models that solve the Navier-Stokes equations are required [120]. CFD models can be used to perform high fidelity simulations and study the design of a specific WEC [21, 154, 185], investigate particular non linear phenomena in the fluid-device interaction [9, 19], reproduce experimental test in numerical wave tanks (NWT) [41, 161] or investigate wave loadings to characterize the device survivability in extreme seas [131, 187].

The Navier-Stokes equation that describe the physic of a fluid flow are partial differential equations (PDEs) that cannot be solved analytically (see Chapter 2). In general approximate solutions are obtained via numerical algorithms that solve the equations numerically discretized in space and time. Two different approaches are present for the numerical solution: mesh-based (Eulerian approach) used in most of CFD codes, or particle based (Lagrangian approach) used in the smooth-particle hydrodynamics (SPH) codes [139]. Eulerian approach is the most popular one and it is computational less demanding with respect to the Lagrangian approach. Three different methods can be used to discretize the computational domain in a finite set of points that constitute the mesh (or grid) at which the approximate solution is computed: finite element method (FEM), finite difference method (FDM) and finite volume method (FVM) [59]. Different CFD software packages are available,

starting from commercial codes like ANSYS CFX [5] and STAR-CCM+ [157], to open-source codes like OpenFOAM [74].

The most appropriate CFD model for the WECs dynamics is the FVM discretization of the incompressible form of the Navier-Stokes equations. In this work, the commercial software STAR-CCM+ was chosen as the most appropriate, after a review of works present in literature that shown its suitability for analogous problems [15, 52, 104, 135, 187, 191].

In wave-floater interaction, the flow is in general considered turbulent, hence a turbulence model needs to be used. In STAR-CCM+ several models are present for simulating turbulent flows, including *Direct Numerical Simulation* (DNS), *Large Eddy Simulation* (LES) and *Reynolds-Averaged Navier Stokes* (RANS). DNS is the most accurate method in which the Navier-Stokes equations are numerically solved without any turbulence model, resulting in an extremely high computational cost. In LES, the cost is reduced ignoring the smallest length scales of turbulence, which are modeled. The least expensive is the RANS model, in which all turbulence's length scales are modeled. For its widespread use and low computational costs, the RANS model is chosen in this work, as recommended by research groups like ITTC committees [96], MARNET-CFD [115] and VIRTUE (The Virtual Tank Utility in Europe) [130]. RANS model is based on the decomposition of the Navier-Stokes equations instantaneous quantities into a time-averaged value and a fluctuation about that value. In the fluctuations is summarized all the unsteadiness. In the mathematical formulation, the equation are identical to the original for the calculation of the mean quantities, while the Reynolds stress tensor appears in the momentum transport equation to account for the fluctuations. To provide a closure of the governing equations system, it is required a turbulence model to solve the Reynolds stress tensor. Most common models are the $k-\varepsilon$ and $k-\omega$ two equations models. In general, a week dependency is observed about the turbulence model [14, 139], thus the choice is most of the cases about the computationally cheaper.

To simulate the floating device interaction with fluid, the water surface needs to be correctly modeled. This is the most demanding task in a CFD simulation of a floating WEC. Indeed, both water and air phases must be modeled, resulting in a multi-phase simulation which is computationally more demanding. The most appropriate methods to model the free-surface in hydrodynamic applications are the interface-capturing methods that do not require remeshing and are numerically

robust. Two possibilities are available, so called volume of fluid (VOF) and level-set formulation, where the first one is the most commonly used.

Numerical Setup

An unsteady fully viscous three-dimensional RANS model is created in STAR-CCM+ to perform the free-decay simulation. The three-dimensional Numerical Wave Tank has been modeled for the full-scale ISWEC device. The size of the numerical domain has been set to avoid wave reflections as described in recommended practices. Thanks to the longitudinal symmetry of the ISWEC, only half of the physical domain has been discretized, reducing the mesh size and consequently computational costs. The overall dimensions of the numerical wave tank are listed in Table 3.3 and the device was located at the tank center.

Table 3.3 Numerical Wave Tank Dimensions

Property	Units	Value
Length	m	160
Half Width	m	40
Water depth	m	40
Air Height	m	20

Transient simulation was set up using the Volume of Fluid method to capture the free surface. A realizable $k-\varepsilon$ turbulence model with all Reynolds Y+ was used to approximate the Reynolds stress tensor and to accurately estimate the shear forces on the device surface. For the interaction between the moving device and the free surface, a moving mesh so-called *overset mesh* is used and a grid interface is created with a background fixed mesh that models the wave tank.

The numerical solution in time is found using an implicit solver together with an iterative solver for each time step, to compute the field of all hydrodynamic unknown quantities. In case of incompressible flow, the pressure field needs to be calculated from the relation to the velocities in the continuity and momentum equations. For this problem a Semi Implicit Method for Pressure Linked Equations (SIMPLE) is

used to conjugate pressure and velocity fields, and an Algebraic Multi-Grid solver to accelerate the convergence of the solution.

Boundary conditions are shown in Figure 3.10 for the three-dimensional model. The numerical wave tank was setup to be used for further studies, including a forced motion induced by the incoming wave. Thus, a velocity inlet and a pressure outlet are identified respectively facing the bow and the stern of the device. Top of the tank is defined as a pressure outlet and the side as a velocity inlet, in order to avoid wave reflection. At the bottom, a wall condition was set while symmetry was imposed at the geometric symmetry of the domain. All the device surfaces were set as no slip walls.

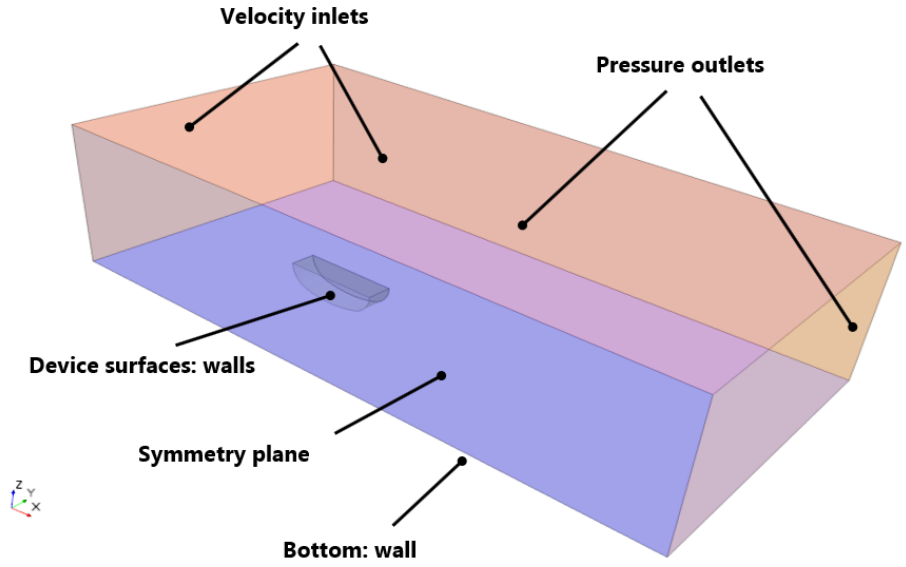

Fig. 3.10 URANS Free Decay test. Boundary conditions for the 3D model.

For this test, the velocity and pressure at the boundaries is defined imposing a flat VOF wave, which means null height and velocity. This way, the free-surface interface is defined. The top boundary is defined as a pressure outlet at constant atmospheric pressure. The ISWEC device geometry is introduced in the domain with the origin of the coordinate system at the model COG. A starting pitch angle is imposed equal to 15 *deg*. The rigid body geometry is integral with the overset mesh. The full scale ISWEC inertia properties, reported in table 3.1 are imposed to its geometry, with respect to the COG of the system. Its dynamics is thus calculated

at each time step and transferred to the moving mesh, simulating the interaction with the surrounding fluid.

Mesh generation and sensitivity analysis

A trimmed mesh of hexahedral type, that guarantees a minimal cell skewness, is used over the entire domain, as recommended by best practices and used in analogous works [15]. To avoid high computational costs, the mesh size needs to be optimized.

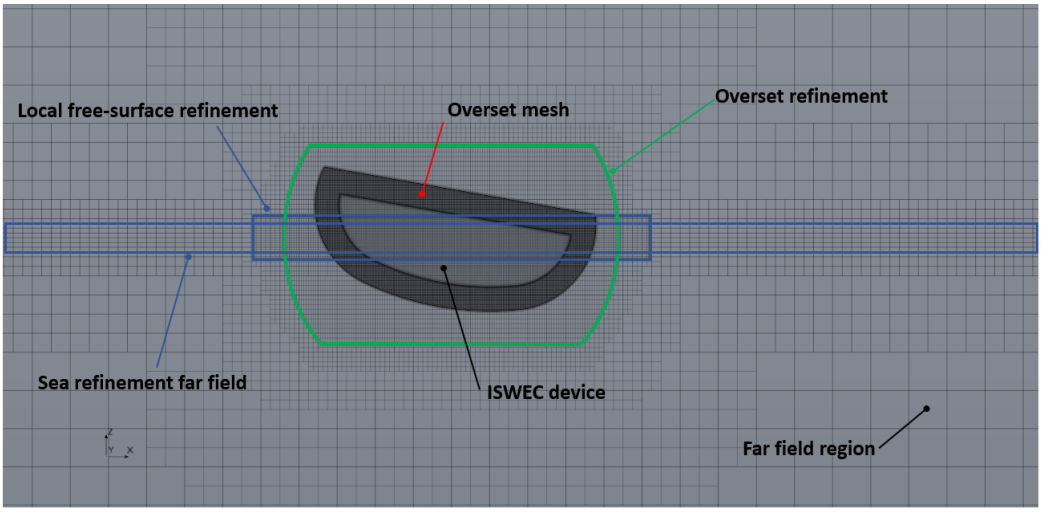

(a) Side view, (x,z) plane.

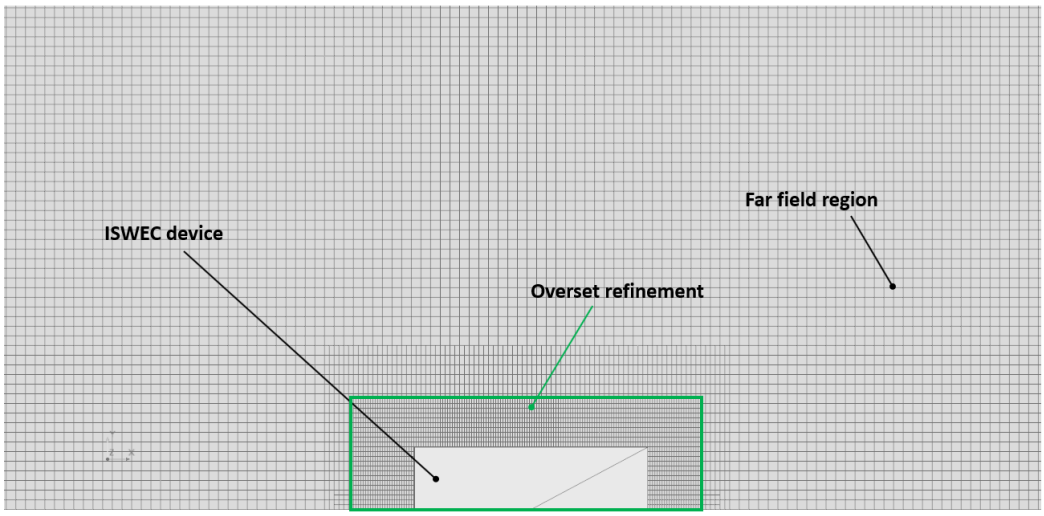

(b) Top view, (x,y) plane.

Fig. 3.11 Hexaedral trimmed mesh with local refinements

Local refinements are set in the areas of interest for the computation of the fluid-floater interaction. The most important area to be refined is the free-surface where a very fine mesh is required to best capture the interface between fluids. Furthermore, a refinement is needed in the swept volume by the free body motion. To obtain a correct interpolation of the scalar fields between the moving and the fixed mesh, the mesh size of the overset region must be similar to the respective region of the background mesh.

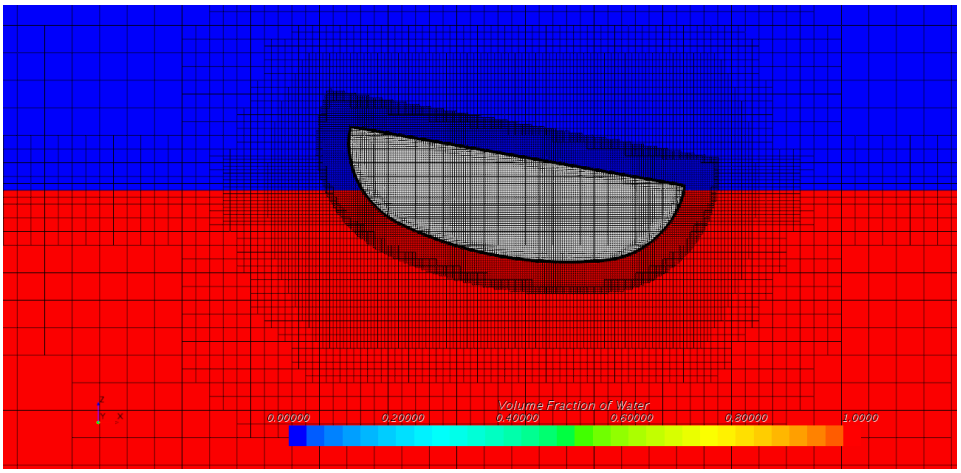

Fig. 3.12 Volume Fraction of water scalar scene. Example with trimmed mesh

According to the presented requirements, different refining regions were generated, as shown in Figure 3.11. It can be observed that a first refined region is defined around the water surface for the total domain (*Sea refinement far field*). Around the hull, the refinement is higher to avoid numerical diffusion and allow the correct interpolation with the overset mesh (*Local free-surface refinement*). The same size is kept for the swept volume by the motion of the moving mesh (*Overset refinement*). A prismatic cells layer is built on the hull surface, that helps to capture the viscous boundary layer accurately. The *Overset mesh* region is the most refined, to guarantee a smooth transition in the mesh size from the prism layer and to accurate capture the free-surface variation induced by the free decay motion. The outer *Far field* region is relatively coarse to save computational resources. Moreover, a general volume growth is obtained with the distance from the floater, that encourages numerical damping in the far field, thus avoiding reflections.

Table 3.4 Solver settings summary

Temporal discretization	2^{nd} order
Time-step	0.001 s
Iterations per time step	5
Turbulence model	$k-\varepsilon$
Total Physical time	40 s

A mesh sensitivity analysis is performed on four different grids, varying the base size of the mesh and the local refinements accordingly, in order to have the same general layout. The time step was chosen guaranteeing the Courant number to be lower than 1, avoiding numerical diffusion [59]. Moreover, based on the *ITTC Practical Guidelines for Ship CFD Applications* [95] and on results obtained by Begovic and al. [14, 15], a time step equal to 0.001 s has been used. A summary of the numerical setup used for the simulation is reported in Table 3.4.

The simulations were carried out using high performance computing on 24 CPUs. Computational resources were provided by HPC@POLITO, a project of Academic Computing within the Department of Control and Computer Engineering at the Politecnico di Torino [87]. Results of the mesh sensitivity analysis are shown in Figure 3.13 and a summary of cell numbers and CPU time is given in Table 3.5.

Table 3.5 Mesh sensitivity analysis summary

Mesh ID	No. of cells	CPU time (h)
GRID 1	3.22×10^5	14
GRID 2	6.86×10^5	27
GRID 3	8.84×10^5	34
GRID 4	2.11×10^6	82

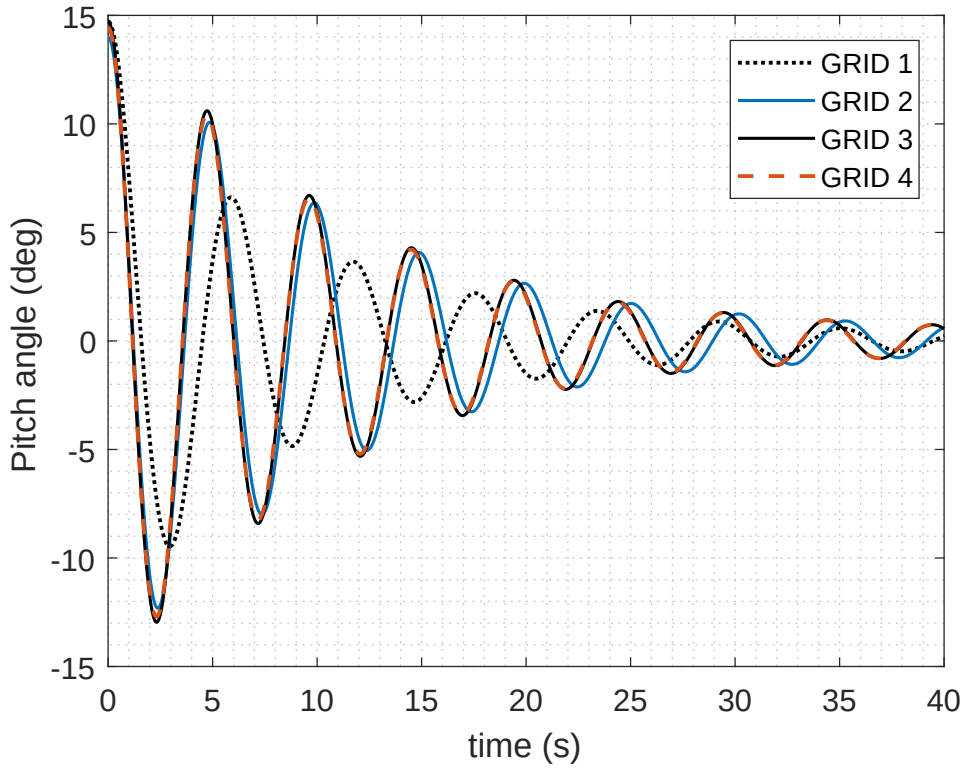

Fig. 3.13 URANS Free Decay test. Mesh sensitivity analysis.

From Figure 3.13 it is possible to observe the significant improvement in the simulation results doubling the number of cells from GRID 1 to GRID 2. This is due to the low quality mesh on the free-surface for GRID 1. A further refinement with GRID 3 showed a small variation in the results, specially in the natural period of the device that decreases with a grid improvement. Eventually, GRID 3 is chosen as good tradeoff, because convergence is achieved and additional refinement is not justified by an improvement in the quality of the numerical results.

Numerical results and damping coefficient identification

Once obtained the grid convergence, it is possible to analyze the numerical time history of the pitch free decay test. A first analysis can be performed to identify the natural period of the device. Maxima and minima of the free decay time series have been identified, excluding the starting position of the analysis. The natural period has been calculated as the average of the time differences between maxima peaks

and minima peaks. A natural period equal to 4.92 s has been identified, which is slightly lower than the one calculated with the linear BEM analysis (98%).

At this point, the identification of the non-linear damping coefficient can be performed. Starting from Equations (3.15) and (3.16), it results:

$$(I_{55}+A_{55})\ddot{\delta}+B_{55-1}\dot{\delta}+B_{55-2}\dot{\delta}|\dot{\delta}|+K_{55}\delta=0 \tag{3.17}$$

that can be written in the canonical form:

$$\ddot{\delta}+2\alpha\dot{\delta}+\beta\dot{\delta}|\dot{\delta}|+\omega_{\delta 0}^2\delta=0 \tag{3.18}$$

where α and β are respectively the linear and quadratic extinction coefficients and $\omega_{\delta 0}$ is the natural pitch frequency:

$$\alpha=\frac{B_{55-1}}{2(I_{55}+A_{55})} \qquad \beta=\frac{B_{55-2}}{I_{55}+A_{55}} \qquad \omega_{\delta 0}=\sqrt{\frac{K_{55}}{I_{55}+A_{55}}}=\frac{2\pi}{T_\delta} \tag{3.19}$$

Numerical simulation advantage is that all the desired quantities can be monitored and acquired. As result, the full time histories of pitch displacement, velocity and acceleration are available. Knowing the quantities at each time step, a *Direct Parameter Estimation* can be used to identify damping coefficients α and β and natural frequency of the device $\omega_{\delta 0}$. This technique is often used in structural dynamics [97, 121] and guarantees the exploitation of all the available information to identify the system unknowns.

To apply the direct parameter estimation, Equation (3.18) must be elaborated to obtain a system of linear equations. For each time step i, it can be written:

$$\ddot{\delta}_i+2\alpha\dot{\delta}_i+\beta\dot{\delta}_i|\dot{\delta}_i|+\omega_{\delta 0}^2\delta_i=0 \tag{3.20}$$

that is a linear equation in three unknowns α, β and $\omega_{\delta 0}$, where the known term is the acceleration and the coefficients are functions of instantaneous displacements δ and velocities $\dot{\delta}$. Considering all the duration of the free decay test, a system of linear equation can be formulated. Using the matrix notation, it results:

$$\begin{Bmatrix} 2\dot{\delta}_1 & \dot{\delta}_1|\dot{\delta}_1| & \delta_1 \\ 2\dot{\delta}_2 & \dot{\delta}_2|\dot{\delta}_2| & \delta_2 \\ \vdots & \vdots & \vdots \\ 2\dot{\delta}_n & \dot{\delta}_n|\dot{\delta}_n| & \delta_n \end{Bmatrix} \begin{Bmatrix} \alpha \\ \beta \\ \omega_{\delta 0}^2 \end{Bmatrix} = - \begin{Bmatrix} \ddot{\delta}_1 \\ \ddot{\delta}_1 \\ \vdots \\ \ddot{\delta}_n \end{Bmatrix} \tag{3.21}$$

where $(1,2,\cdots,n)$ are the simulated time steps. The problem can also be expressed in the well known form:

$$Ax = b \tag{3.22}$$

that can be easily solved in Matlab [118], after checking the condition number of the coefficients matrix. It is due to notice that the presented problem is constituted by a system of over-determined equations that was solved numerically using a least squares algorithm.

Once identified the damping coefficients normalized with respect to the device inertia properties and the natural frequency, it is possible to calculate the dimensional values B_{55-1} and B_{55-2} to be used in the lumped parameters time domain model. At this stage, a fundamental assumption is made, that can be considered valid for the ISWEC device [149]: the hydrostatic stiffness value for pitch motion K_{55} is the one calculated with the BEM analysis and has been calculated using the linear panel method. This hypothesis is valid for the ISWEC, as already explained, mainly because of its hull shape. Knowing K_{55} and $\omega_{\delta 0}$, by using the relation reported in Equations (3.19), it is possible to obtain the added mass value at natural frequency for pitch motion.

Table 3.6 URANS Pitch free decay analysis. Summary results

Property	Symbol	Units	Value
Inertia moment about pitch	I_{55}	$kg\ m^2$	$7.712\ 10^6$
Pitch Hydrostatic Stiffness	K_{55}	$(Nm)/deg$	$1.906\ 10^7$
Pitch Natural Frequency	$\omega_{\delta 0}$	rad/s	1.28
Pitch Natural Period	T_δ	s	4.92
Pitch Added Mass at Natural Frequency	A_{55}	$kg\ m^2$	$3.975\ 10^6$
Linear extinction coefficient	α	s^{-1}	0.05
Quadratic extinction coefficient	β	$-$	0.14
Linear damping coefficient	B_{55-1}	$(Nm\ s)/deg$	$1.169\ 10^6$
Quadratic damping coefficient	B_{55-2}	$kg\ m^2$	$1.636\ 10^6$

Table 3.6 reports the summary of the results of the free decay analysis performed with the URANS model. All the identified values are used as inputs for the Lumped Parameters (LP) non linear model. The comparison between CFD and non-linear LP models is shown in Figure 3.14.

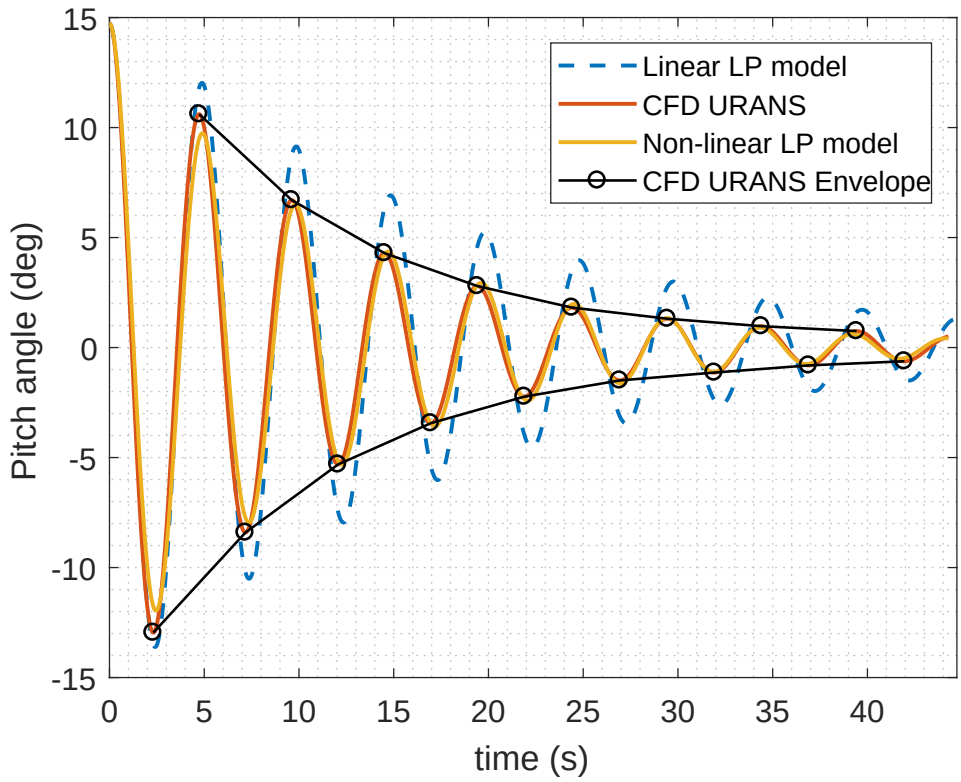

Fig. 3.14 CFD URANS vs Lumped Parameters Model. Non linear damping identification.

It is immediate to notice a very good agreement of the LP model with the identified parameters and the CFD results, thus validating the identification procedure of the damping coefficients. Furthermore, the linear LP model free decay test, without the viscous forces contribution, is reported on the same graph. It is possible to observe significant differences in amplitude and frequency of the response. In particular, the non linear model is characterized by a lower natural period for the pitch response. In conclusion, a very important improvement has been introduced in the non-linear time domain model, that moves the capability of the performance analysis towards more accurate results. This model will be compared against experimental results in model scale, presented in next Chapter, in order to validate the numerical simulations.

Chapter 4

1:20 ISWEC Free-body experimental campaign

To validate the numerical model presented in Chapter 3 an experimental campaign was performed on a 1:20 ISWEC scaled device. The purpose of this campaign was the investigation of the hydrodynamic properties of the device. Hence, no gyroscopic unit was installed on board. Specifically, three main outputs can be obtained: quantification of the hydrodynamic performances, validation of the numerical model and identification of non-linear phenomena. The test campaign was carried out in Napoli, at the towing tank of the Department of Industrial Engineering (DII) of Università degli studi di Napoli Federico II. The model scale was chosen according to the test facility wave-maker capabilities. Free-body tests were performed in regular wave conditions for the determination of the *Pitch RAO* and *Free Decay* tests for both *Pitch* and *Roll* to identify damping factors.

4.1 The 1:20 ISWEC physical model

To represent correctly the full-scale system at a smaller scale, similitude criteria should be used. The scaled model must fulfill *geometric*, *kinematic* and *dynamic* similarities, to guarantee the tests validity. The scaling laws are defined applying the *Buckingham theorem* [112]. According to it, it is possible to derive non-dimensional variables that must be equal for the full-scale prototype and the model. The geometric scale is guaranteed when the length ratio between the full-scale prototype and the

model is constant for both the device geometry and the environment dimensions. To fulfill the kinematic similarity the ratios between velocities in model scale have to be equal to the corresponding ratios in full-scale. To achieve dynamic similarity, the scaling law needs to be defined for the physical phenomena of interest.

Table 4.1 Froude similitude scaling factors

Quantity	Dimension	Scaling
	Geometric	
Length	$[L]$	λ
Area	$\left[L^2\right]$	λ^2
Volume	$\left[L^3\right]$	λ^3
Rotation	$\left[L^0\right]$	–
	Kinematic	
Time	$[T]$	$\lambda^{0.5}$
Frequency	$\left[T^{-1}\right]$	$\lambda^{-0.5}$
Velocity	$\left[LT^{-1}\right]$	$\lambda^{0.5}$
Angular Velocity	$\left[LT^{-1}\right]$	$\lambda^{-0.5}$
Acceleration	$\left[LT^{-2}\right]$	–
Angular Acceleration	$\left[T^{-2}\right]$	λ^{-1}
	Dynamic	
Mass	$[M]$	λ^3
Force	$\left[MLT^{-2}\right]$	λ^3
Torque	$\left[ML^2T^{-2}\right]$	λ^4
Power	$\left[ML^2T^{-3}\right]$	$\lambda^{3.5}$
Power Density	$\left[MLT^{-3}\right]$	$\lambda^{2.5}$

For the offshore structures in general [39, 100] and in particular for floating Wave Energy Converters [53, 136, 119] the main force contributions are the *inertia force* and *restoring force* due to gravity. This means that mass distribution and

inertia moments must be correctly scaled. Hence, the dynamic similarity is obtained applying Froude scaling criteria for which the dimensionless Froude number Fr must be constant:

$$Fr = \sqrt{\frac{inertia\,force}{gravity\,force}} = \frac{\mathrm{v}}{\sqrt{gL}} \tag{4.1}$$

where v is the free stream fluid velocity and L is the characteristic dimension of the problem. The scaling ratios for each characteristic of the experiment are reported in Table 4.1, according to Froude similitude.

The Pantelleria ISWEC hull was scaled using a scaling factor of $\lambda = 1/20$. The scale was chosen as a good trade-off between the performances of the wave tank, the objective of the tests and the further possibility to re-use the model for a second experimental campaign focused on the moored device. The model was designed using a 3D CAD tool to set the mass distribution in order to match the desired values (Figure 4.1). Table 4.2 reports the main properties of the model compared with the full scale device.

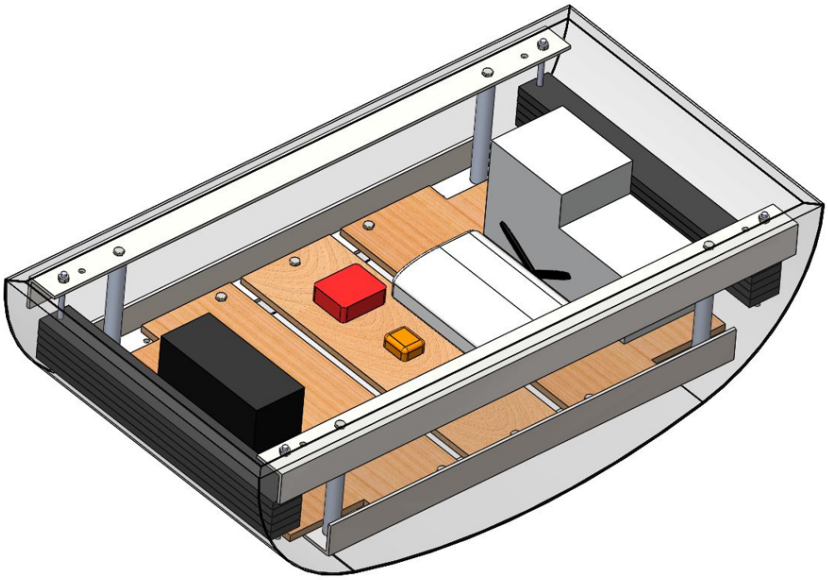

Fig. 4.1 ISWEC 1:20 CAD model

Table 4.2 ISWEC model properties

Property	Symbol	Units	ISWEC 1:1	ISWEC 1:20
Length	L	m	15.33	0.76
Width	W	m	8.0	0.40
Height	H	m	4.5	0.225
Freeboard	FB	m	1.52	0.076
Center Of Gravity	z_{COG}	m	-0.57	-0.028
Mass	M	kg	288000	36
X Inertia moment	I_{xx}	$kg\ m^2$	$1.824\ 10^6$	0.57
Y Inertia moment	I_{yy}	$kg\ m^2$	$7.712\ 10^6$	2.41
Z Inertia moment	I_{zz}	$kg\ m^2$	$7.136\ 10^6$	2.23
Pitch Natural Period	T_n	s	5	1.1

The model's hull is made of 2.5 *mm* thick stainless steel sheets welded together and then matte painted to avoid light reflection. Profile bars are welded inside the hull, on its perimeter, to create a support frame for the steel ballast bars. The ballast mounting is modular to guarantee the setup flexibility and achieve the desired mass distribution, whilst the central volume of the hull is left empty for the installation of the sensors and the data acquisition system. The floater is closed by a transparent PMMA sheet to simplify visual inspections.

Experimental Setup and DAQ System

A Data AcQuisition system is needed to record experimental signals of the physical quantities of interest. To perform free-decay and regular wave tests for the determination of the RAO, the motion of the six DoFs of the hull need to be acquired.

The floater is equipped with an Inertial Unit of Measurement (IMU) installed on board, at the CoG, to record the device motions. More in detail, a **Xsens MTi-30 AHRS** sensor was used [190]. The sensor was rigidly fixed inside the hull, appropriately oriented in such a way that its internal reference system is oriented like the hull reference system. This device can provide the angular velocities on the three

rotational DoFs and the accelerations on the three translational DoFs. An internal data processor uses the velocity and orientation increments and, through a strapdown integration algorithm, gives in output the positions on the three rotational DoFs. The pre-processed data can be acquired at a data rate up to 120 Hz.

The data acquisition is managed by a National Instrument compactRIO **NI cRIO-9030** [127] which is a dual core 1.33 GHz real time control unit. A RS232 serial embedded interface allows to communicate with the MTi. The cRIO is equipped with 2 modules:

- **NI 9207** [125]: 16 channels AI (8 ch ± 20 mA, 8 ch ± 10 V, 24 Bit resolution, 500 $Samples/s$ aggregate rate. This module senses load cell signals.
- **NI 9263** [126]: 4 channels AO ± 10 V, 16 Bit resolution, 100 $kSamples/s/ch$ rate. An output analogical signal is generated in order to synchronize data records with different DAQs.

A WiFi router is connected to the cRIO through a Ethernet embedded interface. Data acquired by the cRIO are transmitted wireless to a remote laptop PC. This feature is used to minimize the number of cables for data transmission. The DAQ system is powered by a 12 V lead acid battery installed on board. On the PC host interface, data were visualized in real time and stored with a sampling frequency of $f_s = 100$ Hz in $.txt$ format using a custom software programmed in LabVIEW. Figure 4.2 shows a scheme of the DAQ system.

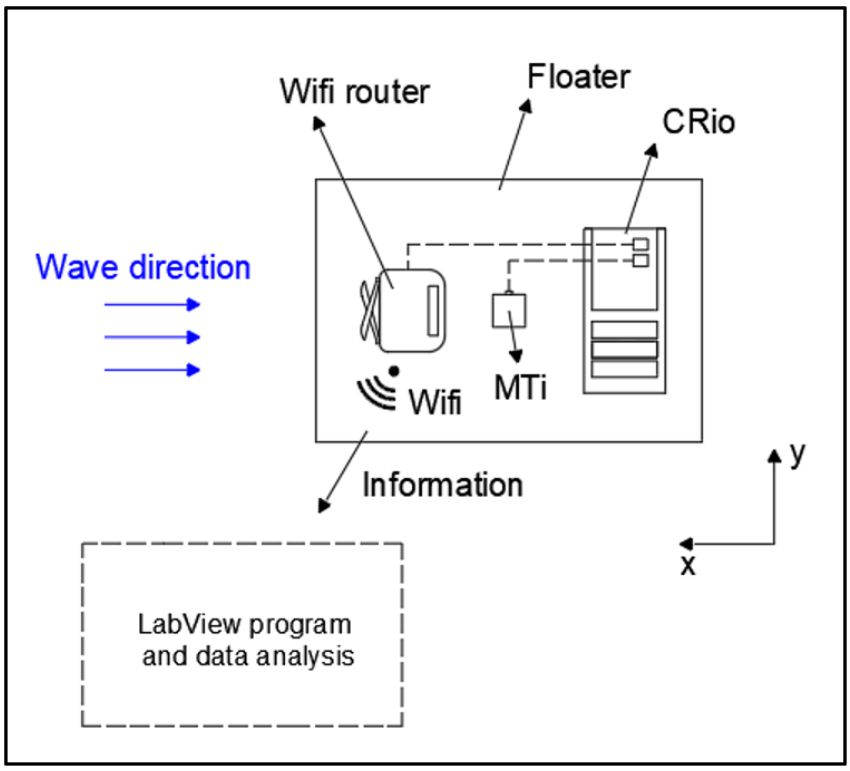

Fig. 4.2 DAQ operating scheme

The prototype setup, including sensors, acquisition and power supply system, was carried out trying to respect as much as possible the mass distribution obtained from the CAD model. The ballast weights were initially installed at the bow and the stern of the hull by means of threaded parts and wooden wedges to properly fix them. Subsequently, three wooden sheets were fixed at the center of the hull to support the battery, the MTi sensor, the cRIO and the WiFi router. Once the electrical connections between the various components was done, the hull was closed by the PMMA sheet. This panel is open in the center to allow battery connection and substitution. Figure 4.3 shows the mounting phases of the prototype.

Dry and Wet validation tests

Mass and inertia properties of the 1:20 ISWEC model were experimentally verified at the wave tank. Specifically, an inertial balance was used to measure the relevant inertia moments (*roll* and *pitch*) and the vertical center of gravity position. The inertial balance of the DII wave tank is a two degrees of freedom physical pendulum

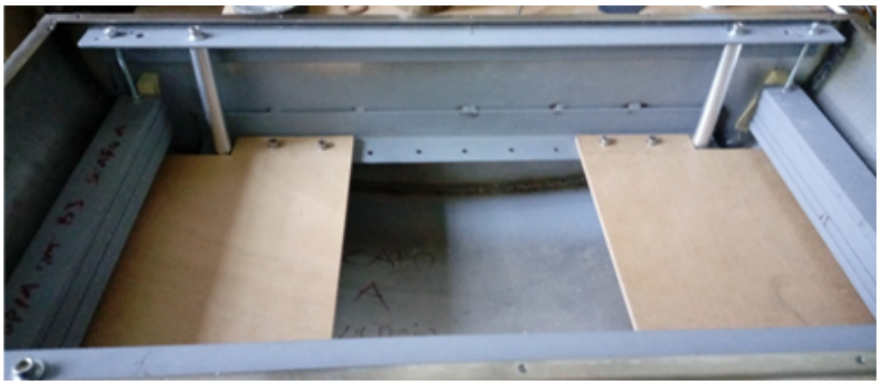

(a) Hull with ballasts detail

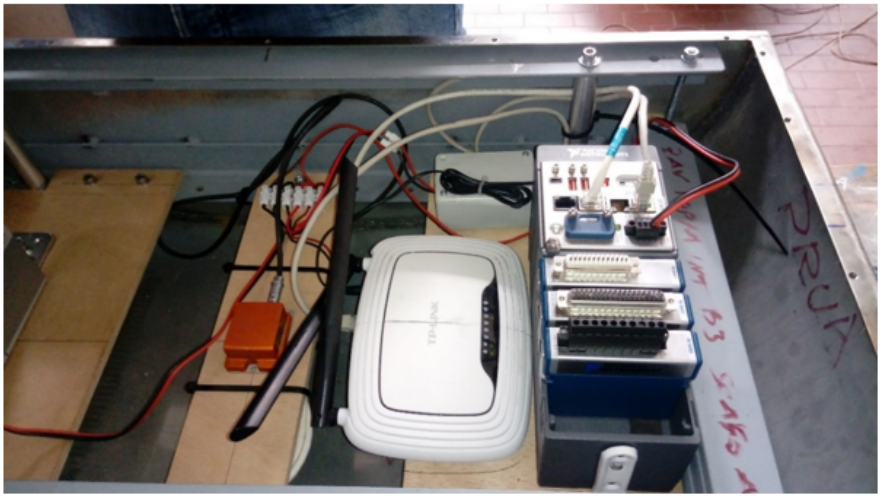

(b) MTi, WiFi router and cRIO inside the hull

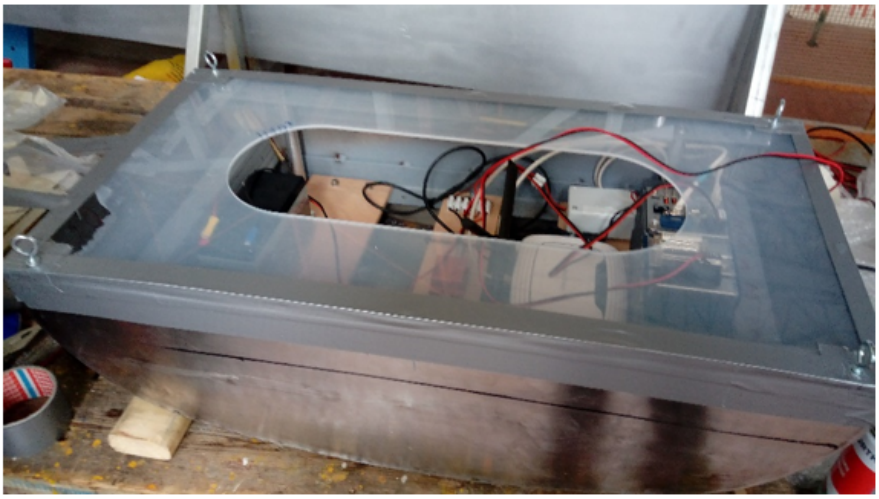

(c) Full prototype

Fig. 4.3 Prototype mounting phases

that allows oscillations about the x and y axes. The inertia properties and the center of gravity position of the unloaded pendulum are known. Adding the model to the pendulum, the properties of the new system can be determined.

First, the correct balancing of the model was checked in a wet test. The model was put in water to verify the correct positioning of the waterline. Trim and heel angles at the equilibrium were guaranteed to be zero by moving the inner ballasts and checking them with a high precision lever.

Then, the model's center of gravity is determined. At the equilibrium position, the vertical z axis of the model coincides with the pendulum vertical axis. Moreover, the model is symmetric and it is put on the pendulum such that the x and y horizontal axes are parallel to the pendulum respective ones. An additional known mass M_b is eccentrically put on the pendulum with its center of gravity at known distances with respect to the oscillation axis d_b and with respect to the pendulum hinge l_b (Figure 4.4). A new equilibrium position is found and the trim angle α can be measured. The moment equilibrium about the vertical axis can be written as a function of the known distances and the angle α:

$$\begin{cases} M_p a_p = M_b a_b \\ a_p = l_p \sin\alpha \\ a_b = d_b \cos\alpha - l_b \sin\alpha \end{cases} \tag{4.2}$$

where M_p is the total mass of the pendulum and the model. The position of the loaded pendulum's center of gravity is calculated from the system of equations (4.2):

$$l_p = \frac{M_b}{M_p}\left(\frac{d_b}{\tan\alpha} - l_b\right) \tag{4.3}$$

Once l_p is known, it is immediate to obtain the position of the model's center of gravity. The experiment was repeated for different values of d_b to improve the measurement accuracy.

Roll and *pitch* inertia moments can be determined from the measurement of the pendulum's oscillation period, under the hypothesis of small oscillations. The moment of inertia of the physical pendulum can be expressed as:

$$I_p = \frac{T^2}{4\pi^2} M_p l_p \tag{4.4}$$

Knowing the inertia properties of the unloaded pendulum and applying the *Huygens-Steiner theorem*, the moment of inertia about a parallel axis through the center of gravity of the model is obtained.

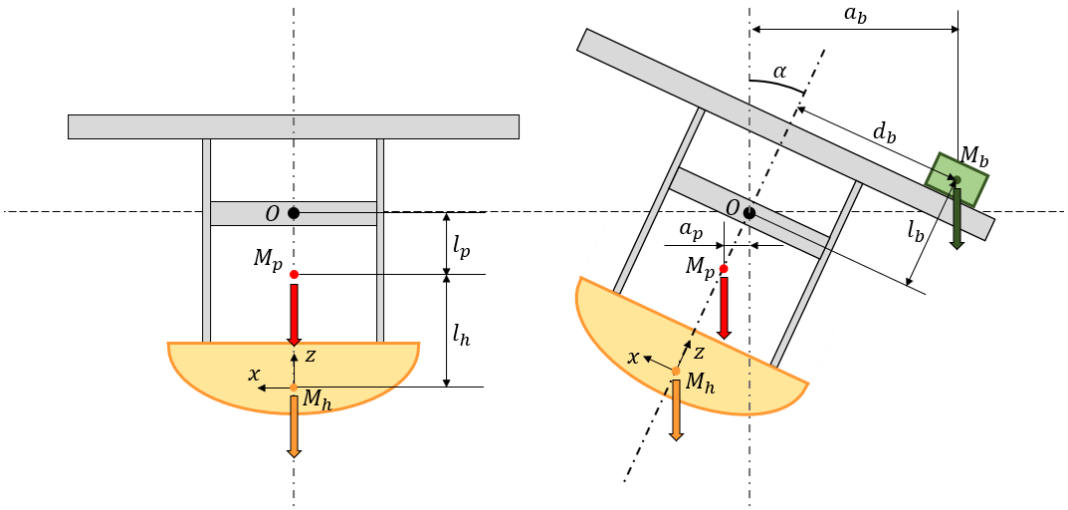

Fig. 4.4 Inertial balance scheme

To measure trim angles and roll and pitch time histories, the inertial balance was equipped with a 3-axis Crossbow accelerometer CXL04GP3-R. Natural periods were obtained from time records of 100 oscillations length. Measurements were repeated three times, at a sampling frequency of 1000 Hz.

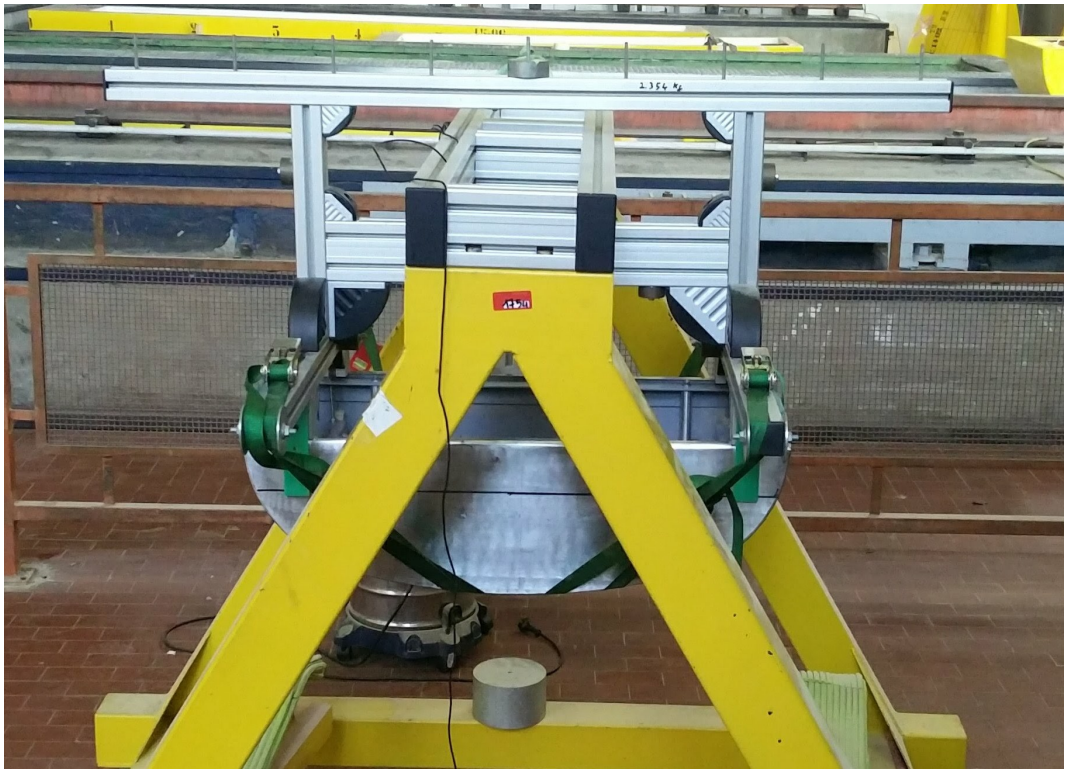

Fig. 4.5 ISWEC model on the inertial balance

At the end of these tests, all the properties of the physical model resulted congruent with the properties reported in Table 4.2.

4.2 Testing facility

The test campaign has been carried out at the towing tank of the Università degli studi di Napoli Federico II. The tank is 135 m long, 9 m wide and 4.25 m deep. In Figure 4.6 the tank sections' sketches are reported, from the facility website [105]. The tank is equipped with a Edinburgh Designs wave-maker and a towing carriage with maximum speed of 8 m/s. The wave-maker (Figure 4.7) is a flap type machine constituted by 8 hinge depth paddles that can generate both regular and irregular waves that propagate parallel to the tank sides. Every paddle is 2 m high and 1.150 m wide and it can oscillate of about ± 20 deg. All the paddles are driven by electric servo-motors and controlled in force. The force transducers measure the incoming wave due to the reflection and the control corrects the paddles motion to

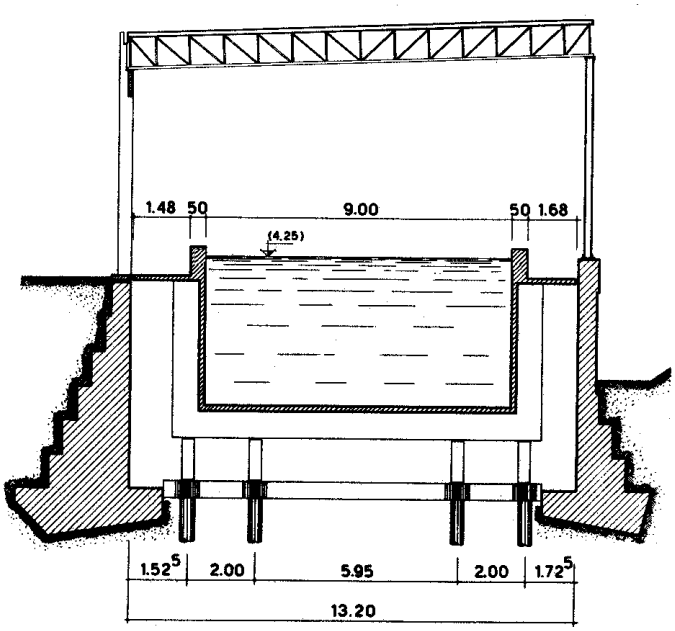

(a) Transversal section

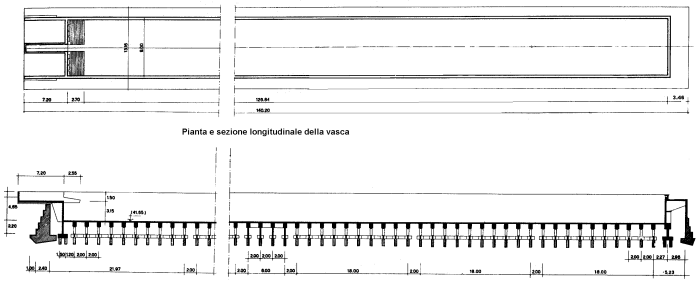

(b) Plan view and Longitudinal section

Fig. 4.6 Napoli Towing Tank detail

absorb it. Regular waves can be generated with wavelength up to 12 m, while the achievable height depends on the wave steepness and goes from $1/100$ up to $1/15$ (H/λ). Irregular waves can also be generated according to any desired sea spectrum condition in appropriate scale. On the other side of the tank with respect to the wave-maker, a sloped beach for fixed water depth is installed. The beach consists of a steel structure 6 m long in longitudinal direction and is able to reduce the amplitude of the incident wave up to 95%.

(a) Flap wave-maker

(b) Absorbing beach

Fig. 4.7 Napoli Towing Tank equipment

Tank DAQ system

According to the seakeeping tests requirements, the tests facility provided the measurements of the wave profile and a redundant measure of the device motions.

The device's motions have been captured by a QUALISYS optical motion tracking. This system consists in tracking the motion of a rigid body through a system of cameras that acquire the motion of specific reflective markers attached to the body itself.

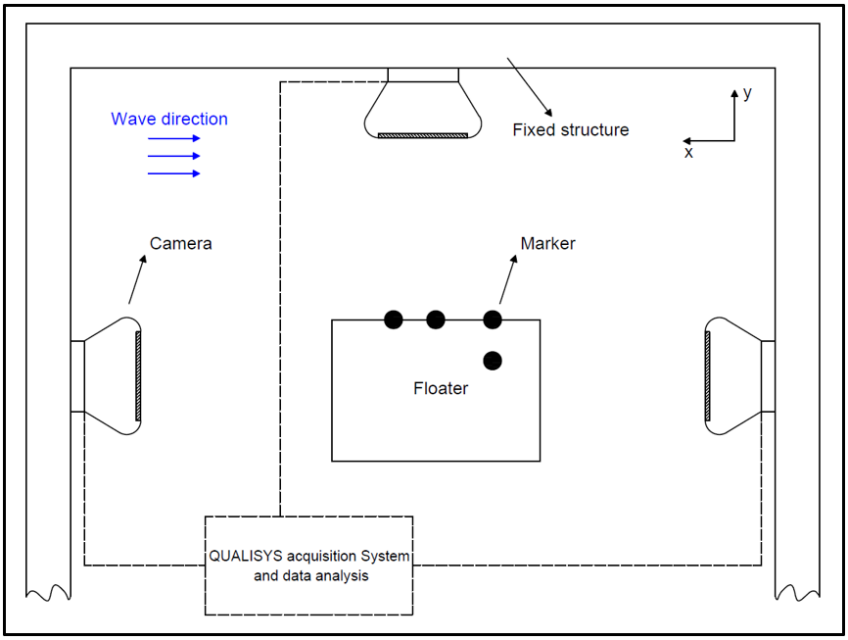

Fig. 4.8 QUALISYS system operating scheme (top view)

As shown in Figure 4.8, the QUALISYS system consists in a set of three cameras that frame the device motion. Each camera, attached to a rigid frame, acquires the motion of four markers attached to the floater, that define the rigid body (Figure 4.9).

The encounter waves are measured by two ultrasonic probes **BAUMER UNDK 301U6103/S14** [11] and one capacitive probe **AKAMINA AWP-24-3** [3]. With reference to Figure 4.10 the three probes are positioned in such a way as to acquire the wave field at different points to have a redundancy on the measure and the possibility to chose the clearest signal for the analysis. One ultrasonic probe is located on the tank side at a lateral distance of 3.96 m from the center-line. The capacitive probe is located at the center-line 3.215 m ahead of the device CoG

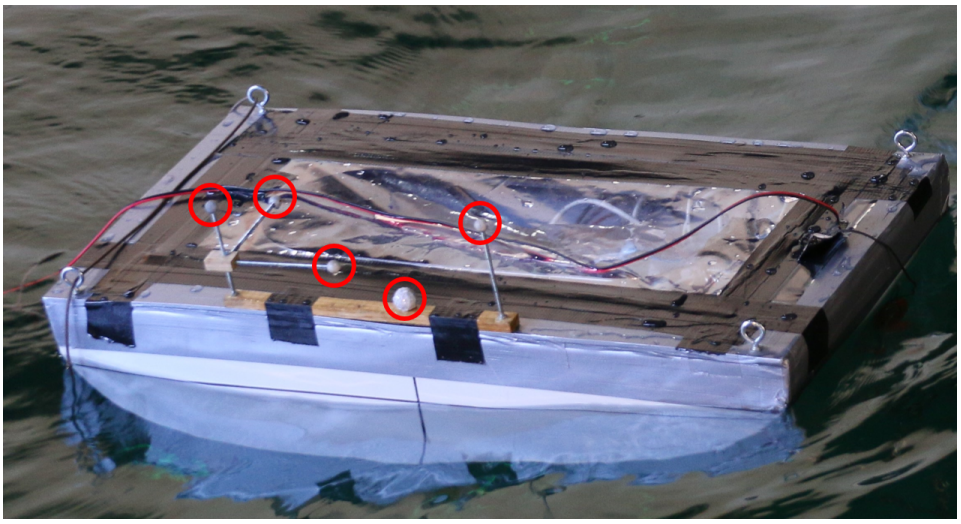

Fig. 4.9 Floater with markers (red circles)

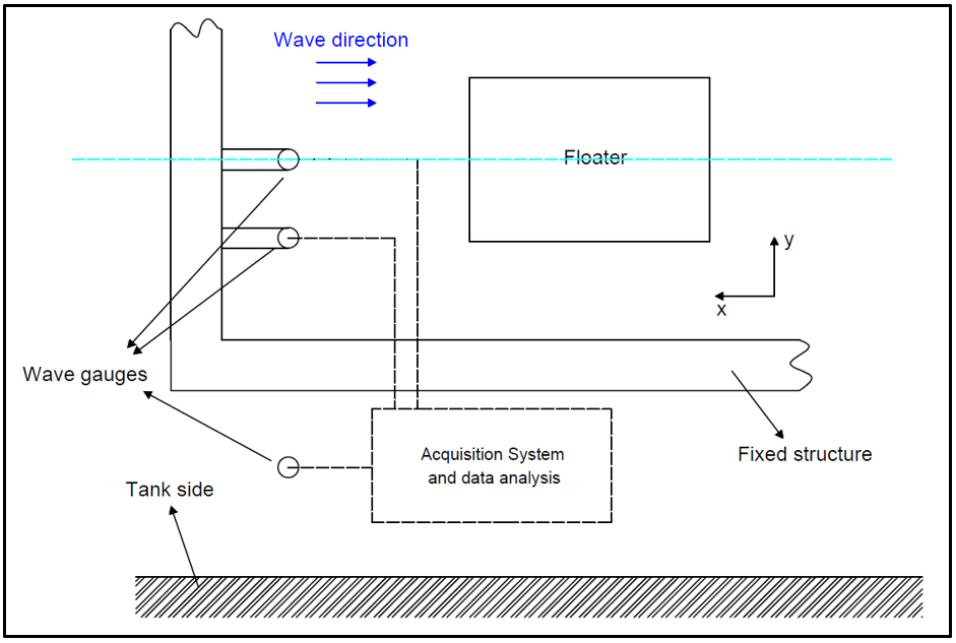

Fig. 4.10 Wave probes operating scheme (top view)

(Figure 4.11). Wave probes and the QUALISYS motion tracking signals are acquired at a sampling frequency $f_s = 500\ Hz$. These sensors are managed by the facility's data logging system that visualizes in real time the signals on a customized LabVIEW software and saves them on *.xls* format files.

For all the tests, the acquired signals from the cRIO and the facility's sensors are synchronized via an analogical trigger signal $(0-5\ V)$ generated by the ISWEC on-board cRIO and acquired by the facility's data logging system.

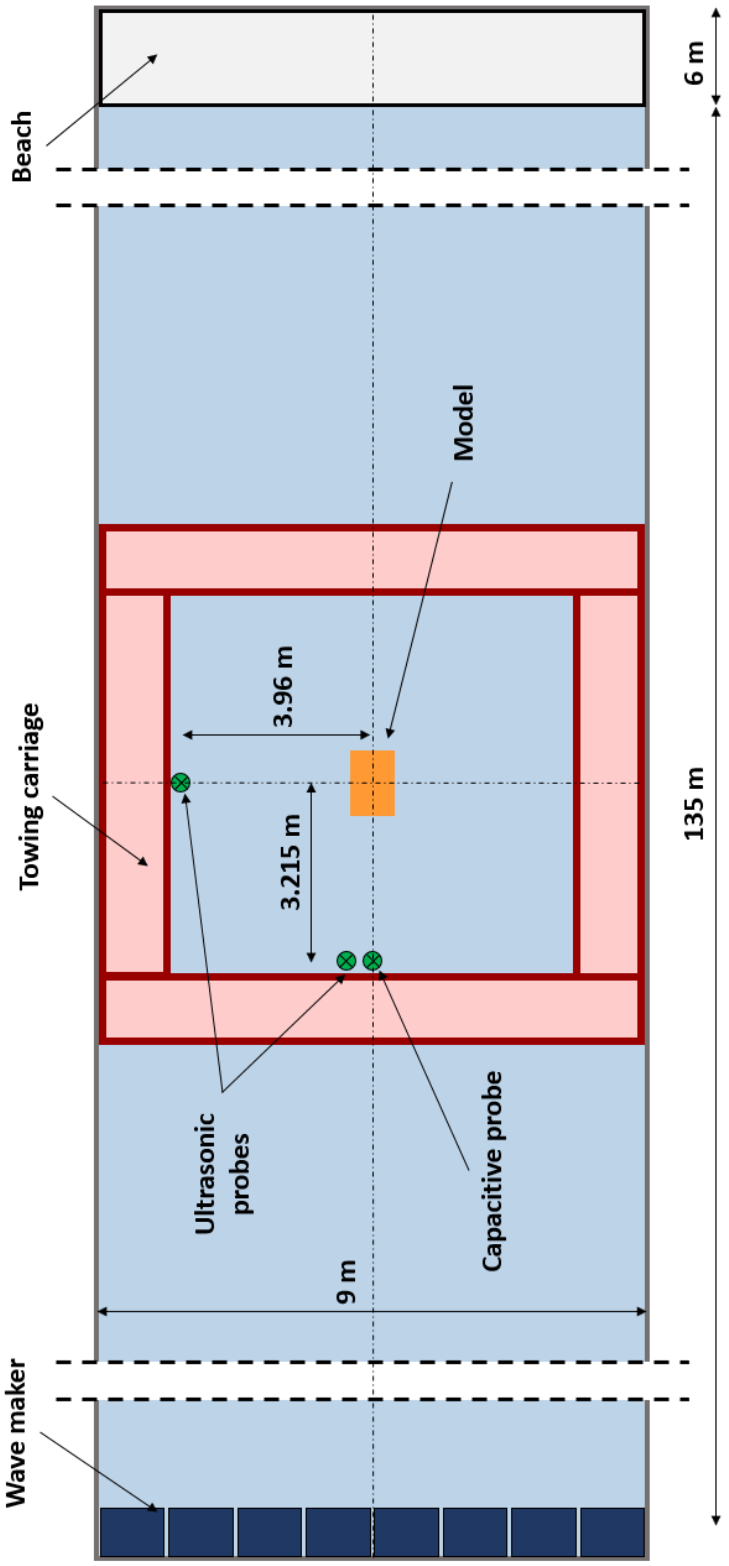

Fig. 4.11 Tank scheme with prototype and wave probes (top view)

4.3 Regular waves tests

In this section the tests in regular waves are presented and analyzed. These tests are performed for the determination of the Response Amplitude Operators of the free device. First, the test plan is presented with all the properties of the tested waves. Secondly, the data processing procedure is discussed and eventually the results are reported and commented.

Test matrices

The test waves are chosen considering a frequency range that is significant for the full-scale device. Furthermore, three different values of steepness H/λ are tested to explore the non-linear effects raising with the wave amplitude. Tables 4.3, 4.4 and 4.5 report the properties of all the tested regular waves. In particular, for the sake of clarity, the correspondent wave period to the 1:1 scale is reported in the first columns ($T_{w,FS}$).

Table 4.3 Regular wave properties - Steepness 1/100

ID	$T_{w,FS}$	$T_{w,m}$	f	a_w	λ	λ/L
	(s)	(s)	(Hz)	(mm)	(m)	(-)
1	3.58	0.800	1.250	5.00	0.999	1.31
2	3.73	0.833	1.200	5.42	1.083	1.43
3	4.00	0.894	1.118	6.25	1.248	1.64
4	4.25	0.951	1.052	7.05	1.412	1.86
5	4.50	1.006	0.994	7.90	1.580	2.08
6	4.70	1.050	0.952	8.61	1.721	2.26
7	5.00	1.119	0.894	9.77	1.955	2.57
9	7.00	1.565	0.639	19.12	3.824	5.03
10	8.00	1.789	0.559	24.98	4.997	6.58
11	9.00	2.012	0.497	31.6	6.320	8.32
12	10.00	2.237	0.447	39.07	7.813	10.28

The wavelength λ is calculated by means of the dispersion relation for deep water:

$$\lambda = \frac{gT_w^2}{2\pi} \tag{4.5}$$

Twelve frequency values are chosen for the determination of the RAOs in the neighborhood of the design natural frequency of the ISWEC device. More in detail, to optimize the test schedule, for the highest steepness value $(1/35)$ only six waves are tested.

Table 4.4 Regular wave properties - Steepness 1/50

ID	$T_{w,FS}$	$T_{w,m}$	f	a_w	λ	λ/L
	(s)	(s)	(Hz)	(mm)	(m)	(-)
1a	3.58	0.8	1.25	9.99	0.999	1.31
2a	3.73	0.833	1.2	10.83	1.083	1.43
3a	4.00	0.894	1.118	12.48	1.248	1.64
4a	4.25	0.951	1.052	14.12	1.412	1.86
5a	4.50	1.006	0.994	15.80	1.580	2.08
6a	4.70	1.050	0.952	17.21	1.721	2.26
7a	5.00	1.119	0.894	19.55	1.955	2.57
8a	6.00	1.342	0.745	28.12	2.812	3.70
9a	7.00	1.565	0.639	38.24	3.824	5.03
10a	8.00	1.789	0.559	49.97	4.997	6.58
11a	9.00	2.012	0.497	63.20	6.320	8.32
12a	10.00	2.237	0.447	78.13	7.813	10.28

Table 4.5 Regular wave properties - Steepness 1/35

ID	$T_{w,FS}$	$T_{w,m}$	f	a_w	λ	λ/L
	(s)	(s)	(Hz)	(mm)	(m)	(-)
3b	4.00	0.894	1.118	17.83	1.248	1.64
5b	4.50	1.006	0.994	22.57	1.580	2.08
6b	4.70	1.050	0.952	24.59	1.721	2.26
7b	5.00	1.119	0.894	27.93	1.955	2.57
9b	7.00	1.565	0.639	54.63	3.824	5.03
12b	10.00	2.237	0.447	111.62	7.813	10.28

Data Processing

Standard data processing, cleaning and filtering were used on the experimental data. The first operation is the decontamination of the signal performing the elimination of any eventual spike and compensation of missing data through an adequate median filter. Data are subsequently filtered with a Butterworth low-pass filter with a frequency cut-off of 10 Hz, ten times the characteristic frequency of the physical phenomenon, in order to eliminate the measurements chain noise.

For the device motion, measured data were compared from both DAQ systems (cRIO and QUALISYS). For all the tests, motion measurements were superimposed, thus the QUALISYS data were used for the analysis, using the same system for all six DoFs motions. Moreover, differently from the IMU sensor, displacement signals did not undergo numerical integration. Hence, no high-pass filter was necessary to remove low frequency components.

The choice of which time interval to analyze is fundamental for a consistent data analysis. The selection was made manually for each test, considering a time window far from any transient and as stationary as possible. Figure 4.12 reports an example of processed data for the six DoFs of the floater and the selected time window for the analysis.

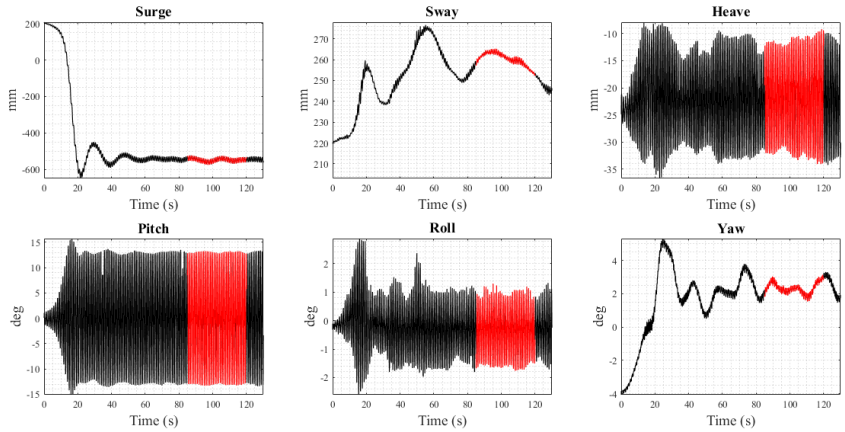

(a) Full experimental record of the device motions

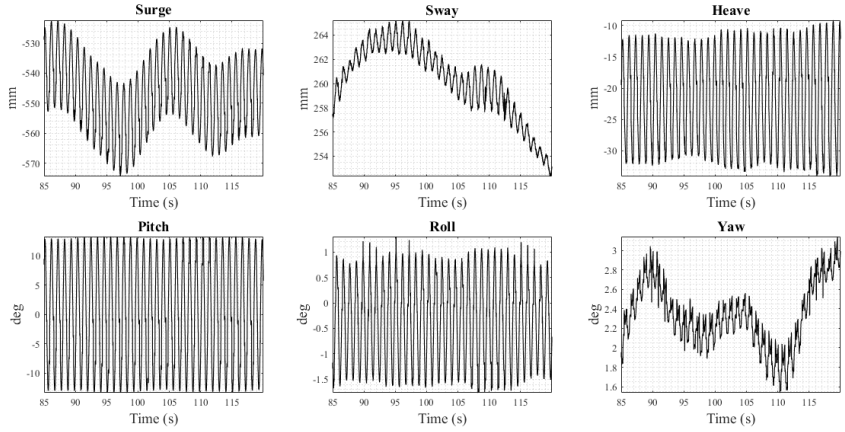

(b) Window selection for the data analysis

Fig. 4.12 Experimental time histories of the device motions. Example

Once the time window has been selected, a Fourier analysis is performed to obtain the signal frequency and amplitude for each DoF of the floater and each incident wave signal.

Wave Records analysis

Three wave probes as described in section 4.2 measured the incident wave. By using the Fourier analysis, all generated waves were analyzed in the frequency domain in order to obtain the real wave frequency that encountered the ISWEC device. It must be noticed that these tests were carried out with a free hull with no moorings.

To follow the surge motion of the device, caused by drift forces, it was necessary to move the carriage in order to allow the device to remain in the field of vision of the QUALISYS system. In addition, since small wires were employed to keep the device in the direction of the incident wave, it was necessary to manually follow its motion without allowing the wires to become taut and preventing any snatch on the device that could affect its motion, thus invalidating the RAO tests.

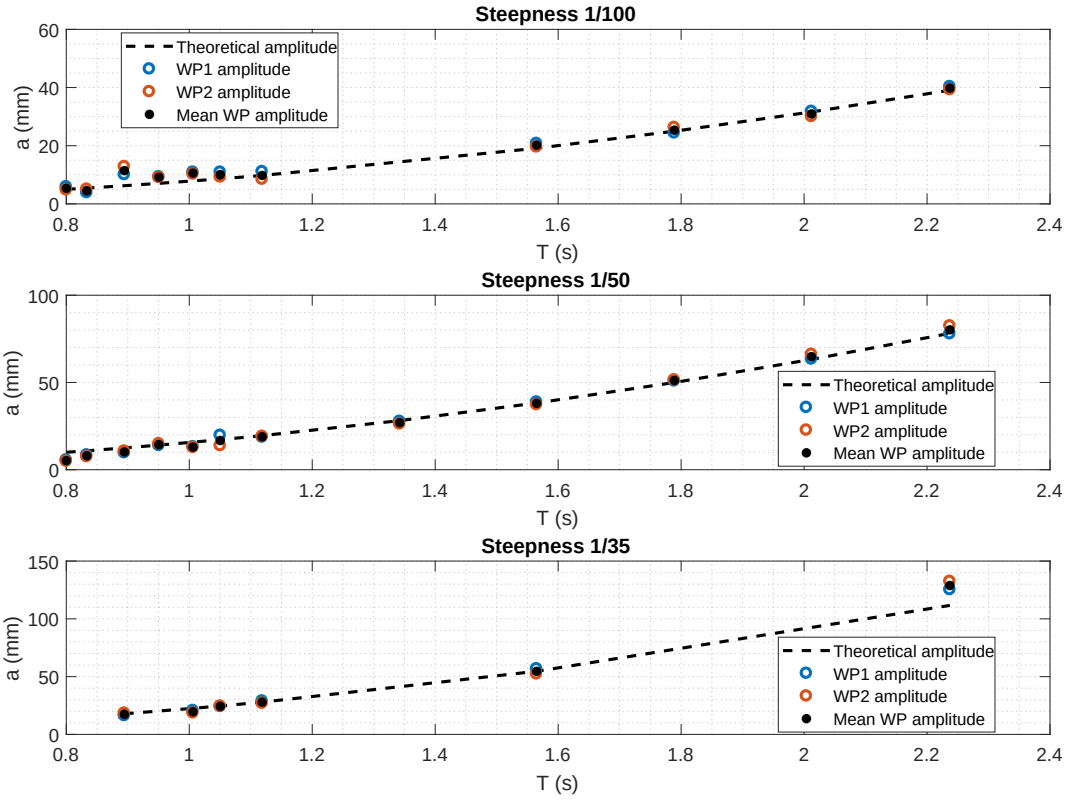

Fig. 4.13 Waves amplitudes for different Steepness

Table 4.6 Wave probes data

Wave Steepness = 1/100												
Wavemaker Frequency (Hz)	1.25	1.2	1.118	1.052	0.994	0.952	0.894	0.745	0.639	0.559	0.497	0.447
Encountered Frequency (Hz)	1.25	1.2	1.016	0.971	0.918	0.899	0.867	-	0.637	0.559	0.497	0.447
Relative Difference (%)	0.0	0.0	-9.1	-7.7	-7.6	-5.6	-3.0	-	-0.4	0.0	0.0	0.0
Device Forward Speed (m/s)	0.0	0.0	0.127	0.114	0.12	0.091	0.053	-	0.009	0.0	0.0	0.0
Wave Steepness = 1/50												
Wavemaker Frequency (Hz)	1.25	1.2	1.118	1.052	0.994	0.952	0.894	0.745	0.639	0.559	0.497	0.447
Encountered Frequency (Hz)	1.19	1.1	1.014	0.922	0.918	0.889	0.85	0.735	0.629	0.559	0.497	0.447
Relative Difference (%)	-4.9	-5.7	-9.3	-12.4	-7.7	-6.6	-4.9	-1.3	-1.5	0.0	0.0	0.0
Device Forward Speed (m/s)	0.061	0.074	0.13	0.184	0.12	0.108	0.086	0.027	0.037	0.0	0.0	0.0
Wave Steepness = 1/35												
Wavemaker Frequency (Hz)	1.25	1.2	1.118	1.052	0.994	0.952	0.894	0.745	0.639	0.559	0.497	0.447
Encountered Frequency (Hz)	-	-	0.959	-	0.879	0.877	0.837	-	0.639	-	-	0.447
Relative Difference (%)	-	-	-14.2	-	-11.5	-7.9	-6.4	-	0.0	-	-	0.0
Device Forward Speed (m/s)	-	-	0.198	-	0.181	0.13	0.112	-	0.0	-	-	0.0

Under the described test conditions, the encountered wave frequency at the device was different from the theoretical frequency of the generated wave. Table 4.6 reports the results of the Fourier analysis for all the tested waves. The second line of the table shows that the encountered wave frequency is different depending on the speed of the carriage needed to follow the device drifting.

Figure 4.13 shows the identified wave properties from the upstream wave probes signals. It can be observed that the mean value between the two wave probes fits the target wave steepness curves. Moreover, results show that the regular waves are generated with a good accuracy for all the considered steepness. More in detail, the biggest error is noticed at high frequencies and small steepness, at which the wave-maker is not able to guarantee the exact wave amplitude that becomes too small.

Response Amplitude Operators

The experimental Response Amplitude Operators were calculated for the three different wave steepness and for both Pitch and Heave DoFs. As already mentioned, the average between the different wave probes results was considered for the wave amplitude identification and the QUALYSIS data were used for the motion amplitude. Roll motion was not considered in this analysis because it was observed that roll angles were negligible, being the device stable for all the tested waves.

Figure 4.14 reports the dimensional motion response values for Pitch and Heave DoFs and for different steepness. It is possible to observe that, as expected, the device motions increase with the wave steepness. At very high frequency, the device is not excited by the waves and works as a filter. At low frequency, the pitch amplitude reaches an asymptotic value. Moreover, it can be observed that for the $1/100$ wave steepness, the pitch amplitude is lower than 10 deg which is the pitch angle that the ISWEC device deck needs to be over-topped by the sea surface. Consequently, it is expected that above this value, the influence of non-linear effects will be relevant, due to the significant change in wet surface and the possible slamming phenomena.

To have a better comparison, it is necessary to represent the results in form of Response Amplitude Operators, normalizing the motion amplitude with respect to the incident wave amplitude. Moreover, to obtain a correct representation at different steepness, RAOs need to be non-dimensional. For the Heave motion, the

non-dimensional RAO is immediately obtained because both excitation and system response have the same units. On the other hand, for the Pitch motion it is necessary to relate the motion amplitude to the wave number $k = 2\pi/\lambda$.

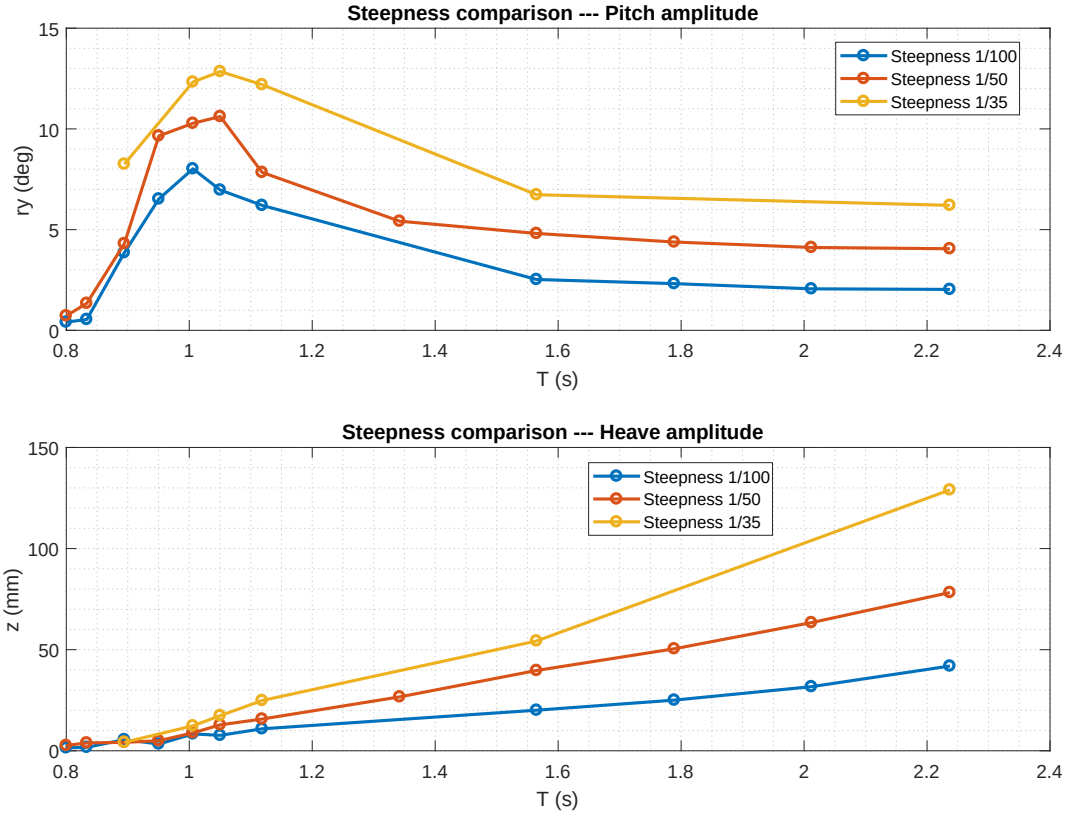

Fig. 4.14 Experimental results. Pitch and Heave motion amplitudes

The experimental non-dimensional RAOs are reported in Figure 4.15 for Pitch and in Figure 4.16 for Heave. As already mentioned, drift forces in regular waves are higher for wave periods close to the natural period of the device. For longer periods, mean drift forces tend to zero. Therefore, the forward speed of the free-device increases close to its natural period, and due to the second order nature of drift forces, increases with the wave steepness. Experimental data are plotted against the results of the BEM linear hydrodynamic model, obtained for 1:20 scaled device, in order to validate the numerical model. Numerical data refer to the zero forward speed condition, hence it can be observed that the RAOs and its peak shift towards higher frequency values. This phenomenon is due to the fact that the device see an encounter wave frequency different from the absolute reference frequency given as input to the wave-maker.

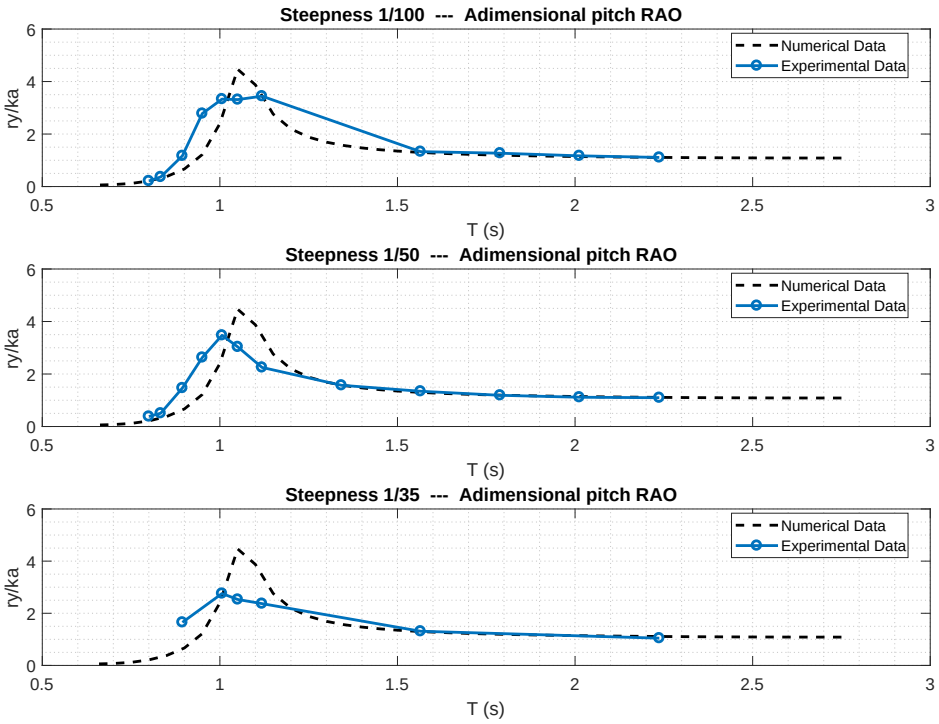

(a) Experimental RAO curves at different wave steepness

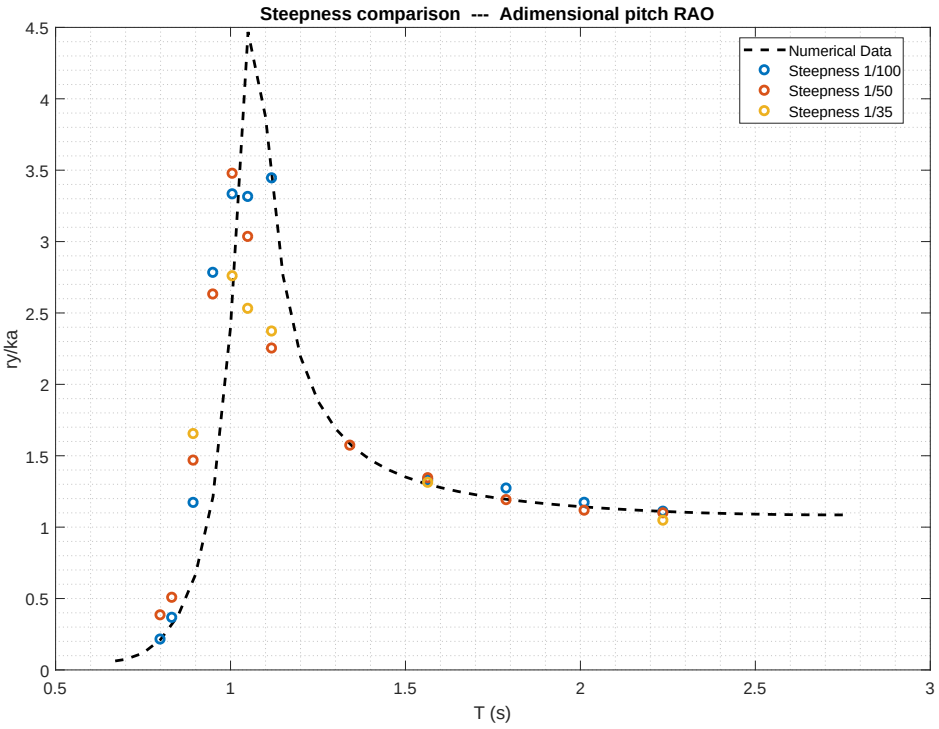

(b) Experimental points VS Numerical results. Full tests comparison

Fig. 4.15 Pitch Response Amplitude Operator - Free body tests

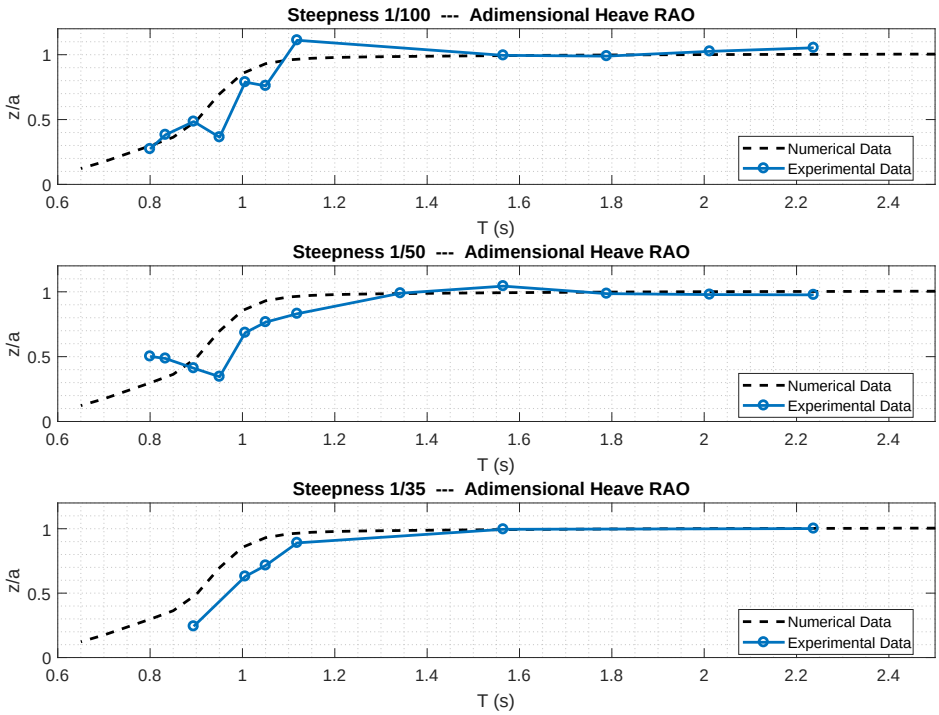

(a) Experimental RAO curves at different wave steepness

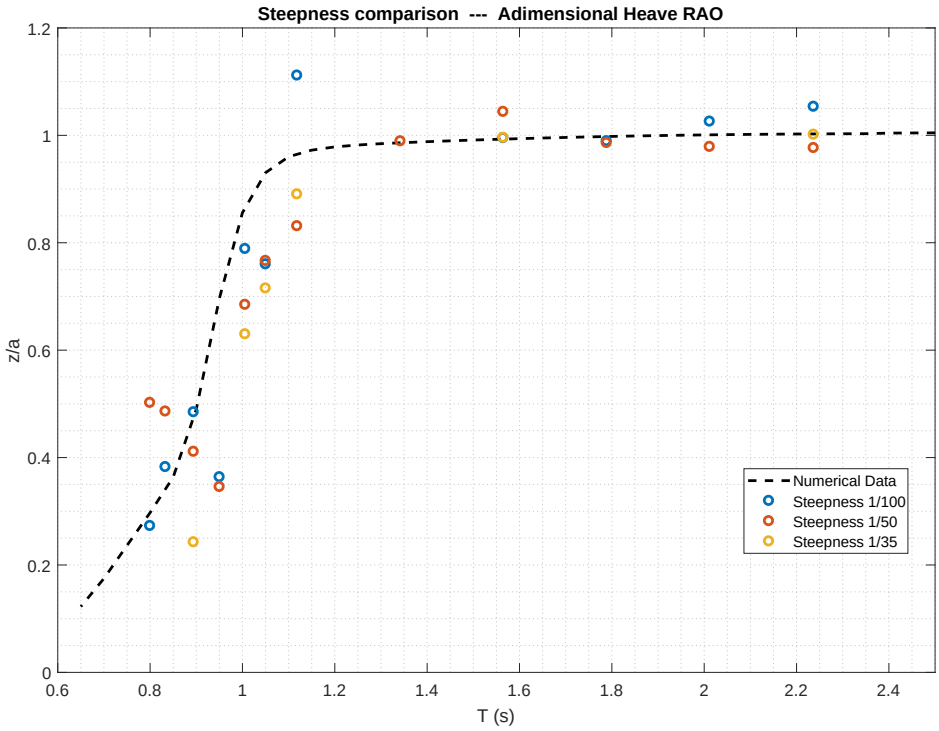

(b) Experimental points VS Numerical results. Full tests comparison

Fig. 4.16 Heave Response Amplitude Operator - Free body tests

It is not possible to shift the response and adjust the results for the zero forward speed condition, because in forward speed case the hydrodynamic coefficients of the device are different, as described by Faltinsen [57]. These considerations are valid for both Heave and Pitch response.

The hydrodynamic behavior is validated against the linear numerical model based on the BEM, for long wave periods. For frequencies close to the device natural period, it can be observed that the RAOs values decrease by increasing the wave steepness. As anticipated, this is due to the influence of non linear phenomena. For a better validation of the numerical model, these phenomena need to be considered. Furthermore, an experimental campaign with the moored device is needed to compare the results at zero forward speed.

4.4 Free decay tests

Last tests performed during this experimental campaign were the free-decay tests for pitch and roll motions. In Chapter 3 was discussed the fundamental importance of the free-decay test for pitch motion that is required to identify viscous forces contributions and improve the accuracy of the numerical time domain model. Roll decay is used to determine the stability at roll of the device. Furthermore, roll decay is important for the identification of viscous damping which can be used at the same way in a 6 DOFs model. In particular, as it will be discussed further, roll viscous damping is introduced in numerical models that simulate the system in extreme conditions, with the addition of the mooring dynamics. These kind of models can lead to numerical instabilities if the roll motion is not correctly damped. For the ISWEC device, linear roll damping is very low and the significant contribution to roll damping is given by the viscous component that can be identified by means of CFD, as explained in Chapter 3 for pitch motion or experimentally, as it will be presented in this section.

Both pitch and roll free decay tests were performed inducing manually an inclination angle with respect to the transverse or longitudinal axis of the device and releasing the body, acquiring its motion with the motion tracking system. Figure 4.17 reports the raw data for all the analyzed free decay tests.

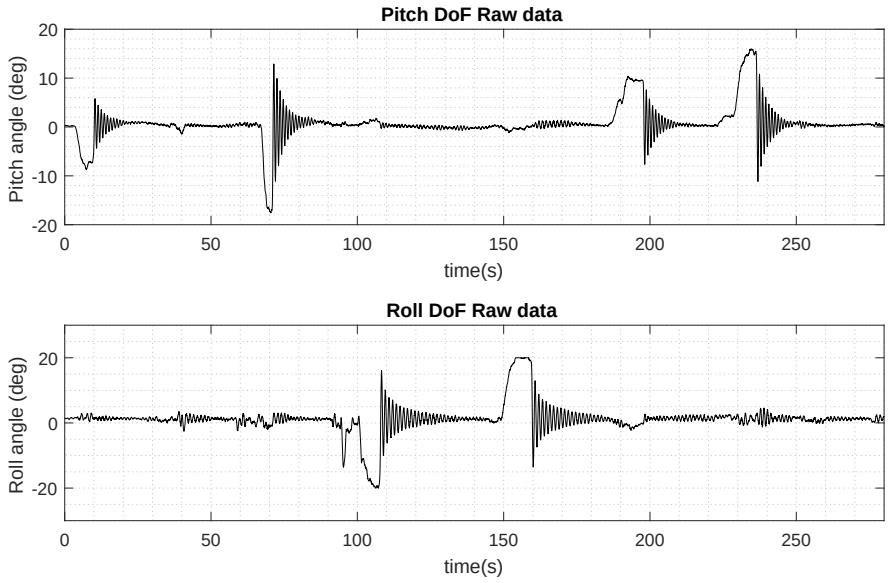

Fig. 4.17 Free decay experimental tests. Raw data

Data cleaning

To analyze the experimental data it is necessary a first data elaboration. Each single free decay test window is cut from the complete record. For each test, the mean value and linear trend in the free decay signal has been eliminated using the Matlab function *detrend* [118]. An example of the resulting signal is shown in Figure 4.18 Moreover, to clean the signal and better identify the signal peaks, it was considered appropriate to filter the signal with a 4th order Butterworth low pass filter with a cutoff frequency of 3 Hz. Thus, fluctuations around crests and troughs are eliminated without modifying the characteristic shape of the free decay signal, as shown in Figure 4.19.

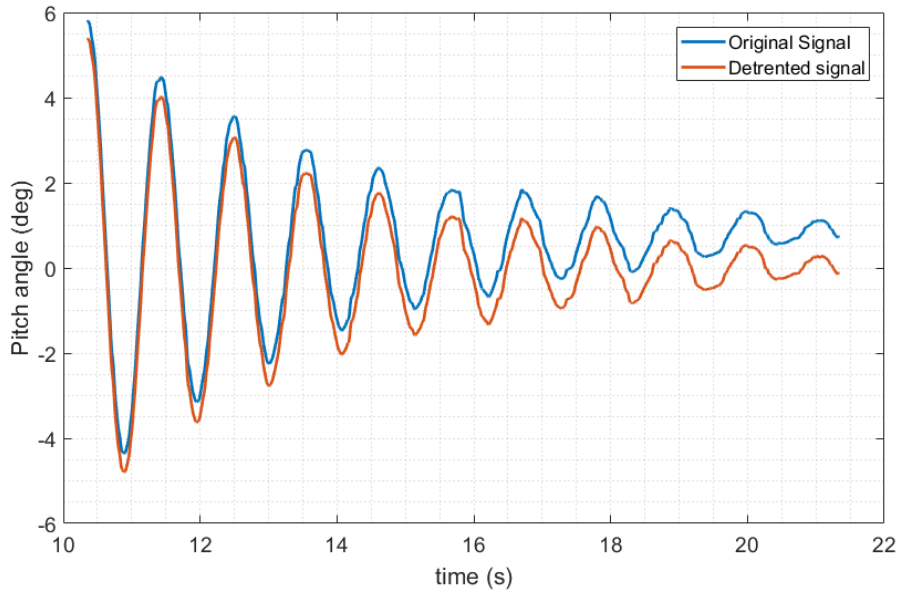

Fig. 4.18 Pitch free decay example. Raw and *detrended* signal

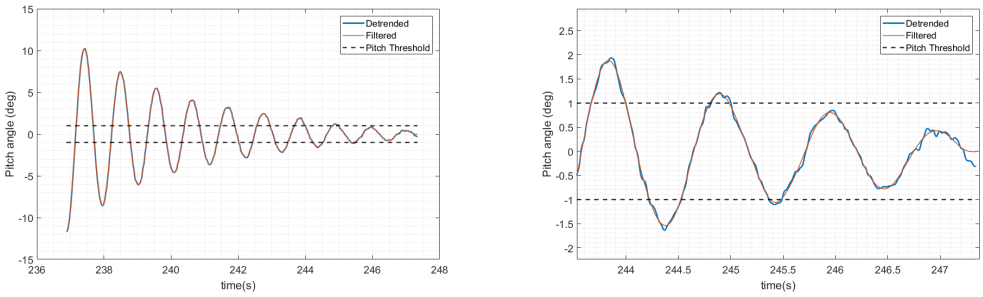

(a) Non-filtered vs Filtered signals

(b) Zoom caption

Fig. 4.19 Pitch free decay. Filter application

Therefore, the signal is clean and can be correctly analyzed.

Damping identification methodology

Differently from the numerical model, for the experimental tests signals of motions velocity and acceleration are not available for the free decay tests. Several techniques are available for the identification of the damping factor from experimental tests data, as reported in [77, 80, 81, 95, 108, 180]. The methodology successfully used in [12, 13, 193] has been selected as the most suitable in this work.

The identification procedure is here described for the pitch motion, but it is analogous for roll. First, the hypothesis of 1DOF dynamics is made. This hypothesis can be assumed valid referring to the experimental raw data reported in Figure 4.17. Indeed, when the pitch decay test is performed, roll motion is negligible and vice versa. For what concerns the heave motion, particular attention was made to minimize its effect during the experiments. Assuming the single DOF dynamics, the free decay equation of motion for pitch is recalled from the canonical form reported in Chapter 3:

$$\ddot{\delta} + 2\alpha\dot{\delta} + \beta\dot{\delta}|\dot{\delta}| + \omega_{\delta 0}^2\delta = 0 \tag{4.6}$$

Furthermore, according to Chakrabarti [39], it is possible to assume that for each half cycle, the oscillation is reasonably sinusoidal. Under this assumption, the non linear term can be linearized using Fourier series expansion:

$$\dot{\delta}|\dot{\delta}| \approx \frac{8}{3\pi}\omega_\delta \delta_i \delta \tag{4.7}$$

where δ_i and ω_δ are respectively the amplitude and the frequency of oscillation of the $i-th$ oscillation cycle. Thus, it is possible to define the equivalent linear extinction coefficient as:

$$\alpha_{eq} = \alpha + \frac{4}{3\pi}\omega_\delta \delta_i \beta \tag{4.8}$$

and, consequently rewrite Equation 4.6 in a linearized form:

$$\ddot{\delta} + 2\alpha_{eq}\dot{\delta} + \omega_\delta^2\delta = 0 \tag{4.9}$$

Equation (4.9) describes a linear underdamped system, for which the envelope curve is defined as:

$$\delta = \delta_0 e^{\alpha_{eq} t} \tag{4.10}$$

Applying Equation (4.10) for two consecutive peaks i and $i+1$ of the decay curve, it is possible to calculate the logarithmic decay:

$$\frac{\delta_i}{\delta_{i+1}} = e^{\alpha_{eq}(t_{i+1}-t_i)} \tag{4.11}$$

thus, identifying the equivalent linear extinction coefficient:

$$\alpha_{eq} = \frac{1}{t_{i+1}-t_i}\ln\left(\frac{|\delta_i|}{|\delta_{i+1}|}\right) \equiv \alpha + \frac{4}{3\pi}\omega_\delta \delta_{mean,i}\beta \tag{4.12}$$

where

$$\delta_{mean,i} = \frac{|\delta_i| + |\delta_{i+1}|}{2} \tag{4.13}$$

and the natural pitch frequency can be calculated as:

$$\omega_{\delta 0} = \sqrt{\omega_\delta^2 + \alpha_{eq}^2} \tag{4.14}$$

This method allows to calculate the extinction curve of the α_{eq} as a function of the mean amplitude δ_{mean} for each cycle. To exploit all the available experimental data and obtain a more accurate estimation, it is possible to calculate α_{eq} and δ_{mean} for each oscillation cycle, considering both maxima and minima peaks and grouping the informations of all the decay tests for a specific DOF.

The linear regression fit is then performed on the calculated points, with respect to the curve expression:

$$\alpha_{eq} = a\delta_{mean} + b \tag{4.15}$$

which allows to identify the linear and quadratic extinction coefficients:

$$\begin{aligned} \alpha &\equiv b \\ \beta &\equiv \frac{3\pi}{4\omega_\delta} a \end{aligned} \tag{4.16}$$

Data elaboration and linear and quadratic damping coefficients identification

Following the presented procedure, the identification of damping coefficients has been performed for both pitch and roll free decay tests. First, peaks maxima and minima are identified for each test, removing the first cycle of oscillation. Figure 4.20 reports an example for pitch free decay peaks, with the minima in absolute value, to highlight the non linear behavior of the decay.

Once calculated minima and maxima for each test, the extinction curve fitting is performed. In Figure 4.21 the extinction curve fitting is reported for pitch decay. The intercept value on the y-coordinates axis represents the linear damping component, while the quadratic extinction coefficient is related to the curve slope. The oscillation cycles have been considered until a threshold value of 1 deg as shown in Figure 4.19a. It can be noticed that the dispersion increases with decreasing values of pitch angle.

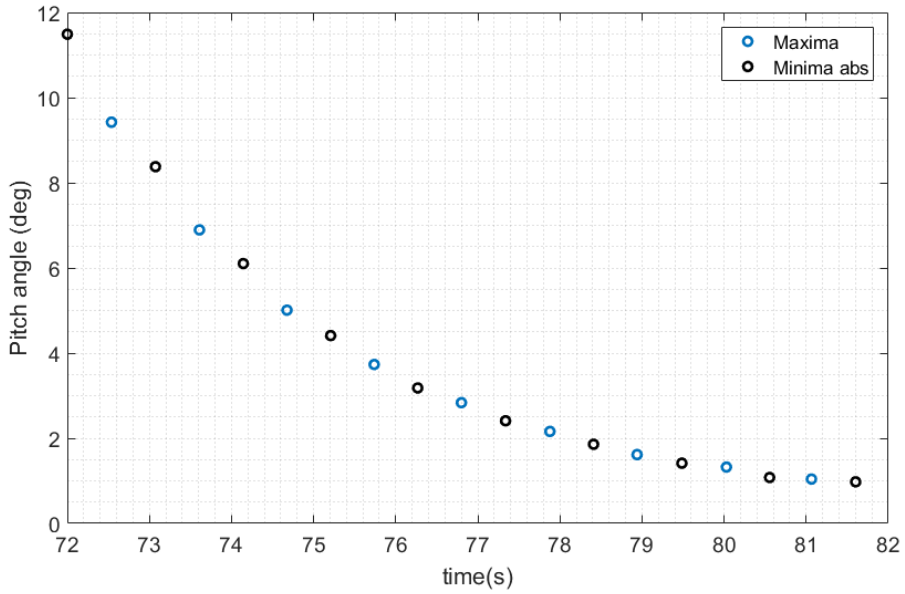

Fig. 4.20 Pitch free decay example. Peaks maxima and minima

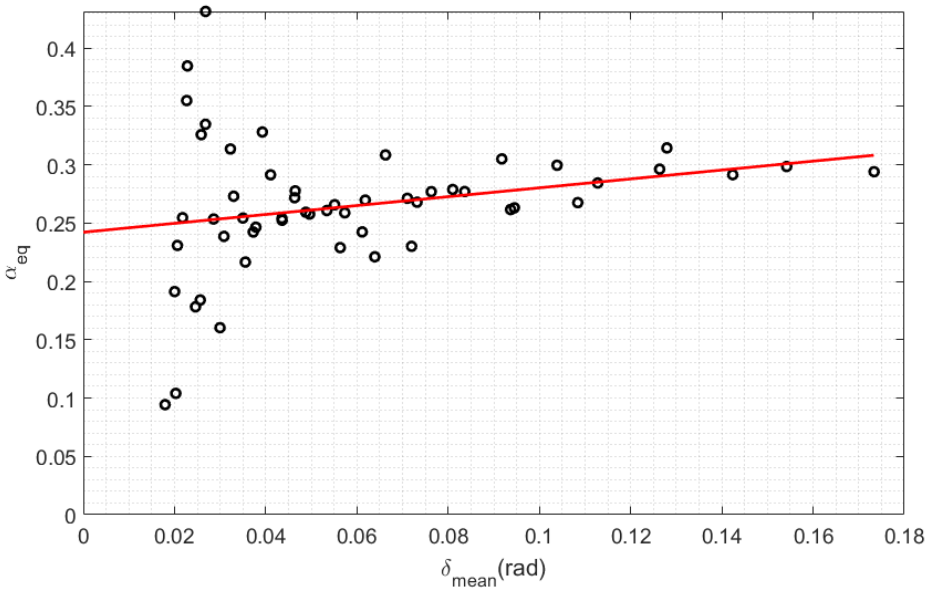

Fig. 4.21 Pitch free decay coefficients analysis. Treshold 1 *deg*

To reduce the dispersion and increase the fitting accuracy a second fit has been performed with a threshold value of 2 deg. Results are shown in Figure 4.22. A reduced dispersion is obtained, although a week dependency to this modification is

observed on the identified coefficients. More in detail, a summary of the obtained results for both thresholds is reported in Table 4.7.

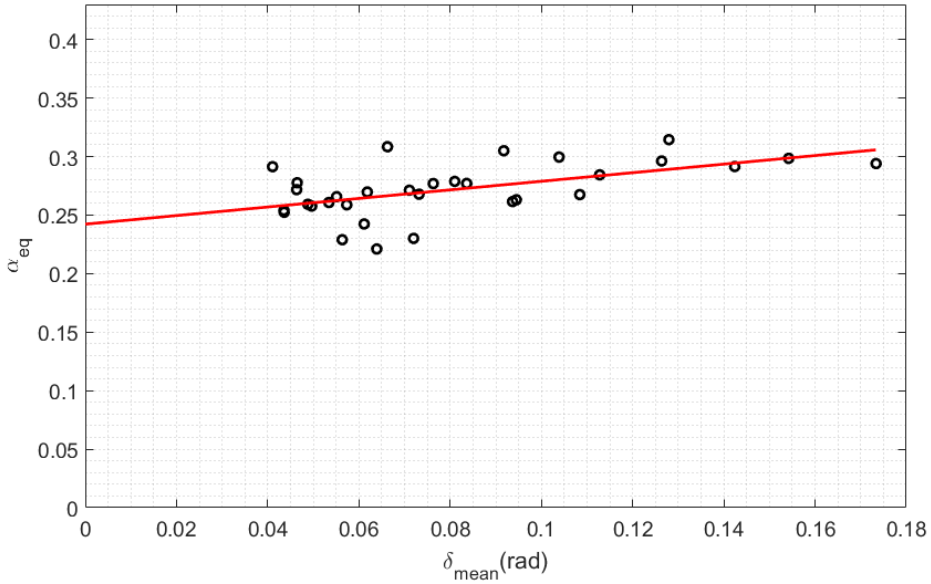

Fig. 4.22 Pitch free decay coefficients analysis. Treshold 2 *deg*

Table 4.7 Pitch damping coefficients identification. Summary results

Threshold	ω_δ	a	b	α	β	T_δ
(deg)	(rad/s)	$(rad^{-1}s^{-1})$	(s^{-1})	(s^{-1})	$(-)$	(s)
1	5.87	0.3808	0.2422	0.242	0.153	1.07
2	5.87	0.3663	0.2423	0.242	0.147	1.07

The same analysis has been performed for roll decay data. Graphical results are shown in Figure 4.23 for 1 *deg* threshold and in Figure 4.24 for 2 *deg* threshold, whilst Table 4.8 reports summary values. It is important to notice that for roll motion, the linear contribution in damping coefficient is negligible with respect to the quadratic one. Furthermore, if the 2 *deg* threshold is considered, linear extinction coefficient is basically absent.

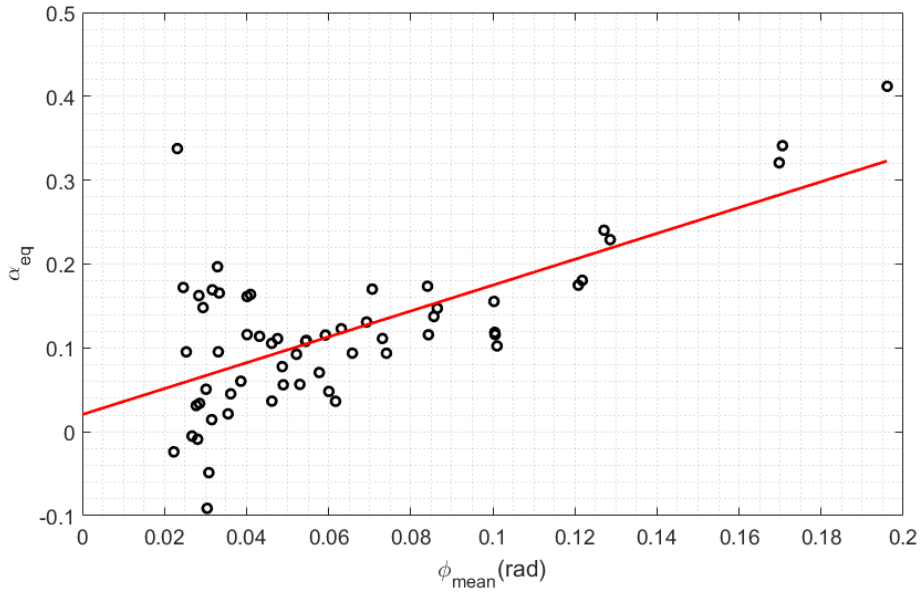

Fig. 4.23 Roll free decay coefficients analysis. Treshold 1 *deg*

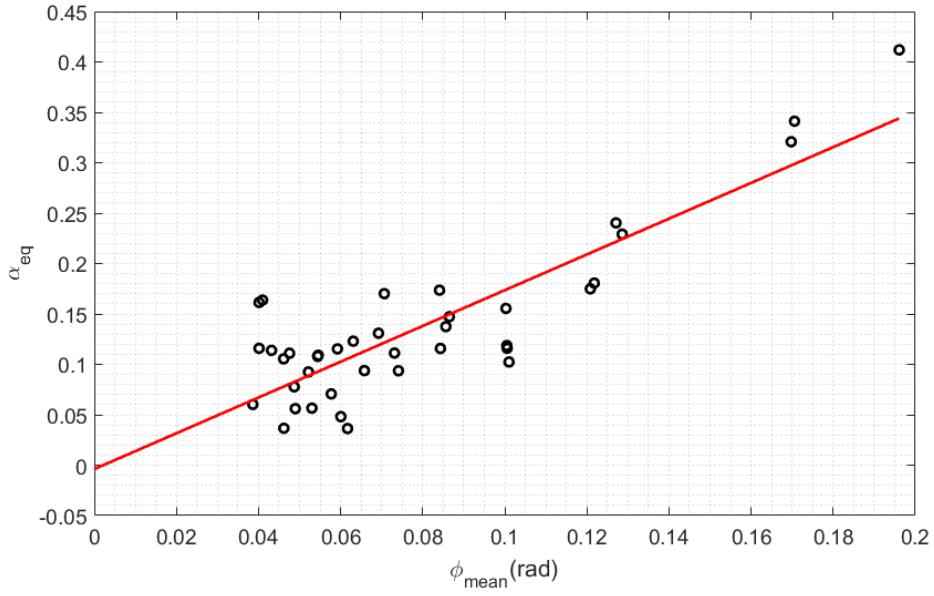

Fig. 4.24 Roll free decay coefficients analysis. Treshold 2 *deg*

Table 4.8 Roll damping coefficients identification. Summary results

Threshold	ω_ϕ	a	b	α	β	T_ϕ
(deg)	(rad/s)	$(rad^{-1}s^{-1})$	(s^{-1})	(s^{-1})	$(-)$	(s)
1	4.99	1.5825	0.0164	0.0164	0.748	1.26
2	4.99	1.774	-0.0039	-	0.838	1.26

Experimental data and Numerical Model Comparison

To evaluate the identification reliability and validate the numerical model against the experimental results, the lumped parameters time domain model is used with the identified values of the damping factors. The free decay simulation is performed according to the model scale of the experimental campaign. As done for the numerical identification proposed in Chapter 3, the hydrostatic stiffness value is calculated using the BEM model and properly scaled, while the added mass is obtained knowing also the inertia moment and natural frequency values.

Graphical results of the comparison are shown in Figure 4.25 for the roll motion and in Figure 4.26 for the pitch motion.

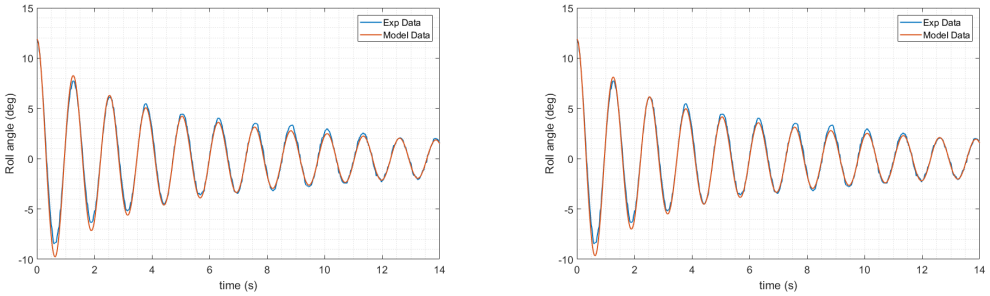

(a) Threshold 1 *deg* (b) Threshold 2 *deg*

Fig. 4.25 Roll free decay. Non linear Lumped Parameters model vs Experimental data

For roll motion, it can be observed that there is negligible influence on the variation of the two identified coefficients. Within this work, the 1 *deg* threshold values will be considered valid for the roll DOF, despite the higher dispersion of experimental values.

In general, a very good agreement between experimental data and non linear model with identified coefficients is obtained. Numerical and experimental curves are almost superimposed for all the analyzed cases, demonstrating the accuracy of the non-linear modeling proposed in this work for the ISWEC device.

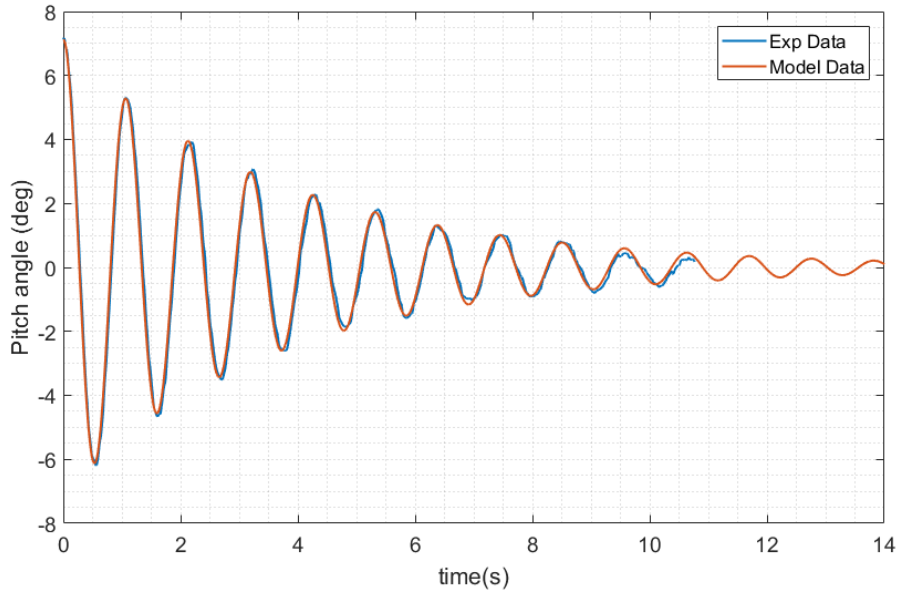

Fig. 4.26 Pitch free decay. Non linear Lumped Parameters model vs Experimental data

Eventually, for pitch motion it is possible to compare the damping coefficients identified from experimental data with the numerical values identified by CFD simulations. To compare model values with numerical results, it is necessary to scale up the experimental values. In particular, the following relations are valid for the linear and quadratic extinction coefficients:

$$\alpha_{ISWEC} = \frac{\alpha_{MODEL}}{\sqrt{\lambda}} \qquad \beta_{ISWEC} = \beta_{MODEL} \tag{4.17}$$

Table 4.9 reports the comparison between experimental scaled up values and CFD URANS results for all the significant quantities of the free decay analysis. The two analyses differ for methods and scale, thus it is not proper to define the differences in results as error. Nevertheless, to demonstrate the validity of both methods, a percentage difference is calculate as:

$$Error = |EXP - URANS|/EXP \times 100 \tag{4.18}$$

It can be noticed that the differences are always lower than 10%. The highest difference is observed in the added mass value, but an overall good agreement is obtained. Furthermore, the damping coefficients are almost identical, confirming the suitability of the CFD simulations for the identification of the viscous forces.

Table 4.9 Solver settings summary

Property	Units	URANS	EXP	Error
ω_δ	rad/s	1.28	1.30	2%
T_δ	s	4.92	4.83	2%
A_{55}	$kg\ m^2$	3.975 10^6	3.566 10^6	10%
α	s^{-1}	0.051	0.054	5%
β	–	0.140	0.147	5%
B_{55-1}	$(Nm\ s)/deg$	1.169 10^6	1.218 10^6	4%
B_{55-2}	$kg\ m^2$	1.636 10^6	1.658 10^6	2%

These results are in general very encouraging, because demonstrate the accuracy of the numerical model and the high potential of CFD simulations for the analysis of specific phenomena. An adequate use of these methodologies leads to high fidelity numerical design tools, that helps the development of the floating WECs.

Chapter 5

ISWEC mooring system

Floating Wave Energy Converters require a mooring system in order to guarantee the station keeping both in operational and extreme storm conditions. As presented in the first part of this work, floating devices are subject to environmental loads, thus the main tasks of a mooring system are to ensure continuity of operations and satisfy compliance requirements to the device dynamics and working principle. The mooring system is a vital part of a WEC design, also because it accounts for a significant proportion of the project's overall capital cost [165]. Therefore, it must have relatively low system and installation costs, guarantee reliability and ensure little downtimes and long intervals between maintenance. Moreover, it is also desirable a small mooring system footprint to minimize the occupied area and achieve bigger concentration of device in WEC farm configurations [63, 68]. Currently, the mooring technologies used for Wave Energy Converters are based on the offshore Oil&Gas industry experience and solutions [10], if also marine energy sector has specific requirements and challenges [98, 134]. In this chapter a brief review of the different conventional mooring solutions is presented and the main aspects of the design procedure are discussed. Then, the design of the ISWEC mooring system is presented.

5.1 Mooring solutions for floating WECs

Mooring solutions are complex systems constituted by different components, generally represented by anchors, mooring lines, buoys, clump-weights and connectors. A

first distinction can be made between slack and taut mooring systems. Slack-moored configurations are typically based on catenary dispositions and rely mainly on the gravity force of the mooring lines in order to provide the necessary horizontal and vertical restoring forces. On the other hand, the restoring capabilities of taut lines, usually composed of either steel wire or synthetic ropes, are based on the axial stiffness of the lines and need to be pre-tensioned before their operation. It is clear that taut mooring systems, although having the advantage of a small footprint, determine a high stiffness that is likely to affect negatively the motion of wave energy devices [102, 152], except for those WECs where mooring system are directly involved in the energy extraction mechanism (e.g CorPower [164, 171] or Ceto [37, 156]). Furthermore, they require very expensive foundations, as vertically loaded piled anchors [162]. These solutions are suitable for active and reactive mooring systems. Actually, active and reactive systems have a significant influence on the device dynamics and can provide a direct link between the floating device and the PTO, especially for axisymmetric point absorbers [155, 99]. In this work the attention will be focused on slack mooring solutions, because the ISWEC device of interest has a PTO enclosed in the floater and active moorings are not suitable. The main mooring system configurations suitable for floating WECs are reported in Figure 5.1 [42, 192, 116, 84]:

- ***Single Catenary***: it is the simplest configuration and the less expensive one. This solution belongs to the single point mooring systems and its geometry provides a high compliance, resulting in possible large motions of the device and weathervaning. The horizontal restoring force is provided only by the weight of the chain. The high footprint and compliance are not suitable for arrays of WECs because collisions may occur. Moreover, no redundancy is present in case of failure.

- ***Multi-catenary***: this configuration allows the sharing of loads among the different lines. A redundancy is provided and allowed motions are reduced by the geometry of the system. If also the size of the chain can be reduced, more components are present, resulting in increased costs.

- ***CALM***: in the Catenary Anchor Leg Mooring a buoy is introduced at the surface, minimizing the influence on the vertical motions of the WEC. The upward force exerted by the buoyancy increases the restoring capabilities of

the system. This system guarantees larger motions with respect to the multi-catenary, reducing the impedance and the damping related to the mooring. The device can weathervane around the buoy but, on the other hand, being at the water surface, the buoy is subjected to current and wind loading. A large number of components is needed with cost implications.

- ***Lazy-wave***: in this case the buoy is submerged and a clump-weight is introduced. This solution provides lower horizontal loads with respect to the CALM system, because no taut lines are present. The geometric compliance of the system is thus increased.

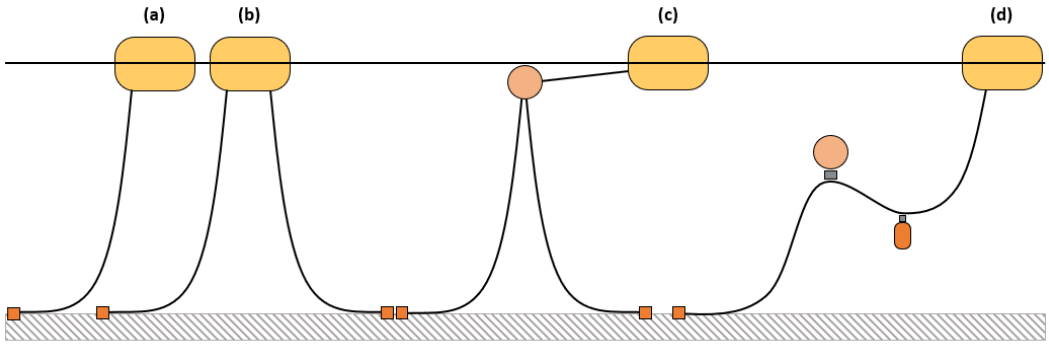

Fig. 5.1 Mooring configurations: (a) Catenary; (b) Multi-catenary; (c) CALM (d) Lazy-wave

Different combinations of the presented configurations can be used for the final design of a mooring system, depending on the specific device of interest.

The mooring line material will influence the dynamic properties of the mooring system. More in detail, it is possible to choose between chains, steel wire ropes or synthetic wire ropes [82]. Steel ropes have a lower weight for the same breaking load, compared to the traditional chains. They are easier to handle but are more sensitive to corrosion. Higher maintenance is needed, thus they are not preferable if not necessary. Synthetic ropes are still at the development stage. They are significantly lighter than other materials and their elastic properties can be adjusted on design. These materials can be advantageous for very deep water installations. Nevertheless their properties change in time because they are more subject to fatigue and creep. Furthermore, the long-term behavior is still unknown because of their relative new employment.

Chains are, at date, the less expensive solution and the more reliable, due to the large experience coming from their long time usage for mooring applications. Different strengths are available and the selection need to be made according to offshore applications standards [7, 50]. Furthermore, chains are characterized by ideal bending properties and very good seabed abrasion resistance.

Eventually, anchors are a fundamental part of the mooring system that guarantee the line connection to a fixed point on the seabed. Several types of anchors exist [178], that go from gravity anchors which use their mass and geometry properties to withstand the loads, to drag-embedment anchors which horizontal holding capacity is given by the drag with the seabed. Other, more expensive solutions are vertical loads anchors and pile or suction anchors. The latter ones need more complex installation procedures such as holes drilling. The choice of the specific anchor type depends on several factors, such as: type of soil, loading direction, seabed slope, load range and last but not least initial and installation costs.

5.2 Mooring design procedure

The design of the mooring system for a floating WEC is a challenging and iterative process, in which non-linear hydrodynamic phenomena are involved. To date, no specific standard regulation is available for the design of these systems. Nevertheless, it is possible to outline a design procedure based on the offshore industry solutions and the experience gained in the wave energy sector through the first deployments of WEC prototypes [99, 116, 18]. The steps followed to develop the ISWEC mooring system are here reported:

1. Definition of the installation site characteristics from metocean data and determination of the design weather conditions.
2. Calculation of the hydrodynamic loads on the device.
3. Definition of the mooring system layout based on its requirements.
4. Calculation of the static properties of the mooring system.
5. Calculation of the dynamic response motion.
6. Mooring line tension verification.

These steps represent a design loop that should be reiterated until the design requirements are met.

5.3 ISWEC Mooring Configuration

Each wave energy device requires a specific and independent design study for the mooring system which is influenced by its energy extraction method. In this section the design of the mooring system for the ISWEC device is discussed, starting from the definition of the requirements to be met, and following the procedure presented in section 5.2. The mooring system design is based on the Pantelleria installation site because it is the best known site from the point of view of Metocean data and it is a significantly severe site from the point of view of extreme wave conditions. It is due to notice that the Mediterranean Sea is not severe as the oceans (e.g. Atlantic Ocean), nevertheless the ISWEC device is particularly designed for the Mediterranean Sea and both the gyroscope and the hull size of the device object of this work are specifically designed for the operational conditions of the Mediterranean. Thus, the secular waves that characterize the Pantelleria installation site, can be considered extreme for this project.

ISWEC mooring requirements

Based on the ISWEC working principle, the mooring system has to guarantee the following requirements:

- **Station keeping**: the device has to be maintained within the specified devoted area.
- **Electrical cable safeguard**: the motion of the device must avoid tension loads in the electrical transmission cable.
- **Compliance**: in order to reduce the environmental loads on the device, the mooring lines and the anchors, the system must be sufficiently compliant. Moreover, the geometry must be designed to accomodate the water level variation due to waves and tidal.

- **Passive behavior**: the mooring system must minimize the disturbance to the device motions appointed to the power conversion chain (i.e. pitch motion). On the contrary, the horizontal motions need to be constrained, limiting the device drift to ensure station keeping.
- **Weathervaning**: the ISWEC device should always orientate towards the incident wave, to exploit its pitch motion.
- **Reduced footprint**: the area dedicated to a single device should be minimized with a view of array installations.
- **Reduced maintenance**: when possible, the use of high durability component is preferred, in order to minimize maintenance operations over the service life.
- **Redundancy**: a degree of redundancy is desirable, according to an appropriate cost analysis.

Metocean conditions

The installation site of the first full scale prototype of the ISWEC system has been chosen for the determination of the environmental loading conditions. The site is offshore Pantelleria island's harbor, in the North Western side of the island. In Figure 5.2 a satellite view of the site location is shown with coordinates: Latitude $36^\circ\ 50'\ 2.52''$, Longitude $11^\circ\ 55'\ 50.40''$.

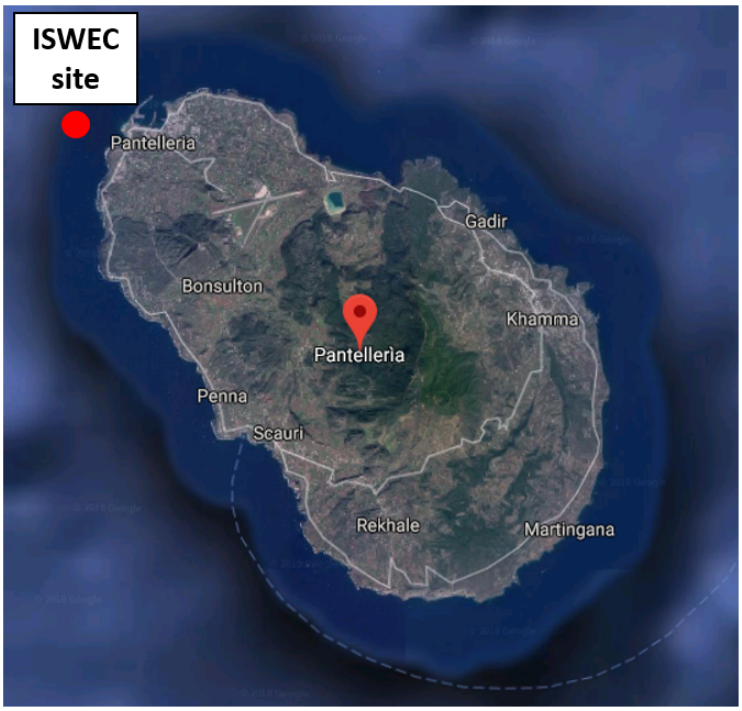

Fig. 5.2 Pantelleria installation site. Latitude 36° 50′ 2.52″, Longitude 11° 55′ 50.40″ [73]

The metocean analysis was made using two time series from different experimental dataset. A first time series has been obtained from the historical data records of the RON *Italian Data Buoy Network* constisting in 15 oceanographic buoys deployed along Italian coasts [16]. The buoy chosen in this case is located offshore Mazara del Vallo at 37° 26′ 24″N Latitude and 12° 32′ 00″E Longitude, and the time period that goes from 1989 to 2002 was taken into account. The second time series resulted from data acquired at the installation site by a Nortek AWAC acoustic wave gauge [106], fixed to the seabed at a depth of 16m. The measurements campaign lasted from January 2010 to December 2012. Data were recorded every 3 hours for a 30 minutes duration and sampled at a frequency of 2 Hz. Because of the limited time history of the second measurements campaign, the RON data were used for the statistical analysis in order to evaluate the extreme events. The two dataset were first compared, demonstrating that Mazara del Vallo is very similar to Pantelleria site but characterized by higher values of significant heights. Eventually, the Mazara site data were chosen as conservative in terms of safety in the design of the mooring system. The data analysis is a part of the PROMO project finalized to the deployment of the first ISWEC full scale prototype [147, 175]. Only the summary result, useful

for the mooring design, will be reported here. A statistical analysis of the extreme events was performed, aimed to the estimation of the characteristics of the wave properties for specified return time periods. The significant height and peak period values are distributed according to the log-normal probability density function. From the cumulative of the identified distribution it was possible to estimate the properties of both 10 years and 100 years return period waves. A Jonswap spectrum is suitable for the description of the real sea states. The results of the spectral properties for the extreme waves are reported in Table 5.1.

Table 5.1 Extreme environmental conditions

Wave	H_s	T_p
	(m)	(s)
10 years	5	8.7
100 years	5.9	10.3

In general, it is a good practice to perform calculations for several sea states conditions to check the mooring system design [18]. In this case, the specific characteristics of the installation site are known, and will be directly used for the mooring design. The currents values measured at the installation site are negligible with respect to the extreme wave conditions. Thus, for this design no currents will be considered.

Preliminary Catenary design

The first step in the mooring design, is the evaluation of the static characteristic of a slack catenary mooring system, which corresponds to the SALM (single anchor leg mooring) reported in Figure 5.1 as Configuration (a). This calculation is useful for a first estimation of the chain size needed to restrain the device horizontal motion. The mooring purpose will be to provide a restoring force for the horizontal motions of surge, sway and yaw, in order to guarantee the return of the device to equilibrium position. For these DoFs the main force contribution are the drift forces. According to Johanning [99], Pecher [137] and Bergdahl [18], for the determination of the static excursion, only the mean drift forces in surge will be used. For the Pantelleria design

site, the mean drift forces have been calculated in both operational (near resonance) and survival conditions by means of the Aqwa BEM software. The resulting values are reported in Table 5.2. No significant differences are present on the mean drift forces values. This can be justified by the fact that drift forces are proportional to the square of the wave amplitude and drift coefficients are higher in resonance conditions (see Chapter 3). These conditions will not be verified in the dynamic behavior, where difference frequency forces contribution are the most relevant.

Table 5.2 Surge Mean Drift Forces on ISWEC

Wave	Drift Force
	(kN)
Operational	10.0
10 years	11.0
100 years	11.6

The static characteristic can be evaluated using the simple catenary equations presented in [57] and reported in Table 5.3, where w is the submerged weight per unit length in (N/m) and L_{tot} is the total length of the chain, from the anchor to the fairlead.

For this preliminary analysis, the fairlead of the catenary coincides with the mooring point of the device and it is considered to be on the water plane. Thus, the vertical scope z of the suspended catenary coincides to the water depth, that for the Pantelleria site is $h = 25\ m$. To guarantee a small footprint of the mooring system and at the same time a small excursion of the ISWEC, the chain length has been selected to be three times the water depth, plus $10\ m$ as safety margin to consider the change in water level due to waves:

$$L_{tot} = 3h + 10 = 85\ m \tag{5.1}$$

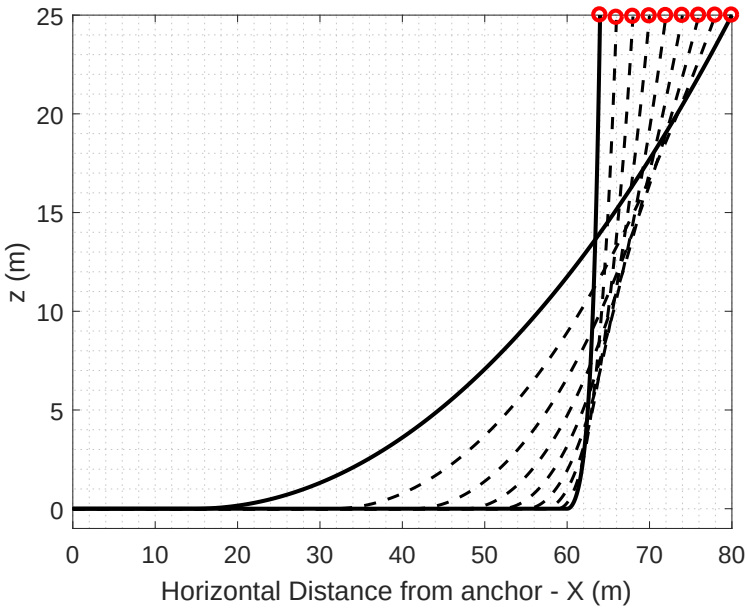

Fig. 5.3 Catenary geometry for different WEC displacements

Table 5.3 Catenary Equations

Property	Units	Equation	
Horizontal distance from the anchor	(m)	$X = L_{tot} - L_s + x$	(1)
Horizontal scope from the touchdown point	(m)	$x = c\cosh^{-1}\left(1+\frac{z}{c}\right)$	(2)
Vertical scope from the touchdown point	(m)	$z = c\left[\cosh\left(\frac{x}{c}\right)-1\right]$	(3)
Suspended length of the catenary	(m)	$L_s = z\left(1+2\frac{c}{z}\right)^{1/2}$	(4)
Catenary constant	(m)	$c = T_x/w$	(5)
Horizontal force at the fairlead	(N)	$T_x = \frac{wz}{2}\left[\left(\frac{L_s}{z}\right)^2-1\right]$	(6)
Vertical force at the fairlead	(N)	$T_z = wL_s$	(7)

Figure 5.3 shows the catenary geometry at different values of surge displacement from the anchoring point. It is important to highlight that to avoid the anchors uplift, a part of the chain should always be laid down on the seabed. At this point, it is possible to calculate the horizontal restoring force for different chains and obtain the load excursion curves. As reported in Table 5.3, the catenary loads are function of the chain weight which depends in turn on the chain diameter. To have a suitable value of the restoring force, it is likely that heavy mooring lines are needed. According to

Johanning [99], as a first approach chain diameters are considered similar to those used for the offshore industry SALM buoys with a similar waterplane area.

Table 5.4 Chain properties [94]

Diameter	Weight in air	Proof Load	Breaking Load
D (mm)	w_a (kg/m)	PL (kN)	BL (kN)
32	22.4	583	833
44	42.4	1080	1540
60	78.8	1940	2770

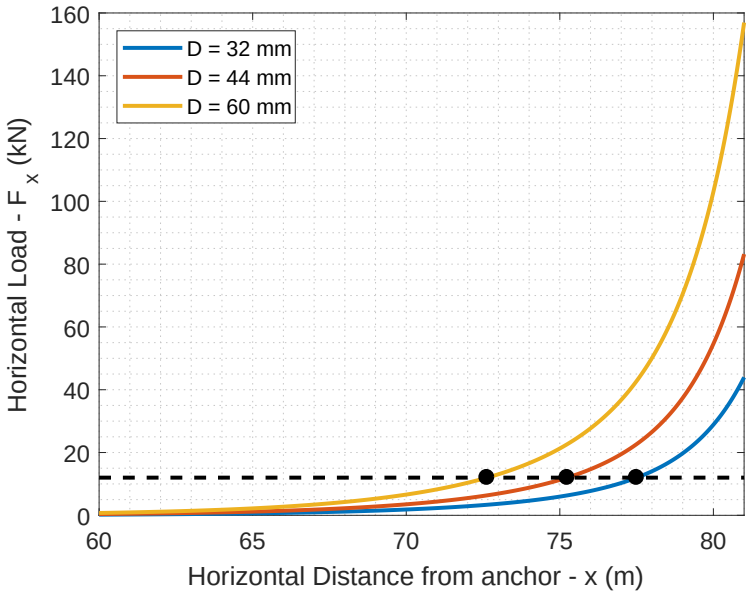

Fig. 5.4 Load excursion curve for different chain diameters

Figure 5.4 reports the static characteristic for three different values of the chain diameter. In Table 5.4 the properties for each diameter of grade Q3 chains are reported from the manufacturer catalogue [94]. The curves are shown starting from the equilibrium position which is obtained when the mooring chain is fully slack and the shape of the catenary is replaced by an L-shape (Figure 5.3). It is observed that for all the considered diameters, the horizontal load meets a drift force value

equal to 12 kN within 20 m of excursion from the equilibrium position. Furthermore, to preserve safety and guarantee a margin for the surge displacement before the mooring line becomes taut, the highest diameter value $D = 60$ mm will be used for the further steps of the design process.

ISWEC mooring layout

A SALM system is not enough to fulfill all the requirements for the ISWEC mooring system. More in detail, the compliance is guaranteed by the slack catenary solution but no redundancy is present. Hence, the next step is to introduce multiple mooring lines. Moreover to guarantee the weathervaning of the device with all the possible wave directions, a proper center of rotation of the system needs to be designed.

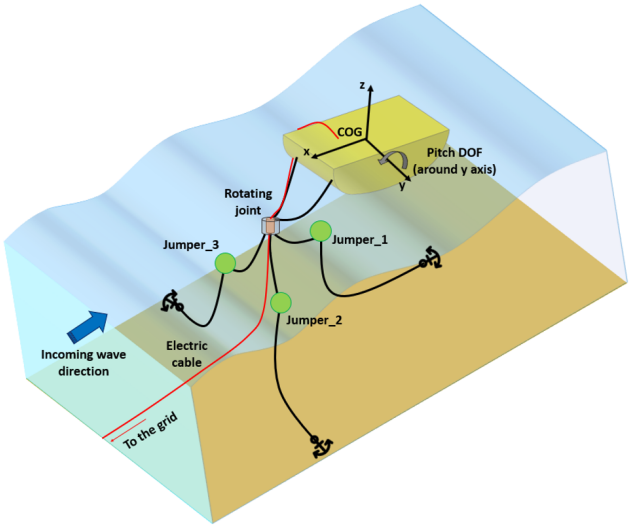

Fig. 5.5 ISWEC mooring layout - Configuration C1

The ISWEC exploits its pitch motion to harvest the incoming wave energy. Its performances are optimal when the hull is directed towards the incident wave direction and the pitch motion is enhanced. The capability of the device to weathervane depends on both the geometry and the mooring system. The ISWEC hull geometry is designed to minimize the resistance at pitch motion and orient with the bow towards the incident wave direction. In order to properly design a mooring system that weathervanes, it is not sufficient to have a hull that minimize its resistance towards the wave direction. The mooring system must not prevent it. Moreover, the ISWEC needs to be connected to the electrical grid with a power transmission cable. To

install the electric cable for the grid connection, interference between the cable and the mooring must be avoided while the device is moving. On the other hand the electric cable must move together with the hull that weathervanes. Hence, the solution requires an electrical slip ring and mechanical swivel to guarantee the correct operation. Figure 5.5 shows the proposed design configuration layout. The mooring system is composed of three main catenary lines arranged every 120 deg. The catenaries are anchored to the bottom of the sea and connected to the centre of the circumference through a suitable connecting triplate (according to DNV standards [50]) to a mechanical rotary joint that allows the top of the system to rotate. The joint includes also an electric slip ring able to transmit power. The ISWEC device is connected to the swivel by means of two hawsers attached to the hull. The chains connected to the two hawsers constitute a bridle that prevents the roll motion of the device. The mooring connection point are placed towards the bow, with respect to the centre of gravity of the device, in order to guarantee a lever arm that stabilizes the device at yaw and guarantees the alignment. On each of the bottom catenary a buoyancy component (jumper) is installed to enhance the elastic recall to the system and avoid snatches. The joint represents the centre of the mooring system and it is slack moored and able to move. Thus, the needed compliance to the electric cable is allowed.

The cable will be connected to the hull deck by a waterproof connector and properly steered to the slip ring. At the bottom part of the slip ring the first part of the submarine cable will be attached. The cable will be then connected to the grid submarine cable with a second waterproof connector. This configuration allows to guide the cable, avoiding bending and tensile stresses and interference with the mechanical components of the system.

In this mooring system, the most critical component, from the system continuity point of view, is the rotating joint. Indeed, it is a single component that connects the upper part of the mooring with the bottom one and failure of this component must be avoided. Moreover, both electrical and mechanical functions are integrated in it. To be the mooring system correctly designed, it must satisfy both the economic requirements (low installation costs) and certification constraints. The certification is usually carried out according with guidelines defined by certification agencies [50]. In order to achieve the certification and lower the costs, the use of commercial component (non-custom) is preferred. Thus, the design of the mooring must satisfy the reliability and survivability of these components. For the ISWEC mooring design,

particular attention will be paid on the loads sustained by the joint, according to the properties of commercially available components.

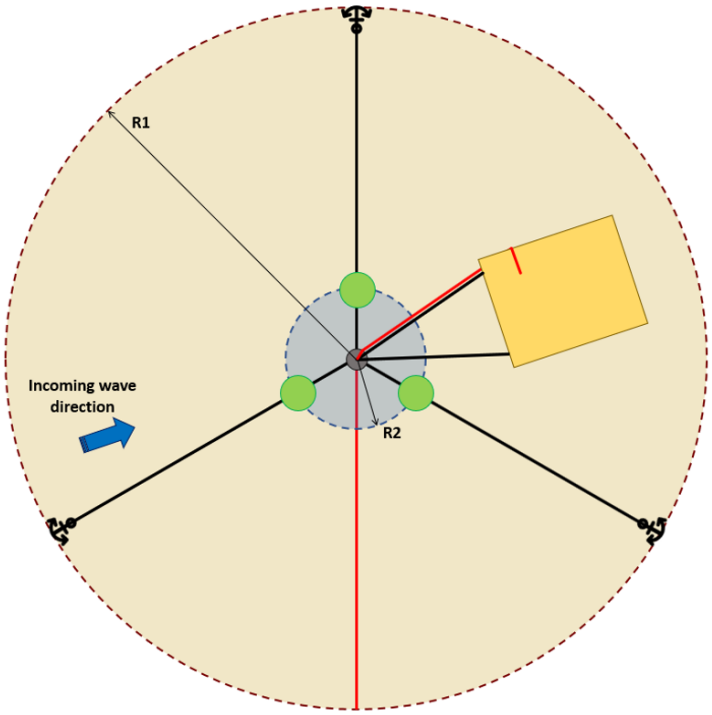

Fig. 5.6 ISWEC mooring layout. Top view - Configuration C1

Referring to Figures 5.5 and 5.6 the main properties of the mooring system are listed in Table 5.5. It is due to notice that for the upper part of the mooring system a smaller chain diameter is used. This solution can be adopted because the load discharged by the device on the mooring system is divided on the two lines of the bridle.

For the preliminary analysis, the quasi-static approach can be appropriate for the mooring design [137]. Moreover, Bhinder et al. [20] show that a simplified model is sufficient and usually reliable to have accurate results for the motions of the WEC [4]. Nevertheless, for a correct calculation of the mooring loads a full dynamic analysis is recommended. In the next section, the dynamic design of the ISWEC mooring system is discussed.

Table 5.5 Mooring System Properties

Property	Symbol	Units	Value
Geometry			
Water Depth	h	m	25
Anchors Positioning radius	R_1	m	60
Anchor to Jumper line	L_1	m	65
Jumper to Central Joint line	L_2	m	10
Joint to ISWEC line	L_3	m	10
Chain Properties for L_1 and L_2			
Nominal Diameter	D_1	mm	60
Mass per unit length	w_a	kg/m	78.8
Axial Stiffness	EA	N	3.24×10^8
Proof Load	PL	kN	1940
Chain Properties for L_3			
Nominal Diameter	D_1	mm	44
Mass per unit length	w_a	kg/m	42.4
Axial Stiffness	EA	N	1.74×10^7
Proof Load	PL	kN	1080
Jumper Properties			
Structural mass	M_s	kg	364
Displaced water mass	M_w	kg	1864
Added mass	M_a	kg	670.9
Drag area	DA	m^2	2.15

5.4 ISWEC Mooring Dynamic Analysis

The quasi-static approach for the mooring design is recognized as an appropriate methodology for the oil and gas sector [7, 50]. However, the offshore structures in this sector are characterized by large mass and low motion responses, hence mooring system are designed to minimize the responses in order to do not compromise the safety of the structure. Floating Wave Energy Converters instead, are characterized by smaller mass and usually desire large displacements for energy conversion purposes. These properties motivate the need of a dynamic analysis for the mooring design [166]. To guarantee the deployment of the mooring system, the mooring design needs to be certified according to existing standards [170]. In this work the DNV-OS-301 [50] standard will be considered as reference. Several numerical tools are available for the dynamic analysis of mooring systems, and different works on screening and comparisons are present in literature, as [20, 42, 138, 167]. In general, also according to certification agencies, there is no specific requirement on the choice of the software package. Moreover, Bhinder et al. [20] shown that results obtained with different software are comparable and in agreement. In this work, the software package Ansys Aqwa [6] will be used for the dynamic analysis of the mooring system.

Numerical model properties

The dynamic analysis in Ansys Aqwa is performed in time-domain. The governing equations of motion presented in Chapter 2 is integrated numerically, with the introduction of the mooring forces applied to the device $F_m(t)$ [6]:

$$(M+A_\infty)\ddot{X}(t)+\int_0^t h_r(t-\tau)\dot{X}(t)d\tau+KX(t)=F_w(t)+F_m(t) \tag{5.2}$$

The mooring lines are discretized into a number of finite elements where the properties of mass of each element are concentrated into a corresponding node: *lumped mass model*. This means that each element is considered as a point mass with a non dimensional massless spring. The loads are calculated solving the equations of motions for each element of the mooring line, derived from the equilibrium of forces and moments [6]. Hence, the analysis is fully coupled between the mooring and floater dynamics: the equation of motion of the mooring lines are solved at each

time step and the resulting mooring load is given as input to the floater equation of motion [42, 167]. To integrate in time the discretized equations of motions, the code uses a two-stage predictor corrector method. Moreover, the Aqwa package has the capability to calculate the environmental loads on the floating device, performing both first and second order potential flow analysis (see Chapter 3).

The time domain analysis performed in Aqwa provides, as result, time histories of both motions displacements and mooring tensions. All the simulations consider the following phenomena:

- Six degree of freedom motion analysis.
- First order wave forces (diffraction and radiation problem).
- Second order wave forces (mean and low frequency drift forces).
- Geometric non-linearities arising from the cable dynamics solution. The non-linearity is due to the catenary effect of the compliant mooring. This results in a non-linear restoring force.
- Representation of the buoyancy, gravity and drag forces due to the presence of jumpers and, potentially, clump-weights.
- Viscous loads on the mooring lines by means of drag coefficients.

The mooring system to be analyzed was presented in section 5.3. The main properties are listed in Table 5.5. Viscous effects on the mooring lines are introduced by means of the Morison's equation valid for slender bodies [57]:

$$F_D = 0.5\rho_w C_D v|v| \tag{5.3}$$

where $\rho_w = 1025\ kg/m^3$ is the water density and v is the relative velocity between the water and the mooring line. The generalized drag coefficients C_D and added mass coefficients C_a are obtained from DNV-RP-F205 [48] and DNV-RP-C205 [49] recommended practices and listed in Table 5.6.

The analysis of the mooring system performances is performed on different sea states conditions, to test the efficiency in both operational and survival conditions. All the analyses are performed without considering the gyroscopic power conversion system in the model. This results in a conservative approach: indeed, the motion

response of the floater will be damped with the active gyroscope and the loads on the mooring system will be lower.

Table 5.6 Stud Chain Drag and Added Mass coefficients

Property	Symbol	Value
Transverse Drag Coefficient	$C_{D,t}$	2.6
Longitudinal Drag Coefficient	$C_{D,l}$	1.4
Added Mass Coefficient	C_a	1

Operational conditions analysis

The mooring system is first tested in operational sea states conditions. Numerical simulations in time domain with mooring dynamics are computationally and time expensive due to the very small time step needed to correctly solve both low and high freqeuncy events as snatches conditions [42]. In this work, the time step was chosen to be $dt = 0.002\ s$. Consequently, to reduce simulation time without affecting the reliability of the analysis, an accurate selection of the test cases need to be realized. Referring to Pantelleria installation site, eight different sea states were chosen, according to Vissio [175], to represent the whole scatter diagram. The simulations are performed in irregular waves, considering a standard Jonswap spectrum with peak enhancement factor $\gamma = 3.3$. The irregular waves are generated, according to the defined Jonswap spectrum, directly by Aqwa that receives as input properties the peak period T_p and the significant height H_s for each sea state. Starting from the energy period of the selected waves, it is possible to obtain the peak period values using the relation proposed by the ITTC [160]:

$$T_p = T_e/(0.8255 + 0.03852\gamma - 0.005537\gamma^2 + 0.0003154\gamma^3) \tag{5.4}$$

Table 5.7 reports the properties of the tested sea states while Figure 5.7 shows the distribution of the selected sea states in the Pantelleria scatter diagram of both occurrences and energy density.

All the simulations are performed for a time duration of 1000 s to guarantee at least 10 wave periods (with reference to T_p) and eliminate transient phenomena. The starting position is the same for each simulation and equal to 6 m in the leeward

Table 5.7 Operational Sea states properties

WAVE ID	T_e (s)	T_p (s)	H_s (m)
IW01	5.5	6.09	0.5
IW02	6.5	7.19	0.5
IW03	5.5	6.09	1.5
IW04	6.5	7.19	1.5
IW05	7.5	8.30	1.5
IW06	6.5	7.19	2.5
IW07	7.5	8.30	2.5
IW08	8.0	8.85	3.25

direction with respect to the incident wave. This position has been chosen in order to avoid numerical problems due to the initialization of the catenary shape that needs to be not fully slack.

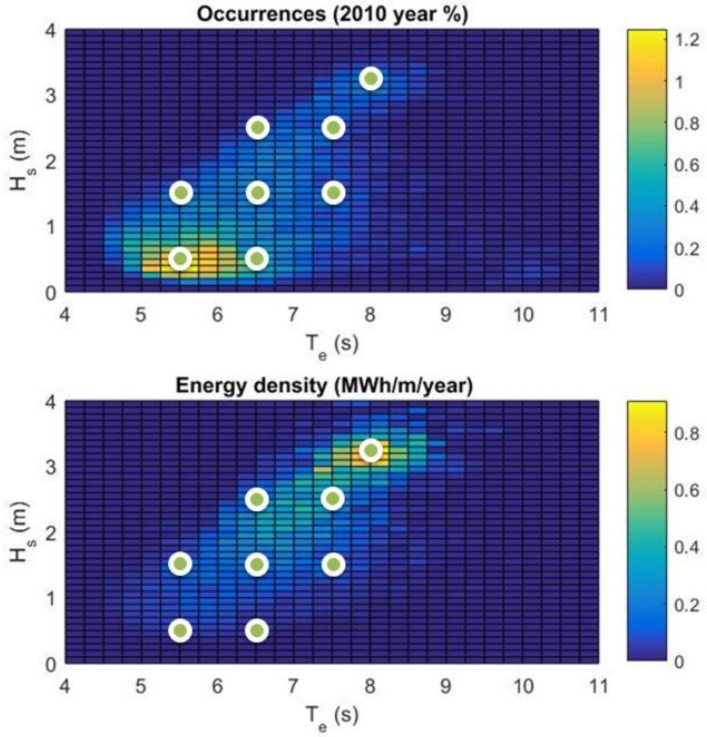

Fig. 5.7 Pantelleria, Italy. Occurrences and energy scatter diagram from 2010 experimental campaign. Selected sea states

To analyze the performances of the mooring system, the attention is mainly focused on Surge motion and mooring loads.

Figure 5.8 shows time-series samples of the Surge motion for each of the tested waves. The origin of the inertial reference frame with respect to the surge motion is calculated, corresponds to the centre of the mooring system (i.e. the rotating joint position). It is possible to observe that two predominant frequencies are present in the signals. More in detail, the high frequency corresponds to the wave frequency and varies according to the incident wave, while the low frequency corresponds to the moored system natural frequency. A Fourier frequency analysis has been performed to identify the surge natural frequency of the moored system. Consistently with the mooring design requirements, the identified natural period for this configuration is $T_n = 200\ s$. This value is far from the wave frequencies characteristic of the sea states. Hence, no resonance conditions will be achieved for the mooring system. The surge displacement will be determined by drift forces.

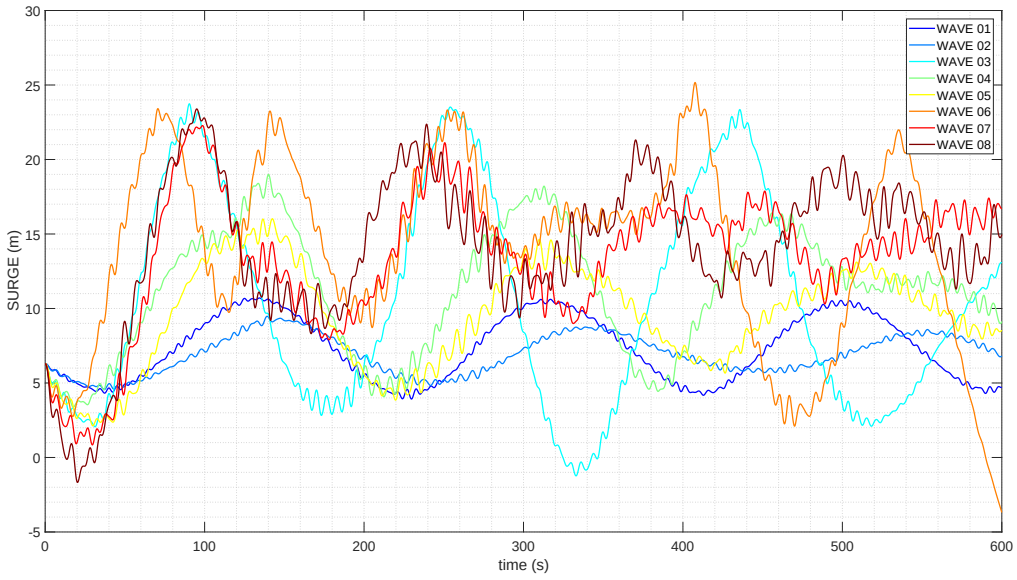

Fig. 5.8 Operational sea states. Surge time-series samples

Table 5.8 reports the results of the time-domain analysis for the surge motion. It is observed that the surge motion is amplified for high amplitude waves and, independently from the wave amplitude, near the natural frequency of the device. Moreover, the maximum displacement falls always within the anchoring position radius and the mooring lines never reach the taut condition.

Table 5.8 Surge Motion Properties

WAVE ID	IW01	IW02	IW03	IW04	IW05	IW06	IW07	IW08
max (m)	10.7	9.5	23.7	19.0	16.0	25.2	22.3	23.4
min (m)	3.9	4.6	-1.2	3.4	2.1	-6.7	0.8	-1.7
rms (m)	7.6	7.1	12.7	11.9	10.0	15.3	14.2	15.0

For the structural design verification, mooring loads must be analyzed. As previously stated, the most critical component from the mechanical resistance point of view is the rotary joint. Mooring loads are calculated in correspondence of the joint, which is the most stressed component of the mooring system.

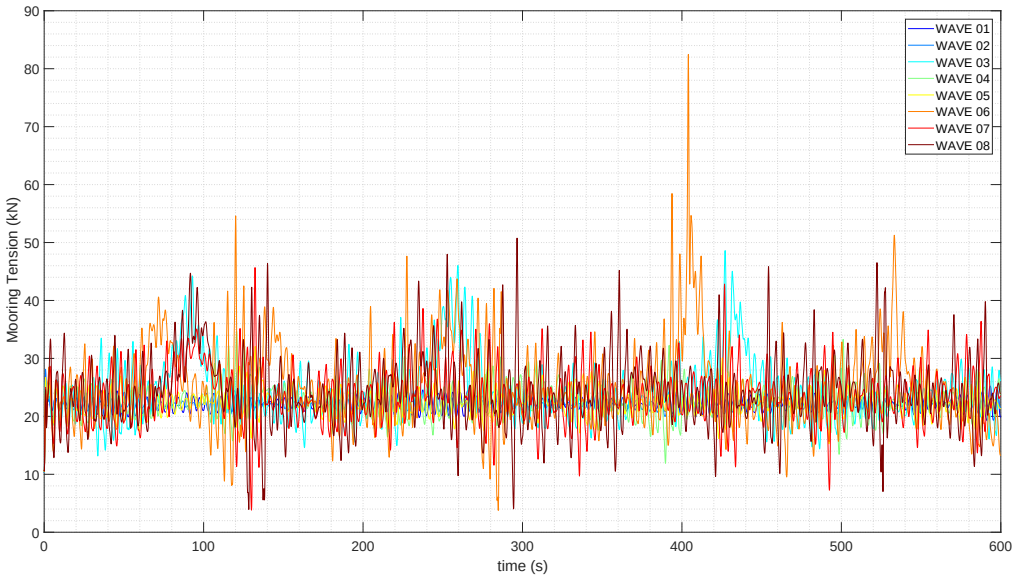

Fig. 5.9 Operational sea states. Time-series samples of the mooring loads on the rotating joint

Table 5.9 Mooring loads on the rotating joint

WAVE ID	IW01	IW02	IW03	IW04	IW05	IW06	IW07	IW08
max (kN)	28.1	28.1	48.6	34.7	32.1	87.4	45.7	50.7
min (kN)	10.3	10.3	10.4	10.4	3.8	3.8	3.8	3.9
rms (kN)	22.2	22.1	24.9	22.9	22.5	26.4	24.1	25.1

Figure 5.9 shows a time window of the mooring tension time series for all the tested sea states, whilst significant values are reported in Table 5.9. It is possible to observe that, in average, the loads behavior is the same for all the operational conditions: the *rms* value is very similar for each test. The load signal is mainly characterized by the wave frequency with higher peaks in correspondence of large displacements. Moreover, peak loads are induced also by heave and pitch motions that not necessarily are in phase with the surge motion.

The maximum peak is below 100 kN which is less than 10% of the proof load of the smallest chain, used for the bridle sections. This result is encouraging for operational conditions but a survival analysis in extreme wave conditions is needed in order to determine the maximum mechanical load to correctly size the rotary joint.

Another parameter of interest to evaluate the mooring performances, is the device pitch motion. More in detail, in order to do not compromise the power conversion, the influence on the pitch motion must be minimal. To evaluate this phenomenon, a comparison between the moored device dynamic model in Ansys Aqwa and the Simulink Free-body time domain model is performed. The Simulink model described in Chapter 3 was chosen because it is computationally less expensive with respect to the Aqwa one. The time domain models inputs are the same for both models and result from the frequency analysis run in Aqwa. The differences between the Aqwa dynamic model and the in-house Simulink hydrodynamic model for the free-body configuration are: the presence of the mooring system; the calculation of the convolution term of the Cummins equation; the presence of the transversal motions (sway, roll and yaw). In particular, the transversal motions are not relevant for the free body simulation: the wave direction coincides with the longitudinal axis of the device and there are no couplings with the sway, roll and yaw DoFs. Moreover, in the Simulink model the convolution term is modeled using the state space approximation that, for the operational sea states conditions, reproduces a very good fit of the radiation forces. According to these observations, the proposed comparison is consistent.

The comparison on time series basis is not possible because of the difference in phase of the motion with and without the mooring system. This phenomenon is motivated by the surge motion which is different for each wave. Difference in surge position means difference in the actual wave profile that impacts the device, thus resulting in different pitch motion. Figure 5.10 shows an example of pitch time

series for two different irregular waves. It is possible to observe that for the IW02 test case, the two models' results are very similar, also in phase. This is due to the low surge drift. More in detail, being the surge displacement limited, the wave surface that hits the device does not present significant differences. This result is not confirmed by the IW08 test case for which the surge displacement is significantly higher (see Figure 5.8). More in detail, the time series are initially superimposed for both models. Successively, the difference is evident, due to the contribution of the mooring system and the different wave surface.

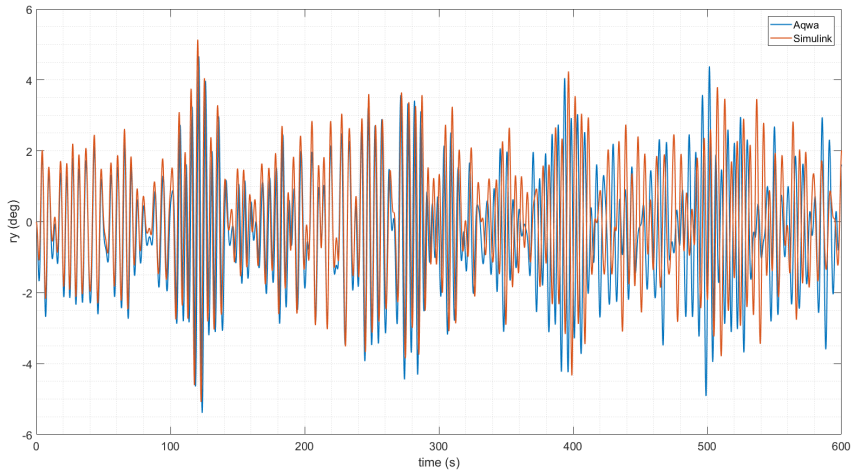

(a) WAVE ID: IW02

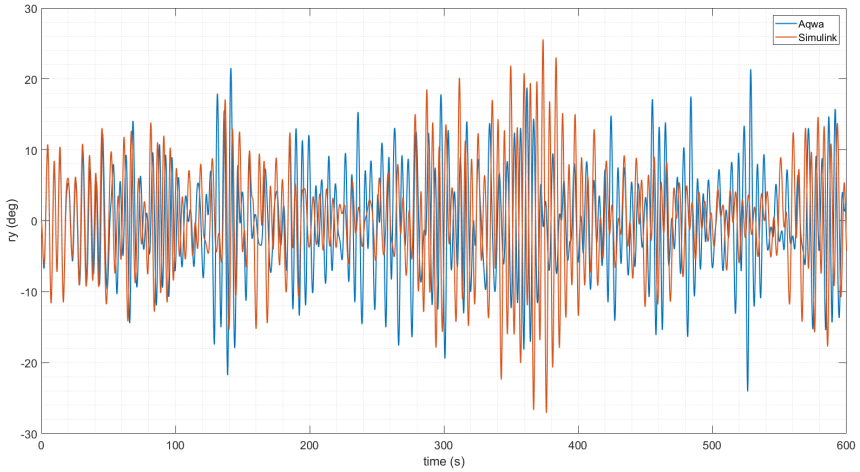

(b) WAVE ID: IW08

Fig. 5.10 Numerical models comparison. Pitch time series samples

Nevertheless, the statistical properties of the pitch motion can still be compared. Therefore, the maxima, minima and rms values of the pitch motion have been compared with and without the mooring system.

Table 6.10 reports the result of the comparison in terms of the significant properties of the pitch motion. More in detail, it has been calculated the relative difference between the free-body and the moored device model for the rms value of the pitch motion:

$$rms_{err} = \frac{ry_{rms}(Simulink) - ry_{rms}(Aqwa)}{ry_{rms}(Simulink)} \times 100 \tag{5.5}$$

Table 5.10 Pitch motion significant values

WAVE ID	IW01	IW02	IW03	IW04	IW05	IW06	IW07	IW08
Aqwa Moored Device Dynamic Analysis								
ry_{max} (deg)	5.34	4.67	14.53	14.11	12.10	21.65	18.87	21.54
ry_{min} (deg)	-5.86	-5.39	-14.57	-15.01	-12.34	-22.43	-20.33	-24.07
ry_{rms} (deg)	2.11	1.61	5.49	4.52	3.84	6.59	6.24	7.11
Simulink Free-body Time Domain Model								
ry_{max} (deg)	6.76	5.54	17.06	16.31	13.31	24.94	21.95	25.17
ry_{min} (deg)	-7.04	-5.42	-19.94	-16.23	-13.04	-25.34	-22.25	-27.04
ry_{rms} (deg)	2.21	1.68	5.80	4.82	4.13	7.07	6.71	7.66
rms_{err}	4.5%	4.1%	5.3%	6.3%	7.1%	6.8%	7.1%	7.2%

Results show, in general, good performances of the mooring system. More in detail, the influence on the pitch motion rms value is always lower than 10% which is a desirable result. The compliance is thus guaranteed in operational conditions. Moreover, it is due to highlight that, taking into account an error of $\pm 10\%$, it is possible to evaluate the device productivity in operational conditions without using a detailed mooring model that has a high impact on the computational cost of the calculation. This cost is not justified for a first productivity analysis aimed to estimate the feasibility of the project.

Survival conditions analysis

To ensure the survivability of the mooring system, and consequently of the floating WEC, it is necessary to evaluate motions and tensions in extreme environmental conditions. During these conditions, the device will be in safety mode and the PTO system will be shut down. Thus, differently from the operational conditions, the only analysis of the hydrodynamics is realistic and not conservative.

The extreme conditions are chosen according to the analyzed deployment site, as reported in Table 5.1. Both 10 years and 100 years return period waves are tested, for a simulation time of 1400 s, compatibly with the software limitations. More in detail, the number of time steps to be simulated are limited by the software. Hence, a convergence analysis was run on the integration time step suitable to capture the mooring dynamics. A time step of 0.002 s was found to be the best compromise. Consequently, the simulated time duration was set. It is recommended by standards [7, 50] to analyze the full storm duration equal to 30 minutes. In order to represent the full storm duration, 10 different wave time series were generated, characterized by the same Jonswap spectrum properties. The difference in the wave elevation time series is due to the different seed used to generate the random phases between spectral frequency components.

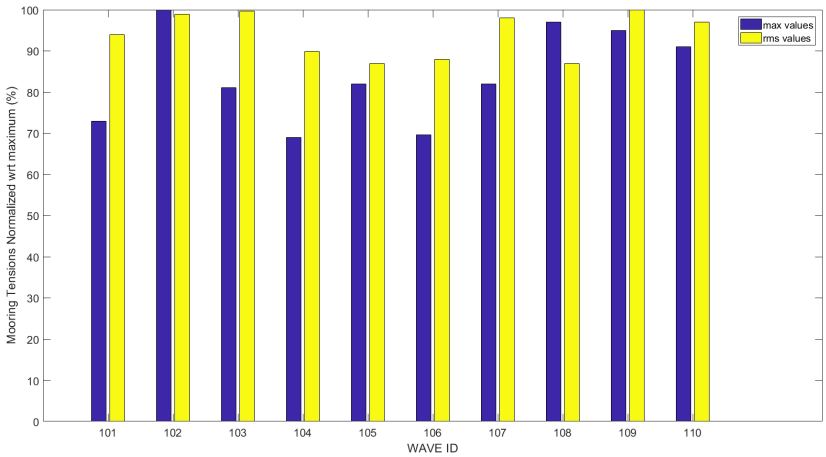

Fig. 5.11 100 years sea states. Peak and rms Mooring tension values normalized wrt their maximum.

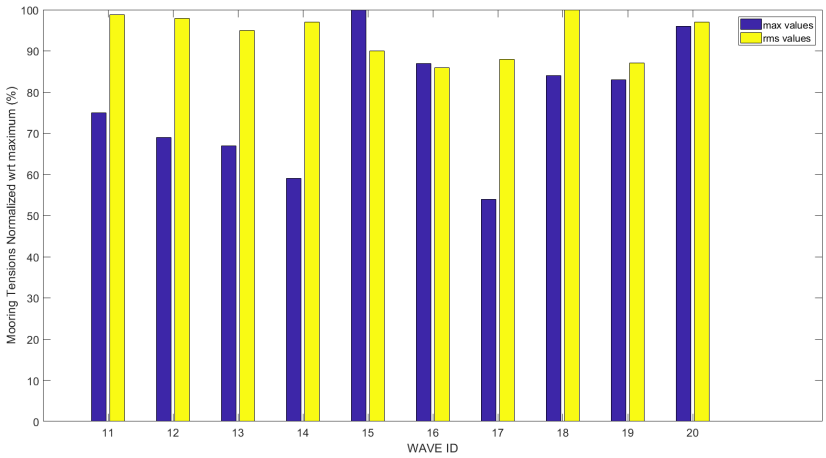

Fig. 5.12 10 years sea states. Peak and rms Mooring tension values normalized wrt their maximum.

Table 5.11 100 years wave - Numerical model significant results

Test ID	Mooring Tension		Surge	Pitch
	max (kN)	*rms* (kN)	*max* (m)	*max* (deg)
IW101	510.4	27.8	27.5	33.7
IW102	699.3	29.3	27.2	31.7
IW103	566.8	29.5	27.1	30.8
IW104	482.7	26.3	26.9	27.4
IW105	573.5	25.7	27.3	30.7
IW106	487.2	26.0	27.0	26.9
IW107	573.4	29.0	27.4	27.2
IW108	678.6	25.7	27.2	24.5
IW109	664.2	29.6	27.5	30.8
IW110	636.1	28.7	27.2	30.1

Table 5.12 10 years wave - Numerical model significant results

Test ID	Mooring Tension		Surge	Pitch
	max (kN)	*rms* (kN)	*max* (m)	*max* (deg)
IW11	747.0	31.8	27.5	30.0
IW12	687.2	31.4	27.3	27.8
IW13	667.3	30.5	26.9	30.6
IW14	587.6	31.1	26.9	28.2
IW15	996.2	28.9	27.2	31.3
IW16	866.5	27.6	27.4	28.2
IW17	537.8	28.2	27.0	27.6
IW18	836.6	32.1	27.3	29.3
IW19	826.7	27.9	27.5	27.8
IW20	956.1	31.1	27.1	38.1

To analyze the simulation results, relevant values for Mooring Tension, Surge and Pitch motions are reported in Table 5.11 for the secular waves and in Table 5.12 for the 10 years return period waves. More in detail, mooring tension was calculated in correspondence of the rotary joint, were the two bridle sections are connected. For each test, maxima values of motions are reported, whilst for mooring tensions also the rms value is reported.

For a better comparison, Figures 5.11 and 5.12 show, respectively for the 100 years waves and for the 10 years waves, the normalized values, in percentage, with respect to the maximum of both rms and peak tension values. Precisely, the normalized values are calculated as:

$$y_{norm} = \frac{y}{y_{max}} \times 100 \tag{5.6}$$

It is possible to observe that tension peaks present a high variance with peaks values that reach the 70% of the maximum for the secular wave and 54% for the

10 years wave. On the other hand, the rms values are similar for different waves, with a maximum variation from the absolute peak equal to the 14%. Furthermore, the 10 years wave appears to be the worst loading condition for the mooring system, with a maximum tension value of 996 kN with respect to 699 kN for the secular wave. Nevertheless, Pitch and Surge maxima values are similar for both extreme contitions. In particular, Surge maxima are almost unvaried for different sea states and correspond to the maximum extension of the mooring lines, when the system becomes fully taut.

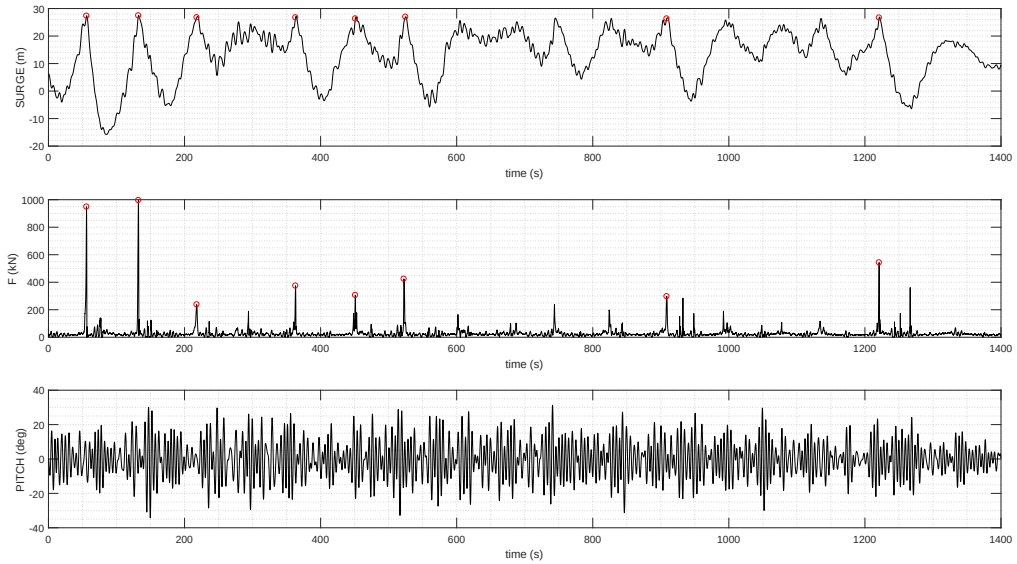

Fig. 5.13 10 years sea state - IW15. Motions and loads time series.

To better investigate the phenomenon, time series of motions and loads for the worst cases are plotted in Figures 5.13 and 5.14. It can be noticed that the load peaks are always in correspondence of the surge motion maxima. Moreover, for the majority of the test duration, mooring loads are of the same order of magnitude of the rms values. In particular, the rms, for all the tested conditions, is always lower than 50 kN. This value is by far lower than the breaking load of the chain. This behavior confirms that the mooring system is correctly sized for the operational conditions and for most extreme conditions. Nevertheless, to ensure the survival of the system, also extreme peaks must be taken into account. More precisely, with the presented tests has been identified a risk condition that is preferable to avoid: mooring snatches when lines become taut.

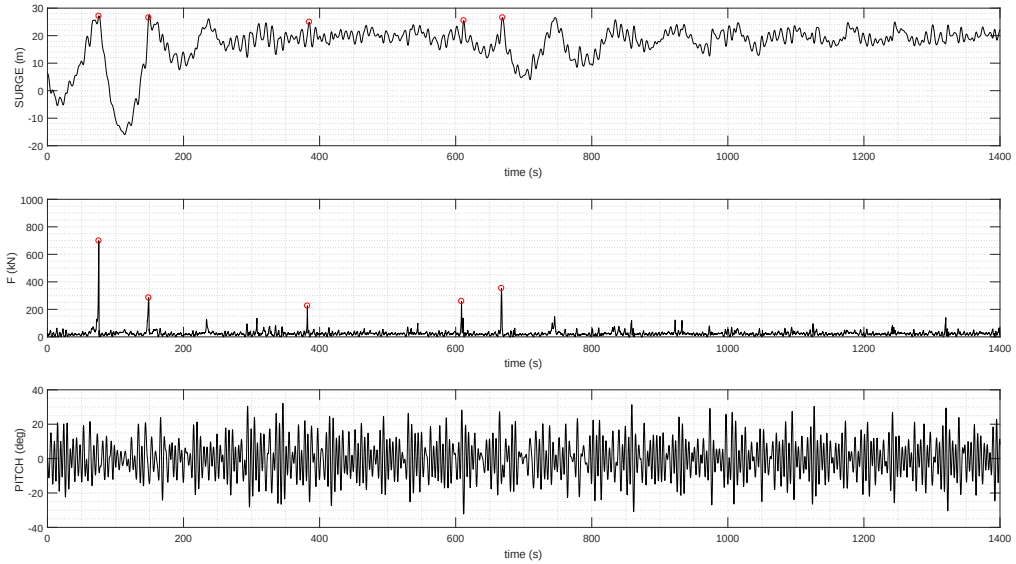

Fig. 5.14 100 years sea state - IW102. Motions and loads time series.

In order to investigate the real occurrence of these events, and to validate the numerical model for the last step of the mooring design, an experimental campaign has been performed and will be described in next Chapter.

Chapter 6

1:20 ISWEC moored device experimental campaign

A second test campaign on the moored 1:20 ISWEC scaled device was performed in Napoli. The purpose was testing the mooring system presented in the previous Chapter, in order to validate the design and the numerical simulations run in Ansys Aqwa. The same model of the free-body campaign was used. The scaling factor selected for the model was identified as suitable for the correct scaling of the mooring system and it is above the minimum recommended values described in [119, 90]. Tests were performed both in regular and irregular sea states. A first part of the campaign was dedicated to the determination of the *Pitch* RAO of the moored device. In the second part, the survivability of the device in extreme conditions has been tested. In particular, both 100 years return period and 10 years return period waves were tested for two different mooring system configurations. A load cell was installed on the mooring lines for the measurement of the mooring forces.

6.1 1:20 ISWEC mooring system

To test correctly the ISWEC moored device, also the mooring system needs to be scaled according to the selected scaling factor $\lambda = 1/20$. In the Napoli experimental campaign two different mooring configurations have been tested. The first configuration coincides with the one presented in Chapter 5 and referred as *Configuration C1*. The second configuration is similar but a clump-weight is introduced on each

of the three mooring bottom lines. The resultant system is a multiple Lazy-wave configuration, referred as *Configuration C2a*. This configuration has been realized to test the effect of the clump-weight on the restoring force of the mooring system and the load peaks reduction in the dynamic behavior.

The two proposed configurations are slack mooring. The dynamic behavior of these systems is principally governed by the gravity and inertia forces, unless the mooring line becomes taut and hydroelastic phenomena are involved. For the correct operation of the mooring system, these phenomena need to be avoided. Hence, the system dynamic properties are scaled according to Froude (see Chapter 4). For what concerns the mooring components, the main properties to be scaled are the catenary lengths, the mass of the chain in water and the net buoyancy of the line in water.

Table 6.1 ISWEC 1:20 mooring properties - Configuration C1

Property	Symbol	Units	Scaling	Value
Geometry				
Water Depth	h	m	λ	1.25
Anchors Positioning Radius	R_1	m	λ	3.0
Anchor to Jumper line	L_1	m	λ	3.25
Jumper to Central Joint line	L_2	m	λ	0.5
Joint to ISWEC line	L_3	m	λ	0.5
Chain Properties for Bottom mooring lines				
Nominal Diameter	D_1	mm	λ	3.0
Mass per unit length	w_a	g/m	λ^2	186
Mass per unit length in water	w	g/m	λ^2	172
Chain Properties for Top mooring lines				
Nominal Diameter	D_1	mm	λ	2.2
Mass per unit length	w_a	g/m	λ^2	90
Mass per unit length in water	w	g/m	λ^2	80
Jumper Properties				
Net Buoyancy	B	g	λ^3	187

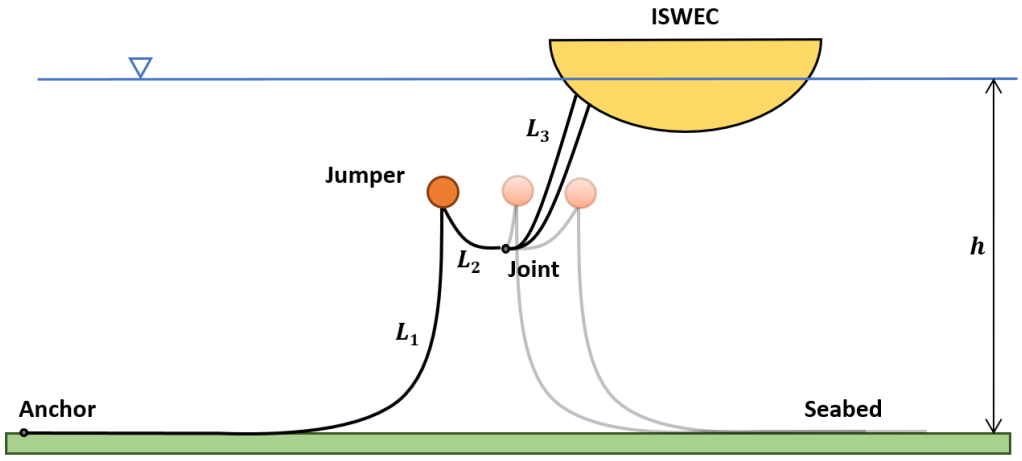

(a) Configuration C1

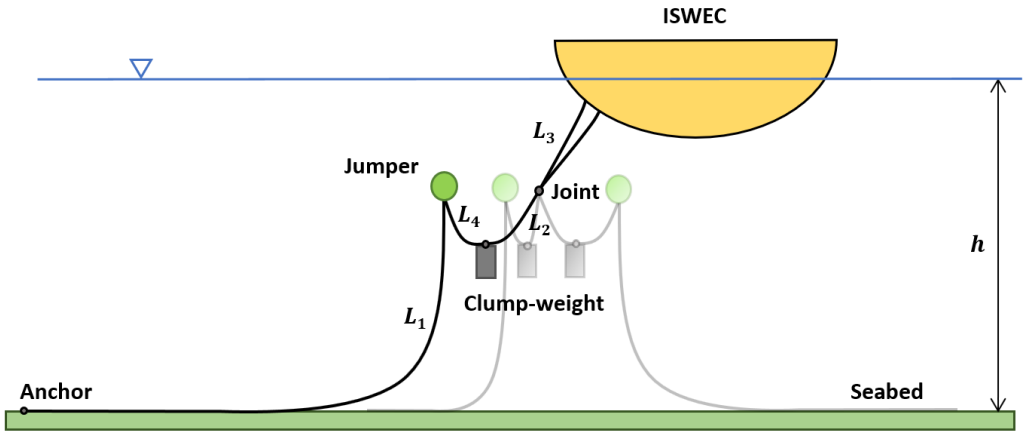

(b) Configuration C2a

Fig. 6.1 ISWEC 1:20 Mooring Configurations schemes

In Figure 6.1 the two tested mooring systems schemes are shown. Table 6.1 reports the values of the scaled properties for the mooring Configuration C1. In Configuration C2a a clump-weight is added. The gravity force of the clump-weight is chosen to be of the same order of magnitude of the buoyancy force of the jumpers. More in detail, it was sized to have a gravity force of 2000 kg in full scale. To compensate the sink due to the clump-weight, the jumpers volume was increased of the same value, obtaining a buoyancy force equal to 3500 kg in full scale. In order to avoid the geometry to become too stiff, another catenary section was added on each line, connecting the jumpers to the clump-weights. This section is referred as L_4 and its length must not be to high in order to avoid the entanglement of the clump-weight

with the bottom catenary. For this design the length is equal to 5 m in full-scale. The other catenaries sections have the same length as for Configuration C1. Same chain diameters were used for both configurations. Table 6.2 reports the properties of the scaled system for the Configuration C2a.

Table 6.2 ISWEC 1:20 mooring properties - Configuration C2a

Property	Symbol	Units	Scaling	Value
Geometry				
Anchor to Jumper line	L_1	m	λ	3.25
Clump-weight to Central Joint line	L_2	m	λ	0.5
Joint to ISWEC line	L_3	m	λ	0.5
Jumper to Clump-weight line	L_4	m	λ	0.25
Jumper Properties				
Net Buoyancy	B	g	λ^3	437
Clump-weight Properties				
Net Weight	G	g	λ^3	250

For the determination of the chain mass in water, a first calculation was made using the relations proposed by Barltrop [10] and Wichers [188]:

$$w = 0.1875D^2 \tag{6.1}$$

where D is the nominal diameter of the chain in (mm). All the properties where experimentally verified during the setup at the testing facility.

6.2 Experimental setup

In this section, the experimental setup of the tested mooring configurations is presented. For the jumpers, compositions of PVC buoys are used to obtain the desired buoyancy force. Clump-weights are realized with lead calibrated masses. Figure 6.2

shows the pictures of the used components. The mooring catenary lines are made of genovese steel chain of the size reported in Table 6.1. The lines are connected to the ISWEC model through snap-hooks couplet to eyelets welded on the hull keel at a position correspondent to the full-scale device (Figure 6.3).

(a) Jumpers - C1

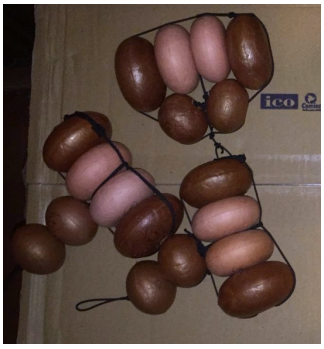

(b) Jumpers - C2a

(c) Clump-weights - C2a

Fig. 6.2 Jumpers and Clump-weights

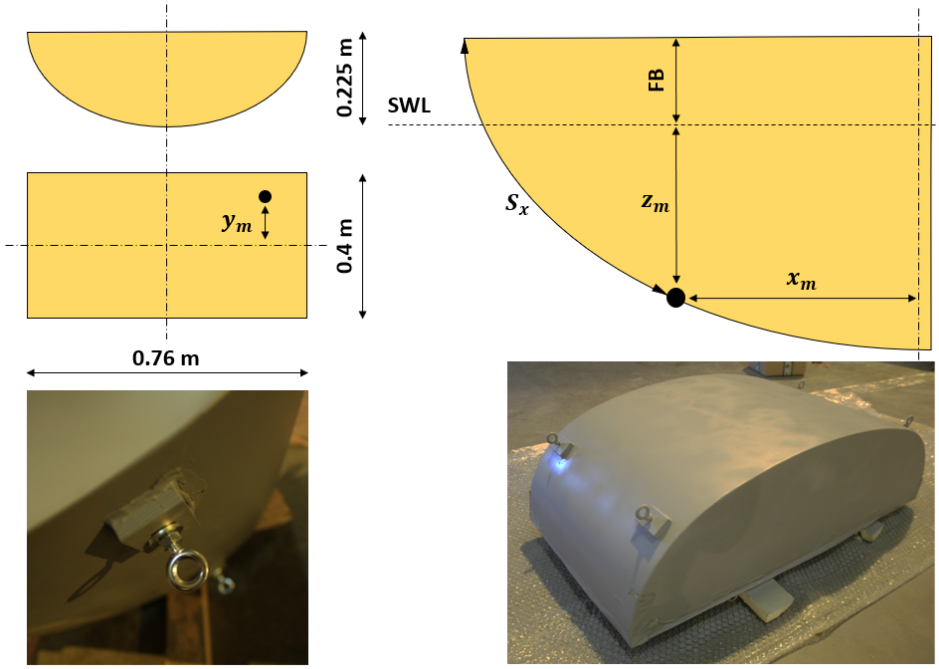

Fig. 6.3 ISWEC mooring connection points

The mooring connection points are located at the ISWEC bow. The measured geometry values are reported in Table 6.3.

Table 6.3 ISWEC 1:20 mooring connections

Property	Symbol	Units	Value
X Coordinate	x_m	m	0.315
Y Coordinate	y_m	m	0.15
Z Coordinate	z_m	m	0.08
Keel curve coordinate	S_x	m	0.175
Freeboard	FB	m	0.075

To ensure a correspondence between the mooring configuration of the experimental prototype and full-scale and therefore the scalability of the results, virtual seabed has been used to correctly simulate the water depth of the installation site. Indeed, the tank water depth is equal to 4.25 m, while a seabed at 1.25 m must be guaranteed. The virtual seabed was built using steel bars and PVC pipes connected by orthogonal joints in order to create a support frame for a movable plane, which position can be regulated in height (Figure 6.4). The seabed was built using a plastic net properly connected to the plastic pipes and stretched in order to guarantee the plane to be horizontal. Three vertical steel bars that support the seabed were fixed to the carriage structure, thus they could be transported at the tank centre. The bars were provided with a telescopic system that allowed the correct positioning in depth. Each bar is positioned on the anchoring radius with respect to the centre of the mooring system. Then, the anchoring points were fixed at the bars base, by means of eyelets at which catenary are connected. For the sake of clarity, a scheme of the whole setup is reported in Figure 6.5.

The rotary joint is realized with a mechanical swivel. No cable that simulates the power transmission is installed for the presented campaign. The connection between different sections of the lines and with buoys and clump-weights are realized with carabiners of the same size as the chain elements.

To monitor and record the mooring tensions along the lines, a load cell is provided. The load cell is connected on one side to the mechanical swivel and on the other side

on both the bridle branches. In this way it is possible to acquire the load signal on the most critical component for the design of the mooring system.

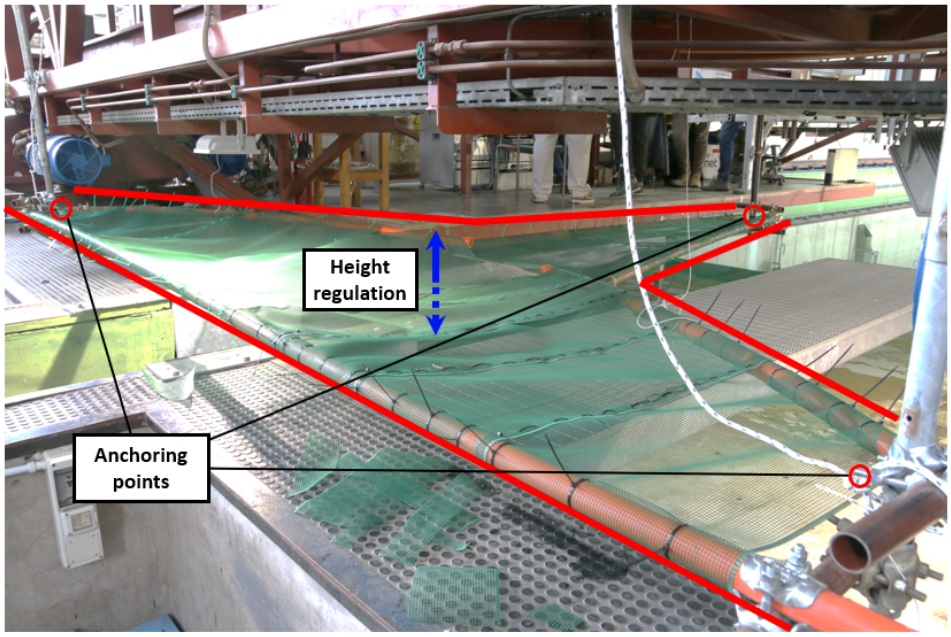

(a) Seabed details

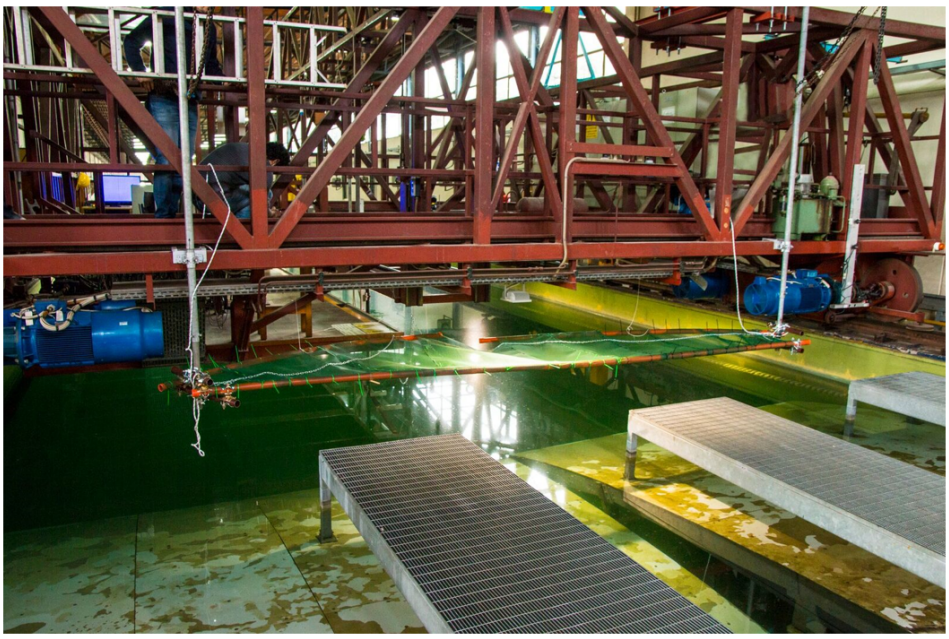

(b) View of the carriage connections

Fig. 6.4 Virtual Seabed

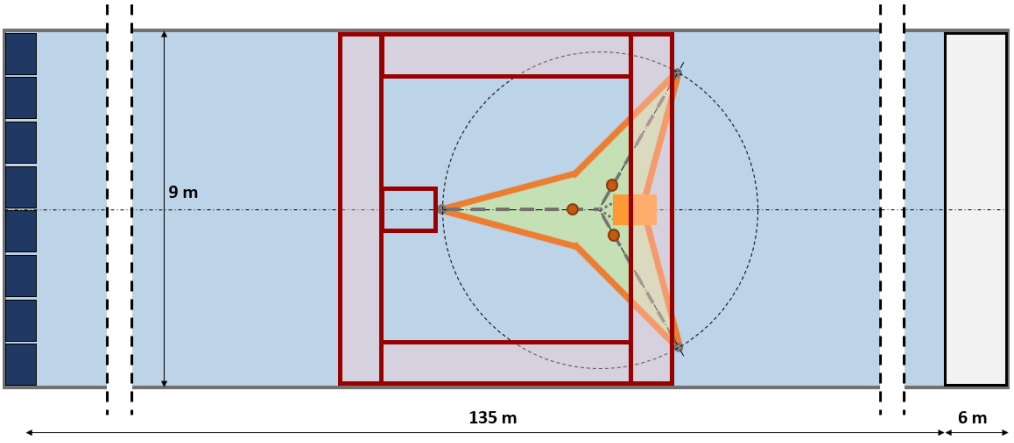

(a) Tank view

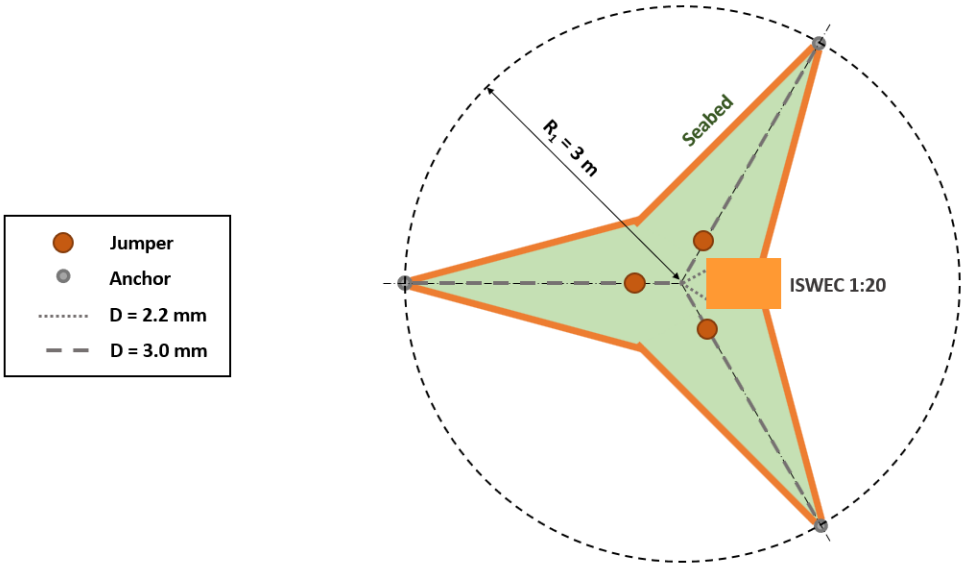

(b) Mooring detail

Fig. 6.5 Mooring setup scheme

A FUTEK LSB210 [67] load cell was chosen. This sensor is submersible and miniaturized in order to do not influence the dynamics of the mooring system. A conditioner FUTEK IAA100 [66] is provided and located onboard the device. It is used to amplify the signal output from the load cell and to transmit the acquired data to the cRIO system installed onboard (see Chapter 4). The new sensor is thus integrated in the DAQ system already described for the free-body experimental campaign. Its setup is shown in Figure 6.6

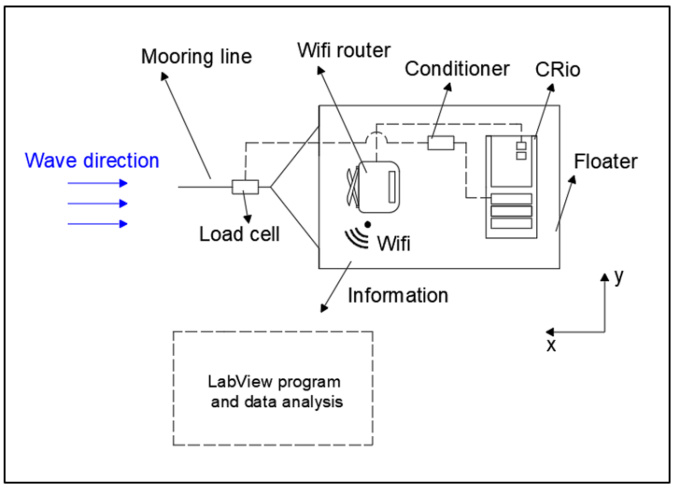

(a) Load cell operating scheme

(b) Load cell connection

Fig. 6.6 Load cell setup

The load cell measuring range is equal to $\pm 445\ N$ that corresponds to $\pm 3560\ kN$ in full scale and the rated output range is equal to $\pm 10\ V$. Its load-output signal characteristic is linear within the working range of interest and was experimentally verified with calibrated masses. The calibration data are reported in Table 6.4.

Table 6.4 Load cell calibration data

Load	Output signal
$(\%)$	(mV/V)
0	0.0
20	0.4463
40	0.8928
60	1.3390
80	1.7853
100	2.2317

6.3 Static Characteristic Identification

The first experimental test was aimed to the identification of the static characteristic of the mooring system. A pull-out test was performed for both configurations in absence of waves. More in detail, starting from the equilibrium condition at the centre of the mooring system, the device was pulled away along the direction of one of the three mooring lines and the restoring force was measured every step of 2 *cm*. This procedure was repeated until the mooring line became fully stretched as shown in Figure 6.7.

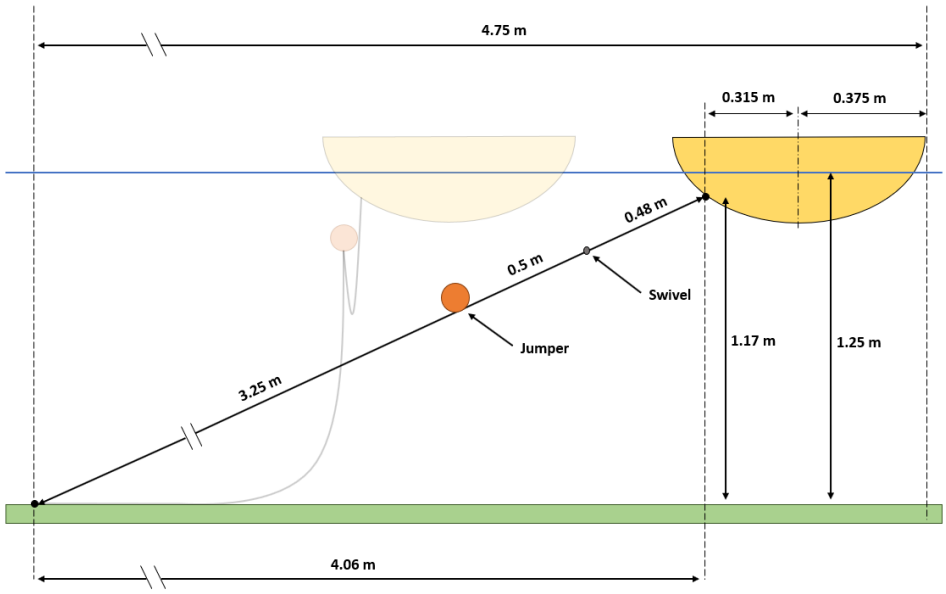

(a) Configuration C1

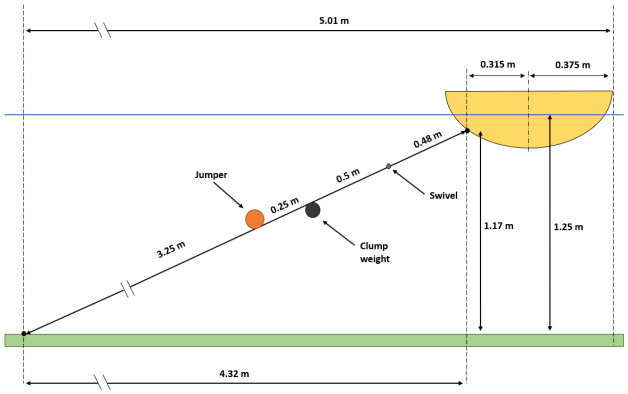

(b) Configuration C2a

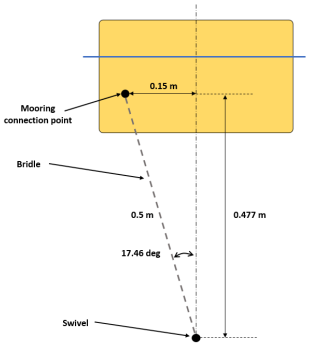

(c) Bridle detail

Fig. 6.7 Pull-out test scheme

The experiments were performed for the worst loading case, in which a single mooring line is working, while the other two are unloaded except for their own weight. The measured tensions along the line can be plotted versus the surge displacement, obtaining the load excursion curve that represents the static characteristic of the mooring system. The experimental tests have been simulated also in Ansys Aqwa for the full-scale system, to compare the numerical results with scaled-up experiments.

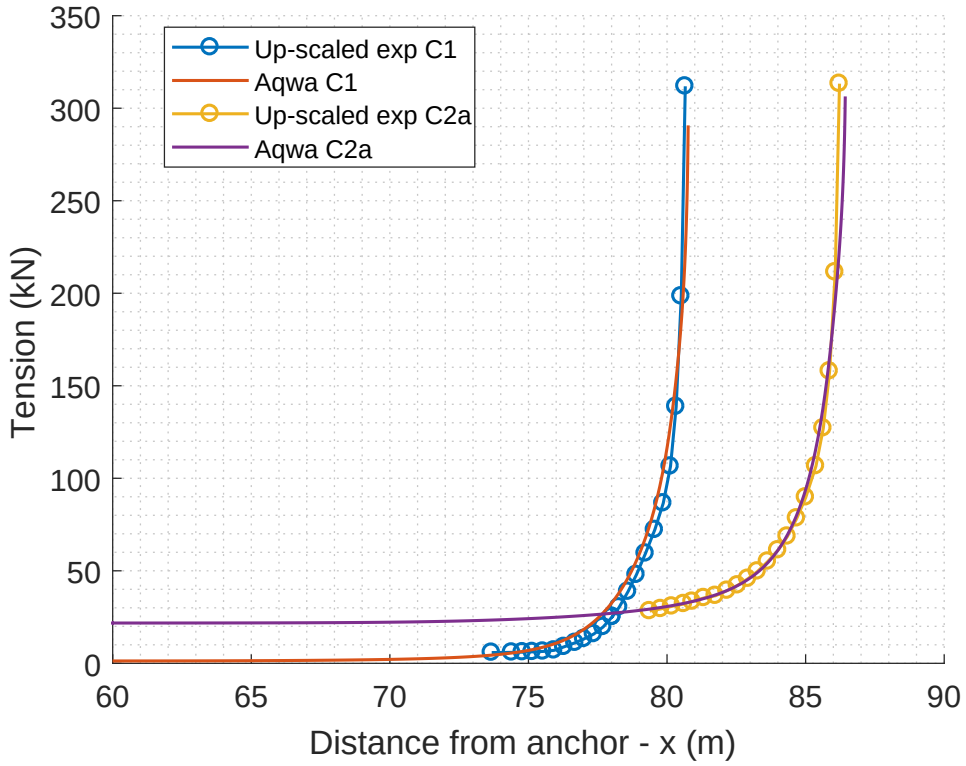

Fig. 6.8 Mooring Static Characteristic. Load-excursion curve

In the numerical model, the reverse experiment was simulated: starting from the fully stretched conditions, the device advances towards the anchor and the mooring load is calculated in static conditions for each step. The static configuration at each step is obtained from the equilibrium between the weight and the buoyancy of the coupled system WEC-moorings. In this test no contribution from environmental dynamic loads is present. Figure 6.8 shows the comparison between the numerical model and the experimental up-scaled. It is possible to observe that numerical results demonstrate an excellent agreement with the experimental results, with a relative error not exceeding 5%. This means, on one hand, that the numerical model is reliable for the calculation of the static characteristic of the mooring system and,

on the other hand, that a correct scaling has been performed, according to Froude scale. Moreover, it is due to notice that in the lower part of the curves the load is almost constant and the resolution of the sensor is too high to measure the change in load. Consequently, the experimental points are limited when the mooring system is fully slack. Additionally, when the mooring line becomes taut, the hydroelastic phenomena become important, and the load will be no more a function of the displacement but a function of the axial stiffness of the material.

The load-excursion curve can be divided in two different areas: in the first area, the load is almost constant, whilst in the second area, the load increases non-linearly until the line becomes taut. The two characteristics are similar in the second part of the curve, when the restoring force starts to be non-linear. More in detail, for Configuration C2a, the stiffness of the mooring line is increased due to the presence of the clump-weight. It is possible to characterize the second configuration as more responsive than the first one. On the other hand, the constant load area is higher for Configuration C2a, because the weight of the line is increased due to the clump-weight and the addition of a catenary section.

In the Aqwa environment is possible to decompose the load applied by the mooring system in the different components with respect to the device COG reference frame. In this way it is possible to obtain a look-up table that can be transferred in Simulink, adding the mooring system modeling to the lumped parameters ISWEC wave-to-wire numerical model.

6.4 Regular waves tests

In this section the results regarding the moored device in regular waves are presented. The tests have been carried out for the two mooring configurations *C1* and *C2a*. The waves list is reported in Table 6.5. Same waves tested for the free-body experimental campaign were used. In particular, for the moored device the only wave steepness of $1/50$ and $1/35$ were tested. More in detail, in Table 6.5 a checkmark is present for the actually performed tests. For Configuration *C2a* the $1/35$ wave steepness tests were not carried out.

Wave Records analysis

The same experimental setup of the free-body campaign was used for the wave probes. Three probes WP1, WP2 and WP3 were installed. WP1 and WP3 are located upstream of the device, where WP3 is the capacitive one. WP2 is mounted between the device and the tank wall.

Figure 6.9 reports the experimental results for the identification of amplitude and frequency of the generated waves. The same post processing analysis used for the first experimental campaign has been performed. Analogous results were obtained: at high frequency the wave-maker is not capable to guarantee the correct wave amplitude. Nevertheless, the results show in general a good agreement with the theoretical desired waves. For the RAOs calculations, the average value of the three wave probes results are considered.

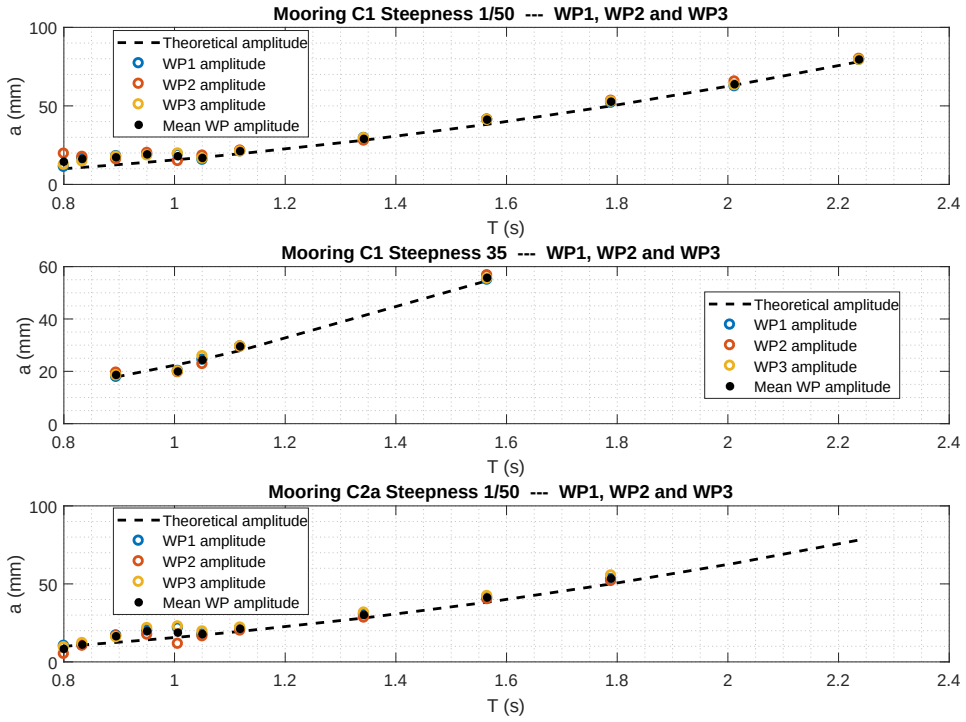

Fig. 6.9 Experimental waves amplitudes. Moored device

Motions analysis

Figure 6.10 shows the experimental results of the motion amplitudes of Pitch and Heave for all the tests performed. From these results, a first comparison between the

Table 6.5 Regular waves list

ID	$T_{w,FS}$	$T_{w,m}$	f	a_w	λ	λ/L	**C1**	**C2a**
	(s)	(s)	(Hz)	(mm)	(m)	(-)		
Steepness 1/50								
1a	3.58	0.8	1.25	9.99	0.999	1.31	✓	✓
2a	3.73	0.833	1.2	10.83	1.083	1.43	✓	✓
3a	4.00	0.894	1.118	12.48	1.248	1.64	✓	✓
4a	4.25	0.951	1.052	14.12	1.412	1.86	✓	✓
5a	4.50	1.006	0.994	15.80	1.580	2.08	✓	✓
6a	4.70	1.050	0.952	17.21	1.721	2.26	✓	✓
7a	5.00	1.119	0.894	19.55	1.955	2.57	✓	✓
8a	6.00	1.342	0.745	28.12	2.812	3.70	✓	✓
9a	7.00	1.565	0.639	38.24	3.824	5.03	✓	✓
10a	8.00	1.789	0.559	49.97	4.997	6.58	✓	✓
11a	9.00	2.012	0.497	63.20	6.320	8.32	✓	✗
12a	10.00	2.237	0.447	78.13	7.813	10.28	✓	✗
Steepness 1/35								
3b	4.00	0.894	1.118	17.83	1.248	1.64	✓	✗
5b	4.50	1.006	0.994	22.57	1.580	2.08	✓	✗
6b	4.70	1.050	0.952	24.59	1.721	2.26	✓	✗
7b	5.00	1.119	0.894	27.93	1.955	2.57	✓	✗
9b	7.00	1.565	0.639	54.63	3.824	5.03	✓	✗

two mooring configurations in operational conditions can be made. It is possible to notice that the introduction of the clump-weight in Configuration C2a has a small influence on the motions amplitude. The difference in Pitch amplitude is, in average, equal to 5%. This result is motivated by the higher stiffness of the mooring Configuration C2a. The loss in performances would be justified if the loads on mooring lines will be significantly reduced. Unfortunately, for lack of time, no regular waves tests were performed for high wave steepness values. Further investigations are needed to understand the influence of the clump-weight in these conditions.

For a better visualization and comparison of the results, non-dimensional Response Amplitude Operators are shown in Figure 6.11. For Pitch motion it is possible to observe a general good agreement with the linear numerical model. It is due to notice that numerical RAOs are obtained for a free body test. Hence, no mooring effects are introduced. These results are encouraging because demonstrate that the catenary mooring is well designed for operational conditions. Higher differences are shown near resonance conditions with the highest error of 15%.

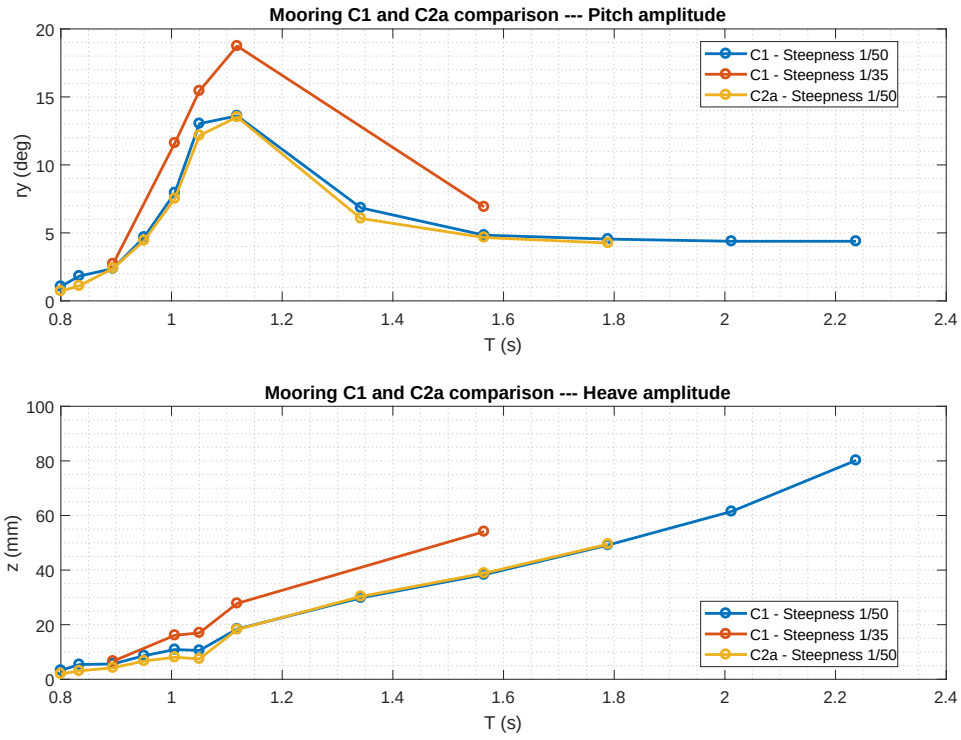

Fig. 6.10 Experimental results. Pitch and Heave motion amplitudes. Moored device

Heave RAO shows a worst agreement with the free body numerical model. In general, the heave response results more damped when the clump-weight is introduced. Nevertheless, heave motion does not contribute to the power conversion chain and lower response can be accepted for the sake of safety.

The influence of the mooring system is, in general, higher for frequencies close to the natural period of the device. As already explained, this result is due to the contribution of drift forces in regular waves. For what concerns numerical results, drift forces are only introduced in the time domain model, which guarantees more accurate results for irregular wave analyses.

Eventually, it is important to highlight that the frequency resolution of the experimental points does not allow a smooth identification of the RAO curves. Nevertheless, in proximity of the Pitch response peak, it is possible to observe the influence of non-linear phenomena which are identified and took into account by the free-decay tests.

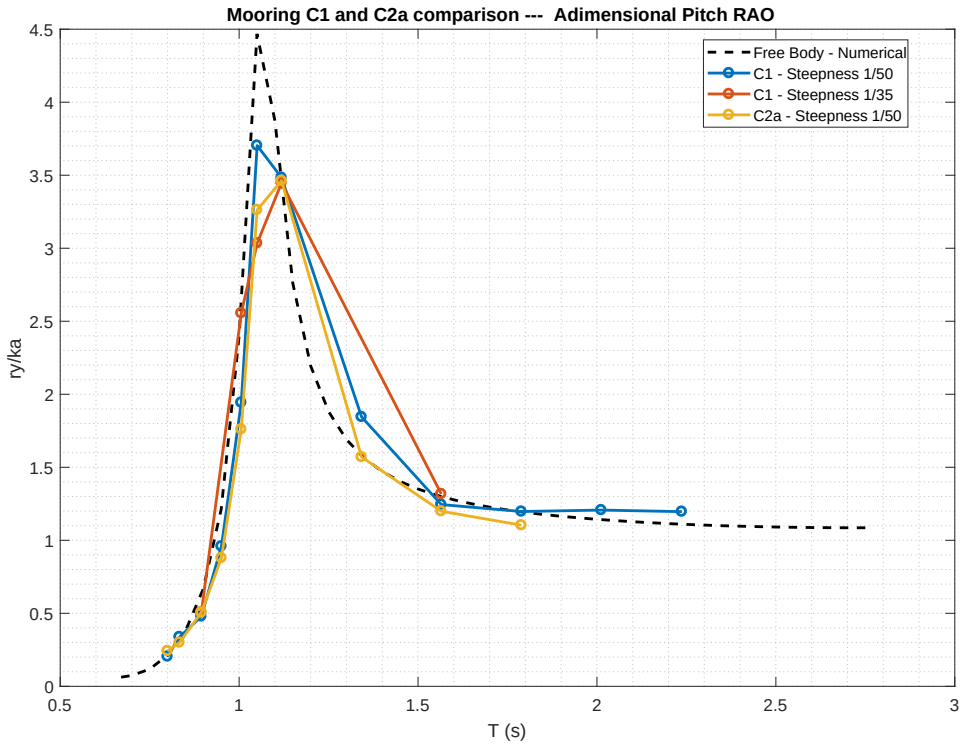

(a) Pitch RAO

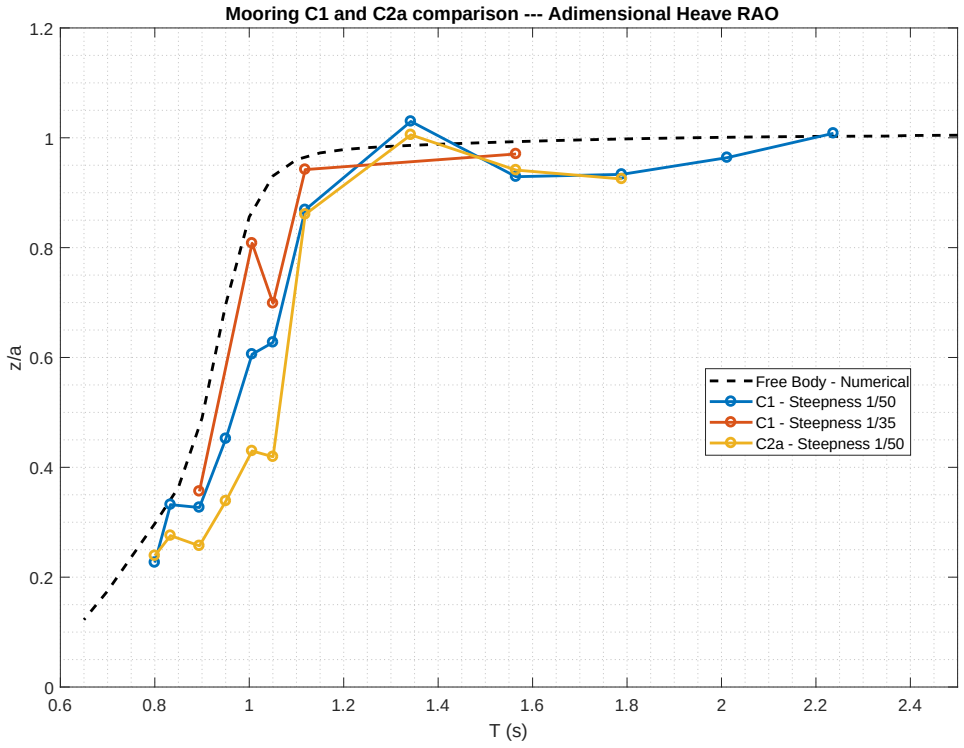

(b) Heave RAO

Fig. 6.11 Non dimensional Response Amplitude Operators. Moored device

6.5 Extreme waves tests

In this section, the results of the experiments in extreme waves are analyzed. According to the test program, three wave records were tested for the 100 years return period sea state. Each wave record is characterized by the same spectral properties and different random phases (seeds) between the spectrum frequency components. Three seeds have been used to build a statistically relevant database for the mooring tensions analysis in extreme conditions. Two different mooring Configurations *C1* and *C2a* have been tested in secular sea states, respectively without and with the clump-weight on the mooring lines. Furthermore, a 10 years sea state was tested for the different mooring configurations. A single wave record was tested in these conditions to optimize the test schedule. More in detail, no relevant differences were observed for a secular sea state with different seeds. Thus, for the 10 years return period wave, the attention was focused on different aspects. In particular, Configuration *C2a* test was repeated because an unexpected peak of tension was detected on the mooring lines. Eventually, a further modification of the mooring system was tested: a bigger clump-weight was introduced to investigate the influence of the mass on the tension peaks. A total of six seakeeping tests were performed for the 100 years return period sea states and four seakeeping tests for the 10 years wave.

Waves spectral analysis

The extreme sea states time records are generated according to a standard Jonswap spectrum with $\gamma = 3.3$. For each test, the spectral analysis has been performed on both the input signal to the wave generator and the measured waves. The detailed results of the analysis are here reported and commented for each test.

Table 6.6 Wave records spectral properties - 100 years wave

Test ID		Time record	H_{m0}	max	min	mean	rms	T_p
		s	mm	mm	mm	mm	mm	s
1	$C1-101$	2417	312	353	-306	0	79	2.29
2	$C1-102$	2423	285	390	-474	13	72	2.28
3	$C1-103$	2496	293	317	-267	17	73	2.28
4	$C2a-101$	2466	294	317	-246	17	73	2.28
5	$C2a-102$	2445	294	312	-263	19	73	2.28
6	$C2a-103$	2431	294	318	-262	19	73	2.28

Figure 6.12 reports the spectral analysis for the wave profile signals of the 100 years return period incident wave tests. The secular wave is characterized by a significant height $H_s = 295\ mm$ and peak period $T_p = 2.3\ s$. In Figure 6.13 the results for the 10 years wave with $H_s = 250\ mm$ and $T_p = 1.95\ s$ are shown. To compensate the wave generator error and the energy dissipation along the tank, the significant height of the input wave was set to $H_{s,in} = 315\ mm$ for the secular waves and $H_{s,in} = 280\ mm$ for the 10 years wave.

Waves spectral analysis exhibits similar results for both the extreme sea states. It must be noticed that for the first two tests $C1-101$ and $C1-102$ there were only ultrasound wave probes installed. During the tests, it was observed that the wave height often overcame the sensors. For their working principle, the ultrasound probes can not get wet. This resulted in frequent signal losses that could not be accepted. For the further tests, a capacitive wave probe was installed and its signal was analyzed as the most accurate.

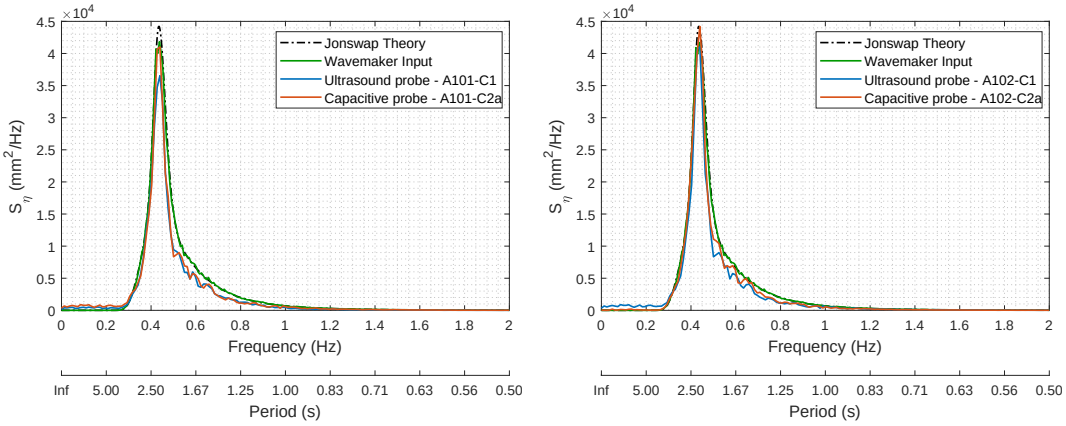

(a) 100 years wave - Seed 1

(b) 100 years wave - Seed 2

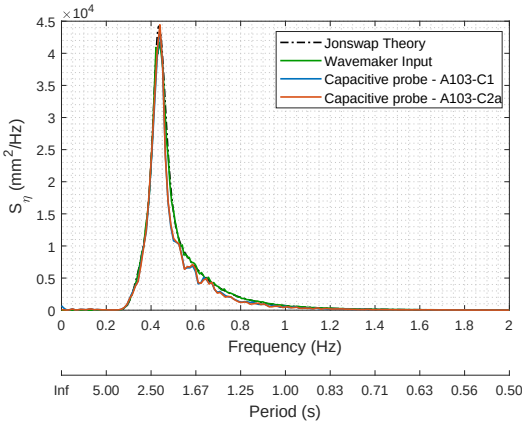

(c) 100 years wave - Seed 3

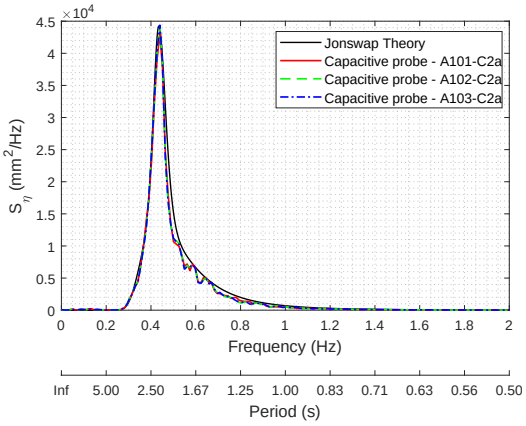

(d) 100 years wave - Configuration *C*2*a*

Fig. 6.12 Waves power spectral density - 100 years wave

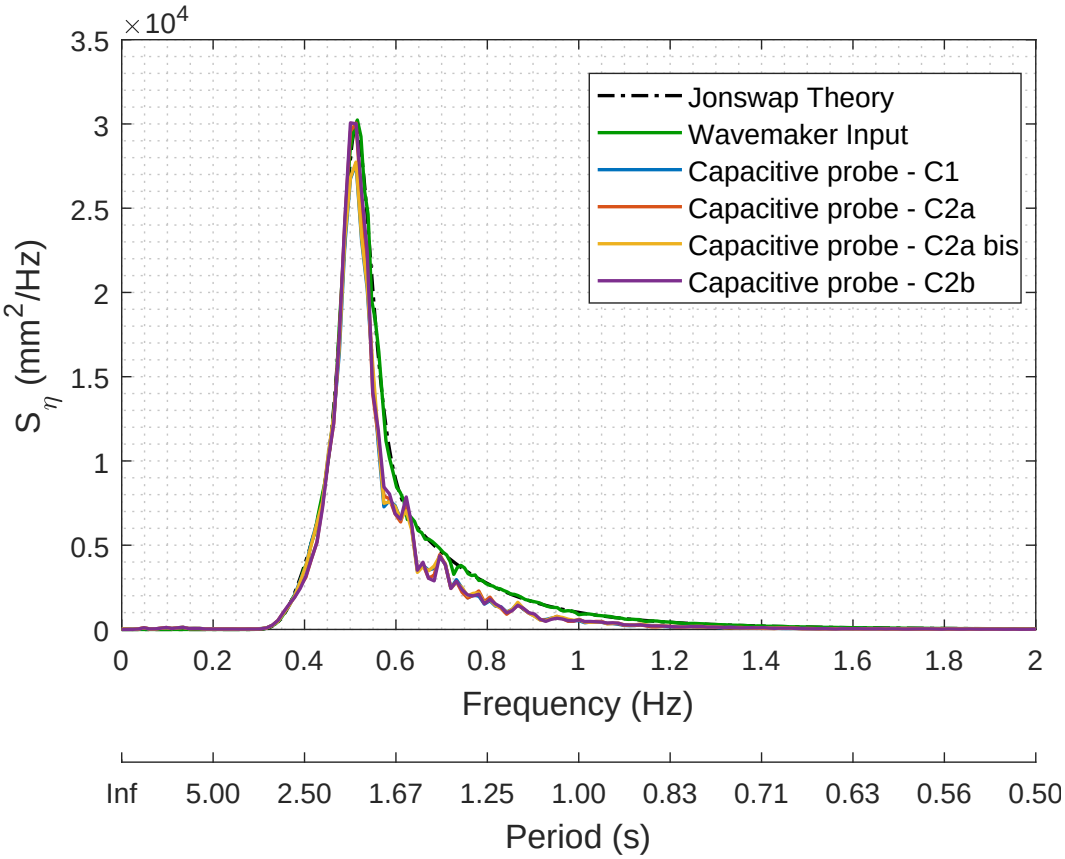

Fig. 6.13 Waves power spectral density - 10 years wave

The spectral analysis has been performed on both the input signal to the wave generator and the measured waves for each test. The input wave spectrum is reported in *green* and it is correctly superimposed to the theoretical Jonswap spectrum (*black*) with $\gamma = 3.3$ and cut-off frequency $f_c = 4\ Hz$.

For each 10 years wave test, the same input wave record has been used. The graph in Figure 6.13 demonstrates a very good repeatability of the wave generator, being the measured wave spectra superimposed. Tables 6.6 and 6.7 summarize the spectral properties of the acquired wave record for each test. The secular wave tests were performed for the full length of the storm record in scaled environment. Tests in extreme waves conditions are very long, while tank test sessions are usually short time windows. Thus, to optimize the test campaign it is often required to update the schedule according to previous tests results. According to the time optimization tests 3 and 4 for the 10 years wave were stopped just after the extreme peak of tension was detected.

Table 6.7 Wave records spectral properties - 10 years wave

Test ID		Time record	H_{m0}	max	min	mean	rms	T_p
		s	mm	mm	mm	mm	mm	s
1	$C1-10y$	2498	251	316	-218	17	63	1.95
2	$C2a-10y$	2468	252	314	-222	16	63	1.95
3	$C2a-10y$ *bis*	1921	253	315	-212	13	63	1.95
4	$C2b-10y$	1803	254	317	-206	1	64	1.95

In short, wave records analysis shows that the main spectral properties H_s and T_p are in perfect agreement with the desired ones.

Motions spectral analysis

Motion analysis is focused on the relevant motions that interact with the mooring system's dynamics. As for the wave profiles analysis, analogous results were find for both secular and 10 years waves conditions. To avoid repetitions, 10 years wave results are presented and commented in detail here. For the sake of completeness, all the results of the secular wave tests are reported in Appendix A.

First, the heave motion is analyzed and compared with the incident wave analysis. Figure 6.14 reports the *heave* power spectral density for each test. It is possible to observe that the heave response is not influenced by the mooring system modifications. This result is confirmed for the increased mass of the clump-weight also. The peak of the motion response coincides with the wave frequency: this means that there is no slow-frequency contribution for heave. More in detail, Figure 6.15 shows how the hull follows exactly the wave in heave because the wave period is longer than the natural period of the device.

This result does not occur for the *pitch* motion. Figure 6.16 relates the pitch motion response to the incident wave. For the sake of clarity, only the theoretical Jonswap spectrum of the input wave has been plotted. The graph has two y axes that correspond respectively to the pitch power spectral densities on the left and to the wave spectrum on the right. The pitch PSDs are similar for each test and exhibit two peaks. The lower frequency peak corresponds to the peak period of the incident wave, $T_{w,p} = 2\ s$, while the higher frequency one corresponds to the natural period of

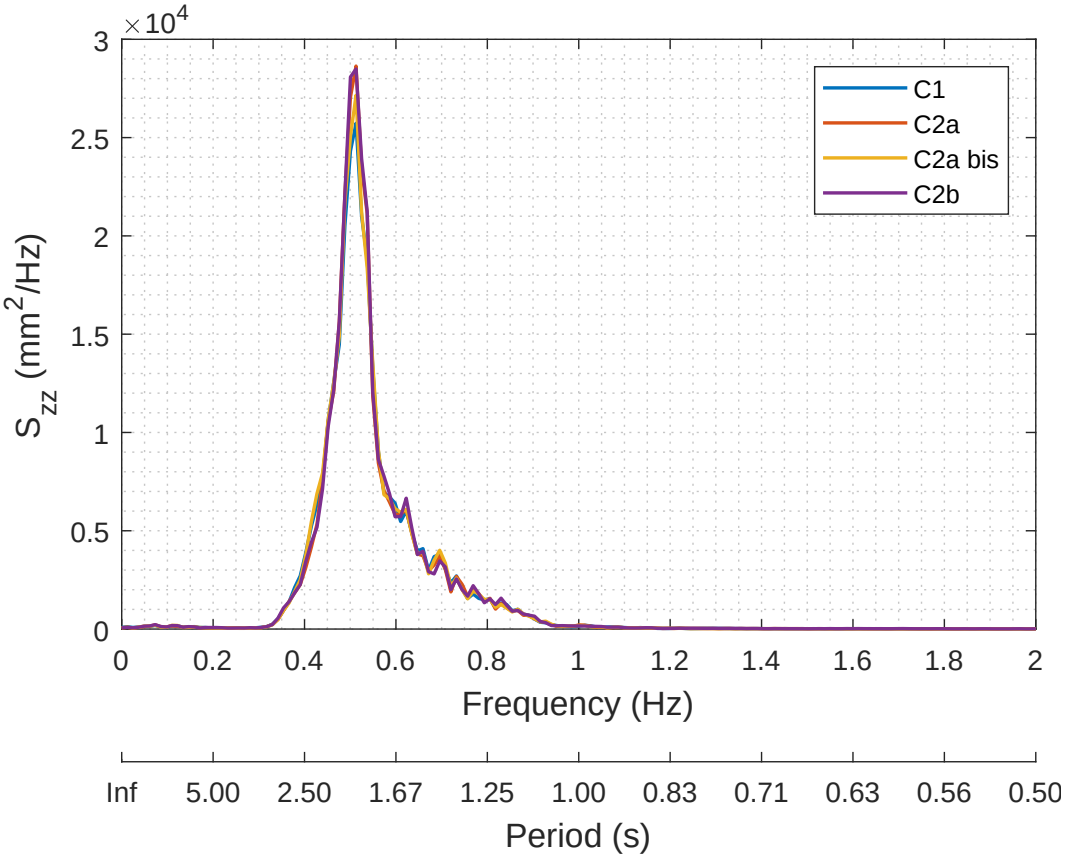

Fig. 6.14 Heave PSD - 10 years wave

Table 6.8 Heave records spectral properties - 10 years wave

Test ID		Time record	z_{m0}	max	min	mean	rms	T_p
		s	mm	mm	mm	mm	mm	s
1	$C1-10y$	2498	237	294	-255	3	60	1.95
2	$C2a-10y$	2468	239	287	-237	2	60	1.95
3	$C2a-10y$ *bis*	1921	239	303	-235	2	60	1.95
4	$C2b-10y$	1803	241	284	-237	3	60	1.95

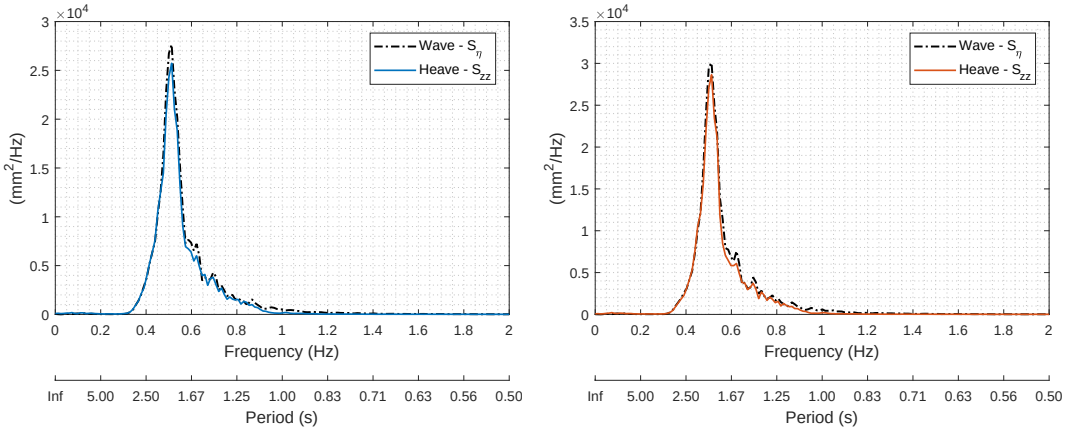

(a) C1 (b) C2a

Fig. 6.15 Wave vs Heave PSD

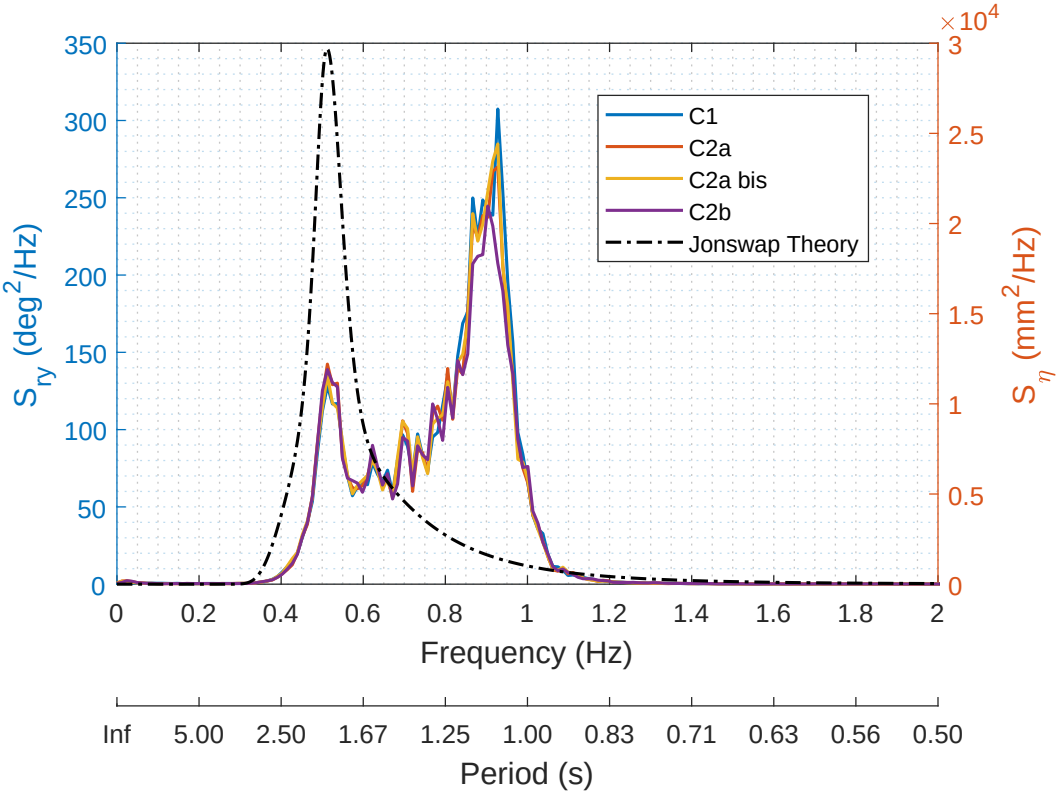

Fig. 6.16 Pitch PSD - 10 years wave

Table 6.9 Pitch records spectral properties - 10 years wave

Test ID		Time record	δ_{m0}	max	min	mean	rms	T_p
		s	deg	deg	deg	deg	deg	s
1	$C1-10y$	2498	33.5	31.4	-30.2	-0.1	8.3	1.1
2	$C2a-10y$	2468	33.1	32.6	-30.2	-0.2	8.3	1.1
3	$C2a-10y$ *bis*	1921	33.0	26.9	-30.2	-0.2	8.2	1.1
4	$C2b-10y$	1803	32.4	25.7	-31.0	-0.1	8.1	1.1

the device, $T_n = 1.1\ s$. It is very interesting to highlight that the wave frequency peak is lower than the natural frequency peak. This means that despite the wave energy contribution is relatively low around 1.1 s, the pitch motion is still amplified due to the inertia properties of the hull. The motion of the device is thus always governed by the its inertia properties. This results more evident for high power waves, where the energy contribution at higher frequencies is still enough to excite the natural frequency of the hull. In general, a design indication can be extrapolated: it is correct to design the hull natural period to be correspondent to low period waves, which usually have a higher occurrence with respect to the long period waves. Indeed, for these waves the low energy content will be compensated by the motion amplification due to resonance condition, while for longer waves, the loss in efficiency of the hull will be partially compensated by the higher power input. As for the heave motion, Table 6.9 shows that also pitch is not influenced by the mooring system in extreme wave conditions.

Last motion to be analyzed in detail is the *surge*, which is the most important from the mooring design point of view. Table 6.10 summarizes the spectral analysis results. From Figure 6.17a, it is possible to observe that the energy contribution to the surge motion is mostly distributed at a very low frequency. This result is in agreement with the comments anticipated in the theoretical background chapter: for surge motion, the second order wave forces are mainly important, because they excite the mooring system natural frequency. A zoom is needed to investigate the second peak of the surge PSD. This peak corresponds to the first order forces contribution of the incident wave. Figure 6.17b reports the surge PSD against the theoretical spectrum of the incident wave. It is immediate to notice that this area of the surge PSD follows the wave power spectrum but its power content is two order of magnitude below the low

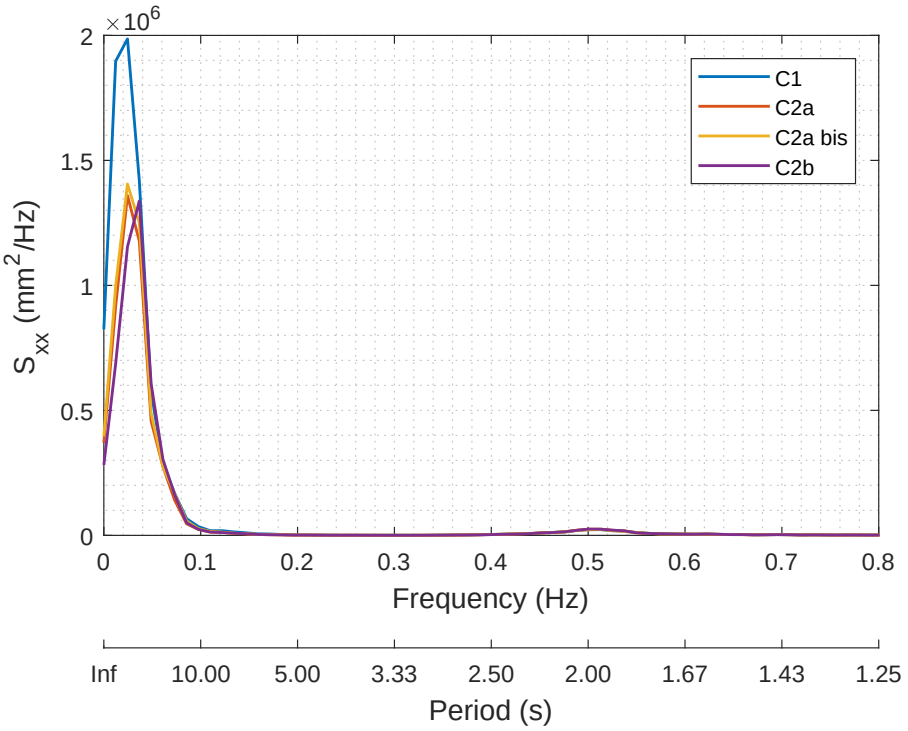

(a) Surge PSD (total frequency range)

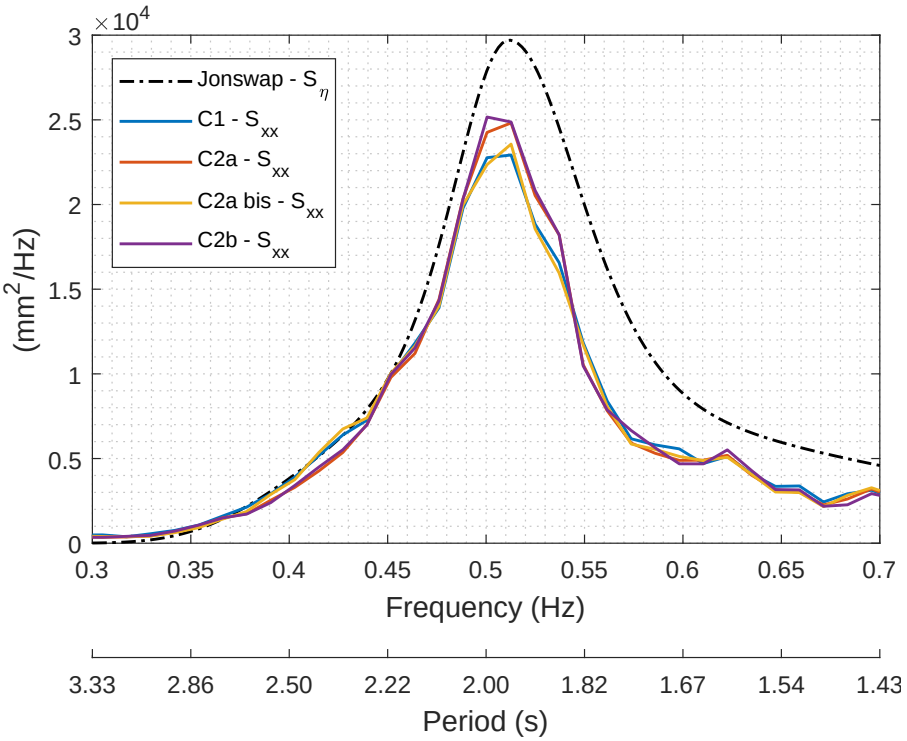

(b) Zoom on Wave frequency

Fig. 6.17 Surge PSD - 10 years wave

Table 6.10 Surge records spectral properties - 10 years wave

Test ID		Time record	x_{m0}	max	min	mean	rms	T_p
		s	mm	mm	mm	mm	mm	s
1	$C1-10y$	2498	1199	3883	1596	3183	305	55
2	$C2a-10y$	2468	1016	4012	1795	3080	257	34
3	$C2a-10y$ *bis*	1921	986	4149	2120	3234	250	34
4	$C2b-10y$	1803	976	4001	2149	3075	246	29

frequency area. This result demonstrates that the first order forces contribution to the surge motion can be neglected with a good approximation.

Furthermore, the mooring systems' natural frequencies can be identified by evaluating the peak frequency of the power spectrum for each configuration. Introducing the clump-weight, the stiffness of the moored system in surge increases, thus reducing the natural period. Consequently the motion of the device is restrained, and the surge displacement results lower in average. This is confirmed by the summary reported in Table 6.10: specifically the rms values reduction is observed. It must be noticed that from configuration $C1$ to configurations $C2a$ and $C2b$ the mooring lines length is increased, hence the motion constrain is not that pronounced. On the other hand, from the spectral analysis nothing can be said about the clump-weight increase in mass and a deepen analysis must be performed on this effect.

From the presented analysis it is not possible to evaluate which mooring system has the best performances. More precisely, all the tested configurations demonstrated good performances in terms of the influence on the dynamics of the floater for high power sea states. On the other hand, the critical design point in extreme wave condition is the evaluation of the survivability of the mooring system in terms of mechanical failures. The motion analysis in frequency domain can not give comprehensive results on the mooring lines loads and dynamics, depending on the wave climate. In the next session a deep analysis of the time-series is provided, to validate the design procedure and evaluate the possibility of failures.

6.6 Mooring loads analysis

To understand the relation between the floater motions and the mooring loads, it is necessary to analyze the time-histories of the signals. For each test in extreme waves, the signal of the load cell installed just after the swivel was acquired. The mooring system is designed to be slack and to do not influence the relevant motions of the system for the wave power absorption. This behavior has been confirmed by the spectral analysis presented in 6.5. On the other hand, the main purpose of the mooring system is the station keeping in surge of the device. It is thus expected that the surge dynamics is mainly influenced by the mooring and, consequently, that loads follow it. Figure 6.18 reports a time series window for the *surge*, *heave* and *pitch* signals, compared against the mooring load signal. The graphs report the secular wave test $C1-101$ but, again, it is representative of the all extreme wave tests. As explained in the previous section, it is immediate to observe that the pitch motion is governed by the natural frequency of the device. Furthermore, the heave signal is characterized by the incident wave frequency, while the surge motion presents also a lower frequency contribution. From the first subplot it is possible to confirm that the low frequency excites the mooring lines. Mooring loads, indeed, are characterized by a very low mean load, which is mainly due to the catenary weight, and singular spikes of higher orders of magnitude.

From the mooring design point of view and for the validation of the numerical tool that can be used in the design procedure, the tension peaks are of interest. These peaks appear when the mooring line becomes fully stretched and snaps occur along the chain. The snaps are governed by the device drifting and they can be identified as isolated events during the storm. To analyze these events, spectral analysis is not appropriate. Hence, a statistical approach is here proposed.

The statistical analysis of the tension peaks is organized according to the following steps:

1. Determination of the Maximum peak of tension for each test in extreme wave environment.
2. Selection of a threshold for the minimum relevant value of the peaks.
3. Evaluation of the probabilistic distribution of the selected peaks.
4. Assessment of the most probable range of tension peaks.

5. Determination of the extreme events that fall beyond a design threshold, selected on the basis of the mechanical failure of the most critical component.

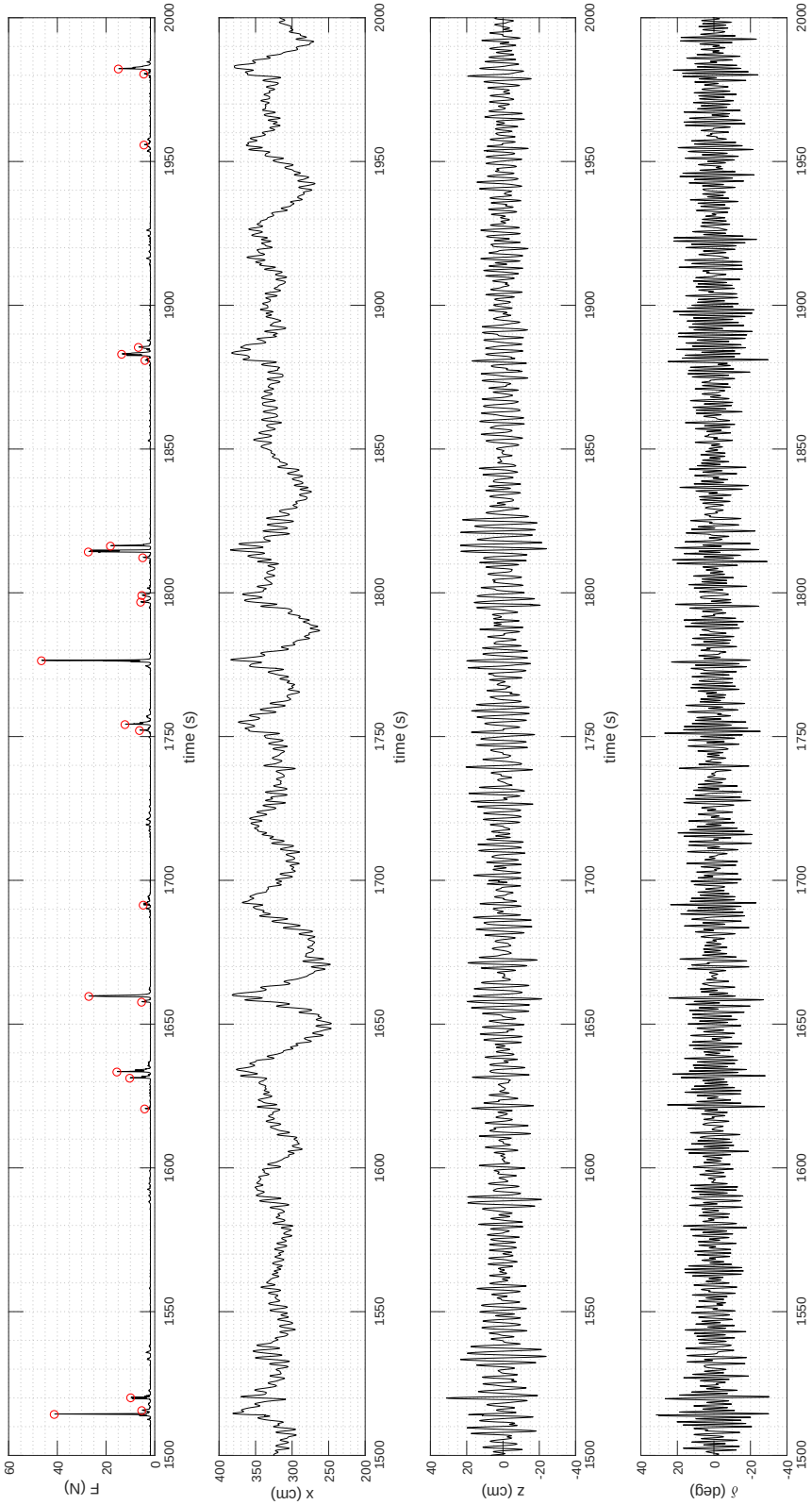

Fig. 6.18 Configuration *C*1 - Time series samples

First, the statistical analysis is performed for the secular waves tests. The two tested configurations $C1$ and $C2a$ are analyzed separately, in order to identify the best solution for the ISWEC mooring system.

Table 6.11 Maxima peaks of tension - 100 years wave

Test ID		ISWEC 1:20		Full Scale	
		rms	*max*	*rms*	*max*
		N	N	kN	kN
1	$C1-101$	2.7	186	22	1488
2	$C1-102$	3.1	210	25	1680
3	$C1-103$	3.2	405	26	3240
4	$C2a-101$	2.3	19	18	152
5	$C2a-102$	1.7	23	14	184
6	$C2a-103$	2.3	61	18	488

Table 6.11 reports the maximum peak of tension for each test in secular waves and the correspondent full scale forces scaled according to Froude. From these results it is possible to observe a clear improvement from configuration $C1$ to configuration $C2a$ in terms of tension peaks reduction. Moreover, an indication on the order of magnitude of the maximum expected tension for the full scale mooring system is obtained. On the other hand, the maxima present relevant differences among the tests with the same mooring configuration. Assuming that the number of peaks per each configuration represent a statistically relevant sample, it is interesting to investigate the probability distribution of the peaks. For the evaluation of the distribution, all the peaks above the *rms* value for each test are selected.

In Figure 6.19 the peak distribution is shown for the Configuration $C1$ in secular waves. The peaks of the three different seeds are grouped together in terms of both *Probability Density Function* (PDF) and *Cumulative Density Function*. It was not possible to obtain a good numerical fitting with a known probability distribution, thus experimental values are reported only. Figure 6.19a shows that the majority of the peaks are distributed in the low tension region, compared to the maximum peak

value. More in detail, it reports a zoom on the peaks distribution for the values less or equal to 10% of the maximum peak detected. The same distribution is observed for this region if each test with different seeds is considered separately. This means that there is no evident influence of the random phase between frequency components on the mooring loads. Moreover, from Figure 6.19b it is possible to observe that the zoomed region corresponds to the 98% of the detected peaks. Below this threshold, it can be assumed with a good fidelity that the mooring loads are representative of the normal working conditions. Above the threshold, the peaks can be considered as extreme isolated events. For the Configuration $C1$, only 12 extreme peaks were detected and their values are reported in the inset plot of Figure 6.19b.

For Configuration $C2a$, results are presented in Figure 6.20. On the basis of the $C1$ results, the isolated events are classified as extreme. The experimental probability density function has the same shape, but in this case the tension's peaks are considerably lower. In particular, only 5 extreme events were recorded corresponding to the 1% of the total.

The introduction of the clump-weight on the mooring system had a significant impact on the reduction of the extreme events and, in general, on the load reduction on the mooring lines. In particular, the mooring load in normal working conditions can be assumed to be lower than 41 N for Configuration $C1$ and lower than 14 N for Configuration $C2a$. These values correspond to Full Scale values equal to 328 kN for Configuration $C1$ and 112 kN for Configuration $C2a$.

The same analysis is performed for three tests in 10 years wave with different mooring configurations. Analogous results to the secular wave tests are obtained for the distribution of the peaks (Figure 6.21), that presents isolated events above the 1% of the maximum peak value. Furthermore, Table 6.12 shows that both the maxima of the extreme events and the rms are comparable with the respective values recorded for secular waves. This means that the worst load case is not necessarily correlated to the power content of the wave. On the other hand, the benefit of the addition of a clump-weight on the mooring line is confirmed by the peak values reduction. More in detail, the maxima reduction is not that sensitive as one could expect from the secular wave tests results.

Figure 6.22 reports the time-series of the peaks for the different mooring configurations. For a better visualization, the tension values are reported on a logarithmic scale and five extreme events are highlighted with markers. It is observed that the

extreme events occur exactly at the same instant for all the tests. Hence, it is clear that these events are related to a specific combination of motion and loads. On the other hand, if also the events are repeated for each configuration, it is not possible to identify a univocal relation between the mooring properties and the peak values.

Table 6.12 Maxima peaks of tension - 10 years wave

Test ID		ISWEC 1:20		Full Scale	
		rms	*max*	*rms*	*max*
		N	N	kN	kN
1	$C1-10y$	3.4	264	27	2112
2	$C2a-10y$	2.0	138	16	1104
3	$C2b-10y$	1.7	107	14	856

To better understand the phenomenon, a deepen investigation is performed for the Configuration $C2a$ in 10 years waves. For the sake of clarity and to avoid redundancy of information, the highest peak of tension is selected and the time series of the motions and the wave profile are analyzed in its surroundings. It is important to highlight that analogous results are observed for the other extreme peaks.

Looking at Figure 6.23 it is possible to relate the extreme event to the previous history of loads and motions. Specifically, in the graphs are reported respectively:

- *subplot 1*: time series of the *mooring tension* in *N*.
- *subplot 2*: time series of the *wave profile* signal acquired by the capacitive probe in *mm*.
- *subplot 3*: time series of the *surge* motion in *cm*.
- *subplot 4*: time series of the *heave* motion in *cm*.
- *subplot 5*: time series of the *pitch* motion in *deg*.

It is clear that the extreme event occurs when high amplitude displacements are recorded in the same instants for surge, heave and pitch motions. The high amplitude

displacements are a consequence of the drift loads due to the wave group which precedes the extreme event (red box in the subplot 2). Unfortunately, it has not been possible to find a relation between the properties of the wave group and the occurrence of the extreme event. More precisely, it can be observed that the wave group doesn't look different from other windows of the time-series sample. Nevertheless, the correspondence of high amplitude displacement is observed only once. This is due to the combination of several factors that can not be controlled or separated in the dynamic evolution of the system. Being the mooring configuration designed to be slack, in order to do not influence the dynamics of the device, the possibilities to constrain high amplitude motions are limited. Consequently, the adverse combination of these motions lead to the full extension of the mooring lines. When the line reach its maximum extension, the chain is completely lifted from the seabed and snatches occur. This is exactly what happens when extreme loads are recorded. Moreover, the peaks of tension in these cases are influenced by the axial stiffness of the chain and their values present a high variability, due to the impulsive nature of the loads.

These events are undesirable not only because of the high loads experienced. On the other end of the mooring line, when the catenary is fully suspended, the anchors do not work in their design conditions anymore. Anchors uplift may occur, leading to a failure of the mooring system. In conclusion, these events must be avoided in a good mooring design.

The introduction of the clump-weight on the mooring line demonstrated to be a relevant improvement to avoid the snatches. In particular, the clump-weight increases the stiffness of the mooring system in surge: when a group of large waves impact the device, it starts to drift and the clump-weight recall force helps to avoid the full extension of the mooring line. Improving the size of the clump-weight, the recall force increases. According to the experimental results, the system efficacy could be improved by extending the bottom mooring line lengths. This way, a twofold positive effect is obtained:

1. A longer advancement range in surge is needed to achieve the snatches conditions.

2. The length of the chain laid on the seabed is greater. The mass of the chain is increased and the anchor uplift is avoided.

The experimental campaign here described, presented important results for the design of slack mooring system for WECs. In particular, the proposed insertion of a clump-weight on the mooring line demonstrated to be a relevant improvement in the design. Nevertheless, the experimental results here presented are not exhaustive and further investigation are needed.

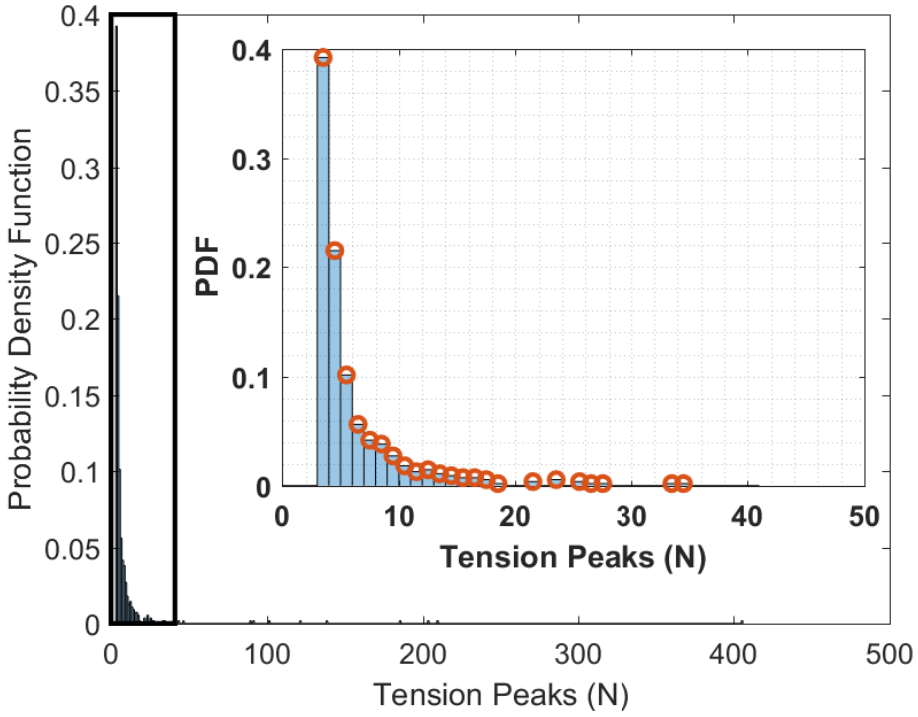

(a) Experimental PDF - Values above the *rms*

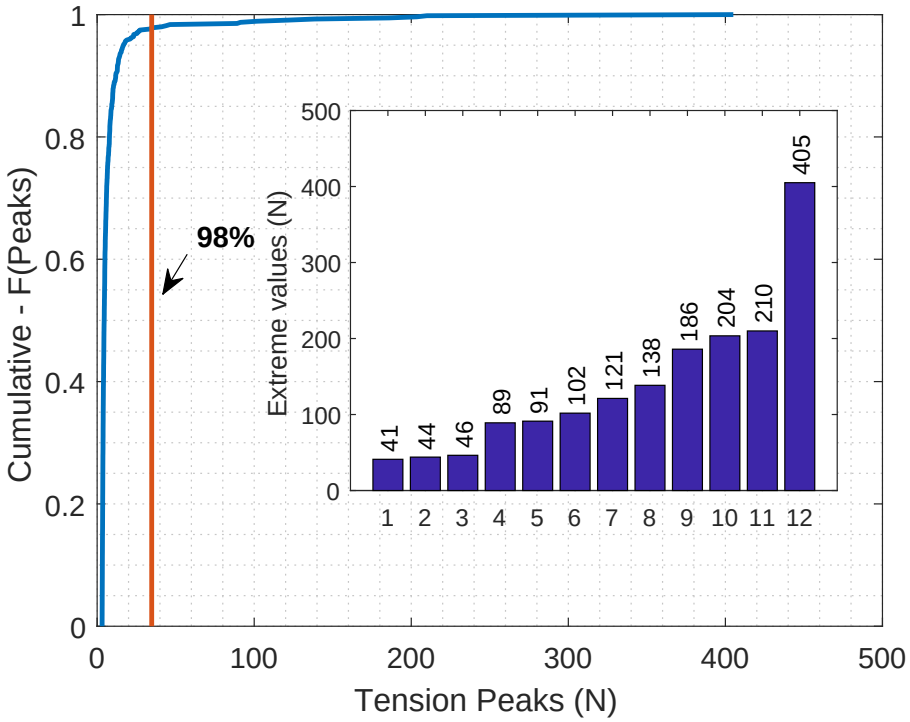

(b) Experimental CDF

Fig. 6.19 Configuration *C*1, 100 years wave - Peaks distributions

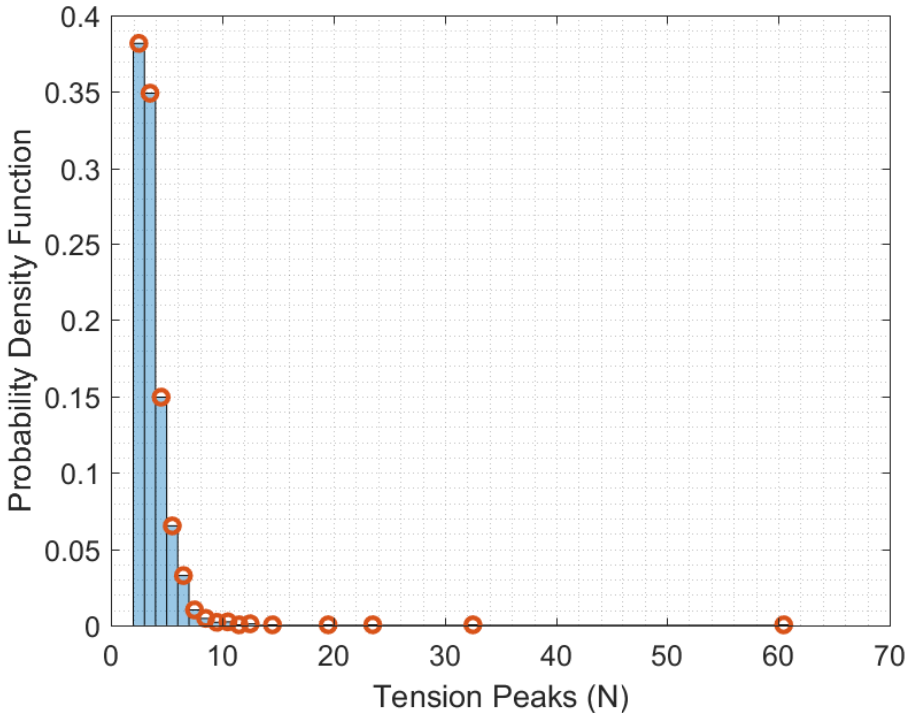

(a) Experimental PDF - Values above the *rms*

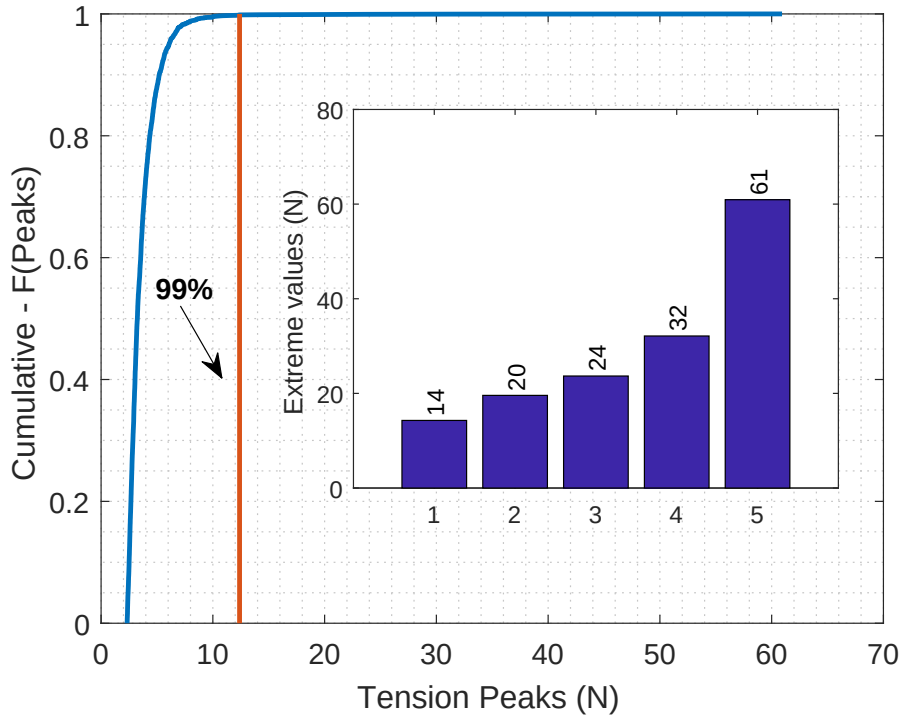

(b) Experimental CDF

Fig. 6.20 Configuration *C*2*a*, 100 years wave - Peaks distributions

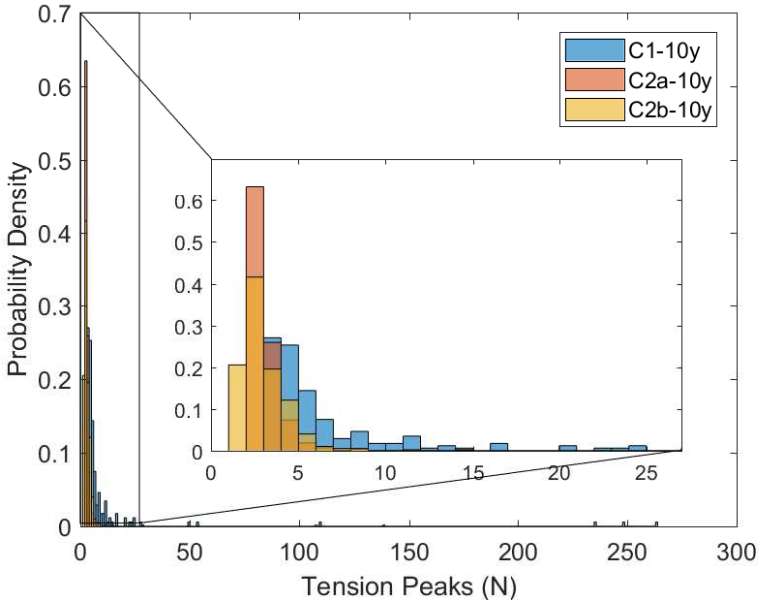

Fig. 6.21 10 years wave - Peaks distributions with different mooring

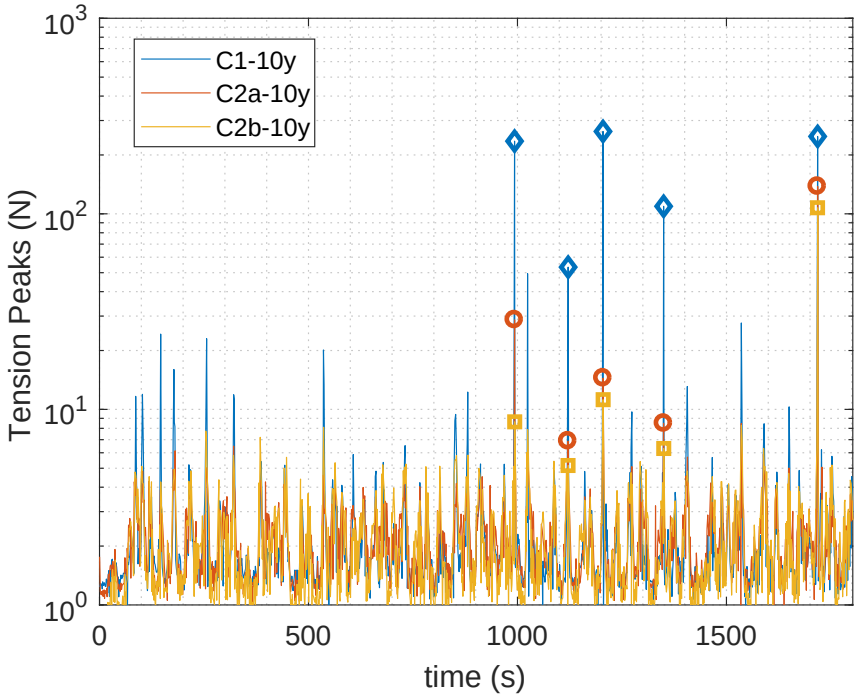

Fig. 6.22 10 years wave - Tension Peaks time series samples

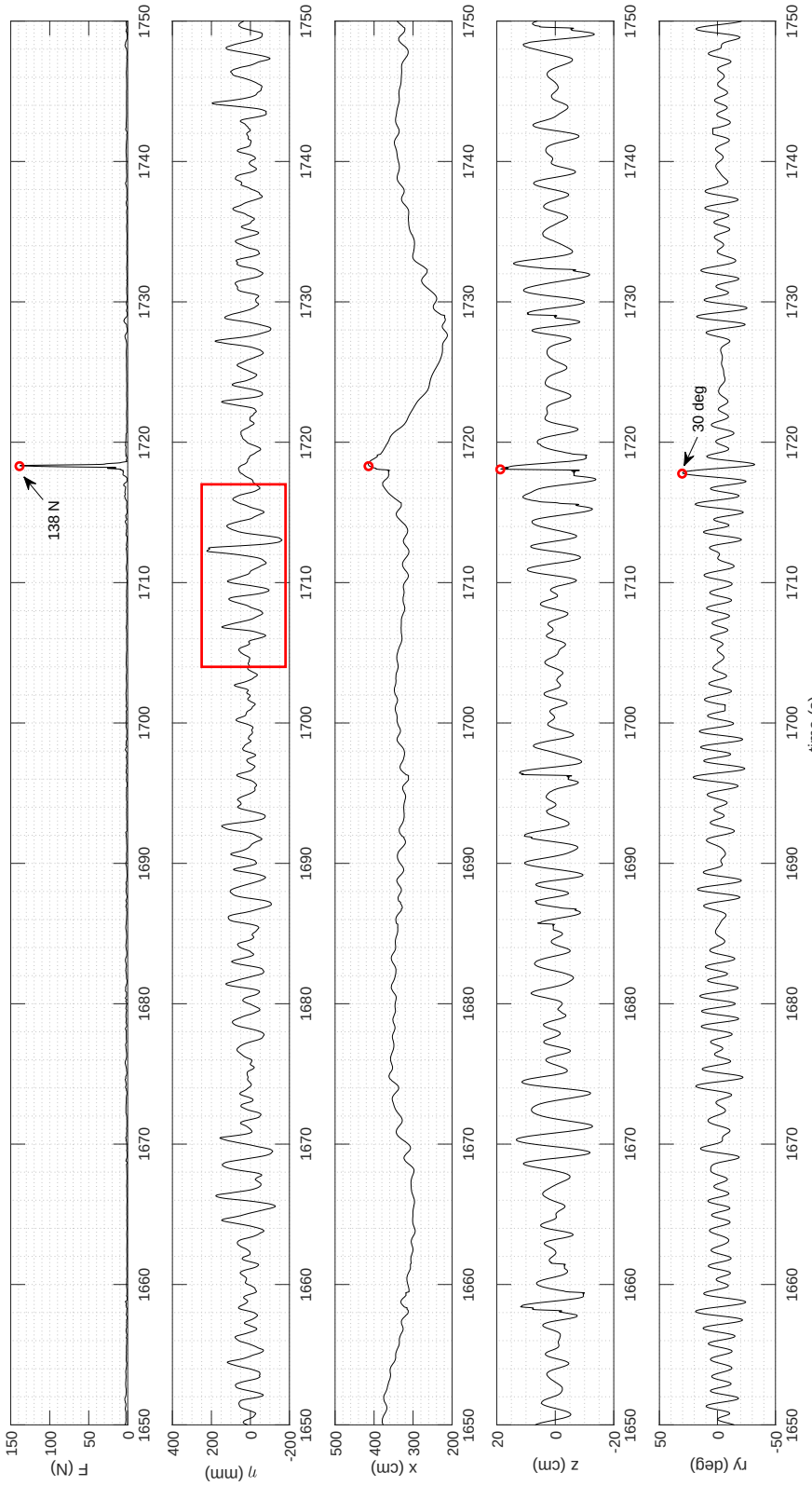

Fig. 6.23 Configuration *C2a* with 10 years wave - Zoom on extreme peak

6.7 Numerical model comparison and further improvements

In this section, the experimental results presented are compared with the numerical model of the moored device built in Ansys Aqwa. The purpose is to validate the numerical model as a useful design tool, identifying differences and approximations that can be still acceptable if correctly considered. Furthermore, the indication output from the experimental campaign and from the first tests of the numerical model are used to improve the mooring layout and achieve the desired design.

Numerical and Experimental results comparison

As already described, the dynamic numerical model of the moored device is computationally expensive. Moreover, it is not possible to replicate, referring to the presented experimental tests, the exact starting position of the device in the numerical model. Hence, the direct replication for each test performed at the wave tank, is not possible. The comparison is consequently made with respect to maxima and rms values for the mooring loads, presented and discussed in Chapter 5.

The numerical tests presented in Chapter 5 are performed considering the mooring configuration C1. A first comparison is possible with respect to these results, summarized in Table 5.11 for the secular waves and in Table 5.12 for 10 years waves. From both numerical model and experimental tests, it has been highlighted that extreme peaks correspond to a full extension of the mooring lines. In this case, the hydroelastic phenomena become relevant and a correct scaling of the elastic properties of the material is important. More in detail, for a catenary section, the hydroelasticity of the material influences the mooring tension T_m, that becomes a function of the axial stiffness EA of the chain:

$$T_m = f(EA) \tag{6.2}$$

where E is the Young modulus of the material and A is the equivalent cross sectional area of the line. Moreover, to correctly scale the mass of the mooring line, it was necessary to scale the diameter and thus the area of the mooring chain according with the Froude scale. It is immediate to understand that, being the material of the experiment very similar to the full scale prototype mooring lines, the elasticity of the

line is not properly scaled. Indeed, the Young modulus scaling factor is equal to λ^1. The correct scaling of the hydroelasticity can be experimentally obtained introducing spring components on the lines, to properly tune its stiffness. This process is iterative and requires a lot of time to find the correct setup. For this reason, it was not possible for the presented experimental campaign to obtain a correct scaling of the axial stiffness. Thus, a comparison on the basis of the peak loads due to snatches is not fully correct. Moreover, for the explained reasons, the scaled up experimental results for peak loads are to be assumed conservative for design purposes. On the other hand, a comparison is possible on the rms values of the mooring loads, that well describe the dynamics in most realistic conditions. In particular, it can be observed that rms values are of the same order of magnitude for both experimental and numerical results. Table 6.13 summarizes the comparison results for the extreme waves.

Table 6.13 Maxima peaks of tension - 10 years wave

Test case	Numerical		Experiments	
	rms	*max*	*rms*	*max*
	kN	kN	kN	kN
100 years	30	699	26	3240
10 years	32	996	27	2212

It appears clear that the numerical model for this type of mooring has a very good agreement on the average dynamics of the system with a difference on the rms values lower than 20%. Nevertheless, for the extreme peaks due to snatches, it is safer to rely on the experimental results. On the other hand, for the correct operation of the system, it is preferable to avoid this condition.

Furthermore, experimental tests provided a very important indication in the mooring design for the ISWEC device. More in detail, the installation of a clump-weight showed an important improvement in the mooring dynamics. According to these results, the mooring layout is modified with respect to the one proposed in Chapter 5 and Configuration C2a is chosen as the best. This configuration, has been modeled and tested in Ansys Aqwa, according to the experimental installation. Due to the high computational time required, to test the numerical model of Configuration

C2a, a simulation of the tested conditions in the wave tank is here proposed. In particular, the worst condition has been tested, which corresponds to the 10 years wave.

Figure 6.24 shows time series samples of numerical model and experimental results near the highest peak of tension measured at the wave tank. Surge motion, mooring force and pitch motion are plotted. In the numerical model has been used the acquired time series of the wave height as input.

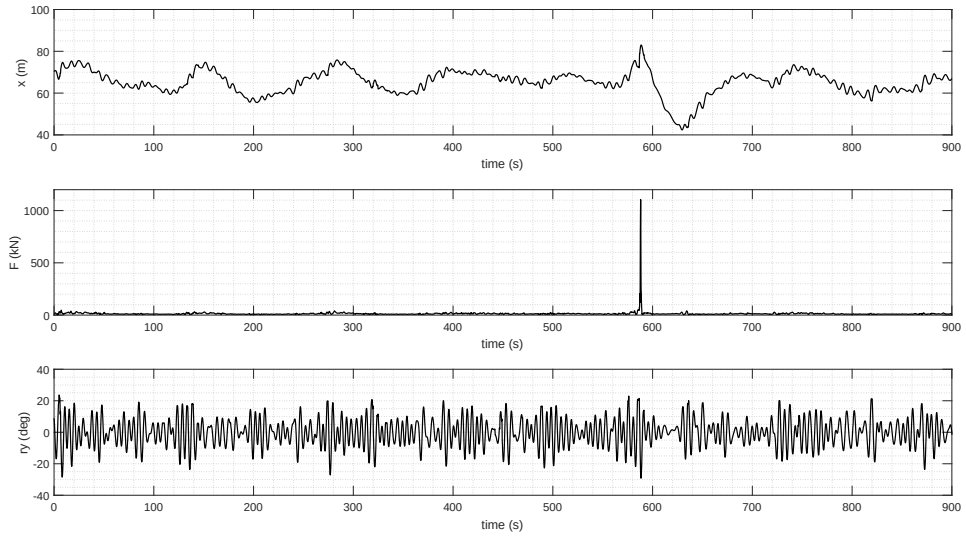

(a) Experimental results - time series samples.

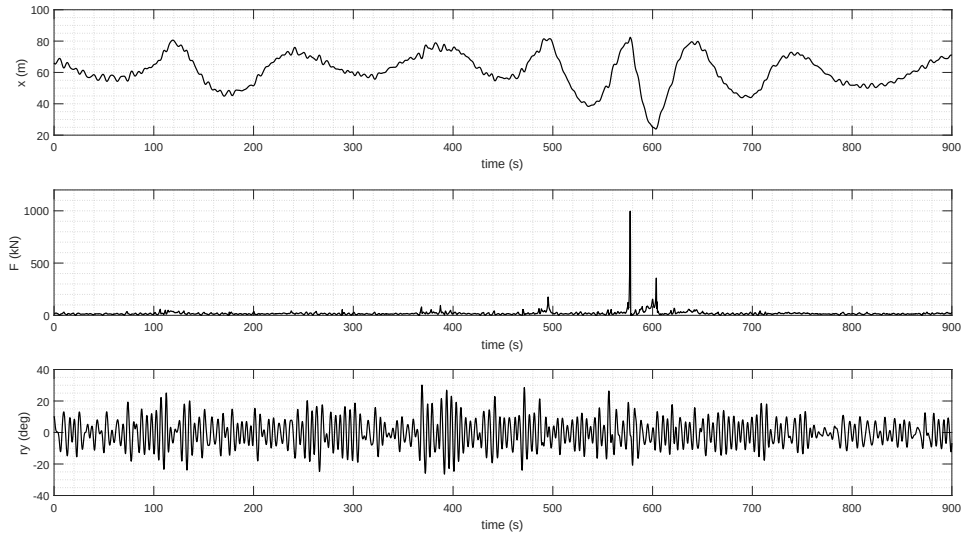

(b) Numerical model - time series samples.

Fig. 6.24 Experimental and Numerical model Comparison. 10 years wave - Configuration C2a

It is due to notice that no absolute reference frame was present for the surge experimental data, thus it was not possible to reproduce numerically the exact starting position of the device. Furthermore, during the experiments, wave height was measured ahead the device, as described in previous chapters. Due to these differences, it is not possible to superimpose the time series correctly and compare them at each time. Nevertheless, a comparison of the dynamics is still possible and very useful. From Figure 6.24, it is possible to observe that the overall modeled dynamic of the device is in good agreement with the experiments. In particular, the surge motion is enhanced by the numerical model. This is due to the absence of a drag contribution on the device in surge. Nevertheless, the summary result reported in Table 6.14 show a good agreement in the rms values. This result is confirmed also for pitch motion and the mooring loads.

Table 6.14 Experimental vs Numerical results. 10 years wave - Configuration C2a.

Property	Units	Numerical		Experiments	
		rms	*max*	*rms*	*max*
Surge	(m)	63	83	65	83
Pitch	(deg)	8.6	30	8.6	25
Mooring Force	(kN)	35	996	30	1104

The mooring force time history shows an identical behavior to the experimental one. It is possible to observe that for almost all the duration of the simulation, the mooring loads are very low and a single isolated peak is present. As for the Configuration C1 results, the numerical model shows to be reliable for most of the conditions. This is not the case for the extreme peak. However, for this simulation the extreme values are very similar between each others, with a difference equal to 10% only.

These results confirm the good reliability of the numerical model to be used as a design tool for the mooring system with an opportune safety factor.

Layout improvement and final design

To completely avoid snatches on the mooring lines and consequently on the rotating joint a further improvement of the layout is considered, referring to the results obtained from the experimental campaign.

At the expense of the mooring footprint and to ensure the survival of the mooring system, an efficient and economical solution to avoid snatches, is to extend the length of the bottom catenary sections. In this way, the stiffness of the mooring system results unchanged in the operational conditions. Moreover, a highest length of chain is laid on the seabed, reducing at minimum the risk of snatches. As a matter of fact, it has been observed during the experimental campaign that the clump-weight helps the device to have a reduced drift motion in surge and a faster recall to the slack condition. The experiments have been performed in the worst case conditions, highlighting that snatches occur very rarely and consequently to waves trains that lead the device to the maximum drift extension. Increasing the length of the catenaries on the bottom should act positively in two directions: first, a very high drift value is needed to reach the taut condition. As already discussed, this is very unlikely to happen, considering the average values of the surge motions. Secondly, the weight of the catenary on the bottom increase the recall force when it starts to be suspended by the device, restraining its motion and avoiding snatches. Eventually, this solution avoids vertical loads on the anchors, reducing the cost of foundations.

Referring to the properties of the mooring configurations reported in Tables 6.1 and 6.2 and the C2a scheme reported in Figure 6.1, the only modification is the anchoring radius R_1 that is changed from 60 m to 100 m and consequently the length L_1 of the catenary sections connected to the anchors that is increased from 65 m to 105 m according to the anchoring radius.

The analysis of the modified mooring system is performed on 10 different sea states characterized by the same spectral properties of the 10 years wave. The 10 years wave is chosen because it was previously demonstrated that corresponds to the most severe load condition for the mooring system.

Table 6.15 reports the summary results of the numerical analysis. It results immediate to notice that the maxima values of mooring loads are significantly lower with respect to the previous layout. In particular, a reduction of the 60% is obtained,

comparing the absolute maximum peak of tension with the respective one for the previous configuration C2a (see Table 6.14).

Table 6.15 Configuration C2a improved. 10 years wave - Numerical model significant results

Test ID	Mooring Tension		Surge	Pitch
	max (kN)	*rms* (kN)	*max* (m)	*max* (deg)
IW11b	325.0	18.3	28.8	28.1
IW12b	347.8	19.3	28.1	28.7
IW13b	302.4	18.7	29.7	29.0
IW14b	378.1	19.7	30.6	30.9
IW15b	279.8	18.1	27.5	27.1
IW16b	355.4	18.3	26.6	29.3
IW17b	294.8	17.9	26.9	26.8
IW18b	332.6	17.7	29.1	27.4
IW19b	362.8	19.5	26.3	31.9
IW20b	340.2	20.3	29.8	30.3

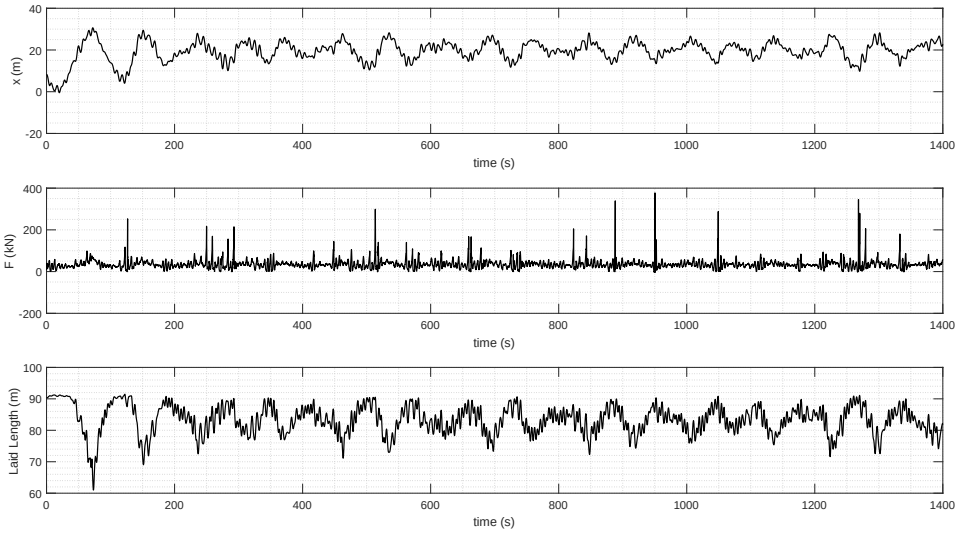

Fig. 6.25 10 years wave - Time series samples

For a clear visualization, time series samples are reported in Figure 6.25, for the worst load case condition, corresponding to IW14b. Surge motion is chosen as a clear indicator of the mooring system behavior, hence it is shown together with the mooring loads and the laid length of the bottom catenary section in wave direction. First, it is possible to notice the peak loads reduction. More in detail, in this case the peaks are present in correspondence of the pitch motion troughs and due to the clump-weight action when the device is pushed away by waves action. Differently from the snatches previously observed, these peaks are significantly lower and can be considered acceptable from the design point of view.

In conclusion, the mooring layout with jumper and clump-weight (lazy-wave) demonstrated to be a suitable solution for the ISWEC device. All the requirements have been satisfied. The experimental campaign has been useful to validate the numerical model in operational conditions and to highlight the presence of snatches. Despite the survival of the system can be guaranteed if also snatches occur, it is preferable to avoid these isolated events. Numerical model has been used to test the modified layout of the mooring system, obtaining important improvements on the mooring load reduction. Since the load peaks are isolated events, their probability is very low, nevertheless, for safety reasons, they must be considered to determine the design load value. Therefore, on the basis of the obtained result, it is decided to take into account the maxima observed values, guaranteeing a conservative approach.

The mooring design is performed considering an *Ultimate Limit State* (ULS) to ensure that the individual mooring lines have adequate strength to withstand the load effects imposed by extreme environmental actions [50]. To take into account the differences of the numerical model with the experiments, and according to the DNV offshore design standards [50], a safety factor must be applied to the dynamic analysis analysis obtained with numerical modeling. The safety factor should be greater or equal to **1.67** with respect to the minimum breaking load of all components of the mooring system. Considering the results presented in Table 6.15 a value of **400 kN** can be considered conservative as design load. Applying a safety factor of **2**, the minimum breaking load for all the component is obtained:

$$MBL = (MaxLoad) \times (SafetyFactor) = 400 \times 2 = 800\ kN \tag{6.3}$$

The design value is significantly lower than the proof load of the selected mooring chains and must be satisfied for the selection of the rotating joint.

Combination of waves and currents

As stated in section 5.3, the currents values at the Pantelleria installation site are negligible in comparison to the extreme wave conditions. Nevertheless, an ultimate test case is conducted with the numerical model, considering the combination of waves and currents. In particular, a conservative value of **1.5 m/s** is considered for the current velocity. This value is obtained from the DNV standard [50] and corresponds to the 10 years current speed for the North Sea sites. The current profile is considered to be constant with depth and the most adverse direction, coincident with the incident wave direction, has been applied.

Table 6.16 Configuration C2a improved. 10 years wave and 10 years current - Numerical model significant results

Test ID	Mooring Tension		Surge	Pitch
	max (kN)	*rms* (kN)	*max* (m)	*max* (deg)
IW11b	348.5	30.1	29.1	29.8
IW12b	377.2	28.4	29.9	31.5
IW13b	328.0	28.1	30.6	30.8
IW14b	409.9	30.6	31.9	35.4
IW15b	319.8	29.1	29.3	34.6
IW16b	369.1	27.5	28.4	32.7
IW17b	344.4	27.8	28.7	33.4
IW18b	368.7	29.4	30.3	30.2
IW19b	393.6	30.0	28.1	35.7
IW20b	319.4	31.6	27.8	33.9

To calculate the current drag force, the Morison's equation has been applied [6, 42, 57]:

$$F_C = \frac{1}{2}\rho_w C_D A^2 |v| v \tag{6.4}$$

where the characteristic surface A is the immerse surface of the device in the current direction. For the sake of simplicity and to be conservative, a rectangular surface has been considered, if also the ISWEC keel is rounded. The drag coefficient C_D is set equal to 0.5 and it has been obtained from DNV standard shapes tables, reported in [49]. The analysis has been performed using the same 10 years sea states as for the final design simulations.

For the sake of completeness, time-series samples of the worst case are shown in Figure 6.26. The surge drift motion experiences a slight increase, due to the current drag contribution. In general, analogous behavior to the test cases without current is obtained.

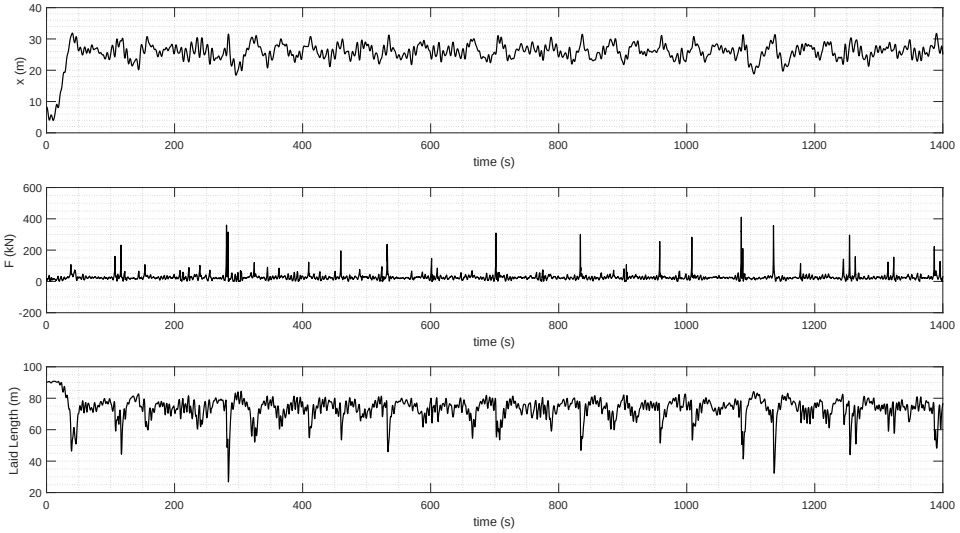

Fig. 6.26 10 years wave and 10 years current - Time series samples

Results of the analysis are reported in Table 6.16. It can be observed that, in average, the load maxima increase of the 9% but the identified Minimum Breaking Load can be still assumed valid. More in detail, referring to the maximum mooring load in presence of current, which is equal to 410 kN, the design safety factor, assuming the MBL constant, results equal to 1.95 which is still higher than the minimum required by standards.

Chapter 7

Conclusions

The objective of this thesis is to improve the design and development tools and methodologies for a floating wave energy converter. The work is focused on the ISWEC technology that can be considered as a representative example of floating WEC. Based on the development stage of this technology, critical aspects have been identified, that needed further investigations and research activities. The main goals of this research activity are the development of the non-linear hydrodynamic model of the ISWEC device, with the introduction of viscous forces and the design of the mooring system. In the package of design and development tools, the main requirements are found to be the low-computational cost and the tools flexibility. These requirement have been pursued identifying a generalized approach that can be used for different WECs and analyses.

Several research activities have been carried out by the candidate during the PhD program, concerning the upgrade and development of wave energy technologies. Both numerical and experimental activities were performed, with different outcomes: development and upgrade of numerical models with high fidelity tools; design, management and execution of experimental campaigns, from the prototype and setup design, the operation activities, analysis and elaboration of experimental data; validation of the numerical methodologies that demonstrate the reliability of the developed tools.

The starting point of the research activity was the state of the art linear hydrodynamic model of the ISWEC device. This model demonstrated its limitation during previous experimental campaigns in model scale, and first data output obtained

from the deployment of the full scale prototype, installed at Pantelleria. The need of more reliable tools was highlighted. A detailed hydrodynamic analysis of the ISWEC device has been carried out, focusing on the possible effects of the non-linear contributions. The drift forces have been introduced in the time domain wave-to-wire model. An unconventional approach was identified and proposed for the numerical modelling of the viscous-forces. A numerical wave tank has been modeled with the use of a high fidelity commercial software for CFD analyses. The wave tank has been tuned and optimized, focusing on the minimization of computational cost and the mesh optimization for wave-floater interaction.

A first campaign analysis was performed to validate the hydrodynamic model and upgrades, identifying the operational areas where non-linearities become important. A general agreement has been found and the suitability of the model was demonstrated for the ISWEC.

In the second part, the attention was focused on the mooring system. Before the work presented in this thesis, the lack of design methodology and performances evaluation characterized the mooring problem for the ISWEC device. Starting from the ISWEC technology requirements a mooring layout has been proposed with the intention to develop a system suitable for different installation sites and completely independent from the wave directions. The author highlighted as main objective the possibility to use, where possible, standardized components and materials to enhance the reliability of the system. A catenary slack mooring system has been designed to meet all the requirements. Critical issues have been highlighted and solutions have been approached.

A second experimental campaign was performed to study in detail the survivability of the system. Extreme irregular waves were tested with different mooring configurations, obtaining a large data set for mooring loads and hydrodynamics analysis. Experimental data were successfully used to validate the numerical methodologies. Furthermore, from this experience, indications on mooring system improvements were obtained and applied to the numerical design tool. Eventually, a successful design has been achieved, minimizing mooring loads and customized components.

The main scope of this thesis was to cover most of the aspects that were still not well defined and organized within the ISWEC project. Starting from the simplified numerical model, the author participated to all the different phases of the project and worked on both numerical and experimental development. The participation to the

deployment of the first device highlighted some of the fundamental aspects of the WECs design.

The hydrodynamics of a WEC is its main driver to be an efficient and sustainable machine. A very good design of the hull geometry and shape is not always the best solution in terms of the overall performance of the WEC: in particular, a complex shape that maximizes the energy input would be probably difficult to control. Even more difficult would be the inner layout of the subsystems which constitute the core of the power conversion technology. Nonetheless, unconventional geometries can cause a substantial increase in cost of desing and construction. WECs are complicated machines that operate in extreme environment. Simplification is the way of their development.

Waave Energy technology needs to go on the market to reach visibility and gain the possibility to play a role in the future of energy. Commercialization is hard to reach in the offshore industry for new and off standard products. To help and drive the technology towards the success, it must be exploited the actual experience of the offshore industry: the number of off standard components must be minimized, using the confidence of the market as a driver for deployment of new prototypes.

Experimentation is the key of the design of a WEC. Mooring systems are complex to be modeled and simulated numerically. Physical phenomena in fluid dynamics are often hard to understand if studied one at the time. In wave energy, different phenomena experience continuous interactions at different scales. The design of a mooring system can not be performed regardless of physical experimentation.

The experience in Napoli demonstrated that controlled environments can also be surprising, and highlight phenomena that are almost impossible to take into account in the numerical design approach.

The scalability of the generalization of the results experienced good and encouraging improvements with this work, but still all the hypotheses made need to be verified on a full scale device in real sea conditions. The work here presented was once more essential to develop a design approach for full scale devices, highlighting all the aspects that need to be monitored and all the properties that need to be measured to have a whole picture of a WEC behavior.

This work has been carried out within an integrated research activity that covers several aspects of the wave energy technology development. The research has been

conducted in collaboration with Wave for Energy srl and different results could not be included in this thesis, for multiple reasons: some results about ongoing research activity are still partial, more are covered by industrial property and others are covered by intellectual property rights and part of patent application. On the basis of these results and the work presented in this thesis, it is possible to outline future research activities for further developments.

The hydrodynamic modelling tools presented in this thesis can be used for specific analysis of non-linear problems involved in the wave-floater interactions, resorting to the high fidelity CFD methods. In particular, the numerical wave tank can be used to reproduce experimental tests or as a valid alternative, in order to reduce costs and with no need to scale down the device. Extreme wave tests can be simulated to investigate the so called green water loads and optimize the floater structure. Drag forces can be identified with higher reliability with respect to simplified shape coefficients. The investigation of interactions between array of WECs can also be carried out, looking forward to a commercial stage of this technology.

The mooring design methodology can be used to explore new mooring layouts and alternative solution to the proposed traditional materials. The latter step cannot be carried out without a detailed experimental campaign to validate the numerical tools for new materials. Also for the mooring system, the interaction between different devices in an array configuration can be tested. For this purpose, a first experimental campaign has been carried out during the writing time period of this thesis. The presented methodology and results have been used to design the mooring systems for this experimental campaign, but data post-processing is still an ongoing activity.

One step more has been done towards the future of blue energy. The results obtained through this work, will be used in the next future for the design and deployment of a new ISWEC prototype, fully equipped with sensors to monitor and analyze each subsystem of the full scale device: from mooring loads, to hydrodynamic interaction and power generation.

References

[1] adn E Giorcelli, G. M. [2007], Mathematical model of a energy converter from sea waves, *in* 'World Energy Congress'.

[2] Airy, G. [1849], *Tides and Waves*, J.J. Griffin.

[3] *Akamina capacitive wave height gauge* [2016], http://www.akamina.com/AWP-24-3.html. Accessed: January 2018.

[4] Alves, M. [2016], Wave-to-wire modelling of WECs, *in* 'Handbook of Ocean Wave Energy', Springer International Publishing, pp. 261–287.

[5] ANSYS, I. [2017*a*], *ANSYS CFX-Solver Theory Guide*.

[6] ANSYS, I. [2017*b*], *Aqwa Theory Manual*.

[7] API [2005], 'Design and analysis of stationkeeping systems for floating structures'. (API RP 2SK), American Petroleum Institute.

[8] Babarit, A., Guglielmi, M. and Clément, A. H. [2009], 'Declutching control of a wave energy converter', *Ocean Engineering* **36**(12-13), 1015–1024.

[9] Babarit, A., Mouslim, H., Clement, A. and Laporte-Weywada, P. [2009], On the numerical modelling of the non linear behaviour of a wave energy converter, *in* 'Volume 4: Ocean Engineering; Ocean Renewable Energy; Ocean Space Utilization, Parts A and B', ASME.

[10] Barltrop, N. D. P. [1998], *Floating Structures: A Guide for Design and Analysis*, Oilfield Pubns Inc.

[11] *Baumer ultrasonic wave height gauge* [2017], https://www.baumer.com. Accessed: January 2018.

[12] Begovic, E., Bertorello, C. and Orsic, J. P. [2013], Roll damping coefficients assessment and comparison for round bilge and hard chine hullforms, *in* 'Volume 9: Odd M. Faltinsen Honoring Symposium on Marine Hydrodynamics', ASME.

[13] Begovic, E., Day, A. and Incecik, A. [2017], 'An experimental study of hull girder loads on an intact and damaged naval ship', *Ocean Engineering* **133**, 47–65.

[14] Begovic, E., Day, A., Incecik, A., Mancini, S. and Pizzirusso, D. [2015], Roll damping assessment of intact and damaged ship by cfd and efd methods, *in* 'Proceedings of the 12th International Conference on the Stability of Ships and Ocean Vehicles'.

[15] Begovic, E., Mancini, S., Day, A. H. and Incecik, A. [2016], Applicability of cfd methods for roll damping determination of intact and damaged ship, *in* 'High Performance Scientific Computing Using Distributed Infrastructures', WORLD SCIENTIFIC, pp. 343–359.

[16] Bencivenga, M., Nardone, G., Ruggiero, F. and Calore, D. [2012], The italian data buoy network (RON), *in* 'Advances in Fluid Mechanics IX', WIT Press.

[17] Bentley [2017], *Reference manual for MOSES*.

[18] Bergdahl, L. [2016], Mooring design for WECs, *in* 'Handbook of Ocean Wave Energy', Springer International Publishing, pp. 159–202.

[19] Bhinder, M., Babarit, A., Gentaz, L. and Ferrant, P. [2011], Assessment of viscous damping via 3d-cfd modelling of a floating wave energy device, *in* 'Proceedings of the 9th European Wave and Tidal Energy Conference'.

[20] Bhinder, M., Karimirad, M., Weller, S., Debruyne, Y., GuÃ©rinel, M. and Sheng, W. [2015], Modelling mooring line non-linearities (material and geometric effects) for a wave energy converter using aqwa, sima and orcaflex, *in* 'Proceedings of the 11th European Wave and Tidal Energy Conference'.

[21] Bhinder, M., Mingham, C., Causon, D., Rahmati, M., Addigis, G. and Chaplin, R. [2009], Numerical and experimental study of a surging point absorber wave energy converter, *in* 'Proceedings of the 8th European Wave and Tidal Energy Conference'.

[22] Bonfanti, M., Sirigu, S., Bracco, G., Passione, B., Vissio, G., Pozzi, N. and Mattiazzo, G. [2017], Application of a passive control technique to the iswec, *in* 'Proceedings of the 12th European Wave and Tidal Energy Conference'.

[23] BP [2017], Statistical review of world energy june 2017, Technical report, British Petroleum.

[24] Bracco, G. [2010], ISWEC: a gyroscopic wave energy converter, PhD thesis, Politecnico di Torino.

[25] Bracco, G., Bonfanti, M., Passione, B., Pozzi, N., Sirigu, S. and Mattiazzo, G. [2017], Integration of renewable energy to power public transport at the island of pantelleria, *in* 'Proceedings of Offshore Energy and Storage 2017'.

[26] Bracco, G., Cagninei, A., Casassa, M., Giorcelli, E., Giorgi, G., Mattiazzo, G., Passione, B., Poggi, D., Raffero, M. and Vissio, G. [2014], 'Modeling and optimization of a wave energy converter using ANSYS AQWA', In: ANSYS User Group Meeting. pp. 79-86.

[27] Bracco, G., Cagninei, A., Giorcelli, E., Mattiazzo, G., Poggi, D. and Raffero, M. [2016], 'Experimental validation of the ISWEC wave to PTO model', *Ocean Engineering* **120**, 40–51.

[28] Bracco, G., Casassa, M., Giorcelli, E., Giorgi, G., Mattiazzo, G., Passione, B., Raffero, M. and Vissio, G. [2015], *Application of sub-optimal control techniques to a gyroscopic Wave Energy Converter*, Renewable Energies Offshore, Taylor & Francis Group, London (UK), pp. 265–269.
URL: *https://dx.doi.org/10.1201/b18973-39*

[29] Bracco, G., Casassa, M., Giorcelli, E., Mattiazzo, G., Passione, B., Raffero, M. and Vissio, G. [2015], 'Stochastic control applied to the iswec wave energy system', *Energia, Ambiente e Innovazione* .

[30] Bracco, G., Giorcelli, E., Giorgi, G., Mattiazzo, G., Passione, B., Raffero, M. and Vissio, G. [2015], Performance assessment of the full scale ISWEC system, *in* 'Industrial Technology (ICIT), 2015 IEEE International Conference', Seville (Spain), pp. 2499–2505.
URL: *https://dx.doi.org/10.1109/ICIT.2015.7125466*

[31] Bracco, G., Giorcelli, E. and Mattiazzo, G. [2008], One degree of freedom gyroscopic mechanism for wave energy converters, *in* 'Volume 2: 32nd Mechanisms and Robotics Conference, Parts A and B', ASME.

[32] Bracco, G., Giorcelli, E. and Mattiazzo, G. [2011], 'ISWEC: A gyroscopic mechanism for wave power exploitation', *Mechanism and Machine Theory* **46**(10), 1411–1424.

[33] Bracco, G., Giorcelli, E., Mattiazzo, G., Orlando, V. and Raffero, M. [2015], 'Hardware-in-the-loop test rig for the ISWEC wave energy system', *Mechatronics* **25**, 11–17.

[34] Bracco, G., Giorcelli, E., Mattiazzo, G., Passione, B., Prudentino, E., Raffero, M. and Vissio, G. [2015], Application of linear model predictive control to the ISWEC, *in* G. Soares, ed., 'Renewable Energies Offshore', Taylor & Francis Group, pp. 257–264.
URL: *https://doi.org/10.1201/b18973-38*

[35] Bracco, G., Giorcelli, E., Mattiazzo, G., Pastorelli, M. and Taylor, J. [2009], ISWEC: Design of a prototype model with gyroscope, *in* '2009 International Conference on Clean Electrical Power', IEEE.

[36] CarbonTrust [2011], Accelerating marine energy: The potential for cost reduction - insights from the carbon trust marine energy accelerator, Technical report, Carbon Trust.

[37] *Carnegie CETO* [2018], https://www.carnegiece.com/wave/what-is-ceto/. Accessed: May 2018.

[38] Chakrabarti, S. [1987], *Hydrodynamics of Offshore Structures*, WIT Press / Computational Mechanics.

[39] Chakrabarti, S. K. [1994], *Offshore Structure Modeling (Series in Machine Perception and Artifical Intelligence)*, World Scientific Publishing Company.

[40] Cummins, W. E. [1962], The impulse response function and ship motions, Technical Report 1661, Department of the Navy, David Taylor model basin, Washington DC.

[41] Davidson, J., Giorgi, S. and Ringwood, J. [2014], Numerical wave tank identification of nonlinear discrete time hydrodynamic models, *in* 'Proceedings of the 1st International Conference on Renewable Energies Offshore'.

[42] Davidson, J. and Ringwood, J. V. [2017], 'Mathematical modelling of mooring systems for wave energy converters—a review', *Energies* **10**(12), 666.

[43] de Andres, A., MacGillivray, A., Roberts, O., Guanche, R. and Jeffrey, H. [2017], 'Beyond LCOE: A study of ocean energy technology development and deployment attractiveness', *Sustainable Energy Technologies and Assessments* **19**, 1–16.

[44] de Andres, A., Maillet, J., Todalshaug, J. H., MÃ¶ller, P., Bould, D. and Jeffrey, H. [2016], 'Techno-economic related metrics for a wave energy converters feasibility assessment', *Sustainability* **8**(11), 1109.

[45] de Andres, A., Medina-Lopez, E., Crooks, D., Roberts, O. and Jeffrey, H. [2017], 'On the reversed LCOE calculation: Design constraints for wave energy commercialization', *International Journal of Marine Energy* **18**, 88–108.

[46] de O. Falcão, A. F. [2007], 'Modelling and control of oscillating-body wave energy converters with hydraulic power take-off and gas accumulator', *Ocean Engineering* **34**(14-15), 2021–2032.

[47] de O. Falcão, A. F. [2010], 'Wave energy utilization: A review of the technologies', *Renewable and Sustainable Energy Reviews* **14**(3), 899–918.

[48] DNV [2010], 'Global performance analysis of deepwater floating structures'.

[49] DNV [2014], 'Environmental conditions and environmental loads'.

[50] DNV [2015], 'Offshore standard - position mooring'. (DNVGL-OS-E301), Det Norske Veritas.

[51] Drew, B., Plummer, A. R. and Sahinkaya, M. N. [2009], 'A review of wave energy converter technology', *Proceedings of the Institution of Mechanical Engineers, Part A: Journal of Power and Energy* **223**(8), 887–902.

[52] Elhanafi, A. [2016], 'Prediction of regular wave loads on a fixed offshore oscillating water column-wave energy converter using cfd', *Journal of Ocean Engineering and Science* **1**(4), 268–283.

[53] EMEC [2009], Tank testing of wave energy conversion systems, Technical report, The European Marine Energy Centre.

[54] ExxonMobil [2018], 2018 outlook for energy: A view to 2040, Technical report, ExxonMobil.

[55] Falnes, J. [2002], *Ocean Waves and Oscillating Systems: Linear Interactions Including Wave-Energy Extraction*, Cambridge University Press.

[56] Falnes, J. and Hals, J. [2011], 'Heaving buoys, point absorbers and arrays', *Philosophical Transactions of the Royal Society A: Mathematical, Physical and Engineering Sciences* **370**(1959), 246–277.

[57] Faltinsen, O. M. [1993], *Sea Loads on Ship and Offshore Structures*, Cambridge University Press.

[58] Fenton, J. D. [1999], Numerical methods for nonlinear waves, *in* 'Advances in Coastal and Ocean Engineering', WORLD SCIENTIFIC, pp. 241–324.

[59] Ferziger, J. H. and Perić, M. [2002], *Computational Methods for Fluid Dynamics*, Springer Berlin Heidelberg.

[60] Fitzgerald, C. [2016], Nonlinear potential flow models, *in* 'Numerical Modelling of Wave Energy Converters', Elsevier, pp. 83–104.

[61] Fitzgerald, J. [2009], Position Mooring of Wave Energy Converters, PhD thesis, Chalmers University of Technology.

[62] Fitzgerald, J. and Bergdahl, L. [2008], 'Including moorings in the assessment of a generic offshore wave energy converter: A frequency domain approach', *Marine Structures* **21**(1), 23–46.

[63] Flory, J. F., Banfield, S. J., Ridge, I. M., Yeats, B., Mackay, T., Wang, P., Hunter, T., Johanning, L., Herduin, M. and Foxton, P. [2016], Mooring systems for marine energy converters, *in* 'OCEANS 2016 MTS/IEEE Monterey', IEEE.

[64] Folley, M., ed. [2016], *Numerical Modelling of Wave Energy Converters: State-of-the-Art Techniques for Single Devices and Arrays*, Academic Press.

[65] Fossen, T. I. [2011], *Handbook of Marine Craft Hydrodynamics and Motion Control*, John Wiley & Sons, Ltd.

[66] Futek [2017*a*], *Analog Amplifier with Voltage Output*.

[67] Futek [2017*b*], *Submersible Jr. Miniature S-Beam Load Cell*.

[68] Gao, Z. and Moan, T. [2009], Mooring system analysis of multiple wave energy converters in a farm configuration, *in* 'Proceedings of the 8th European Wave and Tidal Energy Conference'.

[69] Giorgi, G. and Ringwood, J. [2017*a*], Consistency of viscous drag identification tests for wave energy applications, *in* 'Proceedings of the 12th European Wave and Tidal Energy Conference'.

[70] Giorgi, G. and Ringwood, J. [2017*b*], Importance of nonlinear wave representation for nonlinear froude-krylov force calculations for wave energy devices, *in* 'Proceedings of the 12th European Wave and Tidal Energy Conference'.

[71] Giorgi, G. and Ringwood, J. V. [2016], 'Computationally efficient nonlinear froude–krylov force calculations for heaving axisymmetric wave energy point absorbers', *Journal of Ocean Engineering and Marine Energy* **3**(1), 21–33.

[72] Giorgi, G. and Ringwood, J. V. [2017*c*], 'Nonlinear froude-krylov and viscous drag representations for wave energy converters in the computation/fidelity continuum', *Ocean Engineering* **141**, 164–175.

[73] *Google Maps* [2018], https://maps.google.it/. Accessed: January 2018.

[74] Greenshields, C. [2017], *OpenFOAM User Guide*, OpenFOAM Foundation.

[75] Gunn, K. and Stock-Williams, C. [2012], 'Quantifying the global wave power resource', *Renewable Energy* **44**, 296–304.

[76] Guo, B. and Patton, R. J. [2017], 'Non-linear viscous and friction effects on a heaving point absorber dynamics and latching control performance', *IFAC-PapersOnLine* **50**(1), 15657–15662.

[77] Guzzo, A. D., Tommaso, F. D., Renzi, I., Gaggiotti, F. and Bruschi, R. [2015], Random decrement method: ship roll damping identification based on response in a seaway, *in* 'NAV2015 - International Conference on Ships and Shipping research'.

[78] Hajiarab, M. [2013], Roll Damping Prediction of a Free Floating Barge, PhD thesis, Newcastle University.

[79] Hall, M., Vissio, G. and Passione, B. [2015], Expanding iswec modelling with a lumped-mass mooring line model, *in* 'Proceedings of the 11th European Wave and Tidal Energy Conference'.

[80] Han, S. L. and Kinoshita, T. [2012], 'Stochastic inverse identification of nonlinear roll damping moment of a ship moving at nonzero-forward speeds', *Mathematical Problems in Engineering* **2012**, 1–22.

[81] Handschel, S., Feder, D. and Abel-Maksoud, M. [2015], Estimation of ship roll damping - a comparison of the decay and the harmonic excited roll motion technique for a post panamax container ship, *in* 'Proceedings of the 12th International Conference on the Stability of Ships and Ocean Vehicles'.

[82] Harnois, V. [2014], Analysis of Highly Dynamic Mooring Systems: Peak Mooring Loads in Realistic Sea Conditions., PhD thesis, University of Exeter.

[83] Harnois, V., Weller, S., Johanning, L., Thies, P., Boulluec, M. L., Roux, D. L., Soulé, V. and Ohana, J. [2015], 'Numerical model validation for mooring systems: Method and application for wave energy converters', *Renewable Energy* **75**, 869–887.

[84] Harris, R. E., Johanning, L. and Wolfram, J. [2004], Mooring systems for wave energy converters: A review of design issues and choices, *in* 'Proceedings of the 3rd International Conference on Marine Renewable Energy'.

[85] Hedges, T. S. [1995], 'Regions of validity of analytical wave theories', *Proceedings of the Institution of Civil Engineers - Water Maritime and Energy* **112**(2), 111–114.

[86] Hermans, A. J. [1999], 'Low-frequency second-order wave-drift forces and damping', *Journal of Engineering Mathematics* **35**(1/2), 181–198.
URL: *https://dx.doi.org/10.1023/a:1004323229079*

[87] *HPC@POLITO* [2018], http://www.hpc.polito.it. Accessed: January 2018.

[88] IEA [2017], Key world energy statistics, Technical report, International Energy Agency.

[89] IEA [2018], *World Energy Outlook 2017*, Organization For Economic Co-Operation & Development.

[90] Ingram, D., Smith, G., Bittencourt-Ferreira, C. and Smith, H. [2011], *Protocols for the Equitable Assessment of Marine Energy Converters (Equimar)*, Edinburgh University, School of Engineering.

[91] IRENA [2017*a*], Accelerating the energy transition through innovation, Technical report, International Renewable Energy Agency.

[92] IRENA [2017*b*], Rethinking energy 2017, Technical report, International Renewable Energy Agency.

[93] IRENA [2018], Renewable capacity statistics 2018, Technical report, International Renewable Energy Agency.

[94] Italmet [2014], 'Catalogo generale'.

[95] ITTC [2011*a*], Numerical estimation of roll damping, Technical report, International Towing Tank Conference.

[96] ITTC [2011*b*], Practical guidelines for ship cfd applications, Technical report, International Towing Tank Conference.

[97] Jang, T., Choi, H. S. and Han, S. [2009], 'A new method for detecting non-linear damping and restoring forces in non-linear oscillation systems from transient data', *International Journal of Non-Linear Mechanics* **44**(7), 801–808.

[98] Johanning, L., Smith, G. H. and Wolfram, J. [2005], 'Towards design standards for wec moorings'.

[99] Johanning, L., Smith, G. H. and Wolfram, J. [2006], 'Mooring design approach for wave energy converters', *Proceedings of the Institution of Mechanical Engineers, Part M: Journal of Engineering for the Maritime Environment* **220**(4), 159–174.

[100] JournÃ¨e, J. M. J. and Massie, W. W. [2001], *Offshore Hydromechanics*, first edn, Delft University of Technology.

[101] JRC [2016], Jrc ocean energy status report - 2016 edition, Technical report, JRC Science for Policy Report.

[102] Karimirad, M., Koushan, K., Weller, S., Hardwick, J. and Johanning, L. [2015], Applicability of offshore mooring and foundation technologies for marine renewable energy (MRE) device arrays, *in* 'Renewable Energies Offshore', CRC Press, pp. 905–912.

[103] Khan, N., Kalair, A., Abas, N. and Haider, A. [2017], 'Review of ocean tidal, wave and thermal energy technologies', *Renewable and Sustainable Energy Reviews* **72**, 590–604.

[104] Kim, J., Lakshmynarayanana, P. and Temarel, P. [2014], Added mass and damping coefficients for a uniform flexible barge using vof, *in* 'Proceedings of the 11th International Conference on Hydrodynamics'.

[105] *La vasca navale* [2014], http://www.dii.unina.it/index.php/en/la-vasca-navale. Accessed: January 2018.

[106] *La vasca navale* [2018], http://www.nortek.no/en/products/wave-systems/awac. Accessed: January 2018.

[107] Lawson, M., Hu, Y., Nelessen, A., ruehl, K. and Michelen, C. [2014], Implementing nonlinear buoyancy and excitation forces in the wec-sim wave energy converter modeling tool, *in* 'Proceedings of the 33rd International Conference on Ocean, Offshore and Artic Engineering (OMAE2014)'.

[108] Lewandowski, E. [2011], Comparison of some analysis methods for ship roll decay data, *in* 'Proceedings of the 12th International Ship Stability Workshop'.

[109] Lewandowski, E. M. [2003], *The Dynamics of Marine Craft: Maneuvering and Seakeeping*, World Scientific Pub Co Inc.

[110] Li, Y. and Yu, Y.-H. [2012], 'A synthesis of numerical methods for modeling wave energy converter-point absorbers', *Renewable and Sustainable Energy Reviews* **16**(6), 4352–4364.

[111] Liu, M., Liu, H., Zheng, X., Chen, H., Wang, L. and Zhang, L. [2017], 'Nonlinear PTO effect on performance of vertical axisymmetric wave energy converter using semi-analytical method', *Polish Maritime Research* **24**(s3).

[112] Longo, S. [2011], *Analisi Dimensionale e Modellistica Fisica: Principi e applicazioni alle Scienze Ingegneristiche (UNITEXT) (Italian Edition)*, Springer.

[113] López, I., Andreu, J., Ceballos, S., de Alegría, I. M. and Kortabarria, I. [2013], 'Review of wave energy technologies and the necessary power-equipment', *Renewable and Sustainable Energy Reviews* **27**, 413–434.

[114] Magagna, D. and Uihlein, A. [2015], 'Ocean energy development in europe: Current status and future perspectives', *International Journal of Marine Energy* **11**, 84–104.

[115] MARNET-CFD [2002], Best practice guidelines for marine applications of computational fluid dynamics, Technical report, WS Atkins Consultants.

[116] Martinelli, L., Ruol, P. and Cortellazzo, G. [2012], 'ON MOORING DESIGN OF WAVE ENERGY CONVERTERS: THE SEABREATH APPLICATION', *Coastal Engineering Proceedings* **1**(33), 3.

[117] Maruo, H. [1960], 'The drift of a body floating on waves', *Journal of Ship Research* .

[118] Mathworks [2017], *MATLAB User's Guide - Release 2017a*, The Mathworks, Inc.

[119] McCombes, T., Johnstone, C., Holmes, B., Myers, L., Bahaj, A., Heller, V., Kofoed, J., Finn, J. and Bittencourt, C. [2010], Assessment of current practice for tank testing of small marine energy devices, Technical report, EquiMar.

[120] Mingham, C., Qian, L. and Causon, D. [2016], Computational fluid dynamics (CFD) models, *in* 'Numerical Modelling of Wave Energy Converters', Elsevier, pp. 105–122.

[121] Mohammad, K., Worden, K. and Tomlinson, G. [1992], 'Direct parameter estimation for linear and non-linear structures', *Journal of Sound and Vibration* **152**(3), 471–499.

[122] Newman, J. N. [1967], 'The drift force and moment on ships in waves', *Journal of Ship Research* .

[123] Newman, J. N. [1974], Second order, slowly-variying forces on vessel in irregular waves, *in* 'International Symposium on the Dynamics of Marine Vehicles and Structures in Waves', London IME, pp. 182–186.

[124] Newman, J. N. [1977], *Marine Hydrodynamics (MIT Press)*, The MIT Press. ISBN 978-0262140263.

[125] NI [2009], *NI 9207 Datasheet*, National Instruments.

[126] NI [2015*a*], *NI 9263 Datasheet*, National Instruments.

[127] NI [2015*b*], *NI cRIO-9030 Specifications*, National Instruments.

[128] OES [2016], Annual report, 2016, Technical report, Ocean Energy Systems.

[129] Ogilvie, T. F. [1964], Recent progress toward the understnding and the prediction of ship motions, *in* 'Proceedings of the 5th Symposium on Naval Hydrodynamics', Bergen, Norway.

[130] P. Gallagher, R. Marcer, C. Berhault, C. De Jouette, H.C. Raven, L. EÃ§a, L. Broberg, C.E. Janson, Q.X. Gao, S. Toxopeus, B. Alessandrini, T. Van Terwisga, M. Hoekstra, H. Streckwall and F. Salvatore [2009], 'Best practice guidelines for the application of computational fluid dynamics in marine hydrodynamics'.

[131] Palm, J., Eskilsson, C., Paredes, G. and Bergdahl, L. [2013], Cfd simulation of a moored floating wave energy converter, *in* 'Proceedings of the 10th European Wave and Tidal Energy Conference'.

[132] Palm, J., Eskilsson, C., Paredes, G. M. and Bergdahl, L. [2016], 'Coupled mooring analysis for floating wave energy converters using CFD: Formulation and validation', *International Journal of Marine Energy* **16**, 83–99.

[133] Paredes, G. [2016], Study of Mooring Systems for Offshore Wave Energy Converters, PhD thesis, Universidade do Porto.

[134] Paredes, G. M., Bergdahl, L., Palm, J., Eskilsson, C. and Pinto, F. T. [2013], Station keeping desing for floating wave energy devices compared to offshore oil and gas platforms, *in* 'Proceedings of the 10th European Wave and Tidal Energy Conference'.

[135] Passione, B., Pozzi, N., Sirigu, S., Bracco, G., Brizzolara, S. and Mattiazzo, G. [2017], Numerical and experimental analysis of oscillating fluid tanks, *in* 'Proceedings of the 27th International Ocean and Polar Engineering Conference'.

[136] Payne, G. [2008], 'Guidance for the experimental tank testing of wave energy converters', *SuperGen Marine* .

[137] Pecher, A., Foglia, A. and Kofoed, J. [2014], 'Comparison and sensitivity investigations of a CALM and SALM type mooring system for wave energy converters', *Journal of Marine Science and Engineering* **2**(4), 93–122.

[138] Pecher, A. and Kofoed, J. P., eds [2017], *Handbook of Ocean Wave Energy*, Springer International Publishing.

[139] Penalba, M., Giorgi, G. and Ringwood, J. V. [2017], 'Mathematical modelling of wave energy converters: A review of nonlinear approaches', *Renewable and Sustainable Energy Reviews* **78**, 1188–1207.

[140] Penalba, M., Mérigaud, A., Gilloteaux, J.-C. and Ringwood, J. V. [2017], 'Influence of nonlinear froude–krylov forces on the performance of two wave energy points absorbers', *Journal of Ocean Engineering and Marine Energy* **3**(3), 209–220.

[141] Perez, T. and Fossen, T. I. [2008*a*], 'Joint identification of infinite-frequency added mass and fluid-memory models of marine structures', *Modeling, Identification and Control: A Norwegian Research Bulletin* **29**(3), 93–102.

[142] Perez, T. and Fossen, T. I. [2008*b*], 'Time- vs. frequency-domain identification of parametric radiation force models for marine structures at zero speed', *Modeling, Identification and Control: A Norwegian Research Bulletin* **29**(1), 1–19.

[143] Perez, T. and Fossen, T. I. [2009], 'A matlab toolbox for parametric identification of radiation-force models of ships and offshore structures', *Modeling, Identification and Control: A Norwegian Research Bulletin* **30**(1), 1–15.

[144] Pinkster, J. [1980], Low Frequency Second Order Wave Excitation Forces on Floating Structures, PhD thesis, TU Delft.

[145] Pozzi, N., Bracco, G., Passione, B., Sirigu, S. A., Vissio, G., Mattiazzo, G. and Sannino, G. [2017], 'Wave tank testing of a pendulum wave energy converter 1:12 scale model', *International Journal of Applied Mechanics* **09**(02), 1750024.

[146] Pozzi, N., Castino, A., Vissio, G., Passione, B., Sirigu, S., Bracco, G. and Mattiazzo, G. [2017], Experimental evaluation of different hydrodynamic modelling techniques applied to the iswec, *in* 'Proceedings of the 12th European Wave and Tidal Energy Conference'.

[147] Raffero, M. [2014], Design of a Wave Energy Converter - a case of application: ISWEC, PhD thesis, Politecnico di Torino, Italy.

[148] Raffero, M., Bracco, G., Passione, B., Vissio, G., Mattiazzo, G. and Giorcelli, E. [2015], Identification of the hydrodynamic parameters of a wave energy converter, *in* 'Proceedings of the 11th Eurpean Wave and Tidal Energy Conference'.

[149] Raffero, M., Martini, M., Passione, B., Mattiazzo, G., Giorcelli, E. and Bracco, G. [2015], 'Stochastic control of inertial sea wave energy converter', *The Scientific World Journal* **2015**, 1–14.

[150] REN21 [2017*a*], Renewables 2017 global status report, Technical report, Renewable Energy Policy Network for the 21st Century.

[151] REN21 [2017*b*], Renewables global futures reports: Great debates towards 100report, Renewable Energy Policy Network for the 21st Century.

[152] Ricci, P., Rico, A., Ruiz-Minguela, P., Boscolo, F. and Villate, J. [2012], Design, modelling and analysis of an integrated mooring system for wave energy arrays, *in* 'Proceedings of the 4th International Conference on Ocean Energy'.

[153] Salter, S. H., Taylor, J. R. M. and Caldwell, N. J. [2002], 'Power conversion mechanisms for wave energy', *Proceedings of the Institution of Mechanical Engineers, Part M: Journal of Engineering for the Maritime Environment* **216**(1), 1–27.

[154] Schmitt, P., Whittaker, T., Clabby, D. and Doherty, K. [2012], The opportunities and limitations of using cfd in the development of wave energy converters, *in* 'Marine & Offshore Renewable Energy'.

[155] Sergiienko, N., Cazzolato, B., Ding, B. and Arjomandi, M. [2016], 'An optimal arrangement of mooring lines for the three-tether submerged point-absorbing wave energy converter', *Renewable Energy* **93**, 27–37.

[156] Sergiienko, N., Rafiee, A., Cazzolato, B., Ding, B. and Arjomandi, M. [2018], 'Feasibility study of the three-tether axisymmetric wave energy converter', *Ocean Engineering* **150**, 221–233.

[157] Siemens [2017], *STAR-CCM+ User Guide*, Siemens PLM Software.

[158] Sirigu, S. A., Vissio, G., Bracco, G., Giorcelli, E., Passione, B., Raffero, M. and Mattiazzo, G. [2016], 'ISWEC design tool', *International Journal of Marine Energy* **15**, 201–213.

[159] Sirigu, S., Vissio, G., Bracco, G., Dafnakis, P., Passione, B., Pozzi, N. and Mattiazzo, G. [2017], A performance assessment methodology for floating pitching wec arrays, *in* 'Proceedings of the 12th European Wave and Tidal Energy Conference'.

[160] Stansberg, C. T., Contento, G., Hong, S. W., Irani, M., Ishida, S., Mercier, R., Wang, Y. and Wolfram, J. [2002], The specialist committee on waves: Final report and recommendations to the 23rd ittc, *in* '23rd International Towing Tank Conference', Vol. 2, The Specialist Committee on Waves, pp. 505–736.

[161] Tanizawa, K. [2000], The state of the art on numerical wave tank, *in* 'Proceedings of the 4th Osaka Colloquium on Seakeeping Performances of Ships'.

[162] Technology, S. . S. [2009], Advanced anchoring and mooring study, Technical report, Oregon Wave Energy Trust.

[163] Tetu, A., Kofoed, J., Tully, S. and Roc, T. [2014], Dtocean: Assessment of the capabilities of available tools, Technical report, Aalborg University.

[164] *The CorPower Wave Energy Converter* [2018], http://www.corpowerocean.com/corpower-technology/corpower-wave-energy-converter/. Accessed: May 2018.

[165] Thomsen, J. B., Ferri, F. and Kofoed, J. P. [2015], Assessment of current state of mooring design in the danish wave energy sector, *in* 'Proceedings of the 11th European Wave and Tidal Energy Conference'.

[166] Thomsen, J., Ferri, F. and Kofoed, J. [2016], Experimental testing of moorings for large floating wave energy converters, *in* 'Progress in Renewable Energies Offshore', CRC Press.

[167] Thomsen, J., Ferri, F. and Kofoed, J. [2017*a*], 'Screening of available tools for dynamic mooring analysis of wave energy converters', *Energies* **10**(12), 853.

[168] Thomsen, J., Ferri, F. and Kofoed, J. [2017*b*], 'Validation of a tool for the initial dynamic design of mooring systems for large floating wave energy converters', *Journal of Marine Science and Engineering* **5**(4), 45.

[169] Thomsen, J., Ferri, F., Kofoed, J. and Black, K. [2018], 'Cost optimization of mooring solutions for large floating wave energy converters', *Energies* **11**(1), 159.

[170] Thomsen, J., Kofoed, J., Ferri, F., Eskilsson, C., Bergdahl, L., Delaney, M., Thomas, S., Nielsen, K., Rasmussen, K. D. and Friis-Madsen, E. [2017], On mooring solutions for large wave energy converters, *in* 'Proceedings of the 12th European Wave and Tidal Energy Conference'.

[171] Todalshaug, J., Steinn, G., Hjalmarsson, E., Maillet, J., Moller, P., Pires, P., Guerinel, M. and Lopes, M. [2015], Tank testing of an inherently phase controlled wave energy converter, *in* 'Proceedings of the 11th European Wave and Tidal Energy Conference'.

[172] Tollefson, J. [2014], 'Power from the oceans: Blue energy', *Nature* **508**(7496), 302–304.

[173] Uihlein, A. and Magagna, D. [2016], 'Wave and tidal current energy – a review of the current state of research beyond technology', *Renewable and Sustainable Energy Reviews* **58**, 1070–1081.

[174] Vicente, P. C. and Falcao, A. [2011], Nonlinear slack-mooring modelling of a floating two-body wave energy converter, *in* 'Proceedings of the 9th European Wave and Tidal Energy Conference'.

[175] Vissio, G. [2017], ISWEC toward the sea: Development, Optimization and Testing of the Device Control Architecture, PhD thesis, Politecnico di Torino.

[176] Vissio, G., Bracco, G., Giorcelli, E., Mattiazzo, G., Valério, D. and Beirão, P. [2016], ISWEC control tuning: Lessons learned, *in* 'Progress in Renewable Energies Offshore', CRC Press.

[177] Vissio, G., Passione, B., Carlo, C. D., Bracco, G., Giorcelli, E. and Mattiazzo, G. [2015], Iswec design tool, *in* 'Proceedings of the 11th European Wave and Tidal Energy Conference'.

[178] Vryhof [2010], *Anchor Manual 2010 - The Guide to Anchoring*, Vryhof Anchors BV.

[179] WAMIT [2015], *WAMIT User Manual*. USA.

[180] Wassermann, S., Feder, D.-F. and Abdel-Maksoud, M. [2016], 'Estimation of ship roll damping—a comparison of the decay and the harmonic excited roll motion technique for a post panamax container ship', *Ocean Engineering* **120**, 371–382.

[181] Weber, J. [2012], Wec technology readiness and performance matrix - finding the best research technology development trajectory, *in* 'Proceedings of the 4th International Conference on Ocean Energy'.

[182] WEC [2016], World energy resources, 2016, Technical report, World Energy Council.

[183] WEC [2017*a*], World energy trilemma 2017: Changing dynamics - using distributed energy resources to meet the trilemma challenge, Technical report, World Energy Council.

[184] WEC [2017*b*], World energy trilemma index 2017: Monitoring the sustainability of national energy systems, Technical report, World Energy Council.

[185] Wei, Y., Rafiee, A., Henry, A. and Dias, F. [2015], 'Wave interaction with an oscillating wave surge converter, part i: Viscous effects', *Ocean Engineering* **104**, 185–203.

[186] *Wello Penguin* [2018], https://wello.eu/. Accessed: April 2018.

[187] Westphalen, J. [2011], Extreme Wave Loading on Offshore Wave Energy Devices using CFD, PhD thesis, University of Plymouth.

[188] Wichers, J. [2013], *Guide to Single Point Moorings*, CreateSpace Independent Publishing Platform.

[189] WMO [1998], *Guide to wave analysis and forecasting (WMO)*, Secretariat of the World Meteorological Organization.

[190] Xsens [2017], *MTi User Manual*. Xsens Technologies.

[191] Yu, Y., Rij, J., Coe, R. and Lawson, M. [2015], Preliminary wave energy converters extreme loads analysis, *in* 'Proceedings of the ASME 2015, 34th International Conference on Ocean, Offshore adn Arctic Engineering'.

[192] Zanuttigh, B., Martinelli, L. and Castagnetti, M. [2011], Screening of suitable mooring systems, Technical report, SDWED.

[193] Zhao, W., Efthymiou, M., McPhail, F. and Wille, S. [2016], 'Nonlinear roll damping of a barge with and without liquid cargo in spherical tanks', *Journal of Ocean Engineering and Science* **1**(1), 84–91.

Appendix A

Secular wave - Experimental results

Motions Spectral analysis

Table A.1 Heave records spectral properties - 100 years wave

Test ID		Time record	z_{m0}	max	min	mean	rms	T_p
		s	mm	mm	mm	mm	mm	s
1	$C1-101$	2417	283	357	-292	6	71	2.29
2	$C1-102$	2423	282	406	-250	2	71	2.28
3	$C1-103$	2496	282	349	-265	4	70	2.28
4	$C2a-101$	2466	282	378	-272	3	70	2.28
5	$C2a-102$	2445	282	368	-266	2	70	2.28
6	$C2a-103$	2431	282	341	-279	2	70	2.28

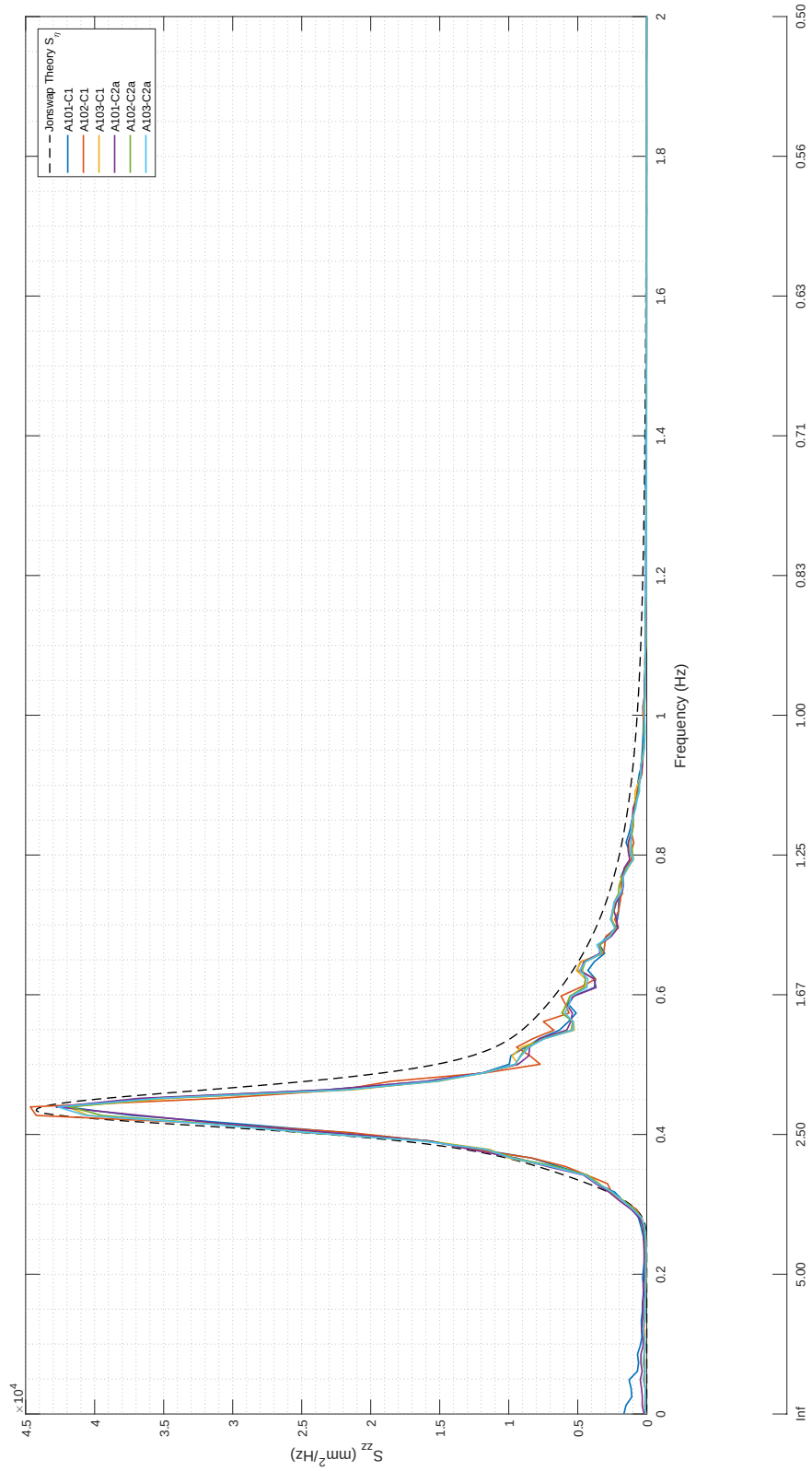

Fig. A.1 Waves power spectral density - 100 years wave

Table A.2 Pitch records spectral properties - 100 years wave

Test ID		Time record	δ_{m0}	max	min	mean	rms	T_p
		s	deg	deg	deg	deg	deg	s
1	$C1-101$	2417	31.0	31.6	-31.8	0.1	7.9	1.1
2	$C1-102$	2423	32.8	30.6	-30.3	0.1	8.2	1.1
3	$C1-103$	2496	33.2	33.7	-31.1	0.1	8.2	1.1
4	$C2a-101$	2466	31.6	30.7	-30.4	0.2	7.8	1.1
5	$C2a-102$	2445	32.4	30.2	-30.4	0.3	8.1	1.1
6	$C2a-103$	2431	32.5	28.0	-30.2	0.2	8.1	1.1

Table A.3 Surge records spectral properties - 100 years wave

Test ID		Time record	x_{m0}	max	min	mean	rms	T_p
		s	mm	mm	mm	mm	mm	s
1	$C1-101$	2417	1022	3857	1993	3189	259	55
2	$C1-102$	2423	1045	3836	1732	3185	263	55
3	$C1-103$	2496	1061	3933	1641	3288	272	55
4	$C2a-101$	2466	883	3940	2306	3126	227	34
5	$C2a-102$	2445	932	4090	2361	3234	238	34
6	$C2a-103$	2431	960	4096	2401	3179	245	34

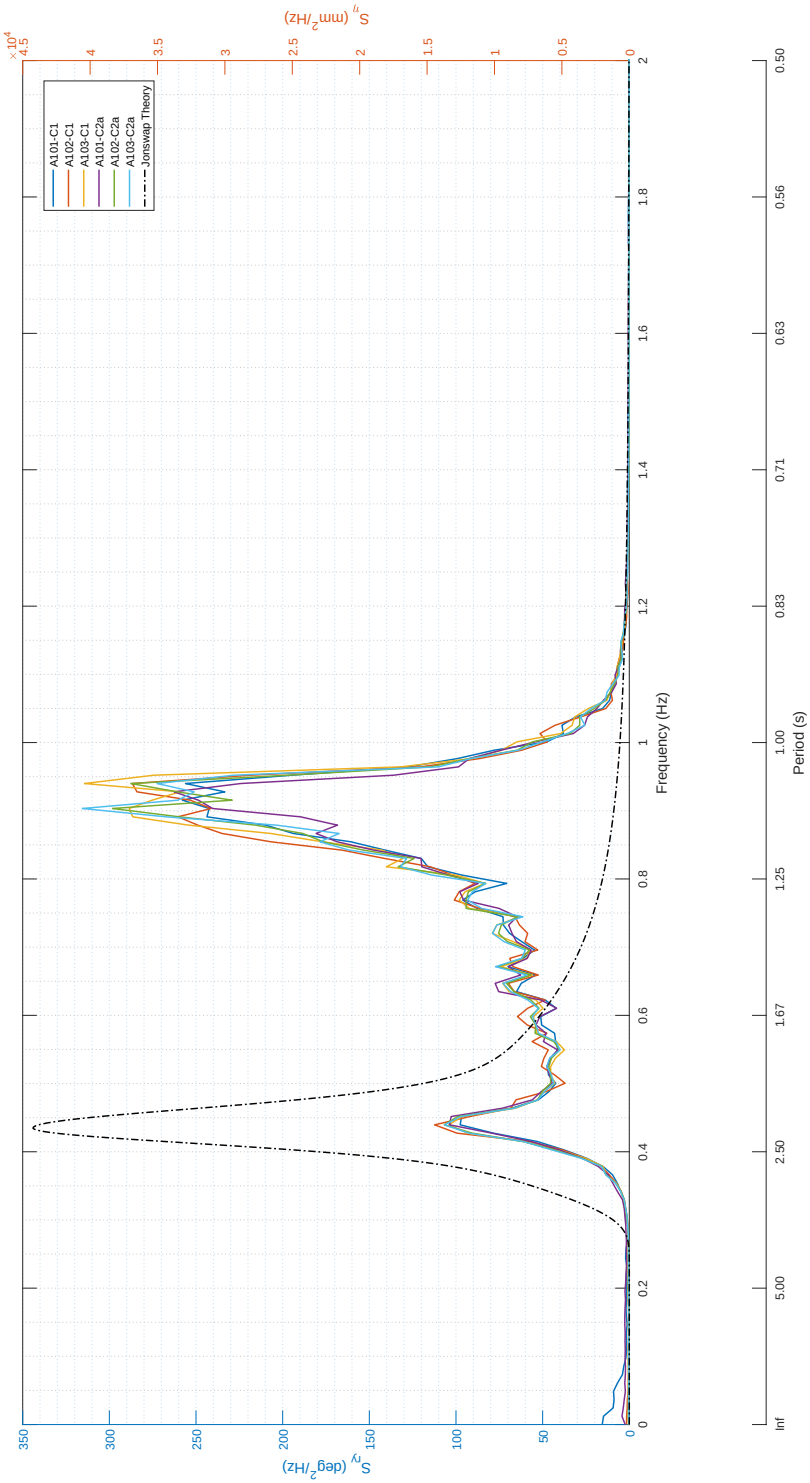

Fig. A.2 Pitch power spectral density - 100 years wave

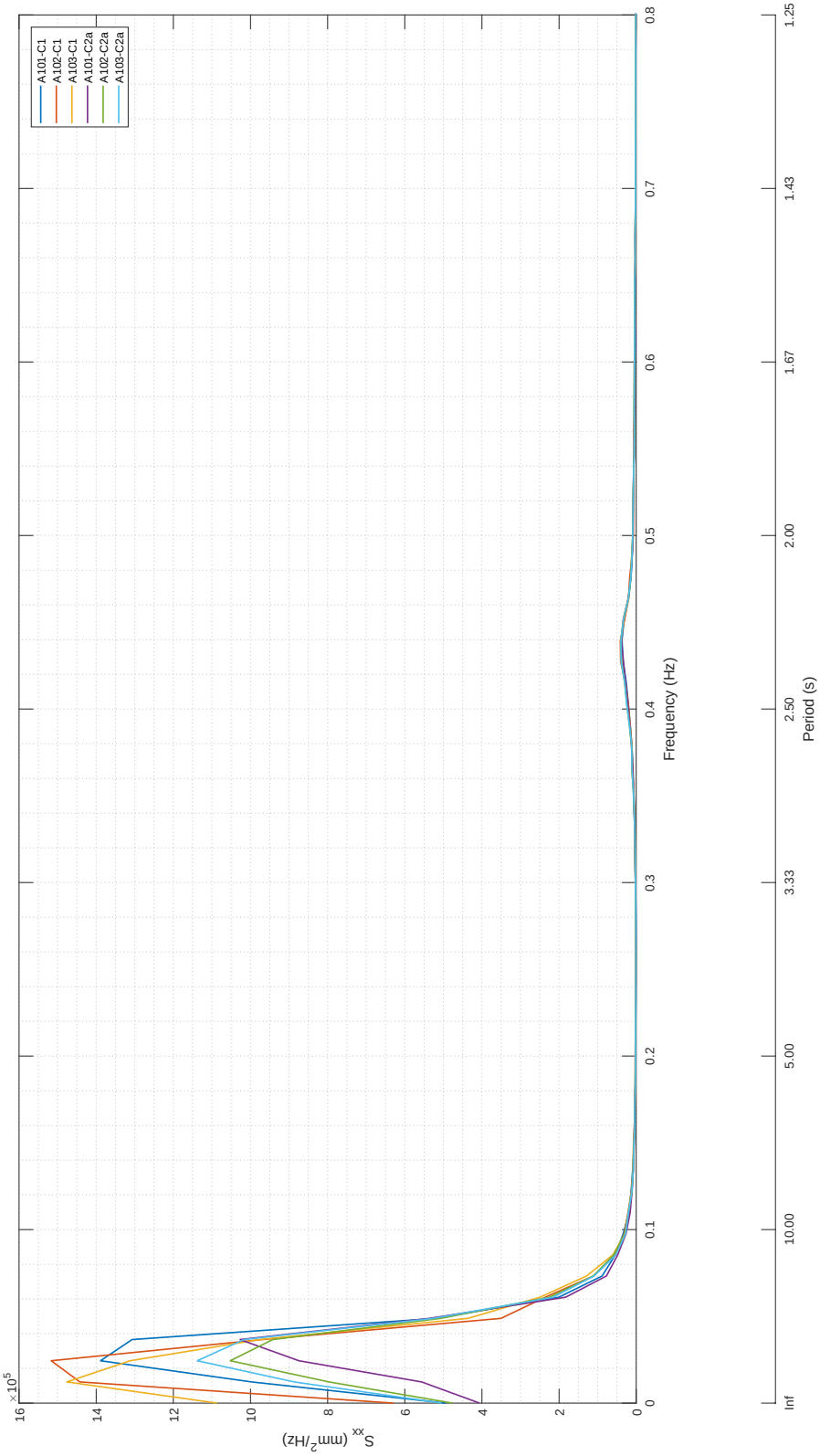

Fig. A.3 Surge power spectral density - 100 years wave (total frequency range)

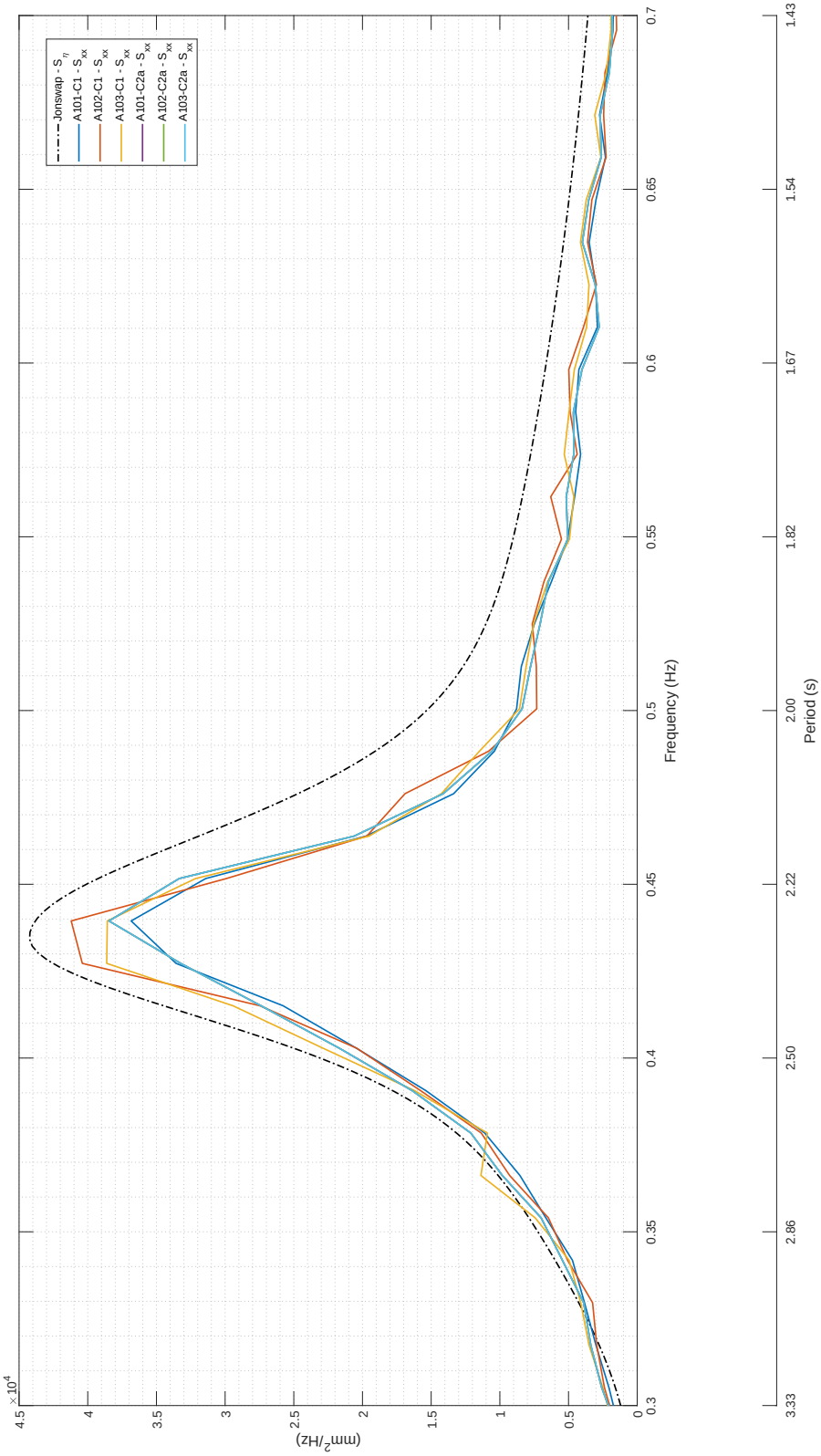

Fig. A.4 Surge power spectral density - 100 years wave (Zoom on wave frequency)